PHOSPHOINOSITIDE SIGNALING AND POLARIZED MEMBRANE GROWTH: A PERSPECTIVE FROM SEC14-LIKE PITPS

DISSERTATION

der Mathematisch-Naturwissenschaftlichen Fakultät
der Eberhard Karls Universität Tübingen
zur Erlangung des Grades eines
Doktors der Naturwissenschaften
(Dr. rer. nat.)

vorgelegt von
Marília Kaphan Freitas de Campos
aus Londrina-Brasilien

Tübingen
2014

Tag der mündlichen Qualifikation:	17.06.2014
Dekan:	Prof. Dr. Wolfgang Rosenstiel
1. Berichterstatter:	Dr. Gabriel Schaaf
2. Berichterstatter:	Prof. Dr. Klaus Harter

I dedicate this work to my sisters and my brothers, with love.

“No mundo do bobol, glosus glass vira savilha. Aquele negocinho, sabe?”

ACKNOWLEDGEMENTS

I first and foremost would like to thank my supervisor Dr. Gabriel Schaaf for the opportunity to come to Germany for pursuing my PhD. I am deeply grateful for his always-open doors, the knowledge he never spares sharing, and the constant and genuine will to help. Thanks, G!

I also thank Prof. Dr. Klaus Harter, Prof. Dr. Claudia Oecking and Prof. Dr. Rita Groß-Hardt, who kindly agreed to take part in the examining committee and surely contributed to the successful conclusion of my PhD studies.

I feel extremely lucky to have had the opportunity to work with the current and former members of the lab Schaaf. Thank you guys, for the day-to-day help, for the lively discussions, for the breaks and for the shared random information that made the days much more interesting! I am especially grateful for the technical support provided by Elke Sauberzweig and for the morning rides that developed in a great friendship.

I thank all members of the ZMBP, especially my colleagues from the Plant Physiology department for the enjoyable working atmosphere.

My sincere gratitude also goes to my dear friend Eva Winklbauer, her mother Regina Ort and her brother Thomas Winklbauer, for the endless support that greatly contributed to a smooth and pleasurable adaptation in Germany. Vielen Dank für alles!

My special thanks go to my parents, for the love and the constant encouragement to go after my dreams, even if they ended up being on the other side of the ocean.

I am especially grateful to my beloved Marek, for the patience and all the technical and emotional support in the last years. I also thank his parents, Monika and Hans-Joachim Dynowski, and his sister Janina Dynowski, who warmly welcomed me in the family.

Finally, I thank Dr. Anderson Rotter Meda, who mediated my first contact with Germany and made this all possible.

TABLE OF CONTENTS

SUMMARY

Sec14-like phosphatidylinositol/phosphatidylcholine (PtdIns/PtdCho) transfer proteins (PITPs) represent important regulatory components that integrate phospholipid metabolism and membrane trafficking in eukaryotes. Data derived from yeast studies suggest that this regulation results from a Sec14-mediated PtdIns/PtdCho exchange reaction that stimulates PtdIns kinase activity, thus facilitating the generation of phosphoinositides (PIPs) such as PtdIns(4)P and PtdIns(4,5)P_2. The present work reports recent findings on the roles and functional mechanisms of yeast and plant Sec14-like PITPs. The Arabidopsis Sec14-nodulin AtSFH1, an important regulator of root hair formation, was used as a model to show that the nodulin domain represents a plasma membrane association module with high binding specificity towards PtdIns(4,5)P_2. A Lys-rich C-terminal motif is necessary for PIP binding activity, which is amplified by homo-oligomerization of the nodulin domain. Both PIP association and homo-oligomerization are essential properties of AtSFH1 and mutants defective in PtdIns(4,5)P_2 binding can be rescued by a translational fusion with a *bona fide* PtdIns(4,5)P_2 binding domain. A model for the mode of action of AtSFH1 is proposed herein, and suggests that the physical linkage of the N-terminal Sec14 and the nodulin domains couples PIP synthesis and organization, so as to promote defined landmarks for PIP effectors that modulate developmental control of polarized membrane growth. A second approach used to gain further insights on AtSFH1 functions is also discussed. EMS-mutagenized plants that suppress the *atsfh1-1*-dependent short root hair phenotype were isolated. By employing next-generation sequencing combined with deep candidate resequencing (dCARE), a mutation in the AtSTR1 sulfurtranferase encoding gene was identified. The preliminary results presented here suggest that cyanide detoxifying enzymes could represent additional cellular components that regulate root hair development, possibly in a pathway that is independent of AtSFH1. Finally, a directed evolution screen was performed in order to identify mutations that confer Sec14-like activities to the functionally inactive yeast Sec14 homolog Sfh1. Biochemical, biophysical and computational approaches helped to discover a network of transient interactions that propagates conformational energy from the lipid binding pocket to the 'helical gating module' that controls lipid access, thus enhancing the rates of phospholipid exchange and presentation in the mutant proteins. Taken together, the discoveries presented herein provide important details into the mechanisms regulating phospholipid exchange and PIP organization by Sec14-like PITPs, as well as comprehensive clues of how these fascinating proteins ultimately promote phosphoinositide homeostasis in eukaryotes.

ZUSAMMENFASSUNG

Phosphatidylinositol/Phosphatidylcholine (PtdIns/PtdCho) Transferproteine (PITPs) der Sec14-Familie sind wichtige Regulatoren eukaryontischer Zellen, die die Feinabstimmung zwischen Phospholipidstoffwechsel und intrazellulärem Vesikeltransport koordinieren. Erkenntnisse aus dem Modellsystem Hefe weisen darauf hin, dass diese regulatorischen Funktionen durch eine von Sec14 vermittelte PtdIns/PtdCho Austauschreaktion verursacht wird, die zu einer Stimulierung von PtdIns-Kinaseaktivitäten führt und dadurch die Synthese von Phosphoinositiden, wie z.B. PtdIns(4)P und PtdIns(4,5)P_2 einleitet. In der vorliegenden Arbeit werden die während meiner Dissertation erhaltenen Erkenntnisse über die Bedeutung und Funktionsweise von Hefe- und pflanzlichen PITPs der Sec14-Familie präsentiert. Von besonderem Interesse waren hierbei die nur in Pflanzen vorkommenden Sec14-Nodulin Proteine, die neben einer N-terminalen Sec14-Domäne eine C-terminale Domäne unbekannter Funktion besitzen, welche Homologie zum Nlj16-Nodulin aus *Lotus japonicus* aufweist. Das Arabidopsis Sec14-Nodulin AtSFH1 spielt eine wichtige Rolle bei der Entwicklung von Wurzelhaaren. In dieser Dissertation konnte gezeigt werden, dass die Nodulin-Domäne von AtSFH1 ein Plasmamembran-Assoziierungsmodul darstellt, das sich durch eine hohe Bindespezifität für PtdIns(4,5)P_2 auszeichnet. Ein Lysin-reiches C-terminales Motiv ist hierbei verantwortlich für die Phosphoinositid-Bindeaktivität, die durch Homooligomerisierung der Nodulin-Domäne verstärkt wird. Die hierzu durchgeführten Experimente ergaben, dass sowohl das Binden von PtdIns(4,5)P_2 als auch die Homooligomerisierung essentielle Eigenschaften von AtSFH1 sind. Des Weiteren werden mutierte Proteine, die nicht mehr in der Lage sind, PtdIns(4,5)P_2 zu binden, durch Fusion mit etablierten, spezifischen PtdIns(4,5)P_2-Bindedomänen wieder funktional. Das auf diesen Arbeiten aufbauende Modell postuliert, dass die physikalische Verknüpfung von Sec14- und Nodulin-Domäne auf einem einzigen Polypeptid diese Proteine dazu befähigt, die Biosynthese von Phosphoinositiden mit ihrer Organisation zu koppeln, und dass Sec14-Nodulin Proteine hierdurch lateral begrenzte, privilegierte Membranbereiche für Phosphoinositid-abhängige Effektoren definieren, die ihrerseits entwicklungsabhängige Prozesse des polaren Vesikeltransportes modulieren. Ein zweiter Ansatz, um weitere Einblicke in die Funktionsweise von AtSFH1 zu erhalten, wird ebenfalls diskutiert. Ausgehend von einer EMS-behandelten Population konnten Mutanten isoliert werden, in denen der *atsfh1-1*-abhängige Wurzelhaardefekt supprimiert wird. Mit Hilfe von Sequenziermethoden der zweiten Generation (Illumina-Brückensynthese kombiniert mit ‚deep candidate resequencing'-Analyse) konnte eine Mutation im für die AtSTR1 Sulfurtranferase-kodierenden Gen identifiziert werden. Die vorläufigen Analysen weisen darauf hin, dass Cyanid-detoxifizierende Enzyme wichtige Regulatoren der Wurzelhaarentwicklung darstellen, die möglicherweise unabhängig von AtSFH1 wirken. In einem letzten Ansatz wurde im Modellsystem Hefe (*Saccharomyces cerevisiae*) ein Screen zur gerichteten Evolution durchgeführt, mit dessen Hilfe Mutationen identifiziert werden konnten, die das nicht-funktionale Sec14-Homolog 1 (SFH1) mit Sec14-ähnlichen Eigenschaften ausstattet. Durch eine Kombination von biochemischen, biophysischen und *in silico*/molekulardynamischen Methoden konnte

hierbei ein Netzwerk transienter Interaktionen identifiziert werden, das Konformationsenergie aus der Lipidbindetasche des Proteins zu einem helikalen Motiv weiterleitet, welches den Zugang von Lipid in die hydrophobe Tasche reguliert. Die Mutationen führen damit zu einer gesteigerten Lipidaustauschrate und Lipidpräsentation. Zusammengenommen erlauben die hier beschriebenen Erkenntnisse wichtige mechanistische Einblicke in die von Sec14-Proteinen vermittelten Phospholipidaustauschreaktionen, sowie ein besseres Verständnis der durch diese Proteine hervorgerufenen Organisation von Phosphoinositiden. Damit liefert die vorliegende Arbeit einen wichtigen Beitrag zum Verständnis der durch Sec14-Proteine vermittelten Phosphoinositid-Homöostase in Eukaryonten.

CHAPTER 1

SEC14 PROTEINS: INTEGRATIVE COMPONENTS OF LIPID METABOLISM, SIGNALING AND MEMBRANE TRAFFICKING

Marília K.F. de Campos

ZMBP, Plant Physiology, Universität Tübingen 72076 Tübingen, Germany

In this chapter I discuss major elements underlying the functions of phosphatidylinositol/ phosphatidylcholine transfer proteins (PITPs): phosphoinositide (PIP) metabolism, signaling and membrane trafficking, and how these aspects are integrated by Sec14-like PITPs. I start defining phosphoinositides, briefly presenting the key components that control their metabolism, and the downstream cellular events that these molecules regulate. I first present a generalized view of the PIP functions in eukaryotic cells, here approached mainly by studies using the baker's yeast *Saccharomyces cerevisiae* as model system, to later emphasize the particular and outstanding roles they play in plants.

On the second part of this chapter I introduce the concept of phospholipid transfer proteins, and explain how recent work on Sec14 sets other functions for PITPs other than vectorial lipid carriers. I then focus on a novel modular arrangement of Sec14 proteins discovered in plants, the Sec14-nodulin, and its importance in regulating polarized cell growth, and finalize with the open questions and objectives of this work, further addressed on the following chapters.

Phosphoinositides: definition and functions

Phosphoinositides (PIPs) are by definition a group of membrane lipids comprised of phosphorylated products of phosphatidylinositol (PtdIns). The hydroxyl groups on positions 3, 4 and 5 of PtdIns inositol ring can be reversibly phosphorylated, potentially generating 7 different PIP species: PtdIns(3)P, PtdIns(4)P, PtdIns(5)P, PtdIns(3,4)P_2, PtdIns(3,5)P_2, PtdIns(4,5)P_2, and PtdIns(3,4,5)P_3 (Di Paolo and De Camilli, 2006; Kutateladze, 2010). All 7 phosphoinositide isoforms have been identified in eukaryotic cells; however, the presence and abundance of these molecules significantly vary among organisms, as well as their spatial and temporal distribution within subcellular compartments.

The heterogeneous localization of specific lipid-modifying enzymes such as PtdIns/PIP kinases, PIP phosphatases, and phospholipases is the major contributor to a distinguished PIP distribution in intracellular membranes, thus endorsing phosphoinositides as important markers for organelle identity (Kutateladze, 2010). For instance, endosomes and vacuolar membranes are enriched in PtdIns(3)P, while PtdIns(4)P and PtdIns(4,5)P_2 are mainly found at the Golgi complex and at the plasma membrane, respectively. Their distinct subcellular distribution supports the concept of PIPs acting as landmarks that

selectively recruit and regulate protein complexes at specific sites at the membrane/cytosol interface, where they perform their cellular functions (Lemmon, 2008; Martin, 1998).

PtdIns(3)P and derivatives

PtdIns(3)P is the product of the 3-OH phosphorylation of PtdIns primarily by the class III PtdIns 3-OH kinase (PI3K) VPS34 (Odorizzi et al., 2000; Schu et al., 1993). It is mainly found on the surface of endosomes and internal vesicles of multivesicular bodies (MVBs) in mammalian cells, and in yeast PtdIns(3)P is enriched on vacuolar membranes and endosomes (Gillooly et al., 2000). PtdIns(3)P-binding modules such as FYVE (acronym of Fab1, YOTB, Vac1, and EEA1) or PX (phox homology) domains are present in several endosomal proteins like the mammalian EEA1 (early endosomal autoantigen 1), which interacts with the small GTPase Rab5 and mediate fusion and docking of early endosomes (Simonsen et al., 1998). Additional roles played by PtdIns(3)P involve key aspects of endosomal function, such as interaction with the cytoskeleton, signaling and motility, as well as acting as a PtdIns(3)P 5-OH kinase (PI3P5K) substrate for the generation of PtdIns(3,5)P_2, required for proper trafficking from late endosomes/MVBs to the vacuolar lumen (Di Paolo and De Camilli, 2006). The rapid accumulation of PtdIns(3,5)P_2 upon hyperosmotic stress in yeast and plants also suggests a conserved and crucial role of this PIP in stress adaptation responses (Dove et al., 1997; Munnik and Vermeer, 2010).

In plant cells, PtdIns(3)P is mainly found in endosomes and vacuolar membranes (Vermeer et al., 2006), and seems to be essential for several aspects of development. Antisense expression of the single VPS34-like PI3K from *Arabidopsis thaliana* (*AtVPS34*) causes severe inhibition of plant growth and development (Welters et al., 1994), and *AtVPS34* T-DNA insertional mutants were found to be gametophytic lethal (Lee et al., 2008b). The authors also showed that heterozygous *AtVPS34/atvps34* plants produced pollen that segregated in fertile grains and sterile pollen with abnormal vacuole organization and nuclear division (Lee et al., 2008b). PtdIns(3)P is also suggested to be required for root hair elongation. By blocking the signal transduction downstream of PtdIns(3)P via the root hair-specific expression of the PtdIns(3)P-binding FYVE domain, as well as the treatment with a specific PI3K inhibitor led to plants with compromised root hair growth (Lee et al., 2008a). PtdIns(3,5)P_2 too is suggested to play critical roles in plants. Arabidopsis mutants that do not express the PI3P5K encoding genes *FAB1* and *FAB2* show defects in vacuolar biogenesis in pollen (Whitley et al., 2009), and presented reduced stomatal closure upon ABA treatment in comparison to wild-type plants (Bak et al., 2013).

PtdIns(4)P

PtdIns(4)P is a monophosphorylated PIP highly enriched at the Golgi complex, where it regulates its function and morphology. Besides, PtdIns(4)P is also found and exerts functions in other cellular compartments, such as the plasma membrane (PM) and the nucleus (D'Angelo et al., 2008). This PIP is generated via the phosphorylation of the 4-OH of PtdIns inositol ring by PtdIns 4-OH kinases

(PI4Ks), categorized into types II and III (Balla and Balla, 2006). The type II enzymes include the mammalian PI4KIIα and PI4KIIβ, and the yeast orthologue Lsb6, which is non-essential and responsible to only a minor fraction of PtdIns(4)P levels in cells under normal conditions (Han et al., 2002). On the other hand, the two isoforms of type III PI4Ks (α and β) are crucial for the generation of distinct PtdIns(4)P pools at the plasma membrane and at the Golgi complex, respectively.

The yeast type IIIβ PI4K Pik1 is localized to Golgi membranes and the nucleus, providing two pools of PtdIns(4)P with distinct functions. In the nucleus, Pik1 may provide substrate for synthesis of PtdIns(4,5)P_2, the main precursor of inositol 1,4,5-trisphosphate ($InsP_3$) and other more highly phosphorylated $InsP_x$s, which apparently play important nuclear functions such as the regulation of mRNA export, chromatin remodeling and telomere length (Strahl et al., 2005). At the Golgi, however, Pik1-derived PtdIns(4)P plays other roles rather than a precursor for second messengers: it is itself crucial for maintenance of Golgi structure and its secretory function (Schuh and Audhya, 2012). Yeast mutants defective in Pik1 activity present severe membrane trafficking defects and accumulate 'Berkeley bodies' (Audhya et al., 2000), aberrant membrane structures typically found in mutants defective in secretion, firstly described on Peter Novick's seminal work (Novick et al., 1980).

Effector proteins known to bind PtdIns(4)P include the major *trans*-Golgi network (TGN) clathrin adaptor AP-1 (Wang et al., 2003), its interactor EpsinR (Hirst et al., 2003), the four-phosphate-adaptor proteins 1 and 2 (FAPP1 and FAPP2) (Godi et al., 2004), members of the oxysterol-binding protein family (OSBPs), including the yeast OSBP homologue Osh4/Kes1 (Li et al., 2002), and ceramide transfer protein (CERT) (Hanada et al., 2003). Most of these effectors bind PtdIns(4)P via lipid-binding domains, which can also act in combination with additional proteins in a coincidence detection mechanism. For instance, FAPPs associate with TGN exit sites through their pleckstrin-homology (PH) domain, that specifically bind PtdIns(4)P and the small GTPase Arf (Godi et al., 2004). This dual recognition further contributes to a specialized membrane composition and the definition of distinct membrane domains (D'Angelo et al., 2008).

The only type IIIα PI4K found in yeast is Stt4, which is responsible for the synthesis of the plasma membrane pool of PtdIns(4)P (Audhya and Emr, 2002), further converted to PtdIns(4,5)P_2 by the PtdIns(4)P 5-OH kinase (PIP5K) Mss4 (Audhya and Emr, 2003). Both Pik1 and Stt4 are essential in yeast, suggesting non-overlapping functions of the distinct PtdIns(4)P pools generated by these enzymes (Audhya et al., 2000). In fact, even though overall PtdIns(4)P levels are decreased upon inactivation of temperature-sensitive (*ts*) alleles of either PI4K genes, *stt4*^{ts} phenotypes do not resemble the secretory defects found in *pik1*^{ts} mutants at restrictive temperatures, but include: loss of cell wall integrity, deranged actin cytoskeleton organization and abnormal vacuolar morphology (Audhya et al., 2000). All except the later phenotype are also found in *mss4*^{ts} strain upon heat inactivation; besides, overexpression of *MSS4* can alleviate cell wall defects of *stt4*^{ts} (Yoshida et al., 1994), strongly suggesting a role for Stt4-derived PtdIns(4)P as a precursor of plasma membrane PtdIns(4,5)P_2 in the regulation of these processes. On the other hand, the changes in vacuolar morphology observed in *stt4*^{ts}

mutants are independent of Mss4 activity, which indicates a function of PtdIns(4)P in regulating organelle homeostasis such as vacuole fusion and fission (Audhya et al., 2000). Finally, an involvement of Stt4 in phosphatidylserine transport from the ER to the Golgi or to the vacuole has also been proposed (Trotter et al., 1998).

In addition to lipid kinases (i.e. Pik1, Stt4 and Mss4), PtdIns(4)P metabolism is also regulated by the activity of Sac1-like PIP phosphatases. In yeast, PtdIns(4)P levels are significantly increased upon Sac1 inactivation, resulting in impaired membrane trafficking, deranged vacuolar morphology, altered lipid metabolism and growth defects (Foti et al., 2001). Sac1 is a type II integral membrane protein localized mainly to the ER. However, upon starvation, yeast Sac1 traffics to the Golgi complex, where it depletes Pik1-generated PtdIns(4)P, consequently slowing down secretion (Faulhammer et al., 2007). Under normal growth conditions, it is actually the Stt4-derived PtdIns(4)P pool at the plasma membrane that is mainly regulated by Sac1 (Foti et al., 2001). In this case, PtdIns(4)P hydrolysis is suggested to take place on plasma membrane/ER contact sites, assisted by the oxysterol-binding homology protein Osh3, which acts as a sensor of plasma membrane PtdIns(4)P, as well as activator of the ER Sac1phosphatase (Stefan et al., 2011).

Recent studies using different plant systems and independent approaches suggest that PtdIns(4)P plays broader and more active roles in plants compared to other eukaryotes (Gagne and Clark, 2010; Preuss et al., 2004; Thole and Nielsen, 2008; Vermeer et al., 2009). One indication comes from the much higher ratio of PtdIns(4)P to PtdIns(4,5)P_2 found in plants (30 to 100 fold) compared to mammals and yeast, where equimolar amounts of both PIPs are commonly detected (van Leeuwen et al., 2007). This suggests that additional important functions for PtdIns(4)P other than a simple precursor role for PtdIns(4,5)P_2 production. A second hint of such complexity could also be the number of presumed PtdIns(4)P metabolizing enzymes encoded by the Arabidopsis genome: 12 putative PtdIns 4-OH kinases and nine SAC domain-containing proteins (Thole et al., 2008; Vermeer et al., 2009).

Similar to yeast, plants also contain different PtdIns(4)P pools, which were visualized by the expression of a YFP-PH_{FAPP1} fusion construct in four different plant systems (Vermeer et al., 2009). This PIP-sensor was shown to strongly stain the plasma membrane and motile punctate structures that co-localized with a Golgi marker. Additionally, PtdIns(4)P accumulated on the cell plate of dividing cells, and both Arabidopsis and *Medicago trunculata* root hairs presented a gradient PtdIns(4)P distribution, with the highest concentration at the tip (Vermeer et al., 2009). Interestingly, root hair defects are observed in Arabidopsis plants lacking proper activity of PtdIns 4-OH kinases PI4Kβ1 and PI4Kβ2 (Preuss et al., 2006), as well as the Sac1-like PtdIns(4)P phosphatase RHD4/SAC7 (Thole et al., 2008). These observations suggest that the precise regulation of PtdIns(4)P levels at tip-localized membranes is crucial for the maintenance of polarized secretion, in a process that involves also the RabA4b GTPase and the calcium sensor AtCBL1 (Preuss et al., 2006; Thole et al., 2008). Moreover, PtdIns(4)P was suggested to play an important role in promoting stem cell specification by binding and activating

POLTERGEIST (POL) and PLL1, two Arabidopsis type 2C protein phosphatases (PP2C) (Gagne and Clark, 2010).

PtdIns(4,5)P_2

Thirty years have passed since the first studies reporting the functions of PtdIns(4,5)P_2 in regulating signaling in animal cells (Berridge and Irvine, 1984). It has then been postulated that this PIP acts as the precursor of two essential second messengers: soluble inositol 1,4,5-trisphosphate ($InsP_3$), involved in mobilization of calcium from internal stores, and diacylglycerol (DAG), that remains at the plasma membrane and activates signaling via protein kinase C (Berridge and Irvine, 1984). In addition to this historical role, recent studies have demonstrated that PtdIns(4,5)P_2 directly regulates several distinct processes such as endocytosis, exocytosis, cytokinesis, maintenance of cell polarity and actin cytoskeleton organization (Schuh and Audhya, 2012).

As previously mentioned, the plasma membrane pool of PtdIns(4,5)P_2 in yeast is generated by the phosphorylation of the 5-OH of PtdIns(4)P by the PIP5K Mss4 (Audhya and Emr, 2003). Interestingly, Mss4 was shown to shuttle between the cytoplasm and the nucleus, thus regulating enzyme activity and the synthesis of PtdIns(4,5)P_2 at the plasma membrane (Audhya and Emr, 2003), as well as providing nuclear phosphoinositide pools suggested to play essential biological roles (e.g. in transcriptional regulation) (Strahl et al., 2005). PtdIns(4,5)P_2 turnover, on the other hand, is regulated by inositol 5-phosphatases (PI 5-Pases) and phospholipases (Schuh and Audhya, 2012). The yeast genome encodes four PI 5-Pases: three synaptojanin-like (Sjl) proteins named Sjl1, Sjl2 and Sjl3 (or Inp51, Inp52 and Inp53), that contain both 5-Pase and Sac1-like domains, and the one ER-localized Inp54, which contains only 5-Pase activity (Stefan et al., 2002; Wiradjaja et al., 2001). The single yeast phospholipase C isoform is Plc1, and it specifically hydrolyzes PtdIns(4,5)P_2 into $InsP_3$ and DAG (Rebecchi and Pentyala, 2000).

Not differently from other PIPs, the precise control of PtdIns(4,5)P_2 levels and distribution is essential for proper functioning of the cellular processes it regulates. Indeed, the manipulation of both yeast PIP5K and PI 5-Pases can lead to cell death or severe defects associated to impaired actin cytoskeleton organization and endocytosis (Audhya and Emr, 2002; Desrivieres et al., 1998; Stefan et al., 2002). For instance, deletion of *MSS4* is lethal and *mss4^{ts}* yeast strains lose viability after incubation at non-permissive temperatures, phenotype that corresponds to the strong reduction in PtdIns(4,5)P_2 levels, defects in cell morphology and disorganization of the actin cytoskeleton upon heat shock (Desrivieres et al., 1998; Homma et al., 1998). Furthermore, deletions of genes involved in actin cytoskeleton organization and cell polarity (e.g. *CAP1*, *CAP2*, *AVO2*, *SPA1*, *BEM4*, *BOI2*, *MYO5*, *CYK3*, *ILM1*, *VAN1* and *API2*), or components of the GimC chaperone complex (suggested to promote folding of actin monomers) were synthetic lethal with an *mss4^{ts}* allele in a genome-wide synthetic screen (Audhya et al., 2004).

Finally, the inactivation of yeast synaptojanins results in unordered accumulation of PtdIns(4,5)P_2, causing defects in the actin cytoskeleton, endocytic transport, cell surface morphology,

and clathrin-dependent transport between the TGN and endosomes (Stefan et al., 2002), indicating that a collected effort between these proteins and Mss4 is essential for precise PIP distribution required for cell viability. One key mechanism by which plasma membrane PtdIns(4,5)P_2 regulates its effectors is by activating the PKC pathway that regulates yeast cell wall integrity (Audhya and Emr, 2002). The authors suggest that PtdIns(4,5)P_2 recruits/activates the GTPase exchange factor (GEF) Rom2 via its PH domain, in turn activating the GTPase Rho1. GTP-bound Rho1 either interacts directly with cell-wall synthesizing enzymes, or additionally triggers a Pkc1-dependent MAP kinase cascade, that ultimately changes transcriptional regulation of several cell wall integrity genes (Audhya and Emr, 2002).

The importance of PtdIns(4,5)P_2 for proper plant development is not understated by the much lower levels detected in this system in comparison to other eukaryotes (van Leeuwen et al., 2007). In fact, the Arabidopsis genome encodes 11 PtdIns(4)P 5-OH kinases, several of which have been characterized and shown to play critical roles in several plant tissues and under distinct environmental conditions (Ischebeck et al., 2008; Kusano et al., 2008; Lee et al., 2007; Mei et al., 2012; Stenzel et al., 2008; Zhao et al., 2010). Plant PIP5Ks are categorized into types A and B; two isoforms (10 and 11) belong to the type A subfamily, with a similar domain structure found in mammalian PIP5Ks, while the remaining nine type B isoforms harbor an additional N-terminal domain that is plant-specific and contain several membrane occupation and recognition nexus (MORN) repeats, hypothesized to facilitate membrane association (Mueller-Roeber and Pical, 2002).

Two workgroups independently characterized one member of the Arabidopsis PIP5K family named PIP5K3, which is expressed in the root epidermis, preferentially in elongating root hairs (Kusano et al., 2008; Stenzel et al., 2008). Recombinant PIP5K3 converts PtdIns(4)P into PtdIns(4,5)P_2 *in vitro*, and fluorescence-tagged protein was visualized at the apex of elongating root hairs, correspondingly to PtdIns(4,5)P_2 localization (Stenzel et al., 2008). Both reports show that root hair elongation was compromised in at least three independent *pip5k3* mutants. However, in the work of Stenzel et al. (2008), root hairs of plants overexpressing PIP5K3 lost polarized growth, and the severity of the phenotype correlated with higher *PIP5K3* transcript levels. Interestingly, a slight increase in the expression levels of *PIP5K3* (Stenzel et al., 2008), as well as its inducible overexpression (Kusano et al., 2008) led to plants with longer root hairs than those of wild-type plants, suggesting that a fine balance of PIP5K3 activity, and thus in PtdIns(4,5)P_2 production, is required for proper control of root hair development.

The connection between PtdIns(4,5)P_2 and the regulation of polarized growth is also evident from studies with pollen tubes. Both PIP5K10 and PIP5K11, as well as members of the type B subfamily (PIP5K2, PIP5K4, PIP5K5 and PIP5K6) are expressed in those cells, and T-DNA insertional mutants present subtle to severe pollen germination or tube growth phenotypes (Ischebeck et al., 2011; Sousa et al., 2008; Stenzel et al., 2011; Zhao et al., 2010). All pollen expressed PIP5Ks were localized at a sub-apical plasma membrane domain close to the growing tip. However, overexpression of different isoforms resulted in distinct effects on pollen morphology and pollen tube growth (Ischebeck et al., 2011; Stenzel et al., 2011). For instance, overexpression of PIP5K4, PIP5K5 or PIP5K6 seems to affect

cell polarity by deregulating components of vesicle trafficking, such as clathrin-mediated endocytosis (Zhao et al., 2010) and membrane secretion (Ischebeck et al., 2008; Sousa et al., 2008). On the other hand, defects caused by overexpression of PIP5K2, PIP5K10 or PIP5K11 resulted in phenotypes associated with deranged actin cytoskeleton organization (Ischebeck et al., 2011; Stenzel et al., 2011), suggesting that even though distinct PIP5Ks are active in the same cell, they might contribute to different regulatory events that channel PtdIns(4,5)P_2 to individual cellular processes (Heilmann and Heilmann, 2013).

Despite regulating cell polarity in tip-growing cells, PtdIns(4,5)P_2 plays crucial roles in environmental stress adaptation. Its levels are dramatically increase in Arabidopsis submitted to osmotic stress (DeWald et al., 2001; Pical et al., 1999), and deletion of SAC9 PIP phosphatase leads to high accumulation of PtdIns(4,5)P_2 that correlates with a systemic stressed phenotype characterized by up-regulation of stress-induced genes, elevated reactive oxygen species (ROS) accumulation, constitutively closed stomata and a slow-growing phenotype (Williams et al., 2005). Besides, stomatal dynamics on guard-cells of *Vicia faba* leaves were inhibited when expressing GFP-$PH^{PLC\delta}$, widely used as a specific PtdIns(4,5)P_2 binding biosensor, which probably interrupts the normal interactions between PtdIns(4,5)P_2 and effector molecules (Jung et al., 2002). A strong staining of GFP-$PH^{PLC\delta}$ at the plasma membrane of guard-cells was detected upon white light illumination, indicating that PtdIns(4,5)P_2 accumulation is required for stomatal opening (Lee et al., 2007). Indeed, this opening was promoted by exogenous application of this PIP, possibly via PtdIns(4,5)P_2-dependent inhibition of anion channels. To support this hypothesis, the authors also showed that *pip5k4* mutants presented slow stomata opening movements, a phenotype that was complemented by exogenous application of PtdIns(4,5)P_2 (Lee et al., 2007).

Yeast PITPs: Sec14 and the regulation of vesicle trafficking

Over the years, numerous reports have extensively shown that phosphoinositide biosynthesis and turnover are regulated by a plethora of lipid-modifying enzymes (i.e. phosphatases, kinases and phospholipases), so far centered in this discussion. On this session, I focus on the roles of phosphatidylinositol/phosphatidylcholine (PtdIns/PtdCho) transfer proteins (PITPs), which represent additional key components that link lipid metabolism with specific membrane trafficking events. PITPs are defined as phospholipid transfer proteins that facilitate the energy-independent transfer of either PtdIns or PtdCho between membrane bilayers *in vitro*. Such transfer assays were interpreted to reflect PITPs' function as carriers that transport lipid monomers between distinct organelle membranes, for example PtdIns from the ER, where it is synthesized, to membranes involved in PIP signaling (Cleves et al., 1991a; Phillips et al., 2006).

The major PITP in *Saccharomyces cerevisiae* is Sec14, which represents the prototype of a large superfamily with members distributed exclusively among eukaryotes (Mousley et al., 2007; Phillips et al., 2006). The yeast genome encodes five Sec14 homologues, Sfh1, Sfh2, Sfh3, Sfh4 and Sfh5 (as

acronyms for Sec-Fourteen Homologues) (Li et al., 2000). Sfh1 is the closest to Sec14, sharing 64% primary sequence identity, yet these proteins perform non-redundant roles (Phillips et al., 2006), features that are addressed in detail in chapters 4 and 5, providing remarkable insights into Sec14-like PITPs functions.

Sec14 is a peripheral membrane protein localized to the Golgi complex, where it plays essential roles for the biogenesis of secretory vesicles that leave the TGN (Bankaitis et al., 1989; Cleves et al., 1991b). The mechanisms underlying this outcome are not fully understood, however, evidences from structural analyses and yeast genetics provided vital information on how Sec14 binds phospholipids, and how these binding reactions orchestrate lipid signaling with the regulation of proteins involved in vesicle budding (Phillips et al., 2006). The available Sec14 crystal structure consists of 12 α-helices, six β-strands and eight 3_{10}-helices. The C-terminal domain forms a hydrophobic pocket that is large enough to accommodate a single phospholipid monomer, while the N-terminal tripod-like motif includes amino acid residues sufficient for Sec14 targeting to Golgi membranes (Sha et al., 1998). The hydrophobic pocket is reinforced by a string-like motif, whose perturbation in the *sec14* temperature sensitive mutant (caused by a G266D substitution) results in destabilization of the phospholipid-binding domain, rendering defects in phospholipid transfer *in vitro* and biological functions *in vivo* (Bankaitis et al., 1989; Sha et al., 1998).

The original structure was crystallized as an apo-Sec14, where the hydrophobic pocket was occupied by two molecules of β-octylglucoside, the detergent utilized for crystallization, and therefore failed to provide information of how biologically relevant phospholipids are bound (Sha et al., 1998). This issue was clarified by structural analysis of the close Sec14 homologue Sfh1 in complex with phosphatidylethanolamine (PtdEtn), PtdIns or PtdCho (Schaaf et al., 2008). The general features of Sec14 and Sfh1 structures are significantly similar, except for a repositioning of a C-terminal helical motif ($A_{10}T_4A_{11}$ in the context of the Sec14 molecule) that is supposed to gate phospholipid access to the binding pocket, and is closed in Sfh1 in contrast to an open conformation in apo-Sec14 (Schaaf et al., 2008; Sha et al., 1998). Because of the high primary sequence identity between Sfh1 and Sec14 (64%) and the structural similarity, information derived from the lipid bound Sfh1 crystal structures could be used for detailed functional analyses of Sec14, leading to the following fundamental conclusions: (1) Sec14 binds PtdIns and PtdCho at overlapping yet not identical positions: while the PtdCho headgroup is buried inside the hydrophobic pocket, the headgroup of PtdIns is positioned close to the protein surface. This finding enabled the generation of specific lipid binding mutants, that allowed to demonstrate that (2) both PtdIns- and PtdCho-binding are individually required for protein function. Furthermore, co-expression of PtdCho- and PtdIns-binding deficient mutant Sec14 molecules failed to rescue defects associated with Sec14 deficiencies, indicating that (3) both lipid binding activities must reside at the same protein molecule to reconstitute a functional Sec14 protein. In agreement with this idea, Sec14 mutants defective in PtdCho binding (but still perfectly functional in *in vitro* PtdIns transfer and binding) fail to stimulate any detectible PtdIns(4)P synthesis *in vivo* (Schaaf et al., 2008).

Collectively, the data presented by Schaaf et al. (2008) proved inadequate the idea of Sec14 operating as a simple lipid carrier. The current model suggests that Sec14 stimulates Pik1 PtdIns 4-OH kinase activity and PtdIns(4)P homeostasis at the *trans*-Golgi network by overcoming an intrinsic inefficiency of the kinase to recognize its liposomal (i.e. membrane located) substrate. Sec14 helps to overcome this intrinsic inefficiency by coordinating a heterotypic (i.e. PtdIns vs. PtdCho and vice-versa) phospholipid exchange reaction, during which the PtdIns headgroup is dislodged from the context of the membrane bilayer and thereby prone for Pik1 kinase attack, thus generating a PtdIns(4)P pool ultimately required for vesicle biogenesis (Bankaitis et al., 2012; Schaaf et al., 2008).

Coupled to the structural information, studies with yeast genetics provided further insights into the biological relevance of Sec14-mediated Pik1 activation, and the downstream effects on the generation of secretory vesicles. Seven individual loss-of-function mutations in nonessential genes were shown to alleviate *sec14-1*^{ts} defects, and this approach proved to be a valuable tool for clarifying Sec14 functions (Mousley et al., 2007; Phillips et al., 2006). In this direction, comprehensive analyses of the 'bypass Sec14' mutants (e.g. strains that harbor mutations in genes encoding enzymes of the CDP-choline pathway for PtdCho biosynthesis, Sac1 PIP phosphatase and the OSBP Kes1) identified positive and negative regulators of Sec14 activity, and connected the process of vesicle biogenesis with metabolism of specific lipids, including PtdCho, diacylglycerol (DAG) and PtdIns(4)P (Cleves et al., 1991b; Cleves et al., 1989; Fang et al., 1996).

Synthetic interactions also represent important tools that help to identify potential Sec14 regulators and effectors (Curwin et al., 2009; Mousley et al., 2008; Yanagisawa et al., 2002). On a synthetic genetic array (SGA) analysis, inactivation of 40 genes exacerbated *sec14-1*^{ts} defects (Curwin et al., 2009). The largest group isolated on this screen included genes involved in the regulation of Golgi-dependent vesicular trafficking, results consistent with the postulated role of Sec14. Examples of genes whose deletions aggravate s*ec14-1*^{ts} growth include: *YPT31*, which encodes a Golgi-localized Rab GTPase that regulates vesicle export and import; components of the TRAPPII complex, proposed to act as a GTPase exchange factor (GEF) required for activation of YPT31 and its homologue YPT32; *GYP1*, that encodes a GTPase activating protein (GAP) for the *cis*-Golgi associated Rab YPT1; and *TLG2*, encoding a syntaxin-like t-SNARE that mediates fusion of endosome-derived vesicles to the TGN (Curwin et al., 2009; Mousley et al., 2008).

Interestingly, many of the gene deletions described on that study were also shown to worsen growth defects associated to the inactivation of the PI4K Pik1 (Sciorra et al., 2005), suggesting that a PtdIns(4)P pool generated by Sec14-activated Pik1 activity plays a pivotal role in connecting a complex network of regulatory proteins (e.g. Rab GTPases, GAPs and GEFs) that converge to regulate Golgi secretory function. One very suitable example for such PtdIns(4)P outcome is its essential requirement for recruiting to Golgi membranes Sec2, the GEF that activates Sec4 Rab GTPase (Mizuno-Yamasaki et al., 2010). In this case, PtdIns(4)P acts together with an active GTP-bound Ypt32, and both signals provide an appropriate environment for Sec2 regulation. In early secretory events, PtdIns(4)P binding

blocks Sec2 association to Sec15, a component of the octameric exocyst complex involved in vesicle tethering and fusion to the plasma membrane. After vesicle budding, Sec2 activates Sec4, and the reduced PtdIns(4)P levels at the vesicle membrane allow the competitive replacement of Ypt32 by Sec15 on Sec2, promoting the later steps of vesicle fusion (Mizuno-Yamasaki et al., 2010).

The complex nature of Sec14 biological functions is reinforced by its contribution to other levels of trafficking regulation. For instance, Sec14 is also involved in the maintenance of a functional cycle of the Arf-GTPase Arf1, a main recruiter of coat components at vesicle budding sites (Rothman, 1996). Secretory derangements observed upon inactivation of Gcs1 and Age2, two lipid-regulated ARFGAPs, resemble *sec14-1^{ts}* phenotypes (Poon et al., 2001), and *gcs1* and *age2* mutants individually show synthetic defects with *sec14-1^{ts}* (Yanagisawa et al., 2002). The mechanisms underlying a Sec14-dependent Arf1 regulation are unclear, though. The authors speculate that Gcs1/Age2 are not stimulated by PIPs, but respond to a Sec14-dependent lipid environment that essentially involves the coordination of DAG, PtdCho, and phosphatidic acid (PtdOH) (Yanagisawa et al., 2002). A graphic summary depicting models of how Sec14 might regulate secretory events in *Saccharomyces cerevisiae* is presented in Figure 1.

Plant PITPs: multi-domain Sec14 proteins and the regulation of polarity

As previously mentioned, the genome of *Saccharomyces cerevisiae* encodes six Sec14-like proteins. A distinct scenario, however, is found in higher eukaryotes (e.g. *Homo sapiens*, *Mus musculus*, *Drosophila melanogaster*, *Caenorhabditis elegans* and *Aradidopsis thaliana*), which individually account for more than 20 Sec14 superfamily members (Bankaitis et al., 2010). The Arabidopsis genome encodes at least 31 proteins that share different degrees of sequence homology to the yeast prototype Sec14. Interestingly, the great majority of these proteins is organized in modules consisting of an N-terminal Sec14 domain connected to a C-terminal polypeptide comprised of either a nodulin or a GOLD (Golgi dynamics) domain (Mousley et al., 2007).

Such modular arrangements suggest a high level of specialization of the biological functions controlled by these proteins. The GOLD domain, for instance, is present in several other proteins involved with Golgi dynamics and secretion, and is predicted to mediate protein-protein interactions required for the assembly of protein complexes to membranes, as well as cargo sorting into vesicles (Anantharaman and Aravind, 2002). Therefore, Sec14-GOLD modules could potentially link, on the

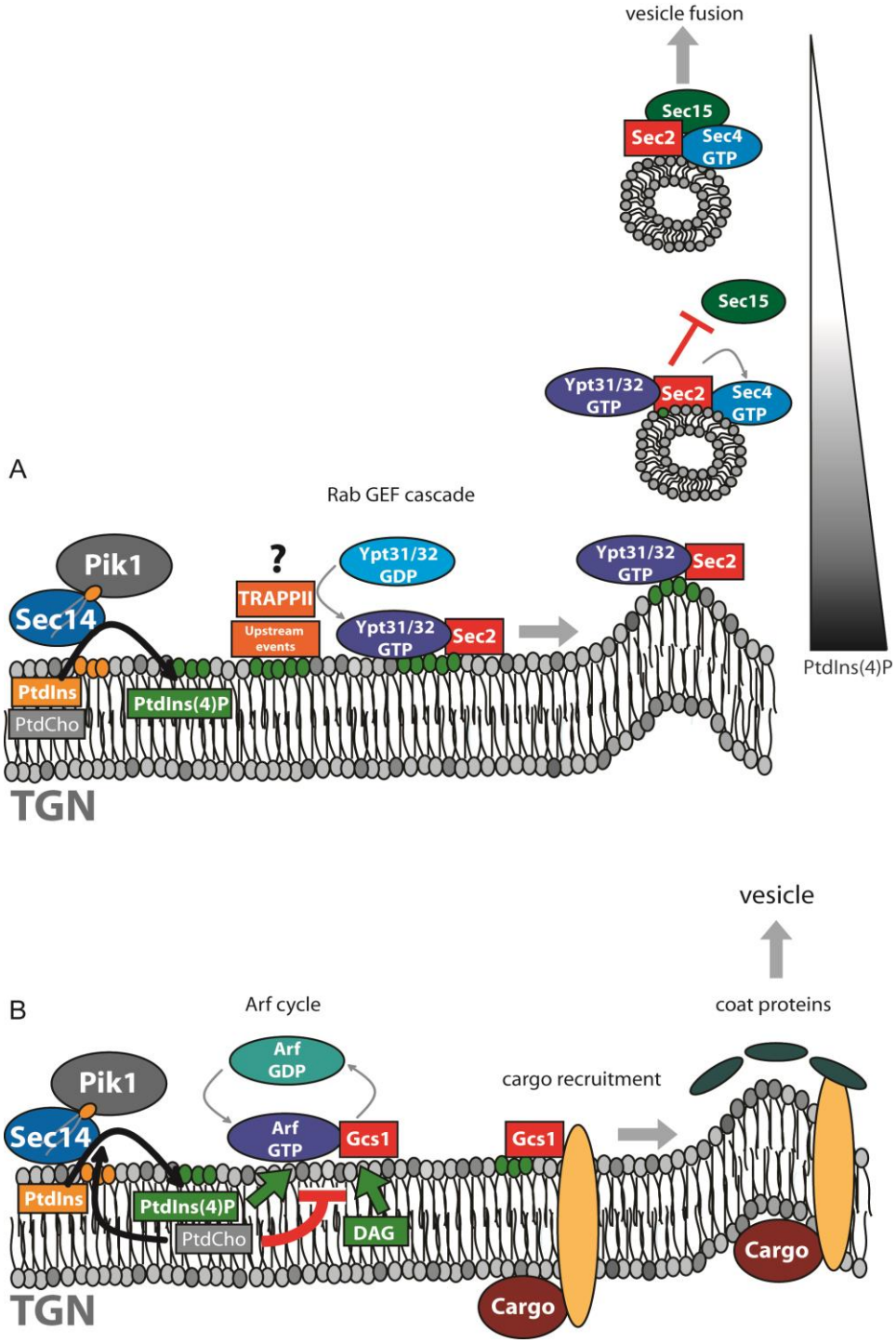

Figure1. Sec14-dependent regulation of vesicle biogenesis in *Saccharomyces cerevisiae*. Sec14 facilitates PtdIns (yellow ovals) headgroup access by Pik1 kinase, stimulating PtdIns(4)P (green ovals) synthesis at TGN membranes. Two putative physiological outcomes are depicted: **(A)** Sec14-derived PtdIns(4)P and the GTP-bound Ypt32 together act as signals for recruitment of the GEF Sec2 to Golgi membranes. Sec2-PtdIns(4)P interactions prevent binding of the exocyst component Sec15, thus promoting a spatial-temporal regulation of vesicle trafficking events. Once the vesicle is formed, Sec2 activates Sec4, and a decreasing PtdIns(4)P gradient allows the replacement of Ypt32 for the Sec4 effector Sec15, promoting later steps of vesicle fusion. PtdIns(4)P may also participate earlier in the Rab GEF cascade by influencing, for instance, the activation of Ypt31/Ypt32 via the TRAPPII complex. **(B)** Sec14 activity promotes a lipid environment at *trans*-Golgi membranes that is enriched in PtdIns(4)P. The involvement of other lipids (DAG and PtdCho) is also highlighted. Such lipid composition favors functional regulation of the Arf-cycle (possibly via Gsc1), essential for the recruitment of coat proteins. Additionally, Gcs1 is required for proper assembly and packaging of cargo proteins.

same protein, Sec14 membrane trafficking functions to cargo sorting. Arabidopsis Sec14-GOLD proteins are represented by six patellins (PATL1-PATL6) that, albeit being more distantly related to Sec14, contain three conserved residues essential for PtdIns binding/transfer (Phillips et al., 2006). The only patellin characterized so far (AtPATL1) preferentially binds phosphoinositides over PtdEtn or PtdCho, and is suggested to play a role in the membrane trafficking involved in the expansion or maturation of the cell plate during cytokinesis (Peterman et al., 2004).

Among the 31 Sec14 homologues, 13 comprise the Sec14-nodulin subfamily, whose N-terminal Sec14 domains share high homology with the yeast Sec14 (Ile et al., 2006; Vincent et al., 2005). Nodulins are broadly defined as the set of genes that are expressed in *Rhizobium*-infected roots of legumes and regulate nodule development and maintenance of the bacteria/plant symbiosis that drive nitrogen fixation (Crespi and Galvez, 2000). The term 'nodulin' in context of Sec14 proteins arises from studies with Nlj16, a 15 kDa polypeptide of the model legume *Lotus japonicas* encoded by the late nodulin *LjNOD16* (Kapranov et al., 1997; Kapranov et al., 2001). It was originally speculated that Nlj16 represented a truncated version of larger proteins (Kapranov et al., 1997) and in an attempt to further investigate its functions, a detailed characterization of Lotus cDNA and genomic sequences related to *LjNOD16* was performed (Kapranov et al., 2001). Indeed, *LjNOD16*-related sequences were identified in association with four genes predicted to encode PITP-like proteins (named LjPLPI-IV), all sharing a two-domain structure consisting of an N-terminal Sec14-like domain linked to a C-terminal amino acid sequence identical to, or highly related to Nlj16 nodulin. This module was shown to associate with the plasma membrane, possibly via a polybasic region followed by two cysteine residues at the extreme C-terminus, preceded by a predicted 2-helical coiled-coil structure. The authors showed that *LjNOD16* expression in nodules results from a remarkable reprogramming of *LjPLP-IV* transcription. Upon nodulation, the *LjPLP-IV* promoter is silenced and a bidirectional nodule-specific promoter, which is located within intron 10 of *LjPLP-IV* (i.e. the intron that separates coding sequences of the two domains), is induced. This promoter has dual activity: it drives the expression of a stand-alone *LjNOD16* nodulin and also generates antisense transcripts derived from the region encoding Sec14-like domain of *LjPLP-IV* (Kapranov et al., 2001).

This rather elegant mechanism for downregulation of LjPLP functions is suggested to fine-tune the developmental programming required for formation and maintenance of the symbiotic nodule (Kapranov et al., 2001). Based on more recent studies with AtSFH1, an Arabidopsis Sec14-like PITP considered a key polarity regulator in root hair cells (Vincent et al., 2005), one can now speculate that the reprogramming of *LjPLP-IV* transcription may promote a break in polarized growth in Lotus root hair tips, favoring the maintenance of the nitrogen-fixing nodule. This scenario would involve the combination of decreased Sec14-like activity (by lowering its transcript levels) and, most interestingly, a dominant-negative effect of Nlj16, which may interact with LjPLP-IV binding sites at the plasma membrane (Phillips et al., 2006).

The large number of Arabidopsis Sec14-like PITPs indicates these proteins potentially regulate widely diverse biological roles. Yet, very little is known about them; the only Arabidopsis Sec14 superfamily member that has been preliminarily characterized is AtSFH1 (*Arabidopsis thaliana* Sec-Fourteen Homolog 1) (Vincent et al., 2005). Analysis of at least five of its loss-of function alleles, named "can-of-worms" *cow1-1* to *cow1-4* (Bohme et al., 2004), and the T-DNA insertional mutant *atsfh1-1* (Vincent et al., 2005), demonstrated that AtSFH1 is essential for proper root hair elongation, a process that relies on a precise cytoplasmic polarization that restricts exocytosis of new membrane and cell wall material to the specific apical area (i.e. root hair tip), where the cell expansion occurs (Carol and Dolan, 2002). The actin and microtubule cytoskeletons, cell-wall modifying enzymes, Ca^{2+} ions and phospholipid signaling are among the plethora of components shown to regulate the elongation of tip-growing cells (e.g. pollen tubes and root hairs) (Bohme et al., 2004).

Indeed, impairment of many of those components was shown to be associated with *atsfh1-1*-dependent short root hair phenotype (Vincent et al., 2005). AtSFH1 is a Sec14-nodulin whose N-terminal lipid binding domain was shown to exhibit intrinsic Sec14 activities: it is able to rescue *sec14-1^{ts}*-associated growth defects, it transfers PtdIns and PtdCho *in vitro*, and it is able to stimulate phosphoinositide biosynthesis in yeast, especially of PtdIns(4)P and PtdIns(4,5)P_2 (Vincent et al., 2005). Differently from the yeast prototype, AtSFH1 seems to act on later stages of secretion; electron micrographs showed undistinguishable Golgi morphology between wild-type and *atsfh1-1* root hair cells. However, the mutant presented a dramatic cytoplasmic vacuolation at the root hair tip, as well as a dispersed vesicle distribution throughout the cytoplasm, in contrast to the vesicle-rich zone (VRZ) that characterizes the tip of wild-type cells. The authors argue that the dispersed vesicle distribution in mutant root hairs coincides with a loss of PtdIns(4,5)P_2 apical enrichment and the tip-directed f-actin microfilament network, derangements on the cortical microtubule network, and with a loss of polarized spatial delivery of Ca^{2+} channels that restrict ion influx to the tip region, resulting in large Ca^{2+} uptake along the whole root hair surface (Vincent et al., 2005).

Final remarks and objectives of this work

The detailed characterization of *atsfh1-1* mutant by Vincent et al. (2005) certainly shed light into the unexplored field of plant Sec14-like PITPs and their roles in regulating phospholipid signaling. However, while it is now clear that AtSFH1 is an essential regulator of polarized membrane trafficking, an understanding of the molecular mechanisms underlying its biological functions is still missing. One intriguing aspect that requires elucidation is the significance of the two-domain composition of Sec14-nodulins. For instance, the roles of AtSFH1 C-terminal nodulin domain in promoting membrane targeting were speculated, yet no functional analysis had been performed. A second aspect that remains elusive is whether Sec14-dependent PtdIns/PtdCho exchange and the regulation of lipid homeostasis are conserved functions among other yeast and Arabidopsis homologues, and also which lipid substrate they

bind. Finally, it is unclear how AtSFH1-dependent regulation of phosphoinositide signaling interconnects with additional cellular components that orchestrate polarized tip-growth.

The objective of this work is to clarify the open questions mentioned above. In chapter 2 I focus on the functional roles of the AtSFH1 C-terminal nodulin domain. By using biochemical, cell biological and physiological approaches, NMR-spectroscopy, as well as structural modeling and molecular dynamics simulations, we were able to confirm its plasma membrane association function and identify the particular residues that mediate this interaction. We also describe novel remarkable features of this module that involves the regulation of the oligomerization status of AtSFH1, and lipid binding specificity towards PtdIns(4,5)P_2.

In chapter 3 I present a strategy for discovering suppressor mutations that bypass the essential requirement of AtSFH1 in root hair development. I employed a combination of forward genetic screen and next-generation sequencing, and isolated 10 independent suppressor alleles. One mutant was studied in more detail and provides interesting clues on how root hairs are able to restore polarity in an AtSFH1-independent mechanism that potentially involves cyanide detoxification.

Finally, on chapters 4 and 5 I deviate the focus from plant PITPs to report how a directed evolution approach led to the isolation of yeast gain-of-function mutations that endow Sec14-like activities to a functionally inactive Sfh1. Biochemical and biophysical analyses, as well as molecular dynamics simulations, suggest that Sfh1 ‘resurrection’ phenotypes result from enhanced ordered H_2O molecules in the protein hydrophobic pocket that stimulate conformational dynamics of the helical gate, ultimately required for proper phospholipid exchange. Discoveries made in chapters 4 and 5 allow the most detailed mechanistic insight into phospholipid exchange and PtdIns presentation mediated by any Sec14 protein to date and open the path for a deeper understanding of Sec14 function and phosphoinositide homeostasis in plants.

References

Anantharaman, V., and Aravind, L. (2002). The GOLD domain, a novel protein module involved in Golgi function and secretion. Genome Biol *3*, research0023.

Audhya, A., and Emr, S.D. (2002). Stt4 PI 4-kinase localizes to the plasma membrane and functions in the Pkc1-mediated MAP kinase cascade. Dev Cell *2*, 593-605.

Audhya, A., and Emr, S.D. (2003). Regulation of PI4,5P2 synthesis by nuclear-cytoplasmic shuttling of the Mss4 lipid kinase. EMBO J *22*, 4223-4236.

Audhya, A., Foti, M., and Emr, S.D. (2000). Distinct roles for the yeast phosphatidylinositol 4-kinases, Stt4p and Pik1p, in secretion, cell growth, and organelle membrane dynamics. Mol Biol Cell *11*, 2673-2689.

Audhya, A., Loewith, R., Parsons, A.B., Gao, L., Tabuchi, M., Zhou, H., Boone, C., Hall, M.N., and Emr, S.D. (2004). Genome-wide lethality screen identifies new PI4,5P2 effectors that regulate the actin cytoskeleton. EMBO J *23*, 3747-3757.

Bak, G., Lee, E.J., Lee, Y., Kato, M., Segami, S., Sze, H., Maeshima, M., Hwang, J.U., and Lee, Y. (2013). Rapid structural changes and acidification of guard cell vacuoles during stomatal closure require phosphatidylinositol 3,5-bisphosphate. Plant Cell *25*, 2202-2216.

Balla, A., and Balla, T. (2006). Phosphatidylinositol 4-kinases: old enzymes with emerging functions. Trends Cell Biol *16*, 351-361.

Bankaitis, V.A., Ile, K.E., Nile, A.H., Ren, J., Ghosh, R., and Schaaf, G. (2012). Thoughts on Sec14-like nanoreactors and phosphoinositide signaling. Adv Biol Regul *52*, 115-121.

Bankaitis, V.A., Malehorn, D.E., Emr, S.D., and Greene, R. (1989). The *Saccharomyces cerevisiae* SEC14 gene encodes a cytosolic factor that is required for transport of secretory proteins from the yeast Golgi complex. The Journal of cell biology *108*, 1271-1281.

Bankaitis, V.A., Mousley, C.J., and Schaaf, G. (2010). The Sec14 superfamily and mechanisms for crosstalk between lipid metabolism and lipid signaling. Trends in biochemical sciences *35*, 150-160.

Berridge, M.J., and Irvine, R.F. (1984). Inositol trisphosphate, a novel second messenger in cellular signal transduction. Nature *312*, 315-321.

Bohme, K., Li, Y., Charlot, F., Grierson, C., Marrocco, K., Okada, K., Laloue, M., and Nogue, F. (2004). The Arabidopsis COW1 gene encodes a phosphatidylinositol transfer protein essential for root hair tip growth. Plant J *40*, 686-698.

Carol, R.J., and Dolan, L. (2002). Building a hair: tip growth in *Arabidopsis thaliana* root hairs. Philos Trans R Soc Lond B Biol Sci *357*, 815-821.

Cleves, A., McGee, T., and Bankaitis, V. (1991a). Phospholipid transfer proteins: a biological debut. Trends Cell Biol *1*, 30-34.

Cleves, A.E., McGee, T.P., Whitters, E.A., Champion, K.M., Aitken, J.R., Dowhan, W., Goebl, M., and Bankaitis, V.A. (1991b). Mutations in the CDP-choline pathway for phospholipid biosynthesis bypass the requirement for an essential phospholipid transfer protein. Cell *64*, 789-800.

Cleves, A.E., Novick, P.J., and Bankaitis, V.A. (1989). Mutations in the SAC1 gene suppress defects in yeast Golgi and yeast actin function. The Journal of cell biology *109*, 2939-2950.

Crespi, M., and Galvez, S. (2000). Molecular Mechanisms in Root Nodule Development. Journal of plant growth regulation *19*, 155-166.

Curwin, A.J., Fairn, G.D., and McMaster, C.R. (2009). Phospholipid transfer protein Sec14 is required for trafficking from endosomes and regulates distinct trans-Golgi export pathways. J Biol Chem *284*, 7364-7375.

D'Angelo, G., Vicinanza, M., Di Campli, A., and De Matteis, M.A. (2008). The multiple roles of PtdIns(4)P -- not just the precursor of PtdIns(4,5)P2. J Cell Sci *121*, 1955-1963.

Desrivieres, S., Cooke, F.T., Parker, P.J., and Hall, M.N. (1998). MSS4, a phosphatidylinositol-4-phosphate 5-kinase required for organization of the actin cytoskeleton in *Saccharomyces cerevisiae*. J Biol Chem *273*, 15787-15793.

DeWald, D.B., Torabinejad, J., Jones, C.A., Shope, J.C., Cangelosi, A.R., Thompson, J.E., Prestwich, G.D., and Hama, H. (2001). Rapid accumulation of phosphatidylinositol 4,5-bisphosphate and inositol 1,4,5-trisphosphate correlates with calcium mobilization in salt-stressed arabidopsis. Plant Physiol *126*, 759-769.

Di Paolo, G., and De Camilli, P. (2006). Phosphoinositides in cell regulation and membrane dynamics. Nature *443*, 651-657.

Dove, S.K., Cooke, F.T., Douglas, M.R., Sayers, L.G., Parker, P.J., and Michell, R.H. (1997). Osmotic stress activates phosphatidylinositol-3,5-bisphosphate synthesis. Nature *390*, 187-192.

Fang, M., Kearns, B.G., Gedvilaite, A., Kagiwada, S., Kearns, M., Fung, M.K., and Bankaitis, V.A. (1996). Kes1p shares homology with human oxysterol binding protein and participates in a novel regulatory pathway for yeast Golgi-derived transport vesicle biogenesis. Embo J *15*, 6447-6459.

Faulhammer, F., Kanjilal-Kolar, S., Knodler, A., Lo, J., Lee, Y., Konrad, G., and Mayinger, P. (2007). Growth control of Golgi phosphoinositides by reciprocal localization of sac1 lipid phosphatase and pik1 4-kinase. Traffic *8*, 1554-1567.

Foti, M., Audhya, A., and Emr, S.D. (2001). Sac1 lipid phosphatase and Stt4 phosphatidylinositol 4-kinase regulate a pool of phosphatidylinositol 4-phosphate that functions in the control of the actin cytoskeleton and vacuole morphology. Mol Biol Cell *12*, 2396-2411.

Gagne, J.M., and Clark, S.E. (2010). The Arabidopsis stem cell factor POLTERGEIST is membrane localized and phospholipid stimulated. Plant Cell *22*, 729-743.

Gillooly, D.J., Morrow, I.C., Lindsay, M., Gould, R., Bryant, N.J., Gaullier, J.M., Parton, R.G., and Stenmark, H. (2000). Localization of phosphatidylinositol 3-phosphate in yeast and mammalian cells. EMBO J *19*, 4577-4588.

Godi, A., Di Campli, A., Konstantakopoulos, A., Di Tullio, G., Alessi, D.R., Kular, G.S., Daniele, T., Marra, P., Lucocq, J.M., and De Matteis, M.A. (2004). FAPPs control Golgi-to-cell-surface membrane traffic by binding to ARF and PtdIns(4)P. Nat Cell Biol *6*, 393-404.

Han, G.S., Audhya, A., Markley, D.J., Emr, S.D., and Carman, G.M. (2002). The *Saccharomyces cerevisiae* LSB6 gene encodes phosphatidylinositol 4-kinase activity. J Biol Chem *277*, 47709-47718.

Hanada, K., Kumagai, K., Yasuda, S., Miura, Y., Kawano, M., Fukasawa, M., and Nishijima, M. (2003). Molecular machinery for non-vesicular trafficking of ceramide. Nature *426*, 803-809.

Heilmann, M., and Heilmann, I. (2013). Arranged marriage in lipid signalling? The limited choices of PtdIns(4,5)P2 in finding the right partner. Plant Biol (Stuttg) *15*, 789-797.

Hirst, J., Motley, A., Harasaki, K., Peak Chew, S.Y., and Robinson, M.S. (2003). EpsinR: an ENTH domain-containing protein that interacts with AP-1. Mol Biol Cell *14*, 625-641.

Homma, K., Terui, S., Minemura, M., Qadota, H., Anraku, Y., Kanaho, Y., and Ohya, Y. (1998). Phosphatidylinositol-4-phosphate 5-kinase localized on the plasma membrane is essential for yeast cell morphogenesis. J Biol Chem *273*, 15779-15786.

Ile, K.E., Schaaf, G., and Bankaitis, V.A. (2006). Phosphatidylinositol transfer proteins and cellular nanoreactors for lipid signaling. Nat Chem Biol *2*, 576-583.

Ischebeck, T., Stenzel, I., and Heilmann, I. (2008). Type B phosphatidylinositol-4-phosphate 5-kinases mediate Arabidopsis and Nicotiana tabacum pollen tube growth by regulating apical pectin secretion. Plant Cell *20*, 3312-3330.

Ischebeck, T., Stenzel, I., Hempel, F., Jin, X., Mosblech, A., and Heilmann, I. (2011). Phosphatidylinositol-4,5-bisphosphate influences Nt-Rac5-mediated cell expansion in pollen tubes of Nicotiana tabacum. Plant J *65*, 453-468.

Jung, J.Y., Kim, Y.W., Kwak, J.M., Hwang, J.U., Young, J., Schroeder, J.I., Hwang, I., and Lee, Y. (2002). Phosphatidylinositol 3- and 4-phosphate are required for normal stomatal movements. Plant Cell *14*, 2399-2412.

Kapranov, P., de Bruijn, F.J., and Szczyglowski, K. (1997). Novel, highly expressed late nodulin gene (LjNOD16) from *Lotus japonicus*. Plant Physiol *113*, 1081-1090.

Kapranov, P., Routt, S.M., Bankaitis, V.A., de Bruijn, F.J., and Szczyglowski, K. (2001). Nodule-specific regulation of phosphatidylinositol transfer protein expression in *Lotus japonicus*. Plant Cell *13*, 1369-1382.

Kusano, H., Testerink, C., Vermeer, J.E., Tsuge, T., Shimada, H., Oka, A., Munnik, T., and Aoyama, T. (2008). The Arabidopsis Phosphatidylinositol Phosphate 5-Kinase PIP5K3 is a key regulator of root hair tip growth. Plant Cell *20*, 367-380.

Kutateladze, T.G. (2010). Translation of the phosphoinositide code by PI effectors. Nat Chem Biol *6*, 507-513.

Lee, Y., Bak, G., Choi, Y., Chuang, W.I., Cho, H.T., and Lee, Y. (2008a). Roles of phosphatidylinositol 3-kinase in root hair growth. Plant Physiol *147*, 624-635.

Lee, Y., Kim, E.S., Choi, Y., Hwang, I., Staiger, C.J., Chung, Y.Y., and Lee, Y. (2008b). The Arabidopsis phosphatidylinositol 3-kinase is important for pollen development. Plant Physiol *147*, 1886-1897.

Lee, Y., Kim, Y.W., Jeon, B.W., Park, K.Y., Suh, S.J., Seo, J., Kwak, J.M., Martinoia, E., Hwang, I., and Lee, Y. (2007). Phosphatidylinositol 4,5-bisphosphate is important for stomatal opening. Plant J *52*, 803-816.

Lemmon, M.A. (2008). Membrane recognition by phospholipid-binding domains. Nat Rev Mol Cell Biol *9*, 99-111.

Li, X., Rivas, M.P., Fang, M., Marchena, J., Mehrotra, B., Chaudhary, A., Feng, L., Prestwich, G.D., and Bankaitis, V.A. (2002). Analysis of oxysterol binding protein homologue Kes1p function in regulation of Sec14p-dependent protein transport from the yeast Golgi complex. The Journal of cell biology *157*, 63-77.

Li, X., Routt, S.M., Xie, Z., Cui, X., Fang, M., Kearns, M.A., Bard, M., Kirsch, D.R., and Bankaitis, V.A. (2000). Identification of a novel family of nonclassic yeast phosphatidylinositol transfer proteins whose function modulates phospholipase D activity and Sec14p-independent cell growth. Mol Biol Cell *11*, 1989-2005.

Martin, T.F. (1998). Phosphoinositide lipids as signaling molecules: common themes for signal transduction, cytoskeletal regulation, and membrane trafficking. Annu Rev Cell Dev Biol *14*, 231-264.

Mei, Y., Jia, W.J., Chu, Y.J., and Xue, H.W. (2012). Arabidopsis phosphatidylinositol monophosphate 5-kinase 2 is involved in root gravitropism through regulation of polar auxin transport by affecting the cycling of PIN proteins. Cell research *22*, 581-597.

Mizuno-Yamasaki, E., Medkova, M., Coleman, J., and Novick, P. (2010). Phosphatidylinositol 4-phosphate controls both membrane recruitment and a regulatory switch of the Rab GEF Sec2p. Dev Cell *18*, 828-840.

Mousley, C.J., Tyeryar, K., Ile, K.E., Schaaf, G., Brost, R.L., Boone, C., Guan, X., Wenk, M.R., and Bankaitis, V.A. (2008). Trans-Golgi network and endosome dynamics connect ceramide homeostasis with regulation of the unfolded protein response and TOR signaling in yeast. Mol Biol Cell *19*, 4785-4803.

Mousley, C.J., Tyeryar, K.R., Vincent-Pope, P., and Bankaitis, V.A. (2007). The Sec14-superfamily and the regulatory interface between phospholipid metabolism and membrane trafficking. Biochim Biophys Acta *1771*, 727-736.

Mueller-Roeber, B., and Pical, C. (2002). Inositol phospholipid metabolism in Arabidopsis. Characterized and putative isoforms of inositol phospholipid kinase and phosphoinositide-specific phospholipase C. Plant Physiol *130*, 22-46.

Munnik, T., and Vermeer, J.E. (2010). Osmotic stress-induced phosphoinositide and inositol phosphate signalling in plants. Plant Cell Environ *33*, 655-669.

Novick, P., Field, C., and Schekman, R. (1980). Identification of 23 complementation groups required for post-translational events in the yeast secretory pathway. Cell *21*, 205-215.

Odorizzi, G., Babst, M., and Emr, S.D. (2000). Phosphoinositide signaling and the regulation of membrane trafficking in yeast. Trends Biochem Sci *25*, 229-235.

Peterman, T.K., Ohol, Y.M., McReynolds, L.J., and Luna, E.J. (2004). Patellin1, a novel Sec14-like protein, localizes to the cell plate and binds phosphoinositides. Plant Physiol *136*, 3080-3094; discussion 3001-3082.

Phillips, S.E., Vincent, P., Rizzieri, K.E., Schaaf, G., Bankaitis, V.A., and Gaucher, E.A. (2006). The diverse biological functions of phosphatidylinositol transfer proteins in eukaryotes. Crit Rev Biochem Mol Biol *41*, 21-49.

Pical, C., Westergren, T., Dove, S.K., Larsson, C., and Sommarin, M. (1999). Salinity and hyperosmotic stress induce rapid increases in phosphatidylinositol 4,5-bisphosphate, diacylglycerol pyrophosphate, and phosphatidylcholine in *Arabidopsis thaliana* cells. J Biol Chem *274*, 38232-38240.

Poon, P.P., Nothwehr, S.F., Singer, R.A., and Johnston, G.C. (2001). The Gcs1 and Age2 ArfGAP proteins provide overlapping essential function for transport from the yeast trans-Golgi network. J Cell Biol *155*, 1239-1250.

Preuss, M.L., Schmitz, A.J., Thole, J.M., Bonner, H.K., Otegui, M.S., and Nielsen, E. (2006). A role for the RabA4b effector protein PI-4Kbeta1 in polarized expansion of root hair cells in *Arabidopsis thaliana*. J Cell Biol *172*, 991-998.

Preuss, M.L., Serna, J., Falbel, T.G., Bednarek, S.Y., and Nielsen, E. (2004). The Arabidopsis Rab GTPase RabA4b localizes to the tips of growing root hair cells. Plant Cell *16*, 1589-1603.

Rebecchi, M.J., and Pentyala, S.N. (2000). Structure, function, and control of phosphoinositide-specific phospholipase C. Physiol Rev *80*, 1291-1335.

Rothman, J.E. (1996). The protein machinery of vesicle budding and fusion. Protein Sci *5*, 185-194.

Schaaf, G., Ortlund, E.A., Tyeryar, K.R., Mousley, C.J., Ile, K.E., Garrett, T.A., Ren, J., Woolls, M.J., Raetz, C.R., Redinbo, M.R., *et al.* (2008). Functional anatomy of phospholipid binding and regulation of phosphoinositide homeostasis by proteins of the sec14 superfamily. Mol Cell *29*, 191-206.

Schu, P.V., Takegawa, K., Fry, M.J., Stack, J.H., Waterfield, M.D., and Emr, S.D. (1993). Phosphatidylinositol 3-kinase encoded by yeast VPS34 gene essential for protein sorting. Science *260*, 88-91.

Schuh, A.L., and Audhya, A. (2012). Phosphoinositide signaling during membrane transport in *Saccharomyces cerevisiae*. Subcell Biochem *59*, 35-63.

Sciorra, V.A., Audhya, A., Parsons, A.B., Segev, N., Boone, C., and Emr, S.D. (2005). Synthetic genetic array analysis of the PtdIns 4-kinase Pik1p identifies components in a Golgi-specific Ypt31/rab-GTPase signaling pathway. Mol Biol Cell *16*, 776-793.

Sha, B., Phillips, S.E., Bankaitis, V.A., and Luo, M. (1998). Crystal structure of the *Saccharomyces cerevisiae* phosphatidylinositol-transfer protein. Nature *391*, 506-510.

Simonsen, A., Lippe, R., Christoforidis, S., Gaullier, J.M., Brech, A., Callaghan, J., Toh, B.H., Murphy, C., Zerial, M., and Stenmark, H. (1998). EEA1 links PI(3)K function to Rab5 regulation of endosome fusion. Nature *394*, 494-498.

Sousa, E., Kost, B., and Malho, R. (2008). Arabidopsis phosphatidylinositol-4-monophosphate 5-kinase 4 regulates pollen tube growth and polarity by modulating membrane recycling. Plant Cell *20*, 3050-3064.

Stefan, C.J., Audhya, A., and Emr, S.D. (2002). The yeast synaptojanin-like proteins control the cellular distribution of phosphatidylinositol (4,5)-bisphosphate. Mol Biol Cell *13*, 542-557.

Stefan, C.J., Manford, A.G., Baird, D., Yamada-Hanff, J., Mao, Y., and Emr, S.D. (2011). Osh proteins regulate phosphoinositide metabolism at ER-plasma membrane contact sites. Cell *144*, 389-401.

Stenzel, I., Ischebeck, T., Konig, S., Holubowska, A., Sporysz, M., Hause, B., and Heilmann, I. (2008). The type B phosphatidylinositol-4-phosphate 5-kinase 3 is essential for root hair formation in *Arabidopsis thaliana*. Plant Cell *20*, 124-141.

Stenzel, I., Ischebeck, T., Quint, M., and Heilmann, I. (2011). Variable Regions of PI4P 5-Kinases Direct PtdIns(4,5)P(2) Toward Alternative Regulatory Functions in Tobacco Pollen Tubes. Front Plant Sci *2*, 114.

Strahl, T., Hama, H., DeWald, D.B., and Thorner, J. (2005). Yeast phosphatidylinositol 4-kinase, Pik1, has essential roles at the Golgi and in the nucleus. J Cell Biol *171*, 967-979.

Thole, J.M., and Nielsen, E. (2008). Phosphoinositides in plants: novel functions in membrane trafficking. Curr Opin Plant Biol *11*, 620-631.

Thole, J.M., Vermeer, J.E., Zhang, Y., Gadella, T.W., Jr., and Nielsen, E. (2008). Root hair defective4 encodes a phosphatidylinositol-4-phosphate phosphatase required for proper root hair development in *Arabidopsis thaliana*. Plant Cell *20*, 381-395.

Trotter, P.J., Wu, W.I., Pedretti, J., Yates, R., and Voelker, D.R. (1998). A genetic screen for aminophospholipid transport mutants identifies the phosphatidylinositol 4-kinase, STT4p, as an essential component in phosphatidylserine metabolism. J Biol Chem *273*, 13189-13196.

van Leeuwen, W., Vermeer, J.E., Gadella, T.W., Jr., and Munnik, T. (2007). Visualization of phosphatidylinositol 4,5-bisphosphate in the plasma membrane of suspension-cultured tobacco BY-2 cells and whole Arabidopsis seedlings. Plant J *52*, 1014-1026.

Vermeer, J.E., Thole, J.M., Goedhart, J., Nielsen, E., Munnik, T., and Gadella, T.W., Jr. (2009). Imaging phosphatidylinositol 4-phosphate dynamics in living plant cells. Plant J *57*, 356-372.

Vermeer, J.E., van Leeuwen, W., Tobena-Santamaria, R., Laxalt, A.M., Jones, D.R., Divecha, N., Gadella, T.W., Jr., and Munnik, T. (2006). Visualization of PtdIns3P dynamics in living plant cells. Plant J *47*, 687-700.

Vincent, P., Chua, M., Nogue, F., Fairbrother, A., Mekeel, H., Xu, Y., Allen, N., Bibikova, T.N., Gilroy, S., and Bankaitis, V.A. (2005). A Sec14p-nodulin domain phosphatidylinositol transfer protein polarizes membrane growth of *Arabidopsis thaliana* root hairs. The Journal of cell biology *168*, 801-812.

Wang, Y.J., Wang, J., Sun, H.Q., Martinez, M., Sun, Y.X., Macia, E., Kirchhausen, T., Albanesi, J.P., Roth, M.G., and Yin, H.L. (2003). Phosphatidylinositol 4 phosphate regulates targeting of clathrin adaptor AP-1 complexes to the Golgi. Cell *114*, 299-310.

Welters, P., Takegawa, K., Emr, S.D., and Chrispeels, M.J. (1994). AtVPS34, a phosphatidylinositol 3-kinase of *Arabidopsis thaliana*, is an essential protein with homology to a calcium-dependent lipid binding domain. Proc Natl Acad Sci U S A *91*, 11398-11402.

Whitley, P., Hinz, S., and Doughty, J. (2009). Arabidopsis FAB1/PIKfyve proteins are essential for development of viable pollen. Plant Physiol *151*, 1812-1822.

Williams, M.E., Torabinejad, J., Cohick, E., Parker, K., Drake, E.J., Thompson, J.E., Hortter, M., and Dewald, D.B. (2005). Mutations in the Arabidopsis phosphoinositide phosphatase gene SAC9 lead to overaccumulation of PtdIns(4,5)P2 and constitutive expression of the stress-response pathway. Plant Physiol *138*, 686-700.

Wiradjaja, F., Ooms, L.M., Whisstock, J.C., McColl, B., Helfenbaum, L., Sambrook, J.F., Gething, M.J., and Mitchell, C.A. (2001). The yeast inositol polyphosphate 5-phosphatase Inp54p localizes to the endoplasmic reticulum via a C-terminal hydrophobic anchoring tail: regulation of secretion from the endoplasmic reticulum. J Biol Chem *276*, 7643-7653.

Yanagisawa, L.L., Marchena, J., Xie, Z., Li, X., Poon, P.P., Singer, R.A., Johnston, G.C., Randazzo, P.A., and Bankaitis, V.A. (2002). Activity of specific lipid-regulated ADP ribosylation factor-GTPase-activating proteins is required for Sec14p-dependent Golgi secretory function in yeast. Mol Biol Cell *13*, 2193-2206.

Yoshida, S., Ohya, Y., Nakano, A., and Anraku, Y. (1994). Genetic interactions among genes involved in the STT4-PKC1 pathway of *Saccharomyces cerevisiae*. Molecular & general genetics : MGG *242*, 631-640.

Zhao, Y., Yan, A., Feijo, J.A., Furutani, M., Takenawa, T., Hwang, I., Fu, Y., and Yang, Z. (2010). Phosphoinositides regulate clathrin-dependent endocytosis at the tip of pollen tubes in Arabidopsis and tobacco. Plant Cell *22*, 4031-4044.

CHAPTER 2

SEC14-NODULIN PROTEINS PATTERN PHOSPHOINOSITIDE LANDMARKS FOR DEVELOPMENTAL CONTROL OF MEMBRANE MORPHOGENESIS

Ratna Ghosh[1‡], Marília K.F. de Campos[2‡], Jin Huang[1], Seong K. Hur[1], Adam Orlowski[3], Yuan Yang[4], Ashutosh Tripathi[1], Aaron Nile[1], Hsin-Chieh Lee[2], Marek Dynowski[5], Helen Schäfer[2], Tomasz Róg[3], Marta G. Lete[6], Hasna Ahyayauch[6,7], Alicia Alonso[6], Ilpo Vattulainen[3,8], Tatyana I. Igumenova[4], Gabriel Schaaf[2*], and Vytas A. Bankaitis[1,4,9*]

[1] Department of Molecular and Cellular Medicine, College of Medicine, Texas A&M Health Sciences Center, College Station, Texas 77843-1114, USA; [2] ZMBP, Plant Physiology, Universität Tübingen, 72076 Tübingen, Germany; [3] Department of Physics‡, Tampere University of Technology, FI-33101 Tampere, Finland; [4]Department of Biochemistry & Biophysics, Texas A&M University, College Station, Texas 77843-2128 [5] ZDV, Universität Tübingen, 72074 Tübingen, Germany; [6] Unidad de Biofísica (CSIC, UPV/EHU), Departamento de Bioquímica, Universidad del País Vasco, Leioa, Spain; [7] Institut de Formation, aux Carrieres de Sante de Rabat (IFCSR), Rabat, Morocco; [8] MEMPHYS – Center for Biomembrane Physics, University of Southern Denmark, DK-5230, Odense M, Denmark; [9] Department of Chemistry, Texas A&M University, College Station, Texas 77843-2128

‡ These authors contributed equally to the work *** Co-corresponding authors**

This chapter has been published:

Ghosh and Campos et al. (2015). Sec14-nodulin proteins and the patterning of phosphoinositide landmarks for developmental control of membrane morphogenesis. **Mol Biol Cell**, 26(9):1764-81. Available at: http://www.molbiolcell.org/content/26/9/1764.full.pdf+html
(Republished according to ASCB license and publishing agreement)

Summary

Polarized membrane morphogenesis is a fundamental activity of eukaryotic cells. This process is essential for the biology of cells and tissues, and its execution demands exquisite temporal coordination of functionally diverse membrane signaling reactions with high spatial resolution. Moreover, mechanisms must exist to establish, and preserve, such organization in the face of randomizing forces that would diffuse it. Herein, we identify the conserved AtSfh1 Sec14-nodulin protein as a novel effector of phosphoinositide signaling in the extreme polarized membrane growth program exhibited by growing Arabidopsis root hairs. The data are consistent with Sec14-nodulin proteins controlling the lateral organization of phosphatidylinositol-(4,5)-bisphosphate (PtdIns(4,5)P_2) landmarks for polarized membrane morphogenesis in plants. This patterning activity requires both the PtdIns(4,5)P_2 binding and homo-oligomerization activities of the AtSfh1 nodulin domain, and is an essential aspect of the polarity signaling program in root hairs. Finally, the data suggest a general principle for how the

phosphoinositide signaling landscape is physically bit-mapped so that eukaryotic cells are able to convert a membrane surface into a high definition lipid signaling screen.

Introduction

A cardinal feature of eukaryotic cells is their ability to register lipid signaling reactions, with high spatial and temporal precision, on large membrane surfaces. Membrane morphogenesis is a fundamental process that relies on this feature, and it is the foundation upon which cell shape control, tissue formation and organogenesis is built (Hepler et al., 2001; Affolter et al., 2009; Cáceres et al., 2012). Polarized membrane growth is developmentally controlled and the process is also induced by environmental factors -- as exemplified by dimorphic switch of fungal pathogens from budding to mycelial growth modes (Richter et al., 2011; Whiteway and Bachewich, 2007). Both modes of membrane morphogenic control are on display in the bacterial-plant symbiosis required for nitrogen fixation (Oldroyd and Downie, 2008; Oldroyd, 2013).

Biological nitrogen fixation is a prokaryotic activity of planetary significance that captures atmospheric N_2 by reducing the gas into 'combined' nitrogen forms suitable for assimilation by plants (Vance, 2001). The primary source for symbiotic N_2 fixation relies on an intimate partnership between highly polarized membrane structures (root hairs) of leguminous plants and N_2-fixing rhizobia bacteria in soil (Oldroyd and Downie, 2008; Oldroyd, 2013). This symbiosis involves a bidirectional chemical dialog between the prokaryotic and eukaryotic partners, culminating in bacterial colonization and infection of growing root hairs. Subsequent formation of specialized microenvironments, termed nodules, provides the anaerobic niche essential for the fixing of N_2 by bacterial nitrogenase (Brewin 2002; Long 2001; Debrosses et al., 2011; Suzaki et al., 2014). Bacteria foster establishment of the symbiotic state by secreting a battery of nodulation factors to which the plant responds by deforming growing tips of root hairs (Irving et al., 2000; Oldroyd et al., 2013). The resulting structures entrap the rhizobia and initiate the infection process through a local invagination of the root hair plasma membrane and establishment of a polarized growing infection structure, termed the infection thread, into underlying cortical cells (van Spronsen et al., 2001, Monahan-Giovanelli et al., 2006). Activation of meristematic activity in cortical cells subsequently initiates formation of a nodule primordium (Oldroyd, 2013). Organ specific plant proteins expressed only during symbiotic nitrogen fixation are called nodulins, and these polypeptides define the plant's contribution to symbiosis (van Kammen 1984; Mylona et al.,1995). Herein, we focus on Nlj16-like nodulins. The founding member of this family, Nlj16, was first described in the legume Lotus japonicus as a 15-kDa protein of unknown function specifically expressed late in the nodulation program (Kapranov et al., 1997).

Sec14-like phosphatidylinositol transfer proteins (PITPs) integrate stimulated phosphatidylinositol-4-phosphate (PtdIns(4)P) production with multiple aspects of intracellular lipid metabolism and diversify biological outcomes for phosphoinositide signaling (Schaaf et al., 2008; Bankaitis et al., 2010). It is from this perspective that discovery of a conserved family of Sec14-Nlj16-

like nodulin proteins in Lotus and other plants brings together root hair development, lipid signaling and nodulation in unexpected ways (Kapranov et al., 2001; Vincent et al., 2005; Huang et al., 2013). Arabidopsis produces 31 Sec14-like proteins. Of the 14 Arabidopsis Sec14-like proteins with highest homology to yeast Sec14, 13 exhibit C-terminal Nlj16-like nodulin domains (Figure 1A). Moreover, these Arabidopsis Sec14-nodulin proteins are expressed predominantly in tip-growing cells that execute developmental programs of extreme polarized membrane growth (pollen, root hairs; Figure 1A). Arabidopsis mutants lacking the AtSfh1 Sec14-nodulin elaborate short, distorted root hairs characterized by loss of tip-directed PtdIns(4,5)P_2 gradients, disorganized cytoskeleton networks, and delocalized Ca^{++} signaling (Vincent et al., 2005). Whereas Sec14-domains are well characterized, the roles of the nodulin domains remain mysterious.

The nodulin domains of all known Sec14-nodulins belong to the Nlj16 family, and the known Nlj16-like nodulins are genetically encoded as C-terminal domains of Sec14-like proteins (Kapranov et al., 2001; Vincent et al., 2005). In Lotus, nodulation-specific production of freestanding Nlj16 results from developmentally controlled reconfiguration of LjPLP-IV (encoding Sec14-Nlj16) gene transcription. This reprogramming drives robust expression of the Nlj16 nodulin as a free-standing domain at the expense of the full-length Sec14-Nlj16 (Kapranov et al., 2001). While the joining of Sec14 modules with Nlj16-nodulins in leguminous and non-leguminous plants forecasts these units execute coordinated activities, the developmental expression profiles indicate these activities are differentially employed in root hair biogenesis vs nodulation (Kapranov et al., 2001).

Herein, we report the first mechanistic insights into the activities of Nlj6-like nodulin domains. We identify the AtSfh1 nodulin as a novel PtdIns(4,5)P_2-binding module whose lipid binding and self-assembly activities are essential for root hair morphogenesis when the nodulin domain is produced in the context of a full-length AtSfh1 protein. By contrast, the stand-alone AtSfh1 nodulin domain exhibits properties of a potent PtdIns(4,5)P_2 sink that antagonizes PtdIns(4,5)P_2 signaling by sequestering the lipid from active signaling pools. The data describe the AtSfh1 Sec14-nodulin as a novel polarity regulator that organizes PtdIns(4,5)P_2 landmarks for root hair morphogenesis. The results further highlight the nodulin domain as a versatile PtdIns(4,5)P_2 clamp whose activities can be developmentally modulated so as to promote or, as in late stages of nodulation, to help subvert polarized morphogenetic programs in developing plant tissues.

Results

Arabidopsis Sec14-nodulin proteins

Nlj16-like nodulin domains share extensive primary sequence homology along their length of ~120 amino acids (Ile et al., 2006), and fall into three classes distinguished by their extreme C-terminal sequences. Class I nodulins (including AtSfh1 nodulin) are characterized by an uninterrupted stretch of > 7 basic C-terminal amino acids with vicinal aromatic residues. The Class I AtSfh10 nodulin domain

additionally harbors a Cys residue that represents a potential palmitoylation site. Class II and Class III nodulins exhibit C-terminal stretches of < 7 contiguous basic residues. All 6 Class II modules show penultimate Cys residues. Class III modules exhibit the least basic C-termini (Figure 1B).

Templated and ab initio modeling simulations, while generating a number of potential structural models, nonetheless consistently predicted the AtSfh1 nodulin adopts an α-helical coiled-coil structure. For example, one templated model predicts the AtSfh1 nodulin domain assumes an elongated anti-parallel three-helix coiled-coil (Figure 1C). Templated modeling of AtSfh3, AtSfh5 and AtSfh9 nodulin domains similarly arrived at elongated three-helix coiled-coil folds. Although these simulations do not confidently generate precise structural details, these experiments nonetheless forecast that a common structural feature of Nlj16-like nodulin domains is an α-helical coiled-coil fold. As described below, the biochemical properties of these nodulin domains are consistent with this inference. The conserved joining of a Sec14-domain with an Nlj16-like nodulin suggests both domains contribute to AtSfh1 function. Indeed, neither expression of the isolated Sec14- or nodulin-domains complemented short root hair phenotypes of Atsfh1$^{0/0}$ plants (Figure 1D).

Class I nodulin domains are PtdIns(4,5)P_2-binding modules

The signature basic patch/aromatic residue motifs of Class I nodulin C-termini resemble mammalian plasma membrane (PM) targeting motifs that bind acidic lipids - including phosphoinositides (McLaughlin et al. 1995; Murray et al., 2002; McLaughlin and Murray 2005). Phosphoinositides, particularly PtdIns(4,5)P_2, are well-established regulators of polarized membrane growth in various unicellular and multicellular organisms and including plant root hairs (Braun et al., 1999; Devreotes and Janetopoulos, 2003; Gervais et al., 2008; Heilmann, 2009; Yakir-Tamang and Gerst, 2009; Krahn and Wodarz, 2012; Yang, 2012). We therefore considered the possibility that nodulin domains play important roles in execution of PtdIns(4,5)P_2 signaling in tip-growing root hairs, and exploited yeast (a system where the composition of a biological membrane can be manipulated) to examine whether nodulin domains display specific lipid interactions. AtSfh1, AtSfh3, AtSfh7 and AtSfh10 Class I GFP-nodulins targeted to the PM, whereas Class II and Class III GFP-nodulins did not (Figure 2A; Supplemental Figure S1A,B). Membrane targeting of Class I nodulins was PtdIns(4,5)P_2–dependent as inactivation of a temperature-sensitive version of yeast PtdIns-4-phosphate 5-OH kinase (Mss4) released Class I GFP-nodulins from the PM (Figure 2B; Supplemental Figure S1C). PtdIns(4,5)P_2 levels were reduced in all *mss4^{ts}* mutants at 37°C (Figure 2C).

Bulk PtdIns(4)P levels were not depressed upon shift of *mss4^{ts}* mutants to 37°C -- suggesting that PtdIns(4)P did not contribute to Class I nodulin association with yeast PM. Indeed, reduction of bulk PtdIns(4)P, by inactivation of the Pik1 or Stt4 yeast PtdIns 4-OH kinases, failed to compromise Class I nodulin PM targeting (Figure 2D; Supplemental Figure S1D). PtdIns-3OH phosphoinositides did not contribute to PM-targeting of the AtSfh1 nodulin domain either. Challenge of cells with 1.4 M NaCl for 5-15 min, to elevate PtdIns(3,5)P_2 levels in the cytosolic leaflets of vacuolar membranes (Dove et al., 1997), failed to redistribute Class I nodulins from PM to vacuoles. Moreover, Class I nodulins

targeted to PM in *vps34*Δ mutants devoid of all yeast PtdIns 3OH phosphoinositides (PtdIns(3)P and PtdIns(3,5)P_2; Figure 2D; Supplemental Figure S1D).

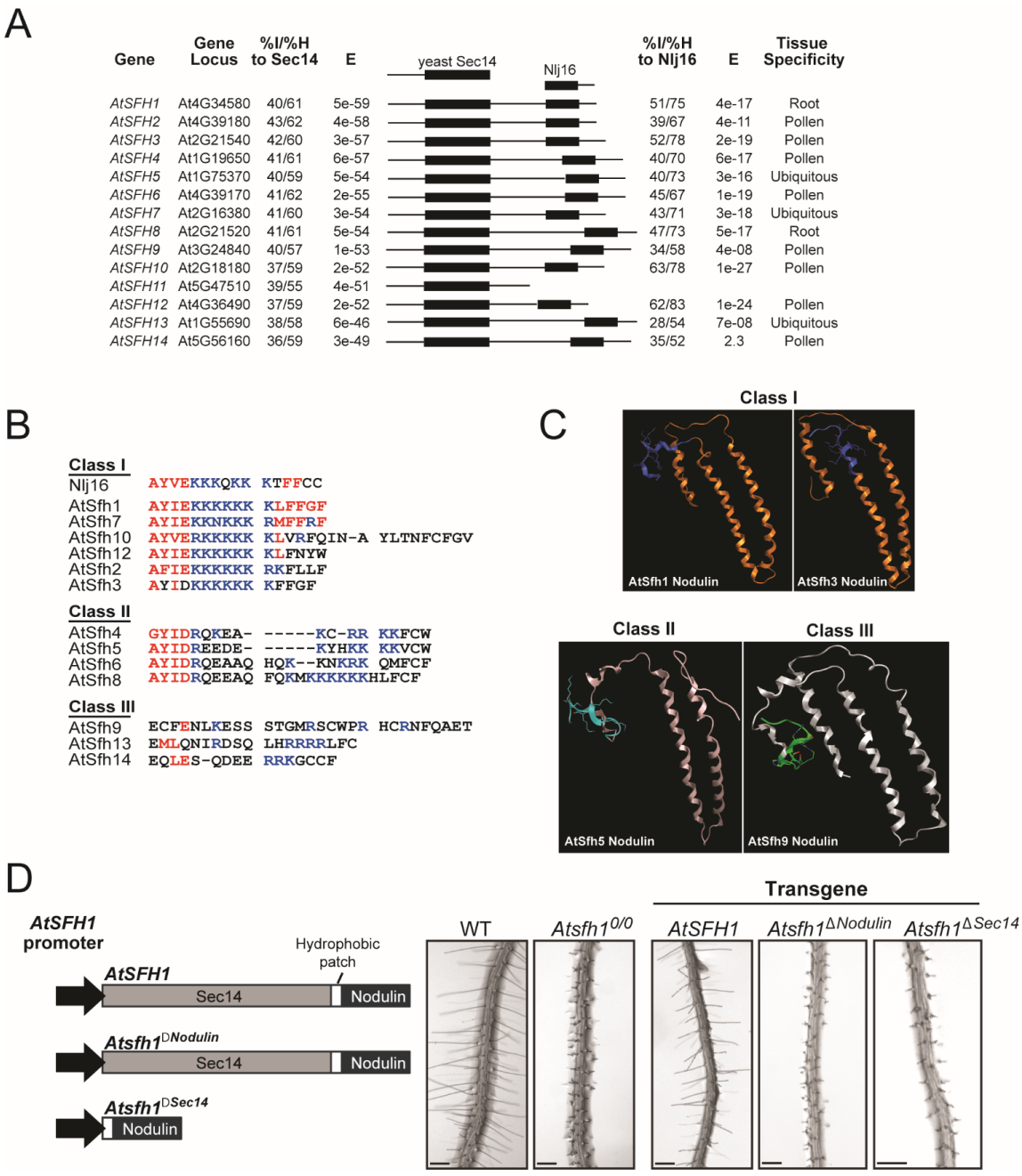

Figure 1. The Arabidopsis Sec14-nodulin protein family. (A) Alignment of the 14 highest scoring Sec14 homologs of the Arabidopsis Sec14-like PITP family. All Arabidopsis proteins with homology to the Lotus japonicus Nlj16 nodulin are also shown. Percent identities (% I) and similarities (% H), and corresponding E-values are indicated (Sec14, left; nodulin, right), as are tissue expression profiles http://www.ncbi.nlm.nih.gov/geo/). (B) Alignments of the C-termini of Class I, II and III nodulin domains. Conserved residues and basic amino acids are in red and blue, respectively. (C) Homology models for nodulin domains are shown. Models were generated by structural templating using nodulin homology to a region of a DNA topoisomerase.(D) Diagram of Atsfh1 constructs used to transform Atsfh10/0 plants. All transgenes were expressed under native AtSFH1 promoter control and encoded epitope-tagged myc-AtSfh1-HA, myc-AtSfh1ΔNodulin-HA and AtSfh1ΔSec14-HA, respectively. Bright field images of root hairs of transgenic seedling are shown. Scale bars: 1 mm

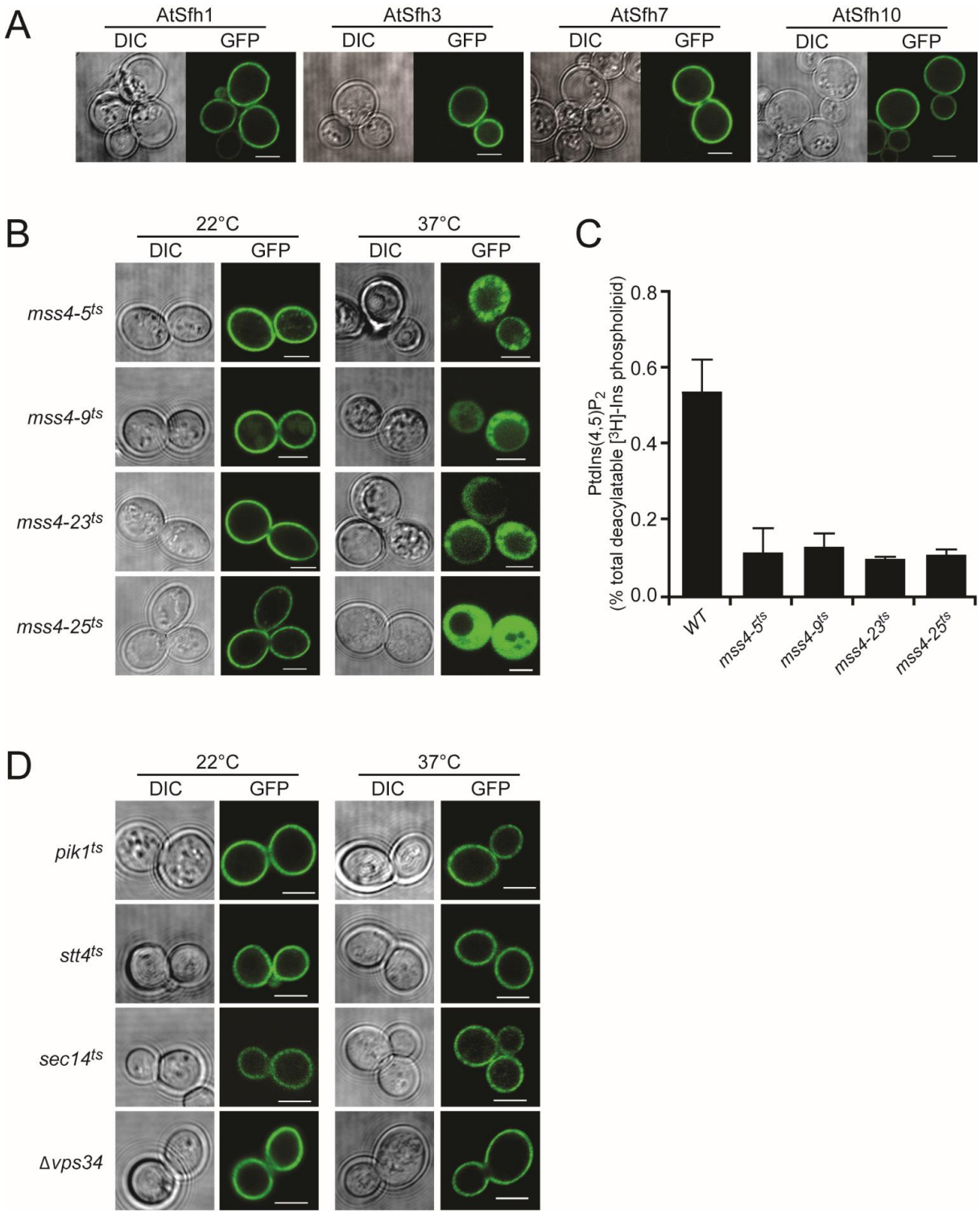

Figure 2. Class I nodulins localize to yeast PM in a PtdIns(4,5)P_2-dependent manner. (A) GFP-tagged Class I chimeras localize to PM when expressed in WT yeast. Images are representative of 158, 261, 352 and 216 cells expressing AtSfh1, AtSfh3, AtSfh7 and AtSfh10 nodulins, respectively. All cells showed exclusive PM localization. (B) GFP-tagged Class I nodulins are released from PM in four independently isolated *mss4^{ts}* mutants when Mss4 is inactivated at 37°C. Images are representative of an aggregate of 901 and 1094 cells imaged at 22°C and 37°C, respectively, and 107-355 cells were scored for each nodulin at each temperature. In all cases, >95% of the cells imaged at 22°C showed PM localization of the GFP-nodulin reporter whereas, in all cases, >93% of the cells imaged at 37°C showed exclusively cytoplasmic localization for the indicated GFP-nodulin reporter. GFP-nodulin profiles were also imaged in WT yeast at 22°C (aggregate of 275 cells) and 37°C (aggregate of 184 cells). As expected, at both temperatures, 100% of the cells showed exclusively PM localization profiles. (C) Quantification of PtdIns(4,5)P_2 in WT and *mss4^{ts}* strains at 37°C.

Figure 2, continued. Analyses involved steady-state radiolabeling of cells with [^{3}H]-inositol at 22°C, shift of cells to 37°C for 2 h, and total deacylated ^{3}H-labeled inositol glycerolipids were quantified by anion-exchange HPLC. PtdIns(4,5)P_2 values are expressed as percentage of total deacylatable [^{3}H]-inositol lipid. The unpaired t-test p value (mutant compared to WT) is <0.012. (D) GFP-tagged Class I nodulins localize to PM when expressed in yeast with temperature sensitive PtdIns-4-OH kinase (*stt4^{ts}* and *pik1^{ts}*), PtdIns-3-OH kinase (*vps34^{ts}*) and Sec14 (*sec14^{ts}*) incubated at 22°C and 37°C. DIC and GFP confocal images are identified, and 107-170 cells were imaged for each mutant at each temperature. For each mutant and condition, >91% of the cells imaged showed exclusive PM localization for the indicated GFP-nodulin reporter. Scale bars: 2 μm.

Nodulin peptide binds PtdIns(4,5)P_2

NMR titration experiments using short-chain PtdIns(4,5)P_2 (di-C4-PtdIns(4,5)P_2) as ligand confirmed the C-terminal region of AtSfh1 nodulin interacts with PtdIns(4,5)P_2. Binding assays were carried out with di-C4-PtdIns(4,5)P_2 below the critical micellar concentration. Addition of di-C4-PtdIns(4,5)P_2 to the wild-type AtSfh1 nodulin peptide (WT, Ac-KKKKKKKLFFGFCOOH) resulted in significant changes in the 1H NMR spectrum. In the presence of equimolar ligand, a new set of 1H peaks appeared in the amide region between 7.9 and 8.0 ppm, and in the aromatic region that contains 1H peaks of all three Phe side-chains (Figure 3). The two –CH3 groups of Leu8 resonated at 0.81 (Hδ1) and 0.89 ppm (Hδ2). While Hδ1 was obscured by the –CH3 protons of di-C4-PtdIns(4,5)P_2, a shifted Leu Hδ2 peak also appeared at equimolar peptide::ligand concentrations. Increasing di-C4-PtdIns(4,5)P_2 concentrations drove full conversion of ligand free peptide to the ligand-bound species (Figure 3).

Two mutant nodulin peptides, K_5A (Ac-KKKKAKKLFFGFCOOH) and $K_{3,5}$A (Ac-KKAKAKKLFFGFCOOH), were also analyzed. 1H NMR spectra of the K_5A and $K_{3,5}$A peptides showed few chemical shifts in the presence of equimolar di-C4-PtdIns(4,5)P_2 (Figure 3). Addition of > 2-3-fold molar excess of the ligand was required to evoke mutant peptide chemical shift perturbations similar to those observed for WT peptide. Using Leu Hδ chemical shifts as reporters of peptide binding to di-C4-PtdIns(4,5)P_2, we qualitatively ranked the relative peptide affinities for di-C4-PtdIns(4,5)P_2 as: WT > K_5A > $K_{3,5}$A.

Modeling nodulin peptide interactions with PtdIns(4,5)P_2

Two-stage atomistic molecular dynamics simulations (MDS) modeled how the AtSfh1 nodulin peptide binds PtdIns(4,5)P_2. In the first stage, WT nodulin peptide folding was simulated in aqueous solution (Figure 4A). The second stage simulated interactions of structured and unstructured peptides (systems 5, 6 and systems 2–4 respectively; Figure 4B, Supplemental Table S1A) to bilayers composed of dilineoylphosphatidylcholine (DLPC), dilineoylphosphatidylserine (DLPS), and PtdIns(4,5)P_2 at 297 K (Figure 4C). Membrane simulations were initiated with 1, 2, 4, or 8 AtSfh1 peptides positioned randomly in water (Figure 4D; details in Materials and Methods). Nodulin peptide bound firmly to the membrane after 300 ns via H-bond interactions with PtdIns(4,5)P_2 (Figure 4E), and the residues engaged in peptide binding to PtdIns(4,5)P_2 were K1-K7 (Supplemental Table S1B and Figure 4F). MDS further predicted that a single peptide bound 1, 2, or 3 PtdIns(4,5)P2 with similar probabilities (~30%), and could engage 4 PtdIns(4,5)P_2 simultaneously (Supplemental Table S1C, Figure 4G). Interestingly,

aggregations of 2 and 3 peptides were observed when binding of multiple nodulin peptides was simulated on membrane surfaces containing PtdIns(4,5)P_2 (Supplemental Table S1A; Figure 4G).

Additional 500 ns MDS were run to examine how the AtSfh1 nodulin peptide might discriminate between PtdIns(4,5)P_2 and PtdIns(3,5)P_2. Indeed, binding of peptide to PtdIns(3,5)P_2 was projected to be weaker than to PtdIns(4,5)P_2. The number of H-bonds established between peptide and phosphoinositide within the 200-500 ns simulation window differed significantly between these isomers (Supplemental Table S1D). Whereas PtdIns(4,5)P_2 presented a conformation suitable for establishment of two H-bonds between a coordinating Lys and an individual headgroup phosphate, PtdIns(3,5)P_2 did not (Figure 4H).

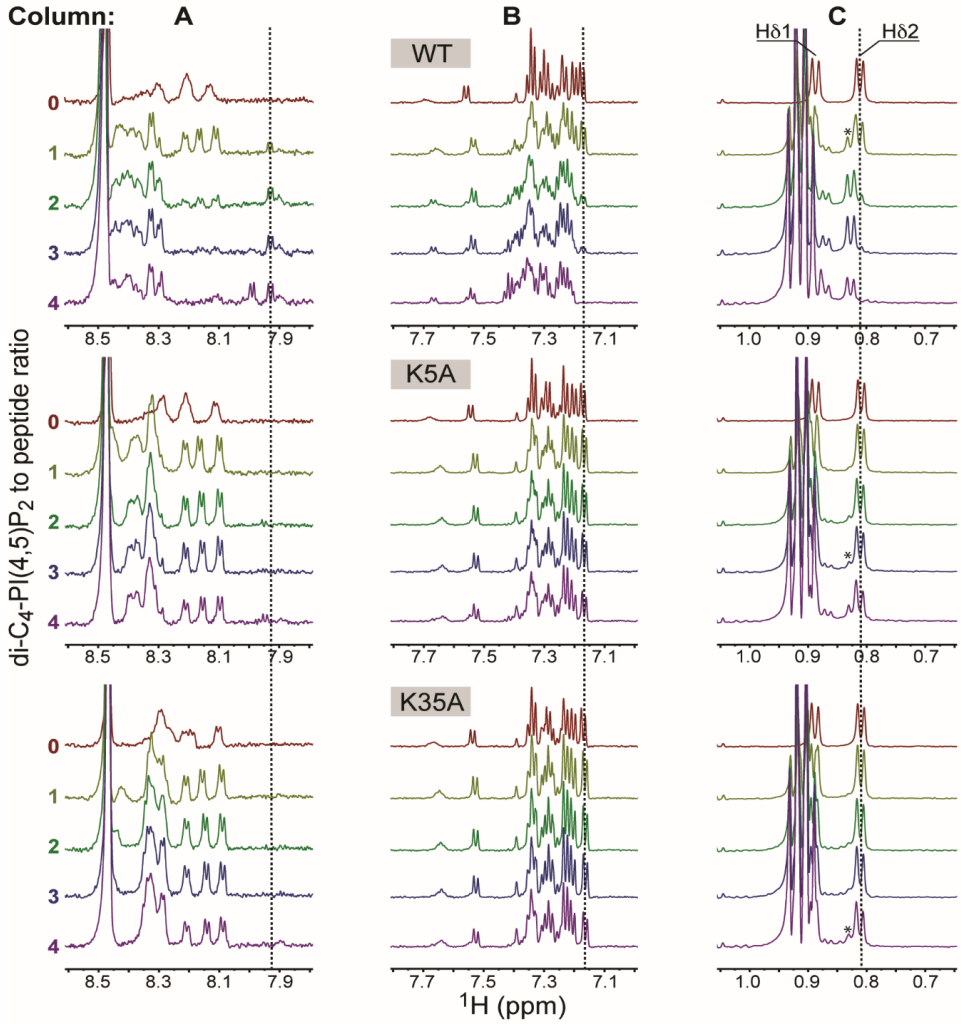

Figure 3. NMR analyses of AtSfh1 nodulin peptide binding to PtdIns(4,5)P_2. ^{1}H NMR spectra of three AtSfh1 nodulin peptide variants (peptide sequences given at bottom; Lys→Ala highlighted in red) are stacked and color-coded according to di-C4-PtdIns(4,5)P_2:peptide molar ratio. Three ^{1}H spectral regions are shown: amide **(column A)**, aromatic **(column B)**, and upfield methyl (0.75-1.05 ppm, **column C**). Significant chemical shift changes resulting from di-C4-PtdIns(4,5)P_2 binding to nodulin peptide are marked (vertical lines). Peaks centered at 0.91 ppm correspond to methyl protons of di-C4-PtdIns(4,5)P_2 acyl chains. The Leu Hδ peak of di-C4- PtdIns(4,5)P_2-bound peptides is marked (*).

C-terminal Lys mediate PtdIns(4,5)P_2 binding

To examine the functional importance of AtSfh1 nodulin peptide::PtdIns(4,5)P_2 interactions, an allelic series of K→A mutants was constructed. Yeast expression experiments demonstrated that PM localization of the AtSfh1 nodulin was dependent on integrity of the C-terminal basic motif, and that individual Lys residues displayed differential contributions to PtdIns(4,5)P_2-binding (Figure 5A,B). Two single substitutions (K_1A and K_6A) and all multiple substitutions tested (i.e. $K_{3,5}$A, $K_{4,5}$A, $K_{3,4,5}$A, $K_{1\text{-}2}$A, $K_{1\text{-}4}$A, $K_{1\text{-}6}$A, $K_{1\text{-}7}$A) compromised nodulin association with PM. By contrast, the AtSfh1^{K2A}, AtSfh1^{K3A}, AtSfh1^{K4A}, AtSfh1^{K5A} and AtSfh1^{K7A} nodulins retained significant PM localization (Figure 5A,B) -- indicating those residues did not play critical individual roles in PtdIns(4,5)P_2 binding, although collective contributions were important. The mutant nodulin localization properties, as scored using the yeast system, were recapitulated in tobacco leaf cells. Whereas AtSfh1 and mutant versions harboring single K→A substitutions targeted to the PM, none of the multiply substituted nodulins did (Supplemental Figure S2A,B).

Bulky aromatic residues, such as the C-terminal Phe residues of the Class 1 nodulin peptides, are a common feature of poly-basic motifs and these residues often stabilize protein::membrane interactions (McLaughlin and Murray, 2005; Gerlach et al., 2010; Li et al., 2014). Therefore, the contributions of these C-terminal Phe residues to nodulin recruitment to membranes were also analyzed in yeast. Whereas single F→A substitutions did not affect PM targeting, the triple F→A substitution did (data not shown).

C-terminal Lys are required for root hair biogenesis

Root hair growth in Arabidopsis requires PtdIns(4,5)P2 synthesis catalyzed by the AtPIP5K3 PtdIns-4-phosphate 5-OH kinase (Kusano et al., 2008; Stenzel et al, 2008; Munnik and Nielsen, 2011). Therefore, the PtdIns(4,5)P_2-binding properties of the AtSfh1 nodulin domain suggested AtSfh1 may itself be a novel PtdIns(4,5)P_2 effector. To examine the biological significance of PtdIns(4,5)P_2-binding by the AtSfh1 nodulin, the K→A substitution series was incorporated into an *AtSFH1* transgene. The allelic series included conversion of all 7 Lys residues to Ala ($K_{1\text{-}7}$A), and the K_1A, K_5A and K_6A single, the $K_{3,5}$A and $K_{4,5}$A double, and $K_{3,4,5}$A triple substitutions. An *Atsfh1$^{0/0}$* Arabidopsis line was reconstituted with either WT or mutant *AtSFH1* transgenes, T3 homozygous transgenic plant lines were generated, and those lines were analyzed for correction of *Atsfh1$^{0/0}$* short root hair phenotypes. Whereas *AtSFH1^{+}* complemented *Atsfh1$^{0/0}$* phenotypes, variable efficiencies of rescue were recorded for Atsfh1 nodulin peptide mutants. Stable expression of *Atsfh1^{K5A}* and *Atsfh1^{K6A}* gene products partially rescued *Atsfh1$^{0/0}$* root hair morphogenetic defects– as exemplified by most *Atsfh1^{K5A}* and *Atsfh1^{K6A}* root hairs

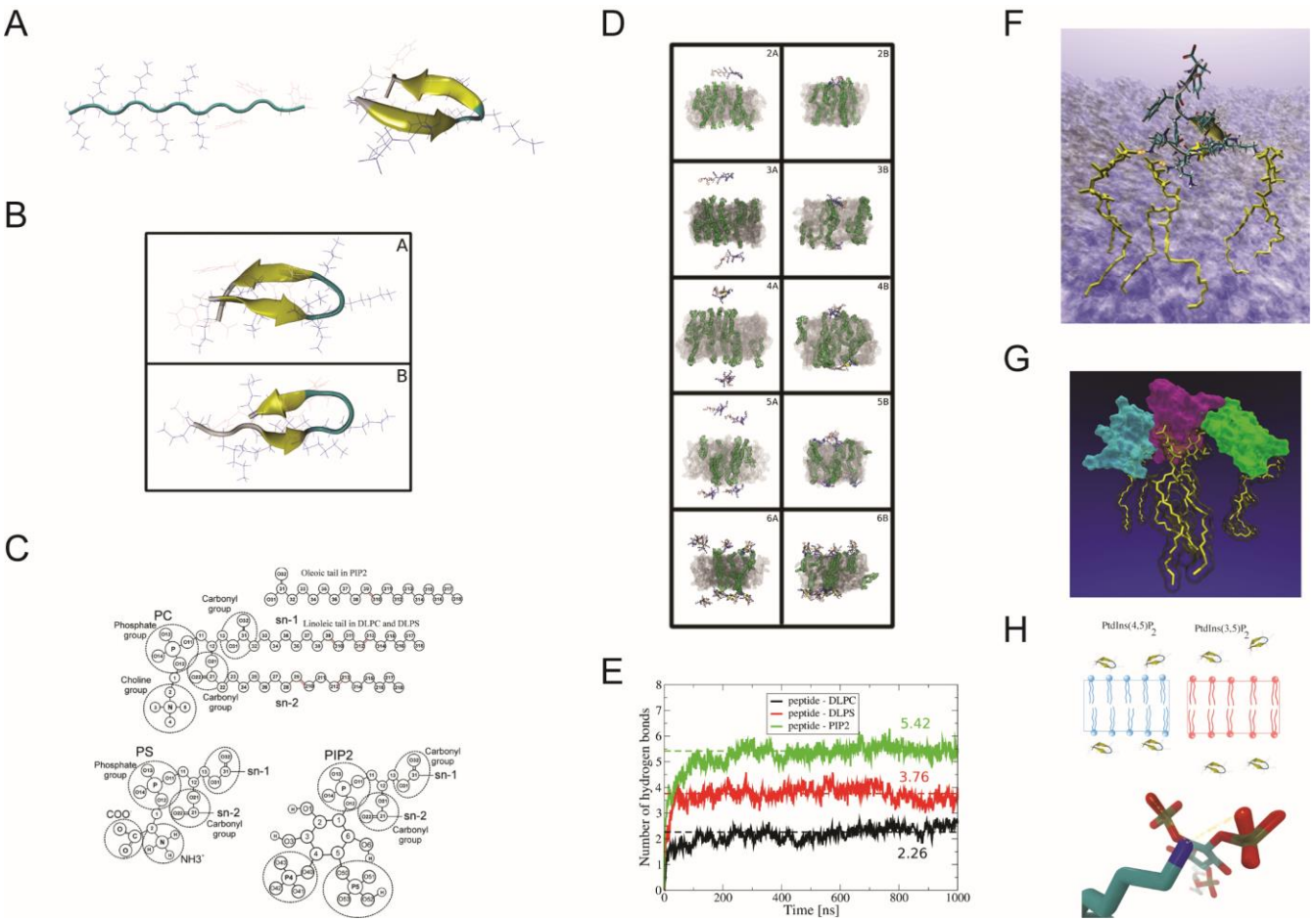

Figure 4. Molecular dynamics simulations of AtSfh1 nodulin peptide on membrane bilayers. **(A)** Unfolded extended structure of the AtSfh1 nodulin peptide (left panel) and folded β-hairpin structure after 4 μs of MDS in water (right panel). **(B)** Two most populated clustered structures from REMD simulation at 297K. Panel A-10.85% probability, and panel B- 8%. Both structures adopt β-hairpins. **(C)** Chemical structures of lipids used in the simulations. **(D)** Snapshots of systems simulated with a lipid bilayer. Beginning (A, C, E, G, I) and end of the simulation (B, D, F, H, J) of systems 2 (A, B), 3 (C, D), 4 (E, F), 5 (G, H), 6 (I, J) in Supplemental Table S1A. PtdIns(4,5)P_2 molecules are in green (H_2O not shown). **(E)** Time development of peptide::lipid H-bonds (DLPC (black), DLPS (red), and PtdIns(4,5)P_2 (green)). Data averaged over simulations 2-6 in Supplemental Table S1A. Dashed lines show average level of H- bonds with each lipid type. **(F)** Snapshot of the peptide (licorice representation together with "new cartoon") bound to 3 PtdIns(4,5)P_2 molecules (yellow licorice) by H-bonds (orange dots). Membrane shown as a transparent surface (H_2O not shown). **(G)** Snapshot of 3 aggregated nodulin peptides (cyan, violet and green surface) bound to 3 PtdIns(4,5)P_2 (yellow licorice). Picture generated by VMD (Humphrey *et al*., 1996). **(H)** Schematic representation of AtSfh1 nodulin peptide bound to PtdIns(4,5)P_2 (blue) and PtdIns(3,5)P_2 (red). Lower panel shows H-bonds established between nodulin peptide Lys side chain (blue) and PtdIns(4,5)P_2 (red).

presenting single growing tips and exhibiting intermediate lengths relative to *AtSFH1*$^{+/+}$ and *Atsfh1*$^{0/0}$ root hairs (Figure 6A-C; Supplemental Table S1E). By contrast, *Atsfh1*^{K3,5A}, *Atsfh*^{K4,5A}, *Atsfh1*^{K3,4,5A} and *Atsfh1*$^{K1-7A}$ plants phenocopied *Atsfh1*$^{0/0}$ mutants (Figure 6A-C; Supplemental Table S1E). The morphological defects of *Atsfh1*$^{0/0}$ root hairs reflect collapse of tip-directed PtdIns(4,5)P_2 gradients (Vincent et al. 2005). While *Atsfh1*$^{0/0}$ root hairs reconstituted for AtSfh1 expression recovered a strong tip-focused PtdIns(4,5)P_2 gradient, expression of the hypomorphic AtSfh1^{K5A} and AtSfh1^{K6A} restored weak tip-directed PtdIns(4,5)P_2 profiles that were reduced ca 50% in magnitude relative to WT

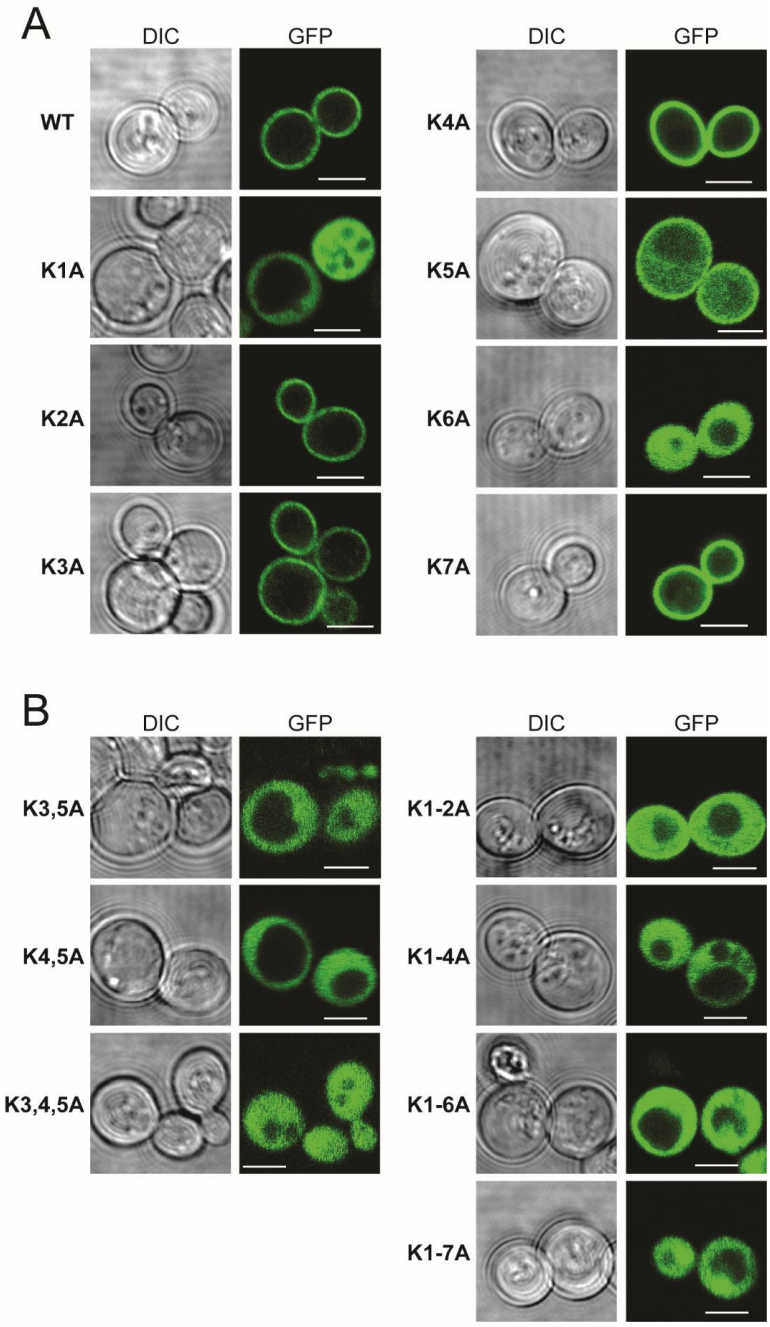

Figure 5. Localization of GFP-tagged WT and the indicated single **(A)** and multiple **(B)** K→A substituted nodulin chimeras in WT yeast. Corresponding DIC and GFP confocal image panels are identified. Scale bars: 2 μm. For all mutants, 100-235 cells were imaged and scored. All cells expressing the single K_1A and K_6A mutant reporters displayed exclusive localization of reporter to the cytoplasm, whereas all cells expressing the K_5A reporter showed both PM and cytoplasmic localization for the reporter. Otherwise, >99% of the cells expressing single mutant K→A derivatives showed exclusively PM localization for the reporter.

(Supplemental Figure S2D). Tip-directed PtdIns(4,5)P_2 gradients were completely ablated in root hairs expressing non-functional mutants as sole AtSfh1 species (AtSfh1^{K3,5A} , AtSfh1K4,5A, AtSfh1^{K3,4,5A}, AtSfh1$^{K1\text{-}7A}$; Supplemental Figure S2D).

An unrelated PtdIns(4,5)P_2 binding unit replaces the nodulin peptide

The severities of AtSfh1 nodulin peptide mutant phenotypes were proportional to the corresponding PtdIns(4,5)P_2 binding defects; suggesting PtdIns(4,5)P_2 binding is the key activity of that motif. As test, a PtdIns(4,5)P_2-specific binding unit (the PH$^{PLC\delta1}$ domain) was appended to a mutant AtSfh1 with a Lys-deficient nodulin peptide (Figure 6D). The consequences of reconstituting PtdIns(4,5)P_2-binding capacity in this way were then determined. Whereas the 'parental' AtSfh1^{K1,4A} was non-functional, AtSfh1^{K1,4A}::PH$^{PLC\delta1}$ expression revived root hair development in *Atsfh1$^{0/0}$* plants (Figure 6D). Similar results were obtained when the PH$^{PLC\delta1}$ domain was appended to the AtSfh1$^{\Delta543\text{-}554}$ C-terminus (lacks the entire polybasic motif -- including the 3 Phe residues). Rescue was dependent on PH$^{PLC\delta1}$ binding to PtdIns(4,5)P_2 since appending binding mutants (K32E and K32L, Yagisawa et al., 1998) failed to rescue *Atsfh1$^{0/0}$* root hair defects (Figure 6D). Thus, PtdIns(4,5)P_2 binding is the crucial activity of the nodulin peptide, and binding of 1 PtdIns(4,5)P_2 per nodulin meets the threshold for biological function.

AtSfh1 nodulin binds PtdIns(4,5)P_2 with high affinity

Two lines of evidence demonstrated Class I nodulins bind PtdIns(4,5)P_2 with high affinity. First, inducible expression of AtSfh1 nodulin interfered with yeast endocytosis -- a PtdIns(4,5)P_2–dependent process (Sun et al., 2007). This interference was manifested by delayed internalization of FM4-64 tracer from PM into endosomes when cells expressed AtSfh1 nodulin, but not mutant versions unable to bind PtdIns(4,5)P_2 (Supplemental Figure S3A). Second, whereas incubation of an *mss4-102^{ts}* strain at 26°C released a GFP-tagged tandem PH-domain from the PM, mRFPnodulin association with PM was not compromised (Supplemental Figure S3B). These data indicate AtSfh1 nodulin binds PtdIns(4,5)P_2 more tightly than does a tandemized PH$^{PLC\delta1}$ and report a high affinity as monomeric PH$^{PLC\delta1}$ binds PtdIns(4,5)P_2 with a KD ~ 1-5 μM (Lemmon et al., 1995).

Nodulin domains homo-oligomerize

Isothermal titration calorimetry reported Ka values for WT, K_5A and $K_{3,5}$A nodulin peptides for PtdIns(4,5)P_2 of 5.4 X 10^4, 2.4 x 10^4, and 1.7 X 10^4 (KD values of ~19 μM, 42 μM and 59 μM; Supplemental Figure S3C-E). The low affinity of WT nodulin peptide for phosphoinositide could not account for the high affinity of AtSfh1 nodulin for PtdIns(4,5)P_2 in vivo, however, and suggested Nlj16-like nodulins self-assemble with accompanying enhancements in PtdIns(4,5)P_2 binding avidity. All 13 Arabidopsis nodulin domains were expressed in *E. coli*, and all but 3 (AtSfh3, AtSfh5 and AtSfh8 nodulins) distributed quantitatively into inclusion bodies. AtSfh1 nodulin was solubilized with 8 M urea and, consistent with formation of homo-oligomers, resolved as a ladder in SDS-PAGE. The ladder

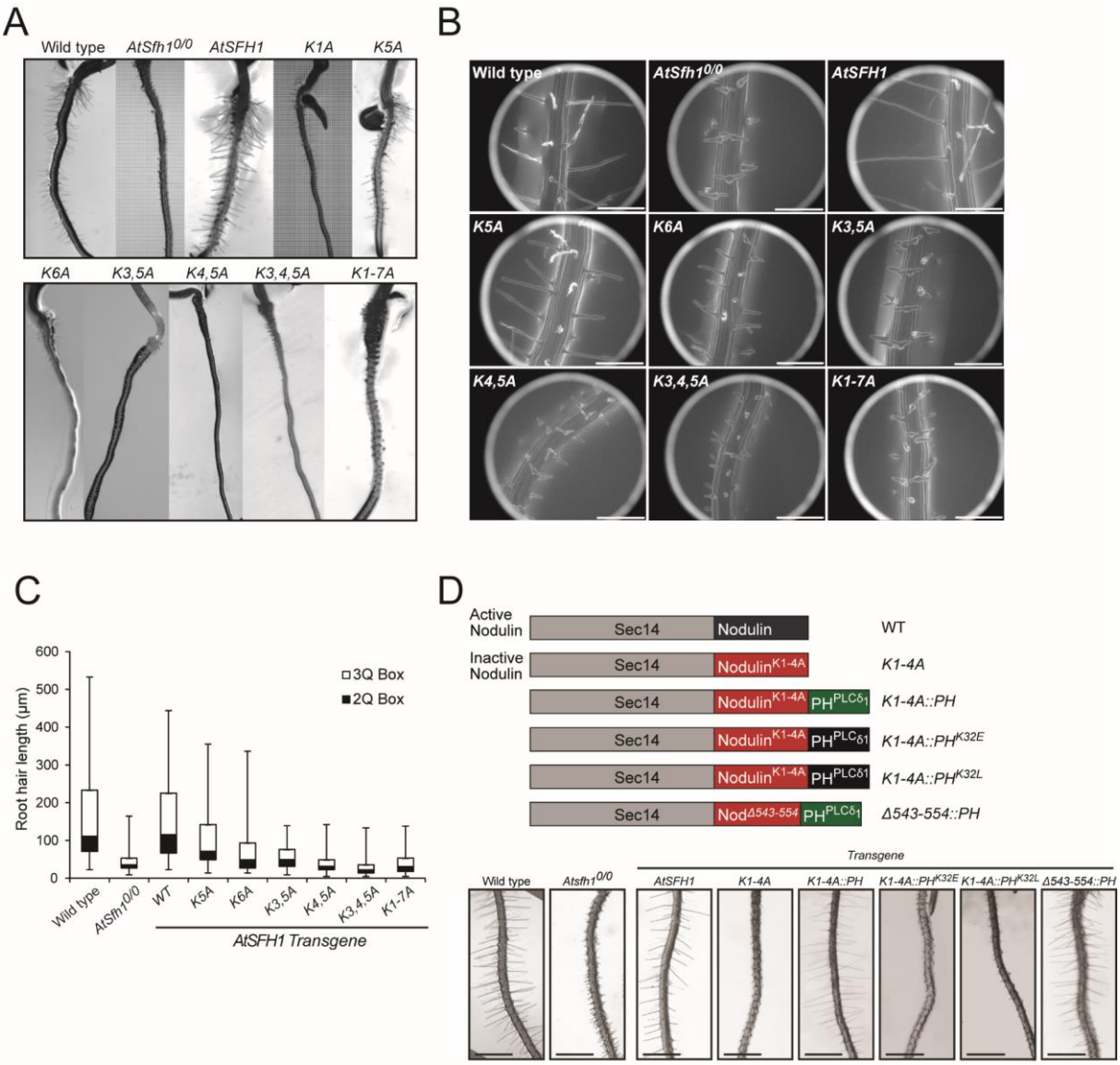

Figure 6. AtSfh1 C-terminal poly-basic motif is required for biological function. **(A)** Bright field images of root hairs of 3-day-old WT, *Atsfh10/0* and T3 seedlings of *Atsfh10/0* plants expressing *AtSFH1* and indicated Lys→Ala transgenes. **(B)** Environmental scanning electron micrograph images of T3 seedlings of the same plant lines as in (A). Single and double tip root hairs, along with notched root hairs, are obvious. Scale bars: 200 µm. **(C)** Box and whisker representation of root hair length distributions measured for 3-day-old seedlings of transgenic plant lines 55 represented in (A) and (B). The 2Q and 3Q boxes represent 2nd and 3rd quartiles of the data set, respectively. Whiskers span the 1st quartile, from the 2nd quartile box down to minimum, and the 4th quartile from 3rd quartile box up to the maximum. **(D)** Bright field images of root hairs of 3-day-old T3 seedlings of WT, *Atsfh1$^{0/0}$*, and *Atsfh1$^{0/0}$* plants expressing epitope-tagged AtSfh1,Atsfh1^{K1,4A} , AtSfh1$^{K1,4A::PHPLC\delta1}$, AtSfh1$^{K1,4A::PHPLC\delta1K32E}$, AtSfh1$^{K1,4A::PHPLC\delta1K32L}$, and AtSfh1$^{\Delta543\text{-}554::PHPLC\delta1}$ proteins. Proteins encoded by the respective transgenes are at top. All constructs were expressed from the native *AtSFH1* promoter.

ranged from 14-kDa to ca. 112-kDa (octamer?) in increments of the monomeric mass of 14-kDa (Figure 7A). Soluble fractions of Class I AtSfh3 nodulin (13-kDa) behaved similarly in SDS-PAGE (Figure 7A). AtSfh3 nodulin, and the soluble Class II AtSfh5 and AtSfh8 nodulins, filtered at apparent molecular masses (Mr) of ~91 kDa; suggesting assembly into hexamers (Figure 7B; Supplemental Figure S3F-G).

The biochemical properties of the AtSfh1 nodulin were examined under native conditions by expressing the isolated domain in yeast and tobacco leaf cells. Size exclusion chromatography of cytosol

prepared from yeast expressing myc-tagged AtSfh1 nodulin reported this domain assembled into presumptive hexamers, octamers and even higher order complexes (Figure 7C). When expressed in tobacco leaf cells, mRFP-AtSfh1 nodulin filtered at an Mr consistent with assembly into homo-tetramers (Figure 7D). Interestingly, native $K_{1-4}A$ and $K_{1-7}A$ nodulins assembled into homo-octamers and even higher order complexes, respectively (Figure 7D). Thus, charge neutralization of the nodulin peptide potentiates homo-oligomerization of the nodulin – an attractive feature as such charge neutralization accompanies PtdIns(4,5)P_2 binding.

Oligomerization-defective nodulins are impaired in membrane targeting

Residues E_{485} and Q_{534} are conserved in all Nlj16-like nodulins, whereas Y_{474} is conserved only in Class I versions. All 3 residues lie outside the motif responsible for PtdIns(4,5)P_2 binding, and each was converted to Pro in attempts to generate new classes of mutant nodulins. Whereas AtSfh1^{E485P}, AtSfh1^{Q534P}, AtSfh1^{E485P,Q534P} and AtSfh1^{E485P,Y474P} nodulins were all stably expressed in yeast and plants, each failed to complement *Atsfh1$^{0/0}$* root hair defects (Figure 8A). Although functionally compromised, the AtSfh1^{E485P} and AtSfh1^{E485P,Y474P} nodulins targeted to PM in a PtdIns(4,5)P_2-dependent manner (Figure 8B; Supplemental Figure S4A). Thus, the biological defects of AtSfh1^{E485P,Y474P} nodulin revealed a critical activity independent of PtdIns(4,5)P_2 binding. PtdIns(4)P or 3-OH phosphoinositide deficiencies were without effect (Supplemental Figure S4B).

By contrast, PM association of the AtSfh1^{Q534P} and AtSfh1^{E485P,Q534P} nodulins was strongly compromised (Figure 8B), suggesting these mutant domains had diminished affinities for PtdIns(4,5)P_2 identifying these as candidates for oligomerization-defective mutants. Indeed, gel filtration of leaf extracts confirmed $E_{485}P$,$Q_{534}P$ missense substitutions collapsed AtSfh1 nodulin tetramers into dimers, and interfered with AtSfh1^{K1-4A} nodulin assembly into its typical octameric form (Figure 8C). These substitutions did not compromise assembly into dimers–indicating AtSfh1^{E485P,Q534P} nodulin was selectively deficient in its polymerization into tetramers and higher order homo-oligomers.

Nodulin interaction with PtdIns(4,5)P_2 is resistant to Ca^{++}-influx

A hallmark feature of root hairs engaged in active tip growth is the coupling of phosphoinositide and Ca^{++}-signaling (Braun et al., 1999; Ryan et al., 2001; Vincent et al., 2005; Cole and Fowler, 2006; Bibikova and Gilroy, 2008; Thole and Nielsen, 2008). As elongating root hair tips are preferential sites of Ca^{++} influx, and direct interaction of Ca^{++} with PtdIns(4,5)P_2 is known to compete with protein binding to this phosphoinositide (Levental et al., 2009; Slochower et al., 2013; Shi et al, 2013; Li et al., 2014), we again exploited a well-characterized yeast model to test whether large local Ca^{++} influxes modulated nodulin::PtdIns(4,5)P_2 interactions. Specifically, we took advantage of previous demonstrations that, relative to wild-type yeast, *vps33Δ* mutants experience rapid, large and sustained elevations in cytosolic Ca^{++} when challenged with high extracellular concentrations of this cation (Miseta et al., 1999).

Wild-type yeast are able to rapidly re-establish cytoplasmic Ca^{++} homeostasis when subjected to Ca^{++} shock. This is exemplified by the fact that challenge of cells with 50 mM extracellular Ca^{++} raises cytoplasmic Ca^{++} from a resting concentration of ~75 nM to 300 nM within seconds, and this elevation is resolved within 90 sec to near resting levels (Miseta et al., 1999). As expected, the AtSfh1

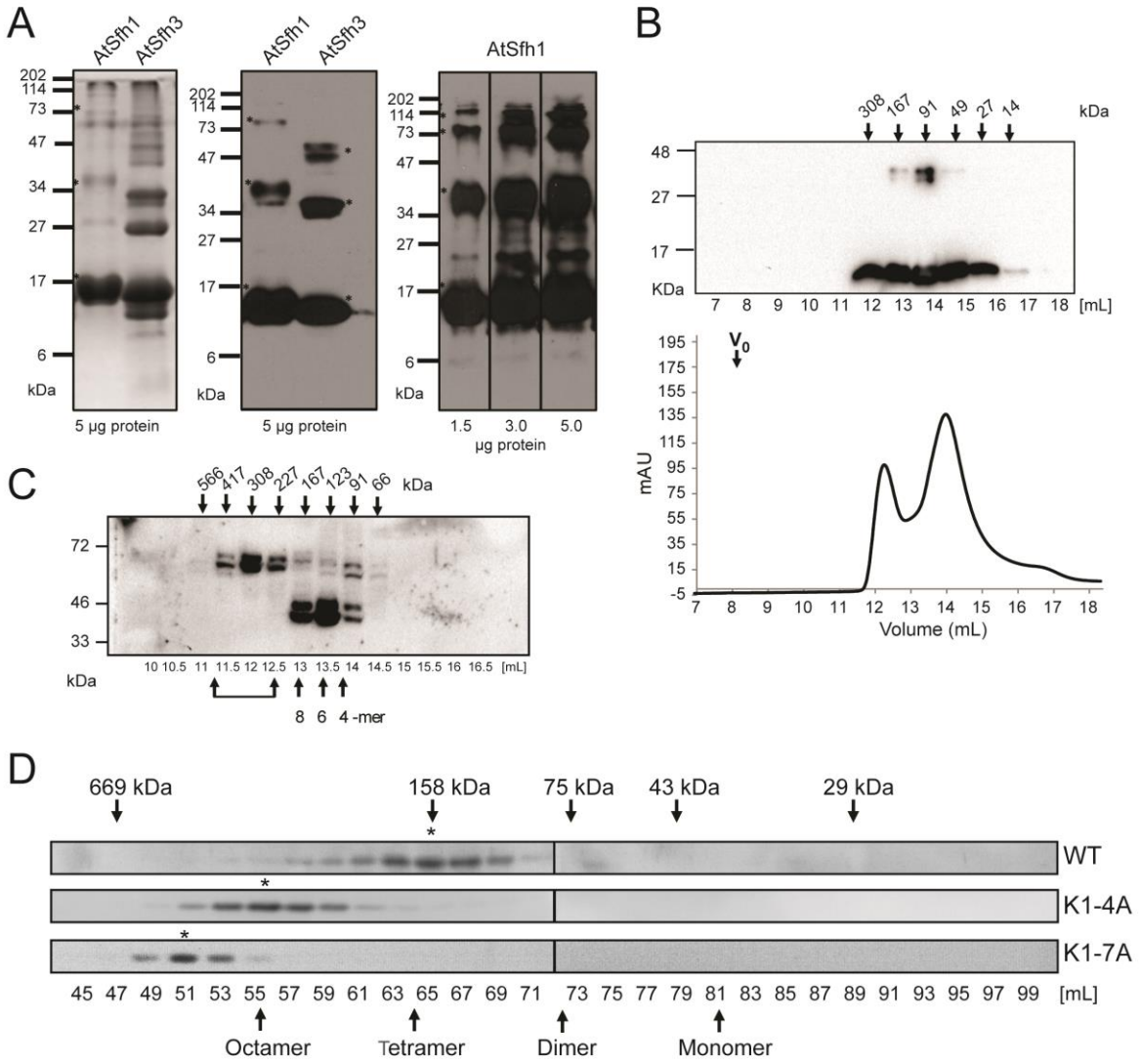

Figure 7. Homo-oligomerization of Class I nodulins. **(A)** Purified recombinant His-tagged AtSfh1- (solubilized in 8 M urea) and soluble AtSfh3-nodulins (5 µg) were resolved by SDS PAGE and visualized by Coomassie-Blue staining (left), and immunoblotting with anti-His tag antibody (middle). Immunoblotting of purified AtSfh1 nodulin with polyclonal AtSfh1 nodulin antibody is shown at right (load at bottom). SDS-resistant homo-oligomeric forms are identified in all panels (*). **(B)** Gel filtration chromatogram for purified native AtSfh3 nodulin. Immunoblot profile across the elution is shown in the upper panel above the chromatogram and elution properties of the indicated standards are identified by arrows. **(C)** Immunoblots of gel filtration column fractions of total lysates from yeast expressing myc-tagged AtSfh1 nodulin. Elution volume (mL) shown at bottom and corresponding apparent molecular masses indicated at top. Presumptive oligomeric states are identified at bottom. Brackets denote higher-order complexes. **(D)** Immunoblot profiles of gel filtration column fractions of lysates from tobacco leaf tissues expressing mRFP-tagged AtSfh1 WT, AtSfh1^{K1-4A}, and AtSfh1^{K1-7A} nodulins using anti-mRFP antibodies to visualize nodulin chimeras. Peak fractions of homo-oligomeric forms are identified (*). Monomeric and presumed homo-oligomeric forms of the mRFP-tagged proteins are identified (arrows).

GFP-nodulin reporter remained associated with yeast PM under these conditions, and even when cells were subjected to a 400 mM Ca^{++} shock (Figure 9A). The isogenic *vps33Δ* partner strain is defective in maintaining Ca^{++} homeostasis. Challenge of the mutant with 50 mM extracellular Ca^{++} raises cytosolic Ca^{++} from a resting concentration of 165 nM to ~1.75 µM, and these levels remain elevated (~470 nM) for prolonged periods (Miseta et al.,1999). Yet, even throughout these conditions of elevated cytoplasmic $Ca^{++,}$ localization of the GFP-nodulin reporter to the PM was not disturbed in the *vps33Δ* strain (Figure 9B). Moreover, subjecting *vps33Δ* cells to an intense 400 mM Ca^{++} shock also failed to

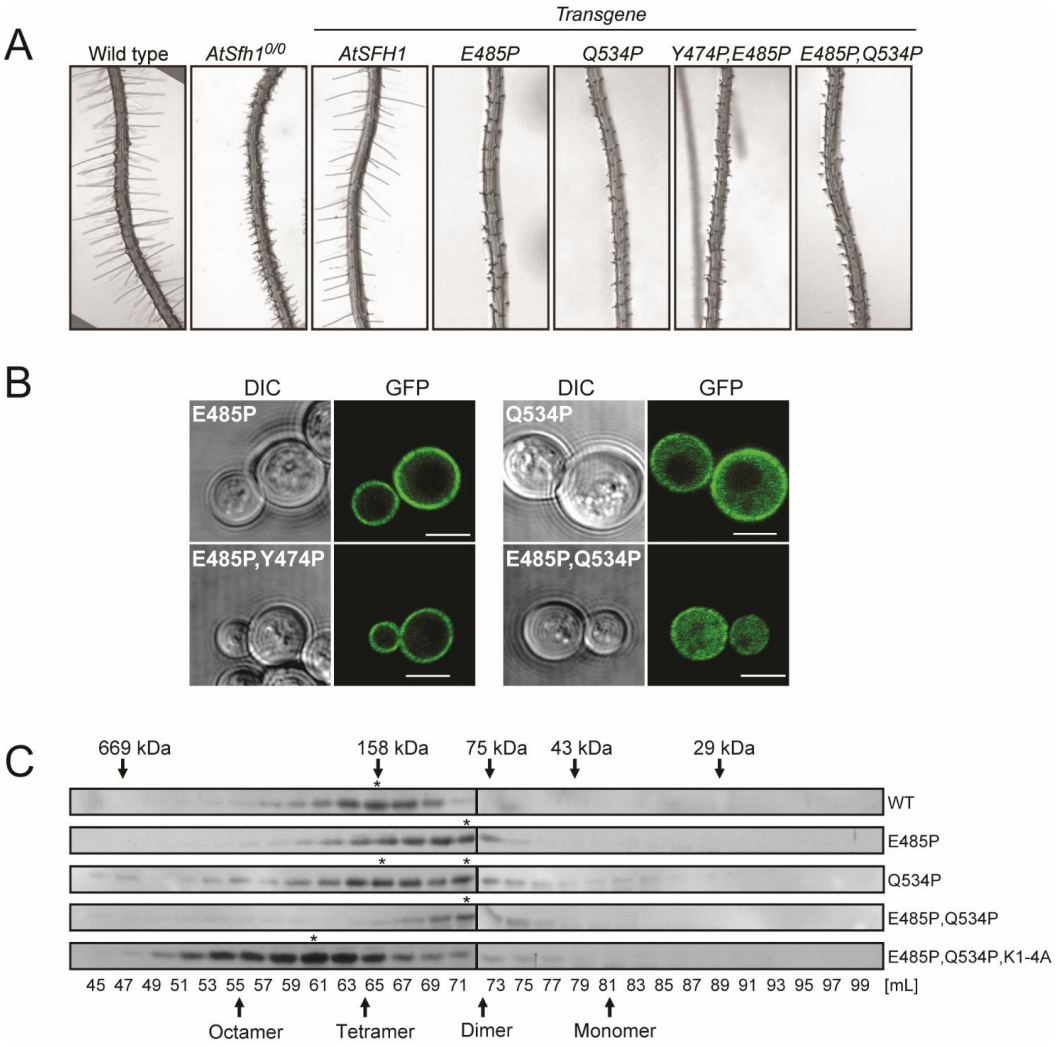

Figure 8. Poly-basic motif-independent functions of AtSfh1 nodulin. **(A)** Bright field images of root hairs from 3–day-old WT, *Atsfh1$^{0/0}$* and T3 seedlings of transgenic *Atsfh1$^{0/0}$* plants expressing *myc-AtSFH1-HA* and *myc-Atsfh1-HA* with indicated Pro-substitutions. Scale bars: 1mm. **(B)** Confocal images of WT yeast expressing GFP-tagged AtSfh1^{E485P}, AtSfh1^{Q534P}, AtSfh1^{E485P,Q534P}, and AtSfh1^{E485P,Y474P} nodulins. These images are representative of 105, 187,114, and 142 cells imaged, respectively. 98% and 92% of the cells expressing GFP-tagged AtSfh1^{E485P} or AtSfh1^{E485P,Y474P} nodulins showed exclusively PM localization of the reporter, respectively. All cells expressing GFP-tagged AtSfh1^{E485P,Q534P} nodulin showed a cytoplasmic localization profile exclusively. For cells expressing GFP-tagged AtSfh1^{Q534P} nodulin, 5% of the cells showed PM localization, 60% showed both PM and cytoplasmic staining, and 35% showed only a cytoplasmic localization of the reporter. Scale bars: 2 µm. **(C)** Immunoblots of gel filtration column fractions of lysates from tobacco leaf cells expressing mRFP-AtSfh1, AtSfh1^{E485P}, AtSfh1^{Q534P}, AtSfh1^{E485P,Q534P} and AtSfh1$^{E485P,Q534P,\ K1\text{-}4A}$ nodulins. Peak fractions of presumptive homo-oligomeric forms are identified (*). Apparent molecular masses and fraction volumes in panels D and E are indicated.

chase the GFP-nodulin reporter from the PM (Figure 9B). These data suggest that elevating cytosolic Ca^{++} to μM concentrations is by itself insufficient to break AtSfh1-nodulin interactions with PtdIns(4,5)P_2.

Discussion

Sec14-nodulin proteins are novel cell polarity regulators whose activities are critical for morphogenesis of highly polarized plant structures such as root hairs. The conserved genetic fusion of Sec14- and Nlj16-like nodulin modules is a biologically striking arrangement that sits at the interface of root hair development, lipid signaling and symbiotic N_2 fixation. Using the nonleguminous plant Arabidopsis thaliana as experimental model, we now demonstrate the nodulin domain is required for coherent organization of polarized root hair growth signaling, and identify the AtSfh1 and related Class I nodulins as functionally versatile PtdIns(4,5)P_2-binding modules. These units can either support, or subvert, polarized cell growth programs as dictated by developmental or environmental demands. Collectively, the data identify Sec14-nodulin proteins as novel scaffolds for templating the patterning of PtdIns(4,5)P_2 signaling in plants. This organization of PtdIns(4,5)P_2 landmarks is an essential aspect of the polarity signaling program in root hairs as the system fails without it -- even in the face of uncompromised PtdIns(4,5)P_2 biosynthetic capability. Taken together, these data reveal new principles for how lipid signaling is functionally diversified, with exquisite spatial and temporal precision, on membrane surfaces.

The three Nlj16-like nodulin classes are distinguished by their C-terminal peptide sequences, and this motif endows Class I nodulins their signature properties as PtdIns(4,5)P_2-binding units. Membrane targeting of Class I nodulins to a model eukaryotic (yeast) PM was dependent on PtdIns(4,5)P2 and no other yeast phosphoinositide – including the positional isomer PtdIns(3,5)P_2. This selectivity was further highlighted by the fact that yeast PM is rich in acidic phospholipids such as PtdIns and PtdSer. As PtdIns and PtdSer mass in yeast exceeds that of PtdIns(4,5)P_2 by ca. 100- and 50-fold, respectively (Zinser et al., 1991), these anionic lipids (as well as the mono-phosphorylated phosphoinositides) would efficiently compete for Class I nodulin binding if the module were to harbor even weak affinities for them. Class I nodulin specificity for PtdIns(4,5)P_2 comes with high affinity. Thus, AtSfh1 nodulin is an avid electrostatic sink for PtdIns(4,5)P_2 whose avidity and capacity are governed by homo-oligomerization into higher order structures (e.g. hexamers/octamers and higher). While an electrostatic sink of the sort presented by the AtSfh1 nodulin is expected to select for the most anionic lipid molecules available, e.g. PtdIns(4,5)P_2 and PtdIns(3,5)P_2, the positional specificity of this sink is a remarkable property.

The Lys-rich C-terminal motif of Class I nodulins prosecutes PtdIns(4,5) P_2 binding by these modules, and PtdIns(4,5)P_2 binding is essential for the biological function of AtSfh1 as polarity regulator in developing root hairs. Evidence to this effect includes: (i) the direct correspondence between strength of lipid-binding defect of a mutant nodulin with severity of loss-of-function phenotype when the defect

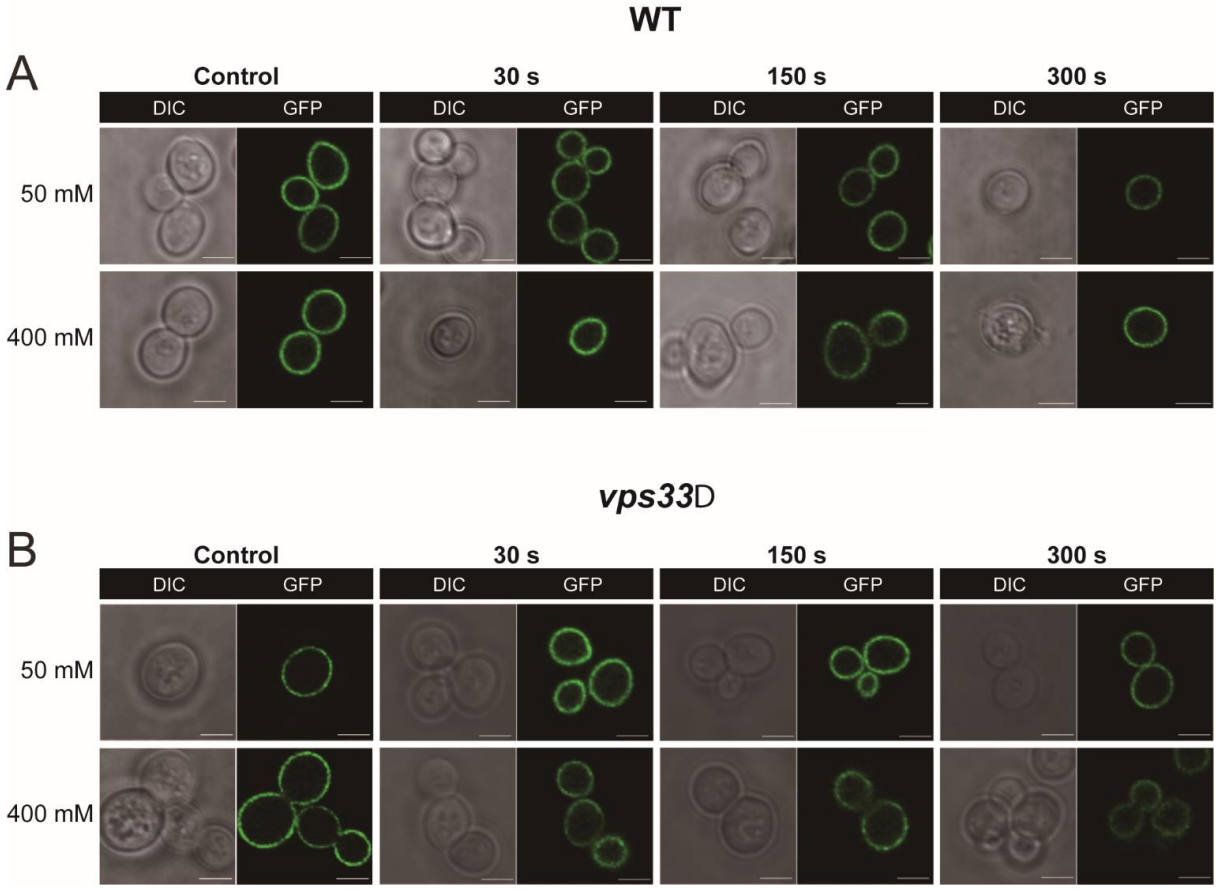

Figure 9. AtSfh1 nodulin domain interactions with phosphoinositide under conditions of Ca^{++} influx. Confocal images of WT yeast cells expressing GFP-AtSfh1 nodulin in wild-type **(A)** and *vps33*Δ strains **(B)** respectively, challenged with 50 or 400 mM $CaCl_2$ as indicated. For both panels, the control images are taken immediately prior to Ca^{++} challenge. Images were collected every 30 sec during a 30-300 sec post Ca^{++}-challenge window of analysis. The time point at which each image was taken is indicated. The *vps33*Δ mutant strain accumulates high levels of cytosolic Ca^{++} under these conditions and sustains these elevated levels throughout the time period the cells were imaged (Miseta *et al*., 1999). The GFP-AtSfh1 nodulin remained bound to PM in all cells observed for both yeast strains, under both Ca^{++} challenge conditions, and at all times imaged. The data are representative of three independent experiments and 160-326 individual cells were analyzed for each strain, under each condition, for each time point. Scale bar: 2 μm.

is incorporated into a full-length AtSfh1, and (ii) the ability of a PtdIns(4,5)P_2-specific binding unit ($PH^{PLC\delta1}$) to act as functional surrogate for the nodulin peptide in the context of a full-length AtSfh1. Physical appendage of a Sec14-domain that stimulates PtdIns(4)P production, to a unit that both laterally sequesters PtdIns(4,5)P_2 and assembles into higher-order structures, recommends AtSfh1-like proteins as novel scaffolds for coupling phosphoinositide production and organization. That is, Sec14-nodulins are well-designed to arrange PtdIns(4,5)P_2 pools so that the nodulin-bound phosphoinositide pool is appropriately pre-patterned to support spatially coherent signaling upon register of physiological trigger. In this model, PtdIns(4,5)P_2–independent mechanisms of AtSfh1 organization template the spatial patterning of PtdIns(4,5)P_2 pools essential for root hair morphogenesis. Supporting evidence comes from demonstrations that the intricate tip-directed distributions of AtSfh1 and PtdIns(4,5)P_2 in Arabidopsis root hairs show similar patterns (Vincent et al., 2005), and that both the Sec14- and nodulin-domains contribute to a functional AtSfh1.

It remains to be determined how AtSfh1-bound PtdIns(4,5)P_2 pools are made available to other effectors. Ca^{++}-calmodulins and related calmodulin-like activities (of which plants express many) remain attractive candidates for PtdIns(4,5)P_2 'displacement factors' as these proteins have high affinities for basic peptides (O'Neil and Degrado, 1990; McLaughlin and Murray, 2005). In this scenario, calmodulins release PtdIns(4,5)P_2 molecules from the AtSfh1 nodulin peptide upon register of a Ca^{++} trigger. Ca^{++}-regulated post-translational modifications of the nodulin domains are also plausible. Such designs hold the appealing feature of spatially and temporally coupling Ca++- and PtdIns(4,5)P_2-regulated signaling reactions; a functional coordination on stark display in tip-growing cells. Our experiments in yeast do suggest that direct Ca^{++}:PtdIns(4,5)P_2 interactions of the sort that would occur at sites of robust Ca^{++} influx into cells (e.g. growing root hair tips) are insufficient to break the nodulin::phosphoinositide interaction, however.

The *Lotus LjPLP-IV* gene, which encodes the AtSfh1 ortholog in this leguminous plant, is subjected to a peculiar transcriptional control involving a bidirectional promoter that is activated in mature nitrogen fixing nodules. This bi-directional promoter resides in intron 10 of the *LjPLP-IV* gene and drives expression of both the stand-alone Nlj16 nodulin and of antisense transcripts directed against Sec14 domain sequences (Kapranov et al., 2001). The biochemical properties of Class 1 nodulins now suggest a molecular rationale for why this major reprogramming of Sec14-nodulin gene transcription occurs. Late stages of nodulation demand that polarized morphogenetic programs, such as root hair formation, root hair curling or growth of the infection thread, be subverted to establish the anaerobic microenvironment suitable for nitrogenase activity (Gage, 2004; Oldroyd, 2013). We posit the nodulation program terminates polarized morphogenetic programs by silencing expression of a master polarity regulator (Sec14-nodulin). This effect is reinforced by production of a potent antagonist of polarized membrane growth (stand-alone nodulin). The basis for the antagonism lies with the Class I nodulin's ability to laterally sequester PtdIns(4,5)P_2 in the absence of auxillary activities supplied by full-length protein. By physically uncoupling the Sec14- and nodulin domains, and by shifting relative stoichiometries in favor of the PtdIns(4,5)P_2 clamp (Nlj16 is highly expressed while expression of full-length protein is silenced; Kapranov et al., 1997, 2001), the phosphoinositide signaling circuit required for polarized membrane trafficking is quenched. We interpret the legume/bacterial symbiosis as a biological context where the nodulin's developmental versatility as PtdIns(4,5)P_2 clamp is on display.

Finally, the biochemical properties of Class I Sec14-nodulins suggest an interesting mechanism for scaffolding assembly of PtdIns kinases and/or appropriate effectors to support exquisite spatial and temporal control of functionally privileged phosphoinositide signaling foci (Figure 10A). These foci could operate on scales as small as single macromolecular complexes, thereby coupling synthesis of a specific phosphoinositide with its channeling to distinct cohorts of privileged effectors (Figure 10B). Higher-order arrangement of such highly integrated signaling 'bits' by homo-oligomeric interactions would have the capacity to organize phosphoinositide signaling into macro-scale patterns. Such a design enables differential functional channeling of even chemically identical phosphoinositide molecules

produced in immediate proximities on the membrane surface. When superimposed upon the phosphoinositide chemical code, this design imprints what is effectively 'point' resolution to the lipid signaling landscape. Point resolution not only provides a facile mechanism for diversifying biological outcomes for phosphoinositide signaling, but it also codifies a versatile principle for the intricate bit-mapping of a large membrane surface for production of a high definition lipid signaling screen.

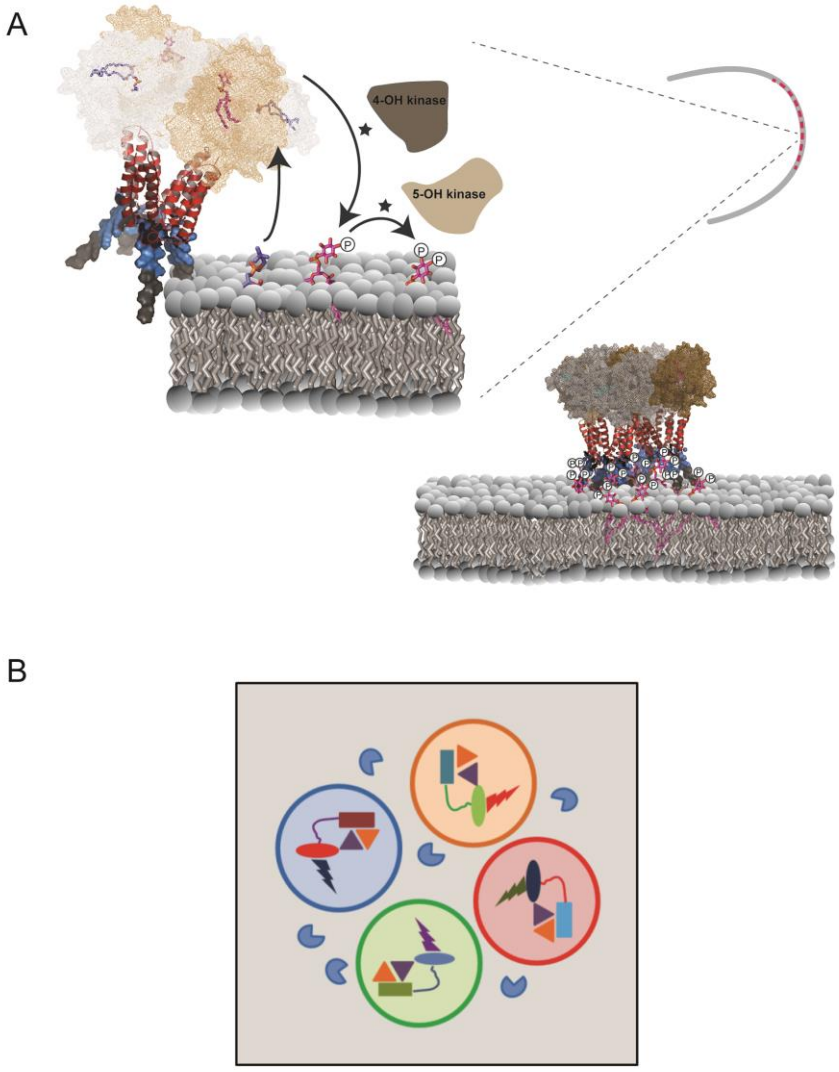

Figure 10. Patterning of phosphoinositide signaling by Sec14-nodulins. **(A)** AtSfh1-dependent patterning of PtdIns(4,5)P_2 in root hair tips. Based on the mechanism for how yeast Sec14 stimulates PtdIns 4-OH kinase activity (Schaaf *et al*., 2008) and our data with the AtSfh1 Sec14 domain (unpublished data), we propose Sec14 domains (mesh) of an AtSfh1 tetramer promote phosphoinositide synthesis by presentation of PtdIns (magenta) to PtdIns 4-OH kinases during heterotypic lipid exchange with amino phospholipid (blue). Specific interaction of C-terminal lysines (blue surface mode) with PtdIns(4,5)P_2, in conjunction with the weak association of the AtSfh1 C-terminal aromatic motif (LFFGF, grey surface mode), stabilizes interaction of the nodulin domain with membranes. Charge neutralization of Lys residues by PtdIns(4,5)P_2 promotes assembly of AtSfh1 into higher order oligomers by interaction of the helical coiled-coil motifs (red ribbon diagram). **(B)** Engineering phosphoinositide signaling with point resolution. Distinct classes Sec14-nodulins (Sec14-domains, rectangles; nodulin-domains, ovals) scaffold PtdIns and PtdIns-phosphate kinase (gold and purple triangles, respectively) assemblies with distinct phosphoinositide effectors (bolts). Classes of individual complexes that prosecute distinct biological outcomes for phosphoinositide signaling are organized into signaling pixels denoted by open circles of different color. Phosphoinositide phosphatases (blue PacMan) hydrolyze phosphoinositides that escape pixel boundaries.

Materials and Methods

Yeast strains and methods

Strains used are as follows: wild-type yeast CTY182 (*MATα ura3-52 lys2-801 his3Δ-200*), CTY1568 (*MATα leu2 ura3 his3 trp lys suc2-Δg stt4Δ::HIS, YCp(URA3, stt4^{ts})*), CTY1537 (*MATα ura3-52 leu2 Gal^{+} pik1^{ts}*), and CTY1-1A (*MATα ura3-52 lys2-801 his3Δ-200 sec14-1^{ts}*). Lipid kinase mutant strains included RG1 (pRS315-*mss4-5^{ts}; mss4Δ::kan^{R},ura3-52, his3-Δ200, ade^{-}*), RG2 (pRS315-*mss4-9^{ts}; mss4Δ::kan^{R}, ura3-52, his3-Δ200, ade^{-}*), RG3 (pRS315-*mss4-23^{ts}; mss4Δ::kan^{R}, ura3-52, his3-Δ200, ade^{-}*), RG4 (pRS315-*mss4-25^{ts}; mss4Δ::kan^{R}, ura3-52, his3-Δ200, ade^{-}*), PtdIns-3-OH kinase mutant strain RG5 (*MATα his3Δ1 leu2Δ0 lys2Δ0 ura3Δ0 vps34Δ::kanMX*). The vps33-deficient strain LBY317 (*MATα ura3-52 leu2-3 112 his3Δ-200 trp1- Δ901 lys2-801 suc2- Δ9 vps33Δ::HIS3*) and its isogenic wild-type partner SEY6210 (*MATα ura3-52 leu2-3 112 his3Δ-200 trp1- Δ901 lys2-801 suc2-Δ9*) were previously described (Miseta et al., 1999). Yeast media, genetic techniques, [^{3}H]-inositol labeling and phosphoinositide determinations by anion exchange chromatography of deacylated inositol lipids are described (Rivas et al., 1999; Guo et al., 1999; Phillips et al., 1999; Li et al., 2000). We are grateful to Jeremy Thorner (Cal-Berkeley) for *pik1^{ts}* and *stt4^{ts}* strains, to Scott Emr (Cornell) for the *mss4-102^{ts}* strain (Stefan et al., 2002), and Tsuyoshi Nakagawa (Shimane University) for providing Gateway binary vectors that contain the bar gene (Nakamura et al., 2010).

Isolation of mss4^{ts} alleles

The *mss4^{ts}* strains were generated by John Moskow in the laboratory of Daniel Lew (Duke University) by gap repair mutagenesis as described (Moskow et al., 2000). Briefly, the entire *MSS4* open reading frame and flanking sequences (1180 bp upstream and 400 bp downstream) were PCR-amplified under conditions of relaxed stringency. The PCR products were cotransformed directly into yeast along with an *MSS4*-containing pRS315 plasmid digested with NheI (to remove the 3.47 kb restriction fragment containing the *MSS4* ORF plus 930 bp and 200 bp of upstream and downstream flanking sequences, respectively). The yeast host for the transformations was an *mss4Δ::kan^{R}* null strain where the normally lethal *mss4Δ::kan^{R}* was complemented by an ectopic *P$_{GAL1}$-MSS4* cassette. KanR transformants were selected on glucose media (PGAL1 inactive) at 24°C. The strains were replica plated at 37°C to screen for mss4ts alleles (identified by lack of growth at this temperature in glucose, but not galactose, media). Ts isolates were cured of the PGAL1-MSS4 cassette and characterized.

Plant materials and cDNA isolation

Arabidopsis thaliana Columbia-0 (Col-0) was used as the wild-type strain (WT). The *Atsfh1$^{0/0}$* mutant refers to the Col-0 AtSFH1::T-DNA insertion line described (Vincent et al., 2005). Total mRNA (~100 μg) was prepared from 100 mg of leaves, flowers or roots using the RNeasy Plant Mini Kit (Qiagen). The 300-400 bp AtSfh mRNAs encoding nodulin domains were amplified by RT-PCR (Superscript FirstStrand Synthesis System; Invitrogen), cDNAs cloned into the pGEM vector using the

pGEMTeasy cloning kit (Promega), and subcloned into the doxycyclinecontrolled yeast expression vector pCM189. A sequence encoding a translational mRFP-AtSFH1 nodulin fusion was amplified from pGWB655-*AtSFH1 nodulin* and subcloned into the yeast expression vector pDR199 (Schaaf et al., 2011).

Templated homology modeling of nodulin domains

Homology models were generated using Schrödinger's – Prime Homology Modeling module (Prime, version 3.1, Schrodinger, LLC, New York, NY 2012). DNA Topoisomerase (pdb ID 1A36) was used as a structural template to build the model. The templating exploited sequence similarity between the topoisomerase linker region and the AtSfh1 nodulin domain. The topoisomerase linker region was pruned and used as a template after sequence realignment. A position-specific substitutional matrix (PSSM) for the query sequence, derived from PSIBLAST, is used to match the template sequence.

In order to minimize the inaccuracy in a secondary structure prediction, a composite secondary structure were predicted for query sequence by iteratively optimization and was aligned to the Secondary Structure Alignment (SSA) of the template. The models were build using 'full build' option that builds insertions, closes gaps, and predicts side-chain conformations of non-conserved residues to produce models with no unphysical clashes. Extensive conformational sampling further refined the structures by particularly refining the regions where insertions were made, gaps closed and re-predicting side-chain conformations.

Several (intermediate) main chains models were generated as a result of permutational selection of different loop candidates and side chain rotamers and were refined using AMBER99 and Generalized Born/Volume Integral methodology (MOE- 2011.10; Chem. Comp. Group Inc.; Montreal, Canada). The model, which scored best according to the selected force-field (AMBER99), was chosen as the final model. Homology models of Atsfh1 mutants were similarly built using the same computational protocol.

NMR of AtSfh1 nodulin peptides

Three C-terminal AtSfh1 nodulin peptides were investigated: the wild-type (WT) peptide, Ac-KKKKKKKLFFGF-COOH; the K_5A variant Ac-KKKK<u>A</u>KKLFFGF-COOH; and the $K_{3,5}A$ variant Ac-KK<u>A</u>K<u>A</u>KKLFFGF-COOH. Peptides of > 95% purity were purchased from Eton Bioscience. Stock solutions of peptides were prepared in HPLC-grade water (Fisher Scientific) and adjusted to pH 6.5 with ammonium hydroxide (EM Science). Stock solution concentrations were determined by measuring absorption at 205 nm. Phosphatidylinositol 4,5-bisphosphate diC4 (di-C4-PtdIns(4,5)P_2) was purchased from Echelon Bioscience. The stock solutions of phosphoinositides were prepared in the NMR buffer containing 5 mM [U-$^2H_4$, 98%] imidazole at pH 6.5 and 8% D_2O. For NMR measurements, the peptide stocks were diluted with NMR buffer to a final concentration of 0.15 mM or 0.25 mM. Binding experiments were conducted by adding aliquots of di-C_4-PtdIns(4,5)P_2 stock solutions to the peptide samples. NMR experiments were carried out at 298.15 K on Varian Inova NMR instruments operating at ^1H Larmor frequencies of 500 and 600 MHz. 1D ^1H NMR spectra of all PtdIns (4,5)-P_2 titration points

were collected using the "water flip-back" technique (Grzesiek and Bax, 1993) to suppress water signal, and processed with MestReNova. Spectra were referenced externally with the chemical shift standard DSS (4,4-dimethyl-4-silapentane-1-sulfonic acid).

Atomistic simulations of the AtSfh1 nodulin peptide

Atomistic 4000 ns molecular dynamics (MD) simulation for AtSfh1 nodulin peptide (N-terminal acetyl cap-KKKKKKKLFFGF) solvated in bulk water was performed. Additionally, five MD simulations were run (> 1000 ns each) of peptide interacting with a lipid bilayer comprised of dilineoylphosphatidylcholine (DLPC), dilineoylphosphatidylserine (DLPS), and PtdIns(4,5)P_2 lipids. In membrane simulations 1, 2, 4, or 8 AtSfh1 peptides were positioned randomly in water, and the simulations were performed at physiological salt concentration of 140 mM NaCl. In all cases counter-ions were included to neutralize the systems.

The OPLS all-atom force field (Jorgensen et al., 1988) was used to parameterize all molecules. For lipids, we used an extension of the OPLS all-atom force field (A. Maciejewski, M. Pasenkiewicz-Gierula, O. Cramariuc, I. Vattulainen, and T. Rog. Refined OPLS all-atom force field for saturated phosphatidylcholine bilayers at full hydration. J. Phys. Chem. B (2014, in press; dx.doi.org/10.1021/jp5016627). For water, we employed the TIP3P model that is compatible with the OPLS parameterization (Jorgensen et al., 1983). The system setup used in this study is identical to that employed in our previous simulations of lipid bilayers with OPLS all-atom parameterization (Kaiser et al., 2011; Orlowski et al., 2011). Periodic boundary conditions with the usual minimum image convention were used in all three directions. The LINCS algorithm (Hess at al., 1997) was used to preserve the length of each hydrogen atom covalent bond. The time step was set to 2 fs and the simulations were carried out at constant pressure (1 bar) and temperature (298 K). The temperature and pressure were controlled by the Parrinello-Rahman and v-rescale methods, respectively (Parrinello et al., 1981; Bussi et al., 2007). The temperatures of the solute and solvent were controlled independently. For pressure, we used a semi-isotropic control for the systems with a lipid bilayer, and an isotropic one for the peptide in water. The Lennard-Jones interactions were cut off at 1.0 nm. For the electrostatic interactions we employed the particle mesh Ewald method (Essmann et al.,1995) with a real space cutoff of 1.0 nm, beta-spline interpolation (order of 6), and direct sum tolerance of 10^{-6}.

The simulations were performed using the GROMACS 4.5.5 software package (Hess et al., 2008) resulting in ~10 μs of trajectories. Nodulin peptide folding was examined in long (4 μs) MDS, as well as in 200 ns atomistic replica exchange molecular dynamics (REMD) simulations (system 1; Supplemental Table S1A). During the 4 μs MDS, the peptide folded from extended to common β-hairpin structures in ~1.3 μs, and remained stable until the end of the simulation with only two brief (~300 ns) episodes of partial unfolding. In all MD simulation runs (systems 2-6; Figure 4D and Supplemental Table S1A), the nodulin peptide secondary structures were monitored throughout. These simulations consumed 400,000 core-hours of computing time.

REMD Simulations of the C-terminal AtSfh1 nodulin peptide

Atomistic replica exchange molecular dynamics (REMD) simulations for a linear extended structure of AtSfh1 used GROMACS 4.5.5 (Hess et al., 2008). REMD is the technique of choice to sample the peptide conformational space. The sequence (see above) was constructed using the VMD (Humphrey et al., 1996) program and solvated with 2423 water molecules and 6 Cl- ions using a simulation box of size 4.29 x 3.62 x 4.87 nm. These dimensions are large enough to prevent interactions between the peptide and its periodic images. The energy of the system was minimized with the steepest descent and conjugate gradients algorithms, and 1 ns simulation in 297 K was performed for equilibration. This system was then used as a starting configuration for the REMD simulations. Simulation parameters were the same as in the above MD simulations except for temperature, for which we used 48 replicas at 275.00, 276.81, 278.64, 280.47, 282.31, 284.16, 286.02, 287.89, 289.77, 291.66, 293.56, 295.46, 297.38, 299.31, 301.24, 303.19, 305.15, 307.11, 309.09, 311.07, 313.07, 315.08, 317.09, 319.12, 321.16, 323.20, 325.26, 327.33, 329.41, 331.50, 333.60, 335.71, 337.83, 339.96, 342.10, 344.26, 346.42, 348.60, 350.82, 353.01, 355.23, 357.45, 359.68, 361.92, 364.18, 366.45, 368.72, and 371.02 K. These temperatures were generated using a temperature predictor for parallel tempering simulations (Patriksson et al., 2008) with a desired exchange probability set to 0.2. Simulations were 200 ns each, and collectively summed to 9.6 microseconds of simulation time. Continuous trajectory at 297 K was used to perform cluster analyses with the pairwise method of Daura et al. (1999). Cluster analyses of the REMD trajectory at 297 K showed the two most populated structures (10.85% and 8%) agreed with 4 μs MDS at the same temperature (Figure 4B) – suggesting the nodulin peptide adopted a β-hairpin conformation where two β-strands (residues 1-5 and 7-9) were separated by a turn at residue 6 (Figure 4B). The REMD simulations consumed 70,000 corehours of computing time.

Isothermal titration calorimetry

ITC was performed using a VP-ITC high sensitivity titration calorimeter (MicroCal, Northampton, MA) with nodulin peptide and lipid vesicle concentrations clamped at 9 mM and 2 mM, respectively. The calorimetric cell was filled with nodulin peptide solution at 9 μM. Lipid vesicles (LUV) at a 2 mM concentration (as phosphate) were injected into the cell (1.43 ml) in 10 μl steps, i.e., leading to a 100–200-fold dilution of lipid vesicles. To minimize the contribution of dilution to the heat of partitioning, all samples were prepared in the same buffer and were degassed under vacuum immediately before use. Typically, the injections were made at 10 min intervals and at 2 s μl^{-1} Constant stirring speed of 290 rpm was maintained during the experiment to ensure proper mixing after each injection. Titration experiments were performed at 25°C in HEPES buffer. Dilution heats of vesicles in buffer were determined separately and subtracted from experimental heats of binding. At each lipid injection, free peptide partitioned into the bilayer membrane and the corresponding heat of reaction was measured. The heat of reaction became smaller as less peptide remained free in solution. The integration of each calorimetric peak yielded a heat of reaction. These heats were plotted versus lipid concentration.

The reaction heat for each injection is related to the calorimetric enthalpy of binding, ΔH. The binding isotherms, ΔH versus molar ratio, were analyzed using MicroCal Origin. The fit of the binding curve yields the binding constant K_a ($K_d = 1/K_a$) and the enthalpy ΔH of the binding reaction. The Gibbs free energy of binding (ΔG) and the entropy (ΔS) are determined from the basic thermodynamic expression $\Delta G=-RT\ln K_a=\Delta H-T\Delta S$, where R and T are the gas constant andthe absolute temperature, respectively.

Protein purification and size exclusion chromatography

Recombinant proteins were expressed in *E. coli* BL21 and expression induced with 100 μM IPTG (see Supplemental Methods). AtSfh1 nodulin was purified from 25 mM sodium phosphate, 300 mM NaCl (pH 7.5), 8 M urea, while AtSfh3 nodulin was purified from 25 mM potassium phosphate, 300 mM KCl (pH 7.5). His-tagged proteins were purified by Talon affinity chromatography. The AtSfh3, AtSfh5 and AtSfh8 nodulin domains were further purified by S200 gel filtration chromatography. mRFP-tagged nodulin proteins expressed in *Nicotiana benthamiana* leaves were isolated with 50 mM Na_2HPO_4, 300 mM NaCl, 1 mM EDTA, 0.5% Triton X-100, 5 mM β-ME (pH 7.5) and separated on a HiLoad 16/600 Superdex 200 column.

Microscopy and imaging

Light microscopy experiments used an Olympus MVX-10 Macroview with CCD camera (Hamamatsu ORCA). Confocal imaging was done using a NikonA1R. Images were processed in Adobe Photoshop 7.0. Confocal and Nomarski microscopy was performed on 3 day-old seedlings mounted in water and covered with number 1.5 coverslips. Fluorescence was scanned with an inverted spinning disk confocal microscope (Olympus DSU; 60X 1.2 NA oil immersion lens) or a Leica TCS SP8 confocal laser scanning microscope. For each experiment, 7 seedlings were analyzed and < 2 root hairs were imaged for each seedling. Yeast cells were imaged on a confocal spinning disk microscope (Olympus DSU; 100X oil immersion lens). FM4-64 staining traced the endocytic pathway as described (Vida and Emr, 1995). For GFP, YFP and FM4-64 fluorescence FITC, YFP and TRITC filter settings were used. Live 3-day-old seedlings mounted on 0.8% (w/v) top agar were imaged by environmental scanning EM using an FEI Quanta 200 Field Emission Gun. Images were taken at 95% humidity and 15 kV at a magnification of 200X. Images were processed in Adobe Photoshop 7.0.

Plant growth and transformation

Seeds were plated in 0.8% (w/v) top agar (low melt agar in 1X Murashige and Skoog salt and vitamin mixture media [MS: Gibco BRL]). Seeds were stratified at 4ºC for 2 days then grown vertically under constant light (90 μM m^{-2} s^{-1}) at 22ºC for 3 days before being imaged for root hair size. *Agrobacterium tumefaciens* (*Rhizobium radiobacter*)-mediated transformation by the floral dip method was used to generate transgenic plant lines (Clough and Bent, 1998). Agrobacterium strain GV3101

strain was used for all transformations. Transformed plants were propagated to the T3 generation to obtain homozygous lines.

Transient expression in tobacco leaves

Agrobacteria were transformed with pGWB655-AtSFH1 nodulin and mutant versions (encoding mRFP-AtSfh1 nodulin chimera), pH7WGF2-BRI1, encoding a Bri1-GFP translational fusion used as a plasma membrane marker (kindly donated by Klaus Harter, University of Tübingen, Germany), and pBIN61-p19, encoding the silencing suppressor p19 (Voinnet et al., 2003). Transformants were then used for co-transfection of Nicotiana benthamiana leaves. For this, Agrobacteria transformants were grown at 28°C in LB medium supplemented with 100 μg ml-1 rifampicin, 30 μg ml-1 gentamycin and appropriate antibiotic for plasmid selection to stationary phase. Subsequently, 1 mL of saturated culture was added to 4 mL fresh media and grown for additional 4 h. Transformants were then sedimented at 4000g for 20 min at 4°C and resuspended in 10 mM MES, 10 mM MgCl2 and 150 μM acetosyringone, and infiltrated into the abaxial air spaces of 2-week-old tobacco plants. Leaves were imaged 5 days after infiltration using a confocal laser scanning microscope (Leica TCS SP8).

Ca++ influx experiments.

Rapid imposition of large Ca++ influx into yeast cell cytoplasm exploited vps33 mutant strains conducted as described previously (Miseta et al., 1999). Isogenic wild-type (SEY6210) and vps33 (LBY317) yeast strains expressing GFP-AtSfh1 nodulin were grown to mid-exponential phase in uracil-free minimal medium buffered with MES-Tris to pH 5.5. Yeast cells from 5 ml cultures were harvested and washed twice with 1 mL test medium (uracil-free minimal medium, 2% dextrose, 2 mM EGTA, 40 mM MES-Tris, pH 6.5). Cells were resuspended in 500μL test medium and allowed to equilibrate for 30 min at room temperature. CaCl2 was then added to the medium to final concentration of 50 mM or 400 mM. The yeast cells were then immediately and continuously imaged by confocal microscopy in the window of 30 - 300 sec with images collected at 30 sec intervals during this time window.

Immunoblotting of root extracts

Proteins were extracted from root hairs in extraction buffer [5 mM HEPES, pH 7.5, 10 mM magnesium acetate, 2 mM EGTA, 2 mM PMSF, 15 mM β-mercaptoethanol, protease cocktail inhibitors (Roche)], resolved by SDS-PAGE, and blotted with AtSfh1 antibodies raised against the linker joining the Sec14- and nodulin-domains. Total proteins from myc-AtSfh1 nodulin proline substitution mutant lines were blotted with anti-myc antibodies.

Supplemental information

Supplemental Figure S1 describes localization of Class II and Class III nodulin domains in yeast and the PtdIns(4,5)P_2-dependence of Class I nodulin localization to the yeast plasma membrane.

Supplemental Figure S2 shows the localization of mutant Class I nodulin domains in tobacco leaves, the stabilities of these chimeric proteins when expressed in leaf cells, and imaging of PtdIns(4,5)P_2 distribution in WT and mutant root hairs. Supplemental Figure S3 documents the high affinity of the AtSfh1 nodulin domain for PtdIns(4,5)P_2- in cells and homo-oligomerization patterns of Class I and Class II nodulin domains. Supplemental Fig S4 describes the biological and biochemical properties of AtSfh1 nodulin domain missense mutants where Pro is substituted for conserved residues outside the nodulin peptide. Supplemental Table S1 documents various nodulin peptide folding, lipid interaction parameters gleaned from atomistic MDS, and lists root hair dimensions and morphologies recorded for plants expressing mutant AtSfh1 proteins.

Acknowledgements

This work was supported by grants GM44530 from the National Institutes of Health and the Robert A. Welch Foundation (BE-0017) to VAB. MKFC, MD, HCL. HS, and GS were supported by Emmy Noether grant SCHA 1274/2-1, grant SCHA 1274/3-1 and SFB 1101/TP A05 from the Deutsche Forschungsgemeinschaft (GS). AO, TR and IV were supported by grants from the Academy of Finland, the Academy of Finland Center of Excellence program (IV), the European Research Council Advanced Grant CROWDED-PRO-LIPIDS (IV), and the Sigrid Juselius Foundation (IV), YY and TII by Welch Research Foundation grant A-1784 (TII), and AA, MGL and HA by grants from the Spanish Ministerio de Economia and the Basque Government (IT838-13) (AA). MGL was a predoctoral student supported by the Basque Government. The Laboratory for Molecular Simulation at Texas A&M University and CSC – IT Center for Science (Espoo, Finland) provided software, support, and computer time. We thank Daniel J. Lew (Duke) for permission to use and report the mss4ts mutant strains constructed in his laboratory by John J. Moskow (supported by NIH grant GM62300 to DJL), David Bedwell (Univ. Alabama-Brimingham Med. Ctr.) for helpful discussions regarding calcium experiments and vps33 mutant strains, and Mark McDermott for assistance in plant maintenance. The authors declare no financial conflicts.

References

Affolter, M., Zeller, R., Caussinus, E. (2009). Tissue remodelling through branching morphogenesis. Nature Rev Mol Cell Biol *10*, 831-842.

Bankaitis, V. A., Mousley, C. J., and Schaaf, G. (2010). The Sec14 superfamily and mechanisms for crosstalk between lipid metabolism and lipid signaling. Trends. Biochem. Science *35*, 150–160.

Bibikova, T., Gilroy, S. (2008). Calcium in root hair growth. In: Emons AMC, Ketelaar T (eds) Root hairs: excellent tools for the study of plant molecular cell biology. Springer, Berlin Heidelberg New York. doi:10.1007/7089_2008_3

Braun, M., Baluska, F., von Witsch M, Menzel, D. (1999). Redistribution of actin, profilin and phosphatidylinositol-4,5-bisphosphate in growing and maturing root hairs. Planta *209*, 435 – 443.

Brewin, N.J., (2002). Pods and nods: a new look at symbiotic nitrogen fixing. Biologist *49*, 1 – 5.

Bussi, G., Donadio, D., Parrinello, M. (2007). Canonical sampling through velocity rescaling. J Chem Phys *126*, 014101–7.

Cáceres, A., Ye, B., and Dotti, C. G. (2012). Neuronal polarity: demarcation, growth and commitment. Current opinion in cell biology, 24(4), 547-553.

Clough, S.J., Bent, A.F. (1998). Floral dip: A simplified method for *Agrobacterium*- mediated transformation of *Arabidopsis thaliana*. The Plant J *16*, 735–743

Cole, R.A., Fowler, J.E. (2006). Polarized growth: maintaining focus on the tip. Curr. Opin. Plant Biology *9*, 579 – 588.

Daura, X., Gademann, K., Jaun, B., Seebach, D., van Gunsteren, W.F., Mark, A.E. (1999). Peptide folding: when simulation meets experiment. Angewandte Chemie International Edition. *38*, 236-240.

Desbrosses, G.J., and Stougaard, J. (2011) Root nodulation: a paradigm for how plant-microbe symbiosis influences host developmental pathways. Cell Host Microbe. *10*, 348-358.

Devreotes, P., and Janetopoulos, C. (2003) Eukaryotic chemotaxis: Distinctions between directional sensing and polarization. J Biol Chem *278*, 20445–20448.

Dove, S.K., Cooke, F.T., Douglas, M.R., Sayers,.L.G., Parker, P.J., and Michell, R.H. (1997). Osmotic stress activates phosphatidylinositol-3,5-bisphosphate synthesis. Nature *390*,187-192.

Essmann, U., Perera, L., Berkowitz, M.L., Darden, T., Lee, H., Pedersen, L.G. (1995). A smooth particle mesh Ewald method. J Chem Phys *103* (19), 8577-8593.

Gage, D.J. (2004). Infection and invasion of roots by symbiotic, nitrogen-fixing rhizobia during nodulation of temperate legumes. Microbiol. Mol. Biol. Rev. *68*, 280-300.

Gambhir, A. et al. (2004). Electrostatic sequestration of PtdIns(4,5)P_2 on phospholipid membranes by basic/aromatic regions of proteins. Biophys. J. *86*, 2188–2207.

Gerlach, H., Laumann, V., Martens, S., Becker, C.F.W., Goody, R.S., and Geyer, M. (2010). HIV-1 NEF membrane association depends on charge, curvature, composition and sequence. Nat. Chem. Biol. *6*, 46-53.

Gervais, L., Claret, S., Januschke, J., Roth, S., and Guichet, A. (2008) PIP5K-dependent production of PIP2 sustains microtubule organization to establish polarized transport in the Drosophila oocyte. Development 135, 3829–3838.

Grzesiek, S., and Bax, A. (1993). The importance of not saturating H_2O in protein nmr - application to sensitivity enhancement and NOE measurements. J. American Chem. Soc. *115*, 12593-12594.

Guo, S., Stolz, L.E., Lemrow, S.M., and York, J.D. (1999). SAC1-like domains of yeast SAC1, INP52, and INP53 and human synaptojanin encode phosphoinotide phosphatases. J. Biological Chemistry *274(19)*, 12990-12995.

Heilmann, I. (2009) Using genetic tools to understand plant phosphoinositide signalling. Trends Plant Sci. *14*, 171-179.

Hepler, P.K., Luis Vidali, L., and Cheung, A.Y. (2001). Polarized cell growth in higher plants. Annu. Rev. Cell and Dev. Biol. *17*, 159-187.

Hess, B., Bekker, H., Berendsen, H.J.C., Fraaije, J.G.E.M. (1997). LINCS: A linear constraint solver for molecular simulations. J Comput Chem *18*, 1463–1472.

Hess, B., Kutzner, C., van der Spoel, D., Lindahl, E. (2008). GROMACS 4: Algorithms for Highly Efficient, Load-Balanced, and Scalable Molecular Simulation. The Journal Chemical Theory and Computation *4*, 435–447.

Huang, J., Kim, C.M., Xuan, Y.-H., Park, S.J., Piao, H.L., Je, B.I., Liu, J., Kim, T.H., Kim, B.-K., and Han, C.-D. (2013). OsSNDP1, a Sec14-nodulin domain-containing protein, plays a critical role in root hair elongation in rice. Plant Molecular Biology *82*, 39-50.

Humphrey, W., Dalke, A., Schulten, K. (1996). VMD: Visual molecular dynamics. Journal of Mol.
Graphics *14*, 33–38.

Irving, H.I., Boukli, N.M., Kelly, M.N., Broughton, W.J. (2000). Nod-factors in symbiotic development of root-hairs. In: Ridge RW, Emons AM, editors. Root hairs cell and molecular biology. Tokyo: Springer; p. 241–65.

Jorgensen, W.L., Tirado-Rives, J. (1988). The OPLS [optimized potentials for liquid simulations] potential functions for proteins, energy minimizations for crystals of cyclic peptides and crambin. J American Chem Soc *110*, 1657–1666.

Jorgensen, W.L., Chandrasekhar, J., Madura, J.D., Impey, R.W., Klein, M.L. (1983). Comparison of simple potential functions for simulating liquid water. J Chemical Phys *79*, 926–935.

Kaiser, H.J., Orlowski, A., Rog, T., Nyholm, T.K., Chai, W., Feizi, T., Lingwood, D., Vattulainen, I., Simons, K. (2011). Lateral sorting in model membranes by cholesterol -mediated hydrophobic matching. PNAS *108*, 16628–16633.

Kapranov, P., de Bruijn, F.J., Szczyglowski, K. (1997). Novel, highly expressed late nodulin gene (*LjNOD16*) from *Lotus japonicus*. Plant Physiol. *113*, 1081-1090.

Kapranov, P., Routt, S.M., Bankaitis, V.A., de Bruijn, F.J., Szczglowski, K. (2001). Nodule-specific regulation of phosphatidylinositol transfer protein expression in *Lotus japonicus.* Plant Cell *13*, 1369 – 1382.

Krahn, M.P., and Wodarz, A. (2012) Phosphoinositide lipids and cell polarity: linking the plasma membrane to the cytocortex. Essays Biochem. *53*, 15-27.

Kusano, H., Testerink, C., Vermeer, J.E., Tsuge, T., Shimada, H., Oka, A., Munnik, T., and Aoyama, T. (2008). The *Arabidopsis* phosphatidylinositol phosphate 5-kinase PIP5K3 is a key regulator of root hair tip growth. Plant Cell *20*, 367-380.

Lemmon, M. A., Ferguson, K. M., O'Brien, R., Sigler, P. B. and Schlessinger, J. (1995) Specific and high-affinity binding of inositol phosphates to an isolated pleckstrin homology domain. Proc. Natl. Acad. Sci. U.S.A. 92, 10472-10476.

Levental, I., Christian, D.A., Wang, Y.H., Madera, J.J., Discher, D.E., and Janmey, P.A. (2009) Calcium-dependent lateral organization in phosphatidylinositol 4,5 bisphosphate (PIP2) and cholesterol-containing monolayers. Biochemistry *48*, 8241-8248.

Li, L., Shi, X., Guo, X., Li, H., and Xu, C. (2014). Ionic protein-lipid interaction at the plasma membrane: what can the charge do? Trends Biochem. Sci. *39*, 130-140.

Li, X., Routt, S. M., Xie, Z., Cui, X., Fang, M., Kearns, M. A., Bard, M., Kirsch, D. R., Bankaitis, V. A. (2000). Identification of a novel family of nonclassic yeast phosphatidylinositol transfer proteins whose function modulates phospholipase D activity and Sec14p-independent cell growth. Mol. Biol. Cell *11*, 1989-2005.

Long, S.R. (2001). Genes and signals in the *Rhizobium*-legume symbiosis. Plant Physiology *125*, 69–72.

McLaughlin, S. and Aderem, A. (1995). The myristoyl-electrostatic switch: a modulator of reversible protein-membrane interactions. Trends Biochem. Sci. *20*, 272–276.

McLaughlin, S. and Murray, D. (2005). PM phosphoinositide organization by protein electrostatics. Nature *438*, 605–611.

Miseta, A., Fu, L., Kellermayer, R., Buckley, J., and Bedwell, D. (1999). The Golgi apparatus plays a significant role in the maintenance of Ca^{2+} homeostasis in the *vps33*Δ vacuolar biogenesis mutant of *Saccharomyces cerevisiae*. J. Biol. Chem. *274*, 5939-5947.

Moskow, J.J., Gladfelter, A.S., Lamson, R.E., Pryciak, P.M. and Lew, D.J. (2000). Role of Cdc42p in pheromone-stimulated signal transduction in *Saccharomyces cerevisiae*. J. Biological Chemistry *20(20)*, 7559-7571.

Munnik, T., and Nielsen, E. (2011) Green light for polyphosphoinositide signals in plants. Curr Opin Plant Biol. *14*, 489-497.

Murray, D., Arbuzova, A., Honig, B., McLaughlin, S. (2002). The role of electrostatic and nonpolar interactions in the association of peripheral proteins with membranes. Curr. Top. Membr. *52*, 271–301.

Myat, M.M., Anderson, S., Allen, L.H., Aderem, A. (1997). MARCKS regulates membrane ruffling and cell spreading. Curr. Biol. 7, 611–14.

Mylona, P., Pawlowski, K., Bisseling, T. (1995). Symbiotic nitrogen fixation. Plant Cell *7*, 869-885.

Nakamura, S., Mano, S., Tanaka, Y., Ohnishi, M., Nakamori, C., Araki, M., Niwa, T., Nishimura, M., Kaminaka, H., Nakagawa, T., et al. (2010). Gateway binary vectors with the bialaphos resistance gene, *bar* , as a selection marker for plant transformation. Bioscience, Biotechnology, and Biochemistry *74*, 1315-1319.

Oldroyd, G.E. (2013) Speak, friend, and enter: signalling systems that promote beneficial symbiotic associations in plants. Nat. Rev. Microbiol. *11*: 252-263.

Oldroyd, G. E., & Downie, J. A. (2008). Coordinating nodule morphogenesis with rhizobial infection in legumes. *Annu. Rev. Plant Biol.*, *59*, 519-546.

O'Neil, K. T., and DeGrado, W. F. (1990). How calmodulin binds its targets: sequence independent recognition of amphiphilic α-helices. *Trends in Biochemical Sci. 15*(2), 59-64.

Orłowski, A., St-Pierre, J.F., Magarkar, A., Bunker, A., Pasenkiewicz-Gierula, M., Vattulainen, I., Róg, T. (2011). Properties of the Membrane Binding Component of Catechol-O-methyltransferase Revealed by Atomistic Molecular Dynamics Simulations. J Phys Chem B *115(46)*, 13541-13550.

Parrinello, M., Rahman, A. (1981). Polymorphic transitions in single crystals: A new molecular dynamics method. J Applied Phys *52*, 7182–7190.

Patriksson, A., van der Spoel, D. (2008). A temperature predictor for parallel tempering simulations. Phys Chem Chemical Phys *10*, 2073–2077.

Phillips, S. E., Sha, B., Topalof, L., Xie, Z., Alb, J. G., Klenchin, V. A., Swigart, P., Cockcroft, S., Martin, T. F., Luo, M., Bankaitis, V. A. (1999). Yeast Sec14p deficient in phosphatidylinositol transfer activity is functional in vivo. Mol. Cell *4*, 187-197.

Preuss, M.L., Schmitz, A.J., Thole, J.M., Bonner, H.K.S., Otegui, M.S., Nielsen, E. (2006). A role for the RabA4b effector protein PI-4K β 1 in polarized expansion of root hair cells in *Arabidopsis thaliana*. J. Cell Biology *172*, 991 – 998.

Richter, S., Müller, L.M., Stierhof, Y.-D., Mayer, U., Takada, N., Kost, B., Vieten, A., Geldner, N., Koncz, C., and Jürgens, G. (2012). Polarized cell growth in *Arabidopsis* requires endosomal recycling mediated by GBF1-related ARF exchange factors. Nature Cell Biol. *14*, 80-86.

Rivas, M.P., Kearns, B.G., Xie, Z., Guo, S., Sekar, M.C., Hosaka, K., Kagiwada, S., York, J.D., and Bankaitis, V.A. (1999). Pleiotropic alterations in lipid metabolism in yeast *sac1* mutants: relationship to "bypass Sec14p" and inositol auxotrophy. Mol Biol Cell *10*, 2235-2250.

Ryan, E., Steer, M., Dolan, L. (2001). Cell biology and genetics of root hair formation in *Arabidopsis thaliana*. Protoplasma *215*, 140 – 149.

Schaaf, G., Ortlund, E., Tyeryar, K., Mousley, C., Ile, K., Woolls, M., Garrett, T., Raetz, C.R.H., Redinbo, M., and Bankaitis, V.A. (2008) The functional anatomy of PL binding and regulation of PIP homeostasis by proteins of the Sec14-superfamily. Molecular Cell *29*, 191-206.

Schaaf, G., Dynowski, M., Mousley, C.J., Shah, S.D., Yuan, P., Winklbauer, E.M., Kaphan Freitas de Campos, M., Trettin, K., Quinones, M.C., Smirnova, T., Yanagisawa, L.L., Ortlund, E.A., Bankaitis, V.A. (2011) Resurrection of a functional phosphatidylinositol transfer protein from a pseudo-Sec14 scaffold by directed evolution. Mol. Biol. Cell *22*, 892-905.

Shi, X., Bi, Y., Yang, W., Guo, X., Jiang, Y., Wan, C., Li, L., Bai, Y., Guo, J., Wang, Y., Chen, X., Wu, B., Sun, H., Liu, W., Wang, J., and Xu, C. (2013) Ca^{2+} regulates T-cell receptor activation by modulating the charge property of lipids. Nature *493*, 111-115.

Slochower, D.R., Huwe, P.J., Radhakrishnan, R., and Janmey, P.A. (2013). Quantum and all-atom simulations of protonation and divalent ion binding to phosphatidylinositol 4,5-bisphosphate (PIP2). J. Phys. Chem. *117*, 8322-8329.

Stefan, C.J., Audhya, A., and Emr, S.D. (2002). The yeast synaptojanin-like proteins control the cellular distribution of phosphatidylinositol (4,5)-bisphosphate. Mol Biol Cell *13*, 542-557.

Stenzel, I., Ischebeck, T., Konig, S., Holubowska, A., Sporysz, M. (2008). The type B phosphatidylinositol-4-phosphate 5-kinase 3 is essential for root hair formation in *Arabidopsis thaliana*. Plant Cell *20*, 124-141.

Stolz, L.E., Kuo, W.J., Longchamps, J., Sekhon, M.K., York, J.D. (1998). INP51, a yeast inositol polyphosphate 5-phosphatase required for phosphatidylinositol 4, 5-bisphosphate homeostasis and whose absence confers a cold-resistant phenotype. J Biol Chem *273(19)*, 11852-11861.

Sun,Y., Carroll,S., Kakosnen,M., Toshima, J.Y. and Drubin, D.G. (2007). PtdIns(4,5)P_2 turnover is required for multiple stages during clathrin and actin dependent endocytic internalization. J. Cell Biol. *177(2)*, 355-367.

Suzaki T., Kawaguchi, M. (2014) Root nodulation: a developmental program involving cell fate conversion triggered by symbiotic bacterial infection. Curr Opin Plant Biol. *21C*:16-22

Thole, J.M., and Nielsen, E. (2008) Phosphoinositides in plants: novel functions in membrane trafficking. Curr. Op. Plant Biol. *11*, 620-631.

van Kammen, A. (1984). Suggested nomenclature for plant genes involved in nodulation and symbiosis. Plant Mo1. Biol. Rep. *2*, 4345.

Vance, C. (2001). Symbiotic nitrogen fixation and phosphorus acquisition. Plant nutrition in a world of declining renewable resources. Plant Physiology *127*, 391-397

Vida, T.A. and Emr, S.D. (1995). A new vital stain for visualizing vacuolar membrane dynamics and endocytosis in yeast. J. Biological Chemistry *128(5)*, 779-792.

Vincent, P., Chua, M., Nogue, F., Fairbrother, A., Mekeel, H., Xu, Y., Allen, N., Bibikova, T.N., Gilroy, S., Bankaitis, V.A. (2005). A Sec14p-nodulin domain phosphatidylinositol transfer protein polarizes membrane growth of *Arabidopsis thaliana* root hairs. J. Cell Biology *168*, 801 – 812.

Voinnet, O., Rivas, S., Mestre, P., Baulcombe, D. (2003). An enhanced transient expression system in plants based on suppression of gene silencing by the p19 protein of tomato bushy stunt virus. The Plant J *33*, 949-956.

Whiteway, M., and C. Bachewich, C. (2007). Morphogenesis in Candida albicans. Annu. Rev. Microbiol. *61*, 529–553.

Yagisawa, H., Sakuma, K., Paterson, H.F., Cheung, R., Allen, V., Hirata, H., Watanabe, Y., Hirata, M., Williams RL, Katan M (1998). Replacement of single basic amino acids in the pleckstrin homology domain of phospholipase C-δ1 alter the ligand binding, phospholipase activity, and interaction with the plasma membrane. J Biol Chem *273*, 417–424.

Yakir-Tamang, L., and Gerst, J.E. (2009) Phosphoinositides, exocytosis and polarity in yeast: all about actin? Trends Cell Biol. *19*, 677-684.

Yang, Z. (2008) Cell polarity signaling in Arabidopsis. Annu Rev Cell Dev Biol. *24*, 551-575.

Zinser, E., Gottlieb-S.D.M., Fasch,E-V., Kohlwein, S.D., Paltauf, F. and Daum, G. (1991). Phospholipid synthesis and lipid composition of subcellular membranes in the unicellular eukaryote S.cerevisiae. J. Bacteriology *173*, 2026-2034.

Supplemental Figure Legends

Supplemental Figure S1. Localization of Class 1-III nodulins in yeast. The indicated GFP- tagged (A) Class II and (B) Class III nodulins were expressed and localized in WT yeast cells. Images are representative of 130, 103, 103, 94, 126, 102 and 138 cells expressing AtSfh4, AtSfh5, AtSfh6, AtSfh8, AtSfh9, AtSfh13 and AtSfh14 nodulins, respectively. Cells expressing GFP-AtSfh6, -AtSfh9, -AtSfh13 and -AtSfh14 nodulins showed exclusive cytoplasmic localization for each of the corresponding chimeras, whereas the GFP-AtSfh4 and –AtSfh5 nodulins localized to the nucleus as evidenced by DAPI co-staining. GFP-AtSfh8 nodulin showed a dual PM and cytoplasmic localization as 67% of the cells showed both PM and cytoplasmic profiles for the GFP-chimera and 33% showed exclusively cytoplasmic profiles. (C,D) Localization of Class I nodulins is PtdIns(4,5)P_2-dependent. Confocal images of GFP-tagged AtSfh3, AtSfh7 and AtSfh10 nodulins expressed in yeast carrying: (C) four independent temperature sensitive alleles of the Mss4 PtdIns(4)P 5-OH kinase responsible for production of PtdIns(4,5)P_2, and (D) temperature sensitive alleles of the genes encoding each of the two essential yeast PtdIns-4-OH kinases (*pik1^{ts}* and *stt4^{ts}*) responsible for PtdIns(4)P production and of the potentiator of PtdIns 4-OH kinase activity Sec14 (*sec14^{ts}*) as indicated. Transformants of a *vps34Δ* strain lack the non-essential PtdIns 3-OH kinase required for production of both PtdIns(3)P and PtdIns(3,5)P_2. None of the lipid kinase defects of panel D affect PtdIns(4,5)P_2 levels under the conditions of these experiments, and inactivation of any one of these functions fails to release Class I nodulins from the PM. But, all Class I nodulins are released from the PM upon reduction of PtdIns(4,5)P_2 levels. All ts alleles have 22°C and 37°C as permissive and restrictive temperatures, respectively. Corresponding DIC and GFP confocal image panels are identified. Scale bars: 2 μm. For panel (C), images are representative of an aggregate of 1284 and 1460 cells imaged at 22°C and 37°C, respectively, and 70-169 cells were scored for each nodulin at each temperature. In all cases, >96% of the cells imaged at 22°C showed PM

localization of the GFP-nodulin reporter whereas, in all cases, >90% of the cells imaged at 37°C showed exclusively cytoplasmic localization for the indicated GFP-nodulin reporter. GFP-nodulin profiles were also imaged in WT yeast at 22°C (aggregate of 829 cells) and 37°C (aggregate of 292 cells). As expected, at both temperatures, >99% of the cells showed exclusively PM localization profiles. For panel (D), 32-302 cells were imaged for each mutant at each temperature. For each mutant and condition, >89% of the cells imaged showed exclusive PM localization for the indicated GFP-nodulin reporter.

Supplemental Figure S2. Localization of WT and mutant AtSfh1 nodulin domains in transiently expressing tobacco leaf epidermal cells and AtSFH1 nodulin-dependent PtdIns(4,5)P_2 homeostasis in *Arabidopsis* root hairs. *Nicotiana benthamiana* leaves transiently expressing mRFP-tagged WT nodulin and mutant versions with indicated single (A) and multiple (B) Lys to Ala substitutions were imaged by confocal scanning microscopy. A Bri1-GFP fusion was cotransfected as a plasma membrane marker. Merged and brightfield images are shown. Scale bars: 5 μm. (C) Proteins expressed in this experiment are stable as indicated by immunoblot analyses. (D) Loss of tip-directed PtdIns(4,5)P_2 gradients in Atsfh1$^{0/0}$ plants expressing Atsfh1 mutant transgenes. PtdIns(4,5)P_2 distribution was visualized as PH$^{PLC\delta1}$-YFP fluorescence in 3-day old Atsfh1$^{0/0}$ seedlings expressing: the AtSFH1 (WT) transgene, the indicated transgenes with single K→A substitutions in the nodulin peptide that yield partially functional AtSfh1 proteins, or transgenes driving expression of the indicated multiply K→A substituted AtSfh1 proteins that are biologically non-functional (bottom panel). The tip directed PtdIns(4,5)P_2 accumulation is highlighted by arrows. Scale bar: 10μm. The relative intensities of PH$^{PLC\delta1}$-YFP fluorescence at the tip plasma membrane (PM) vs cortical PM were calculated using the Image J tool to measure line-scan intensities perpendicularly across tip and cortical membrane at three different positions for each TIFF image file by plot profiling. Background correction was applied to all the images before line scan. The maximum pixel intensities recorded across each set of line scans were averaged for tip PM to cortical PM. These values were used to generate tip PM/cortical PM fluorescence intensity ratios that were interpreted as semi-quantitative readouts for tip-directed PtdIns(4,5)P_2 gradients. In the WT case the tip PM/cortical PM intensity ratio was 4.2, a value in excellent agreement with our previous ratiometric imaging measurements that reported 3- to 4-fold PtdIns(4,5)P_2 enrichments in tip PM relative to cortical PM in growing root hairs (Vincent et al., 2005). AtSfh1-deficient root hairs reconstituted with the hypomorphic AtSfh1K$_5$A and AtSfh1K$_6$A proteins exhibited tip PM/cortical PM intensity ratios of 2.5 and 2.1, respectively. AtSfh1- deficient root hairs reconstituted with the functional null AtSfh1K$_{3,5}$A, AtSfh1K$_{4,5}$A, AtSfh1K$_{3,4,5}$A, and AtSfh1K$_{1\text{-}7}$A polypeptides exhibited tip PM/cortical PM intensity ratios of 1.2, 0.9, 0.7, and 0.5, respectively.

Supplemental Figure S3. High affinity of AtSfh1 nodulin for PtdIns(4,5)P_2 and gel filtration rofiles of Class II nodulins. (A) Time course analysis of FM4-64 internalization in yeast. PMs of WT cells expressing GFP, GFP-AtSfh1 nodulin or GFP-AtSfh1$^{K1\text{-}7A}$ nodulin were loaded with FM4-64 dye (10 μM) at 0°C, warmed to 30°C and imaged at each of the indicated time points. Scale bars: 5 μm. For the

GFP and GFP-AtSfh1^{K1-7A} nodulin-expressing cells, 100-349 cells were imaged and scored for each time point. At 2 min, 60% and 47% of the GFP cells and 53% and 43% of the GFP-AtSfh1^{K1-7A} cells showed both PM + endosome or only endosome staining, respectively. In both cases, 100% of the cells showed only endosomal staining at 7.5. min, both endosomal and vacuolar staining at 12 min, and exclusively vacuolar staining by 15 min. The kinetics of FM4-64 chase were delayed in GFP-AtSfh1-expressing cells. At 2 min, 87% and 13% of the cells showed both PM + endosome or only endosome staining, respectively, 81% of the cells still showed PM + endosome staining at 7.5 min. At 12 min, 90% of the cells showed label in PM, endosomes and vacuoles and >90% of cells still exhibited detectable PM pools of FM4-64 at 15, 30 and 60 min. (B) An mRFP tagged AtSfh1 nodulin remains on the plasma membrane in a yeast temperature sensitive PtdIns 4-P 5-OH kinase mutant (*mss4-102^{ts}*) at a semipermissive temperature (26°C, left panel). By comparison, targeting of the tandemized PtdIns(4,5)P_2 biosensor GFP-2XPH$^{PLC\delta}$ to the PM was compromised at 26°C in the same *mss4-102^{ts}* strain (right panel). The pRS426-GFP-2XPH$^{PLC\delta}$ plasmid expressing the tandemized biosensor was obtained from Addgene (plasmid 36092). Scale bars: 5 μm. (C) Measurement of the binding of AtSfh1 nodulin C-terminal 12-mer peptide and the mutant peptides K_5A and $K_{3,5}$A (peptide sequences at bottom) to small unilamellar vesicles (SUVs) containing 3 mol% PtdIns(4,5)P_2 by isothermal titration calorimetry. Top panel: heat exchange after the successive injections. Bottom panel: heat per mole of lipid as a function of lipid:peptide molar ratio. (D) Table showing thermodynamic parameters of binding of wild-type and mutant peptides to large unilamellar vesicles (LUVs). Data (average values ± S.D., n = 2-3) were obtained from experiments as the one shown in C. (E) Plot of association constants K2 (data obtained from Table shown in D) of WT and mutant nodulin peptides binding to liposomes containing 3 mol% PtdIns(4,5)P_2. Unpaired t-test p value is shown (mutant compared to WT). (F) Gel filtration profile for purified native AtSfh5 nodulin. (G) Gel filtration chromatogram for purified native AtSfh8 nodulin. Immunoblot profiles across the elution window are shown in the upper panels at top, and elution positions for the indicated standards are identified by arrows.

Supplemental Figure S4. Localization of AtSfh1nodulin proline substitution mutants in yeast deficient in defined lipid kinase activities. Confocal images of GFP-tagged AtSfh1 nodulin domains harboring the indicated single and double proline missense substitutions expressed in yeast carrying: (A) four independent temperature sensitive alleles of the Mss4 PtdIns(4)P 5-OH kinase responsible for production of PtdIns(4,5)P_2, and (B) temperature sensitive alleles of the genes encoding each of the two essential yeast PtdIns-4-OH kinases (*pik1^{ts}* and *stt4^{ts}*) responsible for PtdIns(4)P production and of the potentiator of PtdIns 4-OH kinase activity Sec14 (*sec14^{ts}*) as indicated. *vps34Δ* mutants lack the non-essential PtdIns 3-OH kinase required for production of both PtdIns(3)P and PtdIns(3,5)P_2. None of the lipid kinase defects of panel B affect PtdIns(4,5)P_2 levels under these experimental conditions, and inactivation of any one of these enzymes fails to release the mutant nodulins from the PM. But, both mutant Class I nodulins were released from the PM upon reduction in PtdIns(4,5)P_2 levels. All ts alleles have 22°C and 37°C as permissive and restrictive temperatures, respectively. DIC and GFP panels are

labeled. Scale bars: 5 μm. For panel (A), images are representative of an aggregate of 399 and 395 and 220 and 227 cells imaged for GFP-AtSfh1^{E485P} and GFP-AtSfh1^{E485P,Y474P} nodulins at 22°C and 37°C, respectively (41-155 cells were scored for each nodulin at each temperature). In both cases, >94% of the cells imaged at 22°C showed exclusively PM localization of the GFP-nodulin reporter whereas, in both cases, >93% of the cells imaged at 37°C showed exclusively cytoplasmic localization for the indicated GFP-nodulin reporter. GFP-nodulin profiles were also imaged in WT yeast at 22°C (aggregate of 105 cells) and 37°C (aggregate of 143 cells). As expected, at both temperatures, >99% of the cells showed exclusively PM localization profiles. For panel (B), 23-120 cells were imaged for each mutant at each temperature. For each mutant and condition, >93% of the cells imaged showed exclusive PM localization for the indicated GFP-nodulin reporter. GFP-nodulin profiles were also imaged in WT yeast at 22°C (aggregate of 81 cells) and 37°C (aggregate of 114 cells). As expected, at both temperatures, >99% of the cells showed exclusively PM localization profiles.

Supplemental Figures

Figure S1

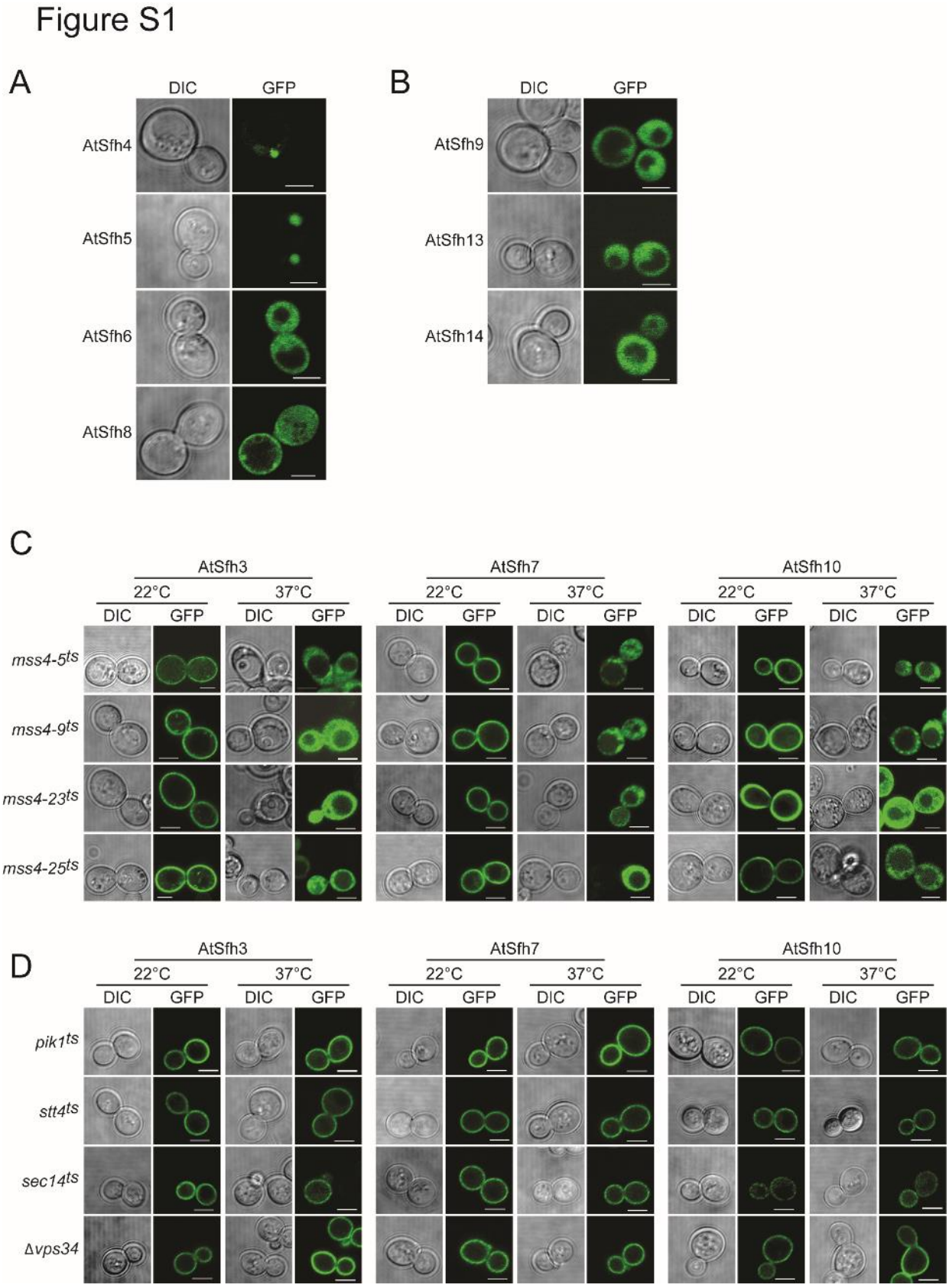

Figure S2

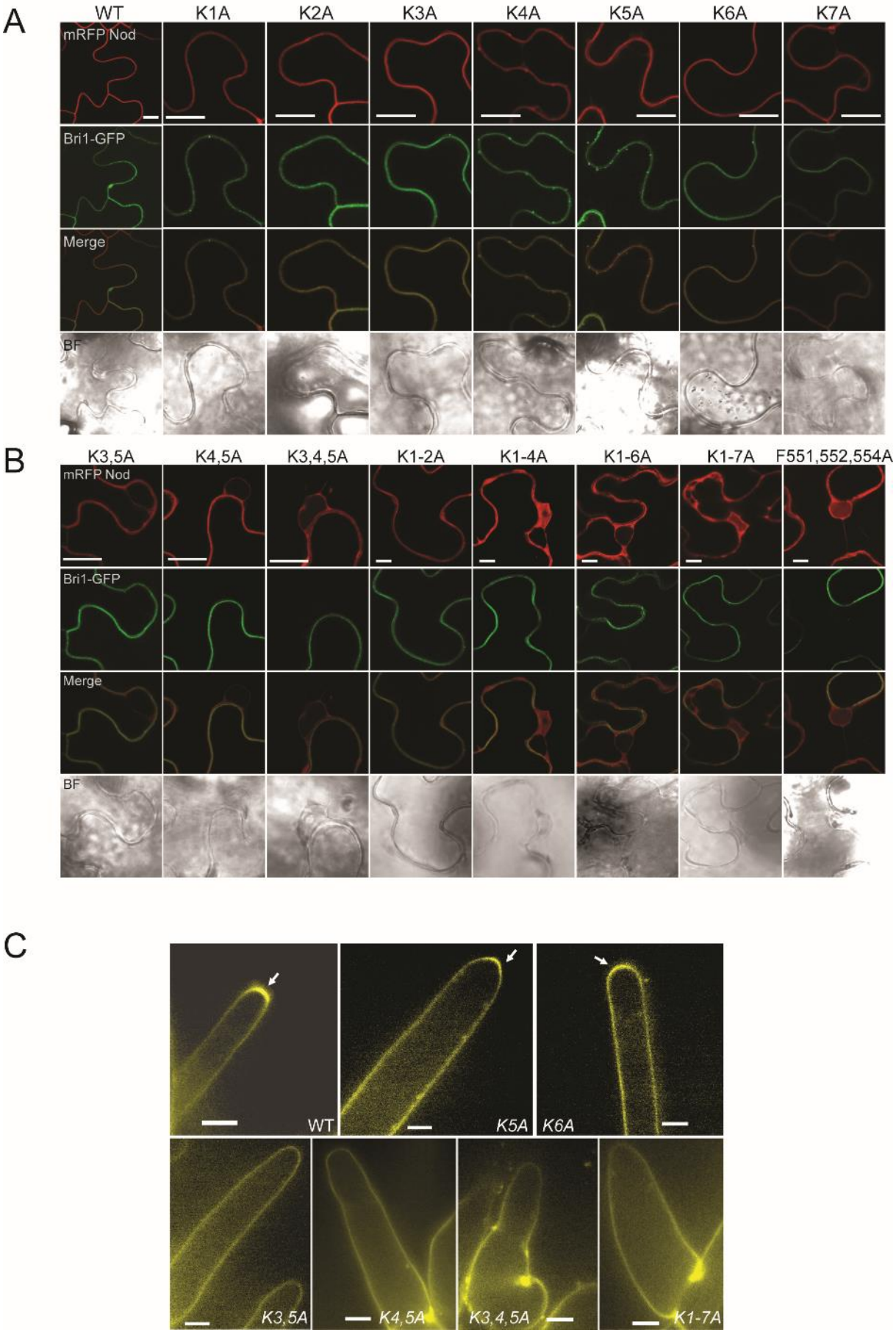
A
WT
K1A
K2A
K3A
K4A
K5A
K6A
K7A
mRFP Nod
Bri1-GFP
Merge
BF
B
K3,5A
K4,5A
K3,4,5A
K1-2A
K1-4A
K1-6A
K1-7A
F551,552,554A
mRFP Nod
Bri1-GFP
Merge
BF
C
WT
K5A
K6A
K3,5A
K4,5A
K3,4,5A
K1-7A

Figure S4

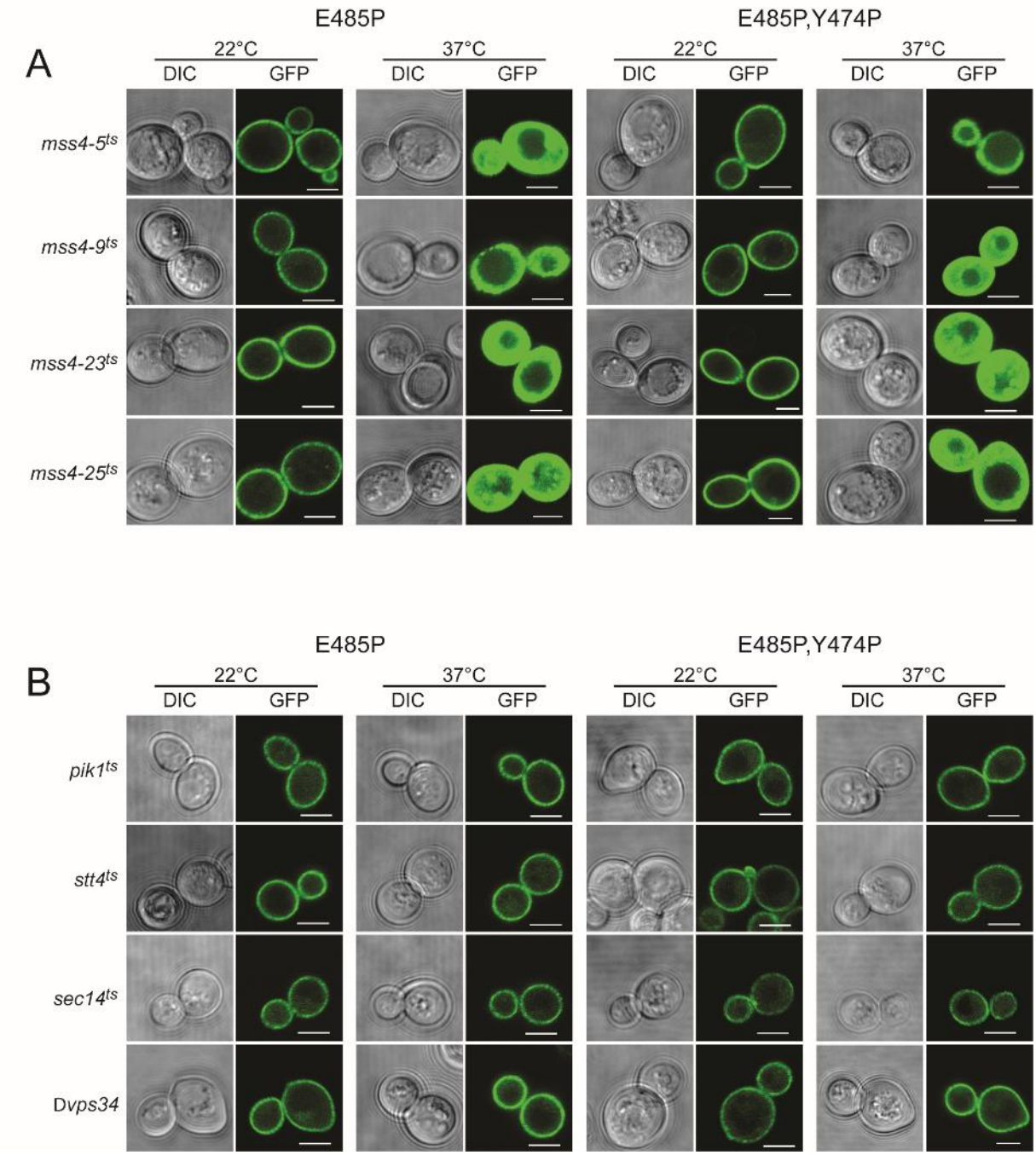
A
E485P
E485P,Y474P
22°C
37°C
22°C
37°C
DIC
GFP
DIC
GFP
DIC
GFP
DIC
GFP
mss4-5ts
mss4-9ts
mss4-23ts
mss4-25ts
B
E485P
E485P,Y474P
22°C
37°C
22°C
37°C
DIC
GFP
DIC
GFP
DIC
GFP
DIC
GFP
pik1ts
stt4ts
sec14ts
Dvps34

CHAPTER 3

A MUTANT ALLELE OF SULFURTRANSFERASE *ATSTR1* PARTIALLY BYPASSES ATSFH1-DEPENDENT ROOT HAIR FORMATION

Marília K.F. de Campos[1], Hsin-Chieh Lee[1], Marek Dynowski[2] and Gabriel Schaaf[1]

[1] ZMBP, Plant Physiology, Universität Tübingen, 72076 Tübingen, Germany
[2] ZDV, Universität Tübingen, 72074 Tübingen, Germany

Abstract

Root hairs are specialized cells of the plant root epidermis that undergo a developmental program regulated by several classes of genes that ultimately culminate in the polarized targeting of vesicles that deposit membrane, proteins and cell wall material to the bulging tip. The Arabidopsis Sec14-Nodulin AtSFH1 plays an essential role in the establishment of polarity in root hair cells. Recent work derived from studies with yeast Sec14 suggests that this class of proteins acts at the interface between lipid metabolism and the biogenesis of secretory vesicles. In plants, AtSFH1 nullzygosity compromises root hair elongation: mutants display short root hairs and an increased number of hairs with multiple tips. This phenotype is associated with defects in several components required for tip-directed growth, such as polarized phosphoinositide distribution, cytoskeleton organization and Ca^{2+} influx. In this work, we attempted to gain insights into the mechanisms by which AtSFH1 performs its functions, and how these roles interconnect with additional players orchestrating polarized secretion in tip-growing cells. We employed a combination of a forward genetic screen and next-generation sequencing to successfully isolate 10 independent *atsfh1*-suppressor mutants (*asm1-asm10*) with restored root hair growth. Using SHOREmapping and deep candidate resequencing (dCARE), we identified a mutation in the *AtSTR1* sulfurtransferase encoding gene as a putative causative candidate, and propose the existence of an AtSFH1-independent pathway that controls root hair elongation in which cyanide detoxification might be involved.

Introduction

Root hairs are long, tubular-shaped expansions that are produced on the differentiating zone of the plant root epidermis (Carol and Dolan, 2002). The major role of these cells is to enhance the root surface area, thus promoting efficient water and nutrient uptake (Grierson and Schiefelbein, 2002), and in legumes, additionally providing the entry sites for symbiotic microorganisms (Oldroyd and Downie, 2008). Root hairs are single differentiated cells with a predicted developmental pattern, they are easily visualized and are not essential for plant viability. These advantages are widely explored by researchers who employ root hairs as experimental platforms for studies on plant development, particularly on events involved in cell-fate specification and polarized growth (Carol and Dolan, 2002).

The formation of a root hair depends on a plethora of cellular and molecular components that stepwise regulate the following developmental processes: (i) cell-fate specification and differentiation of the root epidermis, (ii) root hair initiation and (iii) tip growth/elongation. In fact, web database searches showed that almost 140 Arabidopsis genes are confirmed to be directly involved in root hair formation (www.iroothair.org). These genes encode several classes of proteins that include, among others, transcription factors, receptor-like kinases, hormone receptors and transporters, small GTPases and their regulatory components, actin and actin-binding proteins, cellulose synthesizing and modifying enzymes, ROS-generating proteins, ion channels and proteins involved in phospholipid metabolism (Kwasniewski et al., 2013).

One essential component for proper root hair development is AtSFH1, a phosphatidylinositol/phosphatidylcholine (PtdIns/PtdCho) transfer protein (PITP) of the Sec14 superfamily (Bohme et al., 2004; Vincent et al., 2005). Trichoblasts of an *AtSFH1* loss-of-function T-DNA insertion line (*atsfh1-1*) exhibit correct initiation sites, however, cells fail to complete the elongation process, elaborating short root hairs with multiple tips, which reflect defects in polarized growth (Vincent et al., 2005). The authors showed that the *atsfh1-1*-dependent phenotype associates with derangements of phosphoinositide distribution, calcium influx and actin and microtubule cytoskeletons, suggesting interplay between these cellular components in regulating tip elongation.

Saccharomyces cerevisiae Sec14, the prototype of the Sec14 superfamily, is an essential protein required for the biogenesis of secretory vesicles from the trans-Golgi network (TGN) (Bankaitis et al., 1989). Functional studies based on high-resolution crystal structures demonstrate that Sec14 mediates a lipid exchange reaction between PtdIns and PtdCho, which leads to PtdIns presentation to the PtdIns 4-OH kinase (PI4K) Pik1, thus generating PtdIns(4)P pools at Golgi membranes (Schaaf et al., 2008). While the resolution of crystal structures provided valuable insights into Sec14 architecture and how this protein binds specific phospholipids, this approach provided little information on the Sec14 function in regulating secretion. Important clues that helped to clarify this issue derived from genetic studies, particularly from the discovery of individual yeast loss-of-function mutants that allow cell viability and a functional secretory pathway in the complete absence of the normally essential Sec14 (Cleves et al., 1991; Cleves et al., 1989; Fang et al., 1996). A remarkable aspect of such analyses is that these ‘bypass’

mutants create physiological conditions that mimic the consequences of Sec14 functions *in vivo* (Phillips et al., 2006). These mutants include genes encoding enzymes of the CDP-choline pathway (e.g. choline kinase, choline phosphate cytidylyltransferase and choline phosphotransferase) (Cleves et al., 1991), the PtdIns(4)P phosphatase Sac1 (Cleves et al., 1989) and the oxysterol binding protein homolog (OSBP) Kes1 (Fang et al., 1996). Taken together, data derived from detailed analyses of each of these mutants placed Sec14 in a core hub that links vesicle biogenesis with metabolism of specific lipids, including PtdCho, diacylglycerol (DAG) and PtdIns(4)P.

The characterization of the Arabidopsis Sec14-like AtSFH1 reported by Vincent et al. (2005) showed that this protein is essential for tip-directed vesicle distribution that leads to proper root hair development. However, a mechanistic explanation of how AtSFH1 performs its biological functions, as well as how these roles interconnect with other cellular players that orchestrate polarized tip-growth are questions that remain unanswered. In this work we attempt to clarify these open questions and better understand AtSFH1 functions. For that, we performed an EMS screen on *atsfh1-1* and isolated ten independent suppressor mutants able to partially bypass the requirement for AtSFH1in root hair development. We employed next-generation sequencing coupled to genome mapping to identify the causative mutation on a sulfurtransferase encoding gene (AtSTR1), and propose the existence of an AtSFH1-independent pathway for tip elongation that probably requires cyanide detoxification.

Results

Isolation of mutants that bypass the requirement of AtSFH1 in root hair elongation

In an attempt to gain further insights into the mechanisms by which AtSFH1 promotes proper root hair development, we performed a forward genetic screen using the *atsfh1-1* mutant as background for EMS mutagenesis, and searched for mutant candidates with restored root hair growth. For that, approximately 30,000 seeds of an EMS-mutagenized *atsfh1-1* M2 population were used as starting material for screening seedlings with total or partial rescue of root hair development. In this initial screen, 95 potential suppressor mutants were identified and transferred to soil. A high percentage of M2 plants did not grow further on soil, or did not yield viable progeny, most likely due to loss-of-function mutations in genes essential for plant development, which were probably brought to homozygosis in the M2 or M3 generation, respectively. Ten viable, non-segregating M3 seed populations that developed into seedlings with stable suppressor phenotype were kept for subsequent analyses. We named them *asm1-10* as acronyms for *atsfh1-1* suppressor mutants (Figure 1).

Crossings between the *asm* mutants resulted in F1 offspring that showed exclusively the *atsfh1-1* short root hair phenotype (data not shown), indicating the causative mutations are non-allelic and probably recessive. The phenotypes of the 10 independent suppressor mutants varied according to the root hair length and also to additional developmental defects (e.g. short roots or dwarfism). We chose *asm1* that, despite the longer root hairs, predominantly resembled the characteristics of the parental *atsfh1-1* (e.g. normal root length) for further characterization. It is important to notice that, albeit the penetrance of the *asm1* phenotype, the rescue of *atsfh1-1*-dependent defects was partial, as root hairs exhibited approximately half the length of wild-type cells (Figure 2), as well as a higher number of root hairs with multiple tips (data not shown). Therefore wild-type and *asm1* root hair phenotypes (from now on designated 'WT-like' and 'suppressor', respectively) were distinguishable, which facilitated the mapping analyses.

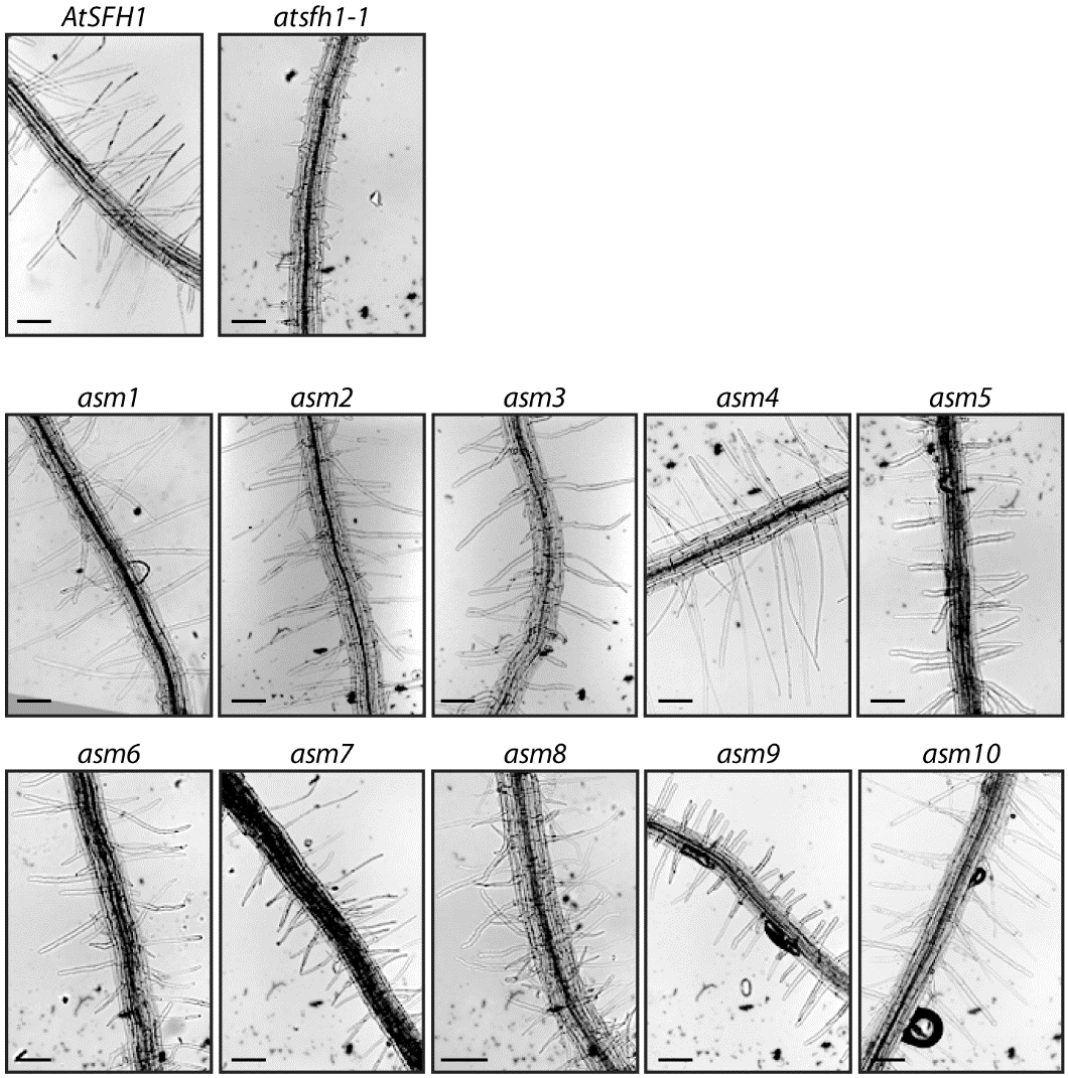

Figure 1. *atsfh1-1* suppressor mutants (asm). Light microscopy images of roots from 4 days-old seedlings of wild-type Col-0 (*AtSFH1*), *atsfh1-1* and 10 independent *asm* mutants with different levels of restored root hair development. Seedlings were grown on vertical plates containing half-strength MS medium supplemented with 2% sucrose, 100 mg.L^{-1} myo-inositol, 500 mg.L^{-1} MES buffer, 0.6% phytagel and vitamins. Images were aquired using Methamorph (version 6.2r4) and processed using Photoshop. Scale bars: 200µm)

Whole genome sequencing as a tool for mapping suppressor mutations

We employed next-generation sequencing (NGS) as a tool for identifying the *asm1* causative mutation. For that, a mapping population was generated by crossing *asm1* M3 plants, which derived from a Columbia (Col-0) background, with the polymorphic Landsberg *erecta* (Ler-1) ecotype. As expected, the F1 progeny consisted exclusively of seedlings with WT-like long root hairs. Self-fertilization of F1 led to an F2 recombinant population that segregated according to Mendelian inheritance: as depicted on Figure 3, approximately 75% of the F2 population had WT-like root hairs, 19% presented short root hairs and only 6% displayed the suppressor phenotype. Leaves of 500 recombinant plants exhibiting suppressor phenotypes were pooled and used for genomic DNA isolation. A paired-end DNA library was sequenced on an Illumina Genome Analyzer, yielding 5.5 Gb of high-quality reads that were aligned to the Col-0 reference genome using SHORE (Ossowski et al., 2008), which provided an average of 30-fold genome coverage.

The aligned reads from the pool of recombinants were used for genetic mapping using the SHOREmap software package (Schneeberger et al., 2009). The SHORE output, high-quality Col-0/Ler-1 SNPs and reference errors were used as input for SHOREmap INTERVAL, which plots the number of reads that support Col-0 and Ler-1 alleles at each marker position. In this way, the frequency of each allele in a recombinant population will be approximately 50% throughout the reads, except for the regions flanking: i) *AtSFH1* and ii) the candidate *ASM1* gene, which should harbor primarily Col-0 alleles, graphically displayed as a peak on the interval plots. Such a peak was apparent on the right arm of chromosome 4 (Figure 3), in a distance of approximately 14 kb from the *AtSFH1* genomic sequence (data not shown). This result validated the method for our analyses and indicated a correct selection of the individuals from the recombinant F2 population. A second mapping interval, most likely harboring the causative mutation, was found on the right arm of chromosome 1 (Figure 4).

Mapping candidates and validation of mutations by PCR

The mutations within the mapping interval from chromosome 1 were ranked according to the closest region from the peak and their effects predicted using SHOREmap ANNOTATE. Table 1 lists

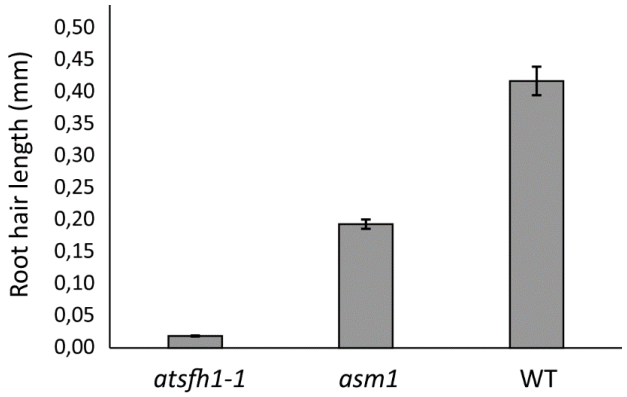

Figure 2. Partial complementation of root hair growth in the *asm1* mutant. Images of 4-day-old Col-0 *atsfh-1*, *asm1* and wild-type (WT) seedlings grown on vertical plates were used for root hair measurements using ImageJ. Means and standard error bars are shown (n > 100 root hairs).

eight gene candidates within the interval harboring non-synonymous mutations, all presenting G/C to A/T transitions typically induced by EMS treatment. Because the reference sequences used for annotation (TAIR9) did not derive from the same Col-0 used for creating the recombinant population, we checked whether the mutations within the interval were already present on the parental Col-0 *atsfh1-*

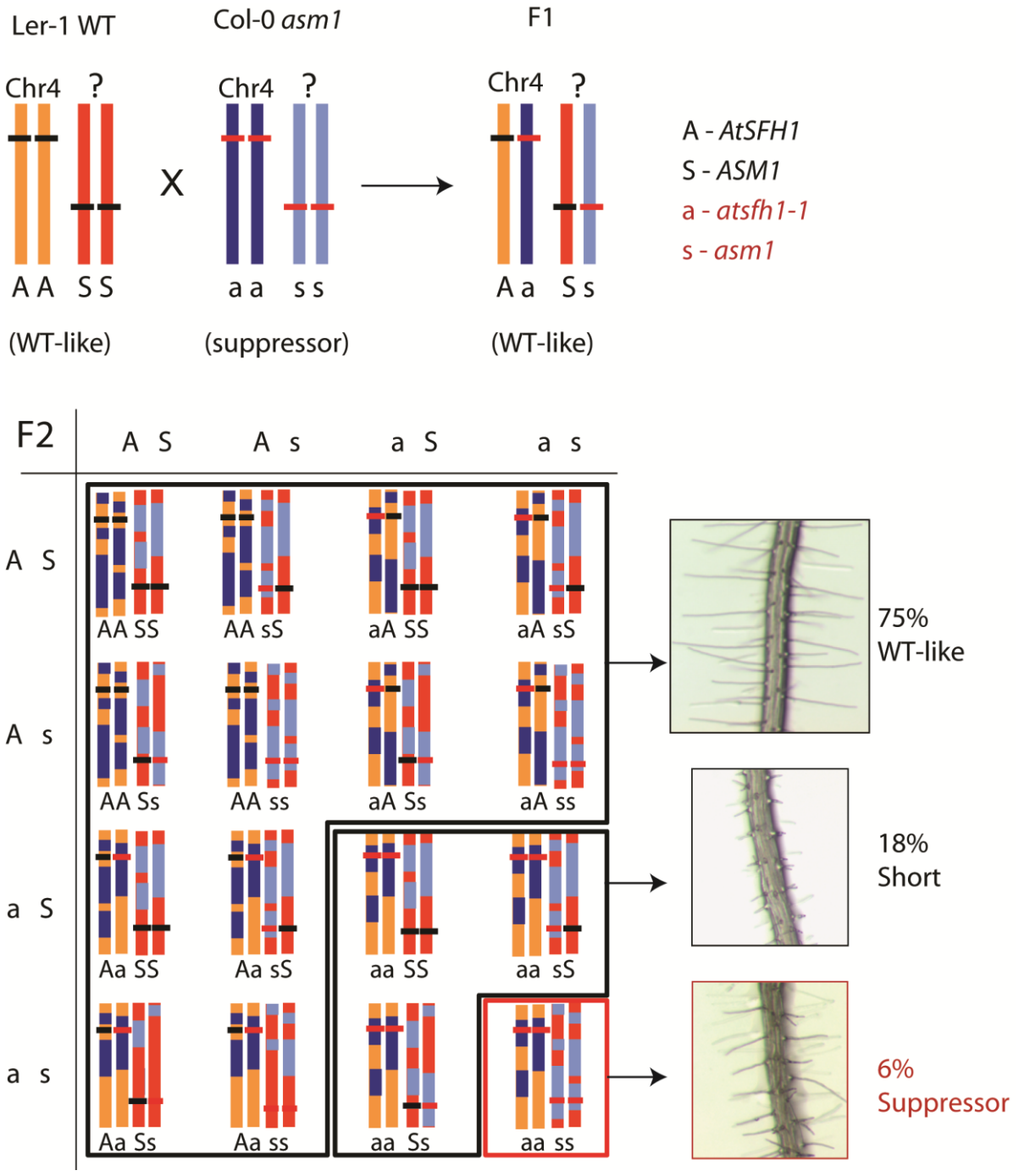

Figure 3. Schematic view of allelic and phenotypic distribution of progenies derived from Landsberg *erecta* (Ler-1) WT x Columbia (Col-0) *asm1* crossings. Dominant wild-type alleles are depicted in uppercase letters/black lines, and mutant alleles in lowercase letters/red lines. Only two relevant chromosomes are shown: chromosome 4, which carries the *AtSFH1* gene (Chr4), and the still unidentified chromosome harboring the *asm1* mutation (depicted by a question mark). Ler-1 and Col-0 derived chromatids are shown in different colors to exemplify recombination events in the F2 generation. Representative images from root hairs of wild-type, *atsfh1-1* and *asm1* seedlings are shown on the right and observed phenotypic distribution is indicated.

1 line. For that, PCR products generated from *atsfh1-1* and *asm1* gDNA that contained the reference base, or the predicted mutated base, respectively, were submitted to conventional dideoxy sequencing. We could indeed validate six of the candidate mutations and discard two in which the base change was either heterozygous in the *asm1* genome, or already present in the parental Col-0 *atsfh1-1* (Figure 5).

The search for the causative mutation

Based on the F2 segregation observed from crossing *asm1* with wild-type Ler-1 (Figure 3), as well as crossings among the independent *asm* mutants, we assumed that *asm1* was a loss-of-function recessive allele. Thus, in order to identify the *asm1* causative mutation, we crossed *atsfh1-1* with homozygous T-DNA insertion lines from four of the six candidates and observed the F2 segregation. Mutant lines from the remaining two candidates (At1g80070 and At1g78580) did not yield homozygous progeny. The phenotypic expectations on the F2 generation were the following: i) if by homozygosis of both *atsfh1-1* and *asm1* T-DNA candidate alleles the root hairs displayed the *asm1* suppressor phenotype, then a frequency of 12:3:1 (WT-like:short:suppressor) was expected; ii) if the homozygosis of both mutant alleles in this situation led to a strong phenotype that is indistinguishable from wild-type root hairs, we expected a frequency of 13:3 (WT-like:short). Finally, iii) crossings between *atsfh1-1* and T-DNA insertion lines from incorrect candidates were expected to segregate in a frequency of 3:1 (WT-like:short).

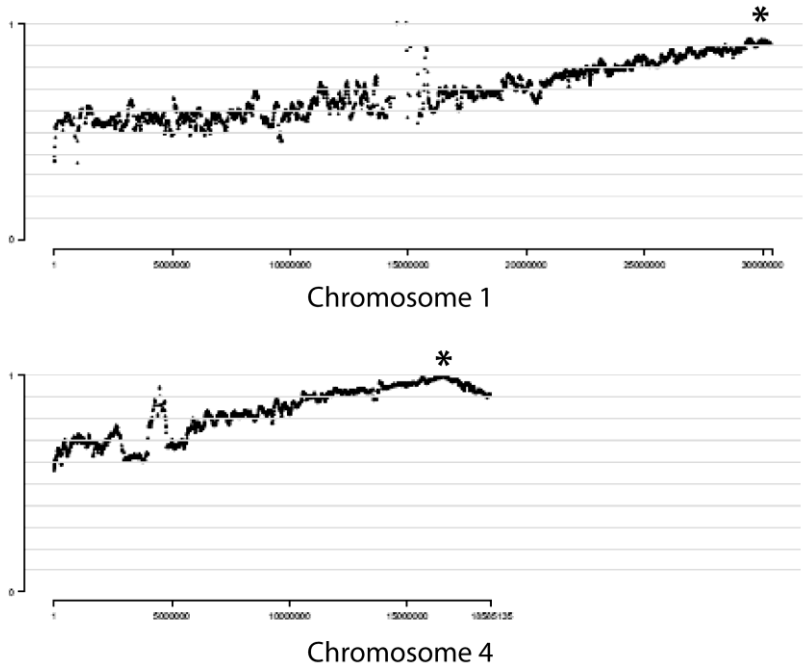

Figure 4. Visual output of SHOREmap INTERVAL. Physical position and frequencies of single nucleotide polymorphisms (SNPs) from two mapping parents (Ler-1 and Col-0) in a sliding window of 150 kb are represented by black dots. Depicted are only relevant chromosomes, where Col-0 derived SNPs gradually increased to values higher than 0.5. Asterisks indicate the maximum peak of the intervals that harbor the *asm1* candidate gene (Chromosome 1) and the *atsfh1-1* T-DNA (Chromosome 4), respectively.

Table 1. SHOREmap ANNOTATE output. Mutations from coding sequences of Chromosome 1 are ranked according to the closest distance to the allele distribution peak of SHOREmap INTERVAL. Listed below is the chromosomal location in the reference sequence (Position), the base in the reference sequence (Ref base), the mutant base in sequenced recombinants (Mut base), number of reads supporting the base change (Support), the gene identifier (ID), the amino acid of the reference (Ref AA), the amino acid after base change (Mut AA) and the annotated protein functions (Annotation).

Position (bp)	Ref base	Mut base	Support	ID	Ref AA	Mut AA	Annotation
30123900	G	A	22	**AT1G80070**	G	D	putative Pro8-type pre-mRNA splicing factor (AtSUS2)
29802634	G	A	23	**AT1G79230**	S	N	sulfurtransferase (AtStr1/AtST1/AtMST1/AtRDH1)
29555127	G	A	17	**AT1G78580**	T	I	trehalose-6-phosphate synthase (AtTPS1)
29556643	G	A	14	**AT1G78580**	P	L	trehalose-6-phosphate synthase (AtTPS1)
28632781	G	A	21	**AT1G76320**	E	K	FRS4, F15M4.18, FAR1-RELATED SEQUENCE 4
28211259	G	A	22	**AT1G75160**	A	T	Protein of unknown function (DUF620)
28062500	G	A	21	**AT1G74690**	S	F	IQ-domain 31
28022871	G	A	20	**AT1G74580**	V	I	Pentatricopeptide repeat (PPR) superfamily protein
27129592	C	T	22	**AT1G72110**	D	N	O-acyltransferase (WSD1-like) family protein;

Unfortunately, the expectation from (iii) was observed in all F2 populations evaluated: 25% of seedlings displayed short root hairs and no suppressor phenotype was observed, indicating that *atsfh1-1* phenotype was not bypassed by any of the crossings. However, the interpretation of these experiments was difficult because it was unclear whether the T-DNA insertion lines employed here represent true loss of function lines. For instance, expression analyses of the candidate genes in the T-DNA insertion lines have not yet been performed, therefore it remains unclear whether the T-DNA was potentially spliced out. Furthermore, truncated *asm1* transcripts generated at the flanking regions of the T-DNA might encode partially functional protein. Therefore, the data resulting from this experiment are not conclusive.

Pinpointing the candidate via dCARE

Because of the experimental drawbacks described on the previous session, we employed 'deep candidate resequencing' (dCARE) (Hartwig et al., 2012) to pinpoint the *asm1* causative mutation. This approach overcomes the issue of the low short-read coverage (30-fold, in our case), which typically underrepresents the number of individuals within the pooled sequenced DNA (500 recombinants). By increasing sequencing data, subtle differences in the allele frequency of closely linked mutations are easily detected, thus allowing the identification of the causative mutation. For that, we used the same pooled genomic DNA used for generation of the Illumina library as template for amplifying regions across the candidate mutations and sequenced the amplicons with an Ion Torrent Personal Genome Machine - PGM (Rothberg et al., 2011).

The Ion Torrent sequencing coverage and the allele frequencies of each candidate are listed on Table 2. One candidate (At1g74690) was excluded from the analysis due to the low coverage (30-fold). Fortunately, the At1g74690 mutation received the lowest score by SHOREmap ANNOTATE, as it is located on the farthest position away from the interval peak (Table1). Based on the relative allele frequencies of the remaining candidates, we conclude that *asm1* phenotype is most likely caused by a G

to A transition in At1g79230, as this base change occurred with the highest relative allele frequency of all non-synonymous mutations in the recombinant F2 population.

At1g79230 encodes a sulfurtransferase

The *asm1* putative candidate displays a G to A transition that results in a Ser to Asn amino acid change in the sulfurtransferase AtSTR1 (AtST1/AtMST1/AtRDH1), a member of a class of enzymes that catalyze the transfer of sulfur ions from a donor molecule to cyanide ions. In an attempt to confirm this is indeed the causative mutation, we again relied on the assumption that *asm1* is a recessive, loss-of-function allele. For that, constructs harboring the *AtSTR1* promoter and ORF were generated and used for transformation of *asm1* plants. Once transgenic plants are selected, they will be evaluated for the presence of *atsfh1-1*-like short root hair phenotype.

Discussion and outlooks

Next-generation sequencing (NGS) represents one of the most powerful present-day technologies used for speeding up the identification of causative mutations in model organisms (Austin et al., 2011; Cuperus et al., 2010; Uchida et al., 2011). In this work, we isolated 10 non-allelic EMS-induced mutants able to bypass the essential requirement for AtSFH1 in root hair elongation in Arabidopsis plants, and identified the putative candidate mutation for one of them (*asm1*) by employing such techniques. Our analysis was based on a bulk segregation approach (Lister et al., 2009), in which a large pool of F2 mutant individuals from a Col-0/Ler-1 recombinant population that exhibited the *atsfh1-1* suppressor phenotype was the staring material used for whole-genome sequencing, following SHOREmapping. Based on the assumption that less recombination events occur

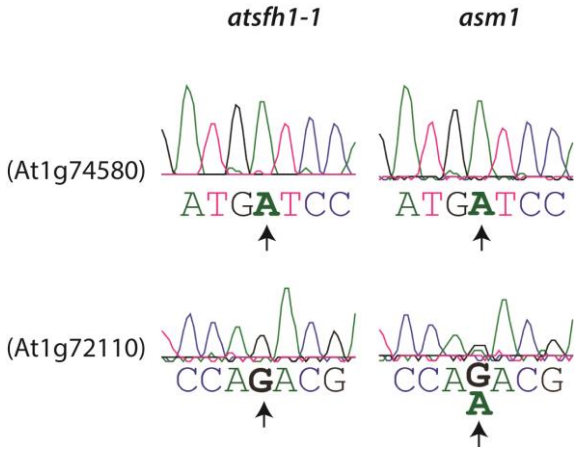

Figure 5. Conventional sequencing allows exclusion of incorrect putative suppressor mutations. Sequencing traces of PCR products generated from *atsfh1-1* and *asm1* genomic DNA are shown. As emphasized with black arrows, the base change relative to the reference sequence was already detected on At1g74580 genome of *atsfh1-1* prior mutagenesis, indicating it did not derive from the EMS treatment. The G to A transition on At1g72110 was indeed confirmed only in the *asm1* genome, however, copies of both bases are detected, indicating this mutation is in heterozygosis.

Table 2.Relative frequencies of reference and mutant alleles by dCARE analysis. Total numbers of reads (Coverage), and reads that support reference (Ref cov) and mutated bases (Mut cov) are shown. The candidate with the highest relative mutant allele frequency is highlighted in bold. Due to low coverage, candidate At1g74690 was excluded from the analysis (light grey).

Position (bp)	Ref base	Mut base	ID	Coverage	Ref cov	Mut cov	Relative mut allele freq
30123900	G	A	AT1G80070	564	206	358	0,635
29802634	**G**	**A**	**AT1G79230**	**1624**	**108**	**1516**	**0,933**
29555127	G	A	AT1G78580	1618	151	1467	0,907
28632781	G	A	AT1G76320	3050	414	2636	0,864
28211259	G	A	AT1G75160	2630	355	2275	0,865
28062500	G	A	AT1G74690	30	1	29	0,967

on loci physically linked to the locus harboring the causative mutation, an enrichment of Col-0-derived SNPs is expected on the candidate region in comparison to other regions of the genome.

The selection of the mutant F2 individuals was possible since suppressor-like Col-0 *asm1* root hairs did not completely resemble the long root hair phenotype of the wild-type Ler-1 polymorphic parent. Indeed, a predicted phenotypic distribution of 12:3:1 (WT-like:short:suppressor) was observed (Figure 3) and the ~6% *asm1*-like plants were selected. These plants were genotyped for the presence of the *atsfh1-1* allele, which assured 98% allele frequency of Col-0-derived markers in a region of mere 14 kb from *AtSFH1* genomic locus (Figure 4). A different situation, however, arose during the evaluation of the region neighboring the putative candidate gene. Even though the frequency of Col-0-derived SNPs clearly increased towards the right arm of chromosome 1, the number of short reads supporting these markers were lower than those neighboring the *atsfh1-1* allele in chromosome 4. The most likely reason for this issue is the misphenotyping of the F2 individuals, as it is known that bulk segregant analysis is prone to such mistakes. Considering the high allelic score on chromosome 4, plants homozygous for *atsfh1-1* that harbored one or two wild-type copies of *ASM1* were selected by mistake. This might have occurred, for instance, due to an effect of the growth medium used for the F2 screening; *atsfh1-1* plants occasionally develop slightly longer root hairs when roots grow inside the media, which might have contributed to the inaccuracy of the selection.

The final SHOREmap output was a list of eight relevant base changes that were ranked according to the closest distance to the maximum peak of SHOREmap interval. The six (Sanger sequencing-) confirmed candidates all contained a G/C to A/T transition in coding sequences that led to an amino acid change. The identification of a causative mutation is not trivial, though. Usual procedures to confirm that a SNP is causing a phenotype include i) the phenotypic complementation of the mutant by introducing corresponding genomic/ORF sequences and ii) evaluation of corresponding T-DNA insertion or other knockout/knockdown lines (Uchida et al., 2014). We experienced drawbacks for both procedures; first, it was not possible to generate constructs carrying large genomic fragments, as it was the case for at least one of the candidates (At1g80070), whose gDNA sequence was over 11kb long. Besides, transformation of *E. coli* with the final plant transformation vector harboring sequences of two

other candidates (At1g78580 and At1g74690) yielded no colonies, hindering following experimental procedures.

In order to confirm the candidate mutation using knockout/knockdown lines, we first relied on the assumption that *asm1* harbors a loss-of-function recessive mutation, to then generate lines that would harbor homozygous mutant alleles for both *ASM1* and *AtSFH1* genes. We obtained T-DNA insertion lines of all candidates (listed on Table S1) for performing theses analyses. However, it was not possible to generate homozygous progeny with two of them (At1g80070 and At1g78580), probably due to embryo-lethality caused by nullzygosity of those genes. Homozygous T-DNA insertion lines of the other candidates were crossed with *atsfh1-1*, and the F2 progeny screened for individuals displaying the suppressor phenotype. Unfortunately, the observed phenotypic distribution did not correspond to the expected in any of the F2 populations. Two aspects need to be considered: first, the F2 progeny was not genotyped for confirming the presence of both *atsfh1-1* and *asm1* homozygous recessive alleles. The PCR results would indicate a possible synthetic lethality between two mutant genes, which would be practically invisible to phenotypic evaluations. In this case, we would consider the *asm1* causative candidate as a gain-of-function allele. Secondly, we do not know whether the T-DNA insertion lines are real loss of function mutants, therefore the data resulted from this experiment still remains inconclusive.

In an attempt to bypass these issues, we employed a technique recently reported by Hartwig et al. (2012) shown to efficiently pinpoint causative mutations by deep-sequencing the candidate region. This procedure (named dCARE, for 'deep candidate resequencing') was originally employed to identify candidate mutations in a bulked F2 population within the same genetic background, a strategy used to avoid phenotypic variations that can be introduced by crossing different ecotypes. The idea is to overcome the fact that the short-read coverage provided by whole-genome sequencing (around 30-fold) is not sufficient to accurately distinguish between the causative and closely linked mutations, since it down-represents the bulked population (500 individuals). By deep-sequencing the interval peak using Ion Torrent we were able to oversample the original pool from 1.1 to up to 6-fold, thus significantly increasing sequencing data that was sufficient to resolve the real allele frequency of the candidates. Technical problems resulted in low coverage of At1g74690, which would mislead our interpretations. Because this candidate received the lowest score from SHOREmap ANNOTATE, we were confident that its exclusion from the analyses would not interfere with the results. Based on these results, we finally pinpointed our hit candidate mutation as being a G to A transition on the 7th exon of At1g79230 gene, which encodes a sulfurtransferase/rhodanese homolog, AtSTR1 (also called ST1 or MST1).

Sulfurtransferases (STR) are enzymes that catalyze the transfer of a sulfur atom from suitable donors [e.g. thiosulfate or 3-mercaptopyruvate (3-MP)] to nucleophilic sulfur acceptors, such as cyanide (Papenbrock et al., 2011). The most well-known STR is the bovine liver rhodanese, which has been crystalized and extensively characterized (Ploegman et al., 1978; Westley et al., 1983). This protein is composed of two domains with highly similar three-dimensional folds connected by a 16-residue hydrophobic linker. Only the C-terminal rhodanese domain harbors the catalytic Cys; the corresponding

residue on the N-terminal inactive domain is substituted by an Asp (Ploegman et al., 1978). This multi-domain organization is also found in the 20 Arabidopsis members of the sulfurtransferase/rhodanese protein family, including AtSTR1 (Papenbrock et al., 2011). The overall predicted structure of AtSTR1 is highly similar to the bovine rhodanese, however, these plant homologues harbor an interdomain linker that is approximately 20 residues longer than in STR sequences from prokaryotes and other eukaryotes (Burow et al., 2002). The authors show that this extension is essential for proper protein stability and enzymatic activity *in vitro*, and suggest that the larger hydrophobic environment of the plant linker could support substrates bigger than thiosulfate or 3-MP, for instance, proteins that could be regulated via direct transfer of the sulfane sulfur.

In *asm1,* the AtSTR1 base change leads to an Asn substitution from a Ser residue that resides within the ~20 extra plant-specific amino acids forming the interdomain linker, which were shown to be essential for proper protein stability and *in vitro* activity (Burow et al., 2002). Even though the biochemical properties, gene expression and subcellular localization of AtSTR1 and other Arabidopsis sulfurtransferases have been well characterized (Bauer et al., 2004; Nakamura et al., 2000), the biological functions of these enzymes remain unknown. This imposes limitations in understanding the mechanism that underlies the *asm1* suppressor phenotype, therefore at this point only conjectures can be made.

The main suggested function of STRs in plants is the detoxification of cyanide, which is naturally produced in plant tissues as a coproduct of ethylene biosynthesis, among other metabolic processes (Peiser et al., 1984). Cyanide strongly inhibits metalloenzymes, for example the mitochondrial cytochrome c oxidase, by binding the heme iron of its prosthetic group, thus blocking oxygen utilization in cellular functions. Due to its toxicity, cyanide needs to be promptly metabolized in plant tissues, via processes catalyzed especially by β-cyanoalanine synthases (CAS) and sulfurtransferases (Garcia et al., 2014). The most abundant Arabidopsis CAS is CYS-C1, a mitochondria-localized enzyme responsible for most of the CAS activity in roots and leaves (Watanabe et al., 2008). A molecular and phenotypic characterization of one *cys-c1* loss-of-function mutant interestingly showed that depleted CYS-C1 activity leads to defects in root hair formation that are associated with higher cyanide levels in root tissues (Garcia et al., 2010). The authors suggest that cyanide acts as a repressive signal for genes involved in root hair growth and also ethylene signaling and metabolism, and that CYS-C1 is essential to maintain low levels of cyanide for proper root hair development.

These results support at some extent our findings that a putative cyanide-detoxifying enzyme is involved in the bypass of the *atsfh1-1*-dependent root hair phenotype. However, based on the data presented by Garcia et al. (2010), it is rather counterintuitive to suggest that a decreased activity of AtSTR1 (and thus higher cyanide accumulation) would be responsible for restoring root hair growth in *asm1* plants. Therefore, we speculate that the Ser to Asn substitution in AtSTR1 might represent a gain-of-function mutation, possibly increasing the cyanide detoxifying capabilities of this enzyme, which would hence promote a more favorable environment for root hair elongation in an AtSFH1-independent

manner. This would explain why we were not able to confirm the causative mutation by complementation of the phenotype by crossings of *atsfh1-1* with *atstr1* T-DNA insertion lines. One additional important aspect to consider is that the phenotypic observations of the F2 progeny from WT Ler-1 x *asm1* Col-0 strongly suggests that recessive homozygous *asm1* alleles would be necessary for causing the suppressor phenotype (Figure 3). In this case, a plausible scenario would be a dose-dependent effect of the AtSTR1^{S235N} protein, in which both copies of the mutant alleles are required for its enhanced detoxifying activity, thus restoring root hair elongation in *atsfh1-1* plants. One can speculate that the mutant enzyme displays higher binding affinity to the substrate, and the presence of wild-type protein molecules would possibly diminish the gain-of-function phenotype by substrate competition. Moreover, the S235N substitution could have positively affected the dimerization/oligomerization status of AtSTR1. Perhaps the gain of function is only achieved by a certain homo-oligomeric state, which could be not efficiently assembled if wild-type protein is also present. Based on these assumptions, one future indispensable experiment to confirm the causative mutation is the evaluation of *atsfh1-1* transgenic lines overexpressing the *AtSTR1^{S235N}* mutant gene. Additionally, one essential question that still remains unanswered is whether cyanide metabolism is indeed the key component regulating the *asm1* suppressor phenotype. One way to address this question could be via genetic or chemical manipulation of plant cyanide levels. For that, future experiments should include the generation of *atsfh1-1* transgenic plants overexpressing known cyanide detoxifying enzymes, such as CYS-C1, and also the cultivation of *atsfh1-1* seedlings in media containing hydroxocobalamin, a potent cyanide-scavenging chemical previously shown to complement the *cys-c1* short root hair phenotype (Garcia et al., 2010).

Materials and methods

Plant material, growth conditions and EMS mutagenesis

Approximately 50,000 seeds from Col-0 *atsfh1-1* mutant (homozygous T-DNA insertion line SALK_002124.54.30.x) were soaked in water and incubated overnight at 4°C prior mutagenesis. Seeds were dried and re-suspended in 0.15% (v/v) ethylmethane sulphonate (EMS), following incubation under slow rotation at room temperature (RT) for 24 h. After EMS treatment, seeds were washed thoroughly with approximately 1L water and distributed on 7 cm x 7 cm pots containing soil. Around 5 - 20 M1 seeds were germinated on each pot and allowed to produce M2 seeds, which were used for phenotypic screen. Unless otherwise stated, all plants were cultivated at 22°C under long-day conditions (16 h light, 8 h dark), with light intensity of 120 µmol. s^{-1} m^{-2}. *Arabidopsis thaliana* Ler-1 seeds used in this work were kindly provided by Dr. Rita Gross-Hardt (ZMBP, University of Tübingen). Candidates T-DNA insertion lines were ordered from the Nottingham Arabidopsis Stock Centre (NASC), and genotyped for the presence of the T-DNA. Ordered T-DNA insertion lines and primers used for their genotyping are listed on Supporting Material session (Table S1 and Table S2, respectively).

Transgenic *asm1* plants were generated via *Agrobacterium tumefaciens*-mediated transformation using floral dip protocol (Clough and Bent, 1998). The selection of transformants and segregation analysis were done on Murashige and Skoog (MS) medium plates supplemented with 10 μM methionine sulfoximine (MSX).

Suppressor screen and generation of a mapping population

EMS-mutagenized M2 seeds were sterilized in 70% ethanol + 0.05% Silwet L-77 for 30 min, and washed in 90% ethanol for 10 min. Seeds were dried under sterile conditions and sown on squared plates with half-strength Murashige and Skoog (MS) medium supplemented with 2% sucrose, 100 $mg.L^{-1}$ myo-inositol, 500 $mg.L^{-1}$ MES buffer, 0.6% phytagel and vitamins (0.5 $mg.L^{-1}$ nicotinic acid, 0.5 $mg.L^{-1}$ vitamin B6, 0.1 $mg.L^{-1}$ vitamin B1 and 400 $mg.L^{-1}$ glycine). After 24 h stratification at 4°C, plates were placed vertically in a growth chamber with similar condition described above and grown for four to eight days. The screening for suppressor mutants was performed using a stereomicroscope (Leica MZ12) connected to a digital camera used for documentation. Four to eight days-old seedlings that displayed longer root hairs than *atsfh1-1* were selected and transferred to soil. M3 seeds were collected and observed again on media, and those consistently presenting the suppressor phenotype were used for further analysis.

To generate the *asm1* mapping population, pollen from wild-type Ler-1 was used to fertilize Col-0 *asm1* M3 plants. The F1 progeny was allowed to self-fertilize, approximately 8,000 F2 recombinants were screened and 500 seedlings displaying the suppressor phenotype were selected and transferred to soil to provide sufficient leaf material for genomic DNA isolation. F2 recombinants were genotyped for the presence of homozygous *atsfh1-1* T-DNA alleles using REDExtract-N-Amp™ Plant PCR Kit (Sigma-Aldrich Co.). Equivalent amounts of leaf material (approx. one rosette) from each PCR-positive F2 plants were pooled, frozen in liquid nitrogen and stored at -80°C.

Nuclei DNA isolation and preparation of sequencing library

Pooled leaves (0.5 - 1.0 mg) from F2 Ler-1 x Col-0 recombinants were ground to a fine powder in liquid nitrogen and used for nuclei isolation using 10 mL ice-cold nuclei extraction buffer [10 mM TRIS-HC1 pH 9.5, 10 mM EDTA pH 8.0, 100 mM KC1, 500 mM sucrose, 4 mM spermidine, 1 mM spermine, 0.1% β-mercaptoethanol (v/v)]. The re-suspension was mixed thoroughly and the homogenate filtered through three layers of Miracloth (Calbiochem). The filtrate was collected in a pre-chilled 50 mL polyethylene centrifuge tube, 2 mL nuclei extraction buffer with 10% Triton X-100 were added and mixture gently shaken for 2 minutes on ice. Nuclei were pelleted by centrifugation at 2000 x g for 10 min at 4°C, and re-suspended in 500 μL CTAB extraction buffer [100 mM TRIS pH 7.5, 700 mM NaCl, 10 mM EDTA, 1% CTAB (w/v) and 1% β-mercaptoethanol (v/v)]. The nuclei/CTAB solution was incubated for 30 min at 60°C, cooled at RT and 350 μL chloroform/isoamyl alcohol (24:1) were added. After centrifugation (10 min at 3000 x g), the upper phase was transferred to a fresh microcentrifuge tube containing equal volume of isopropanol, and DNA was pelleted by centrifuging for 3 min at

maximum speed. The pellet was washed in 75% ethanol, air dried and re-suspended in 100 μL sterile DNAse free water. DNA was incubated for 20 min at 65°C to destroy DNAses and stored at 4°C.

Approximately 3 μg nuclei DNA were sheared into fragments of 500 bp using Covaris S2 instrument and purified using QIAquick PCR Purification Kit (QIAGEN). One μg sheared DNA was used as starting material for the generation of the sequencing library using an Illumina Paired-End Sample Prep Kit (PE-102-1001), following manufacturer's guidelines. The DNA library was quantified using nanodrop photometer, yielding 20 ng.μL^{-1}, and validated using Agilent Bioanalyzer.

Illumina sequencing and SHORE mapping

The DNA sequencing was performed on an Illumina Genome Analyzer GAIIx with 2 x 101 bp paired-end reads. The conversion of the Illumina FASTQ reads into SHORE format and the filtering of the raw short reads were performed using SHORE version 0.5.0 beta (Ossowski et al., 2008). Mapping analysis was executed with SHOREmap software package version 1.2 following manual guidelines and as previously described (Schneeberger et al., 2009). In order to identity the chromosomal region flanking the causative mutation, SHOREmap INTERVAL was used and relative allele frequency plots were generated using the Ler-1 SNP marker file for TAIR9 (http://1001genomes.org/data/MPI/MPISchneeberger2011/releases/current/Ler-1/Marker/Ler-1.SNPs.TAIR9.txt). The selected interval harboring the highest peak at the right arm of chromosome 1 was used as input for SHOREmap ANNOTATE, and a priority list with base changes within the selected interval was generated.

In order to discard candidates in which the mutations predicted by SHOREmap ANNOTATE were already present in the parental *atsfh1-1*, leaves from both *asm1* and *atsfh1-1* were used as genomic DNA template for the generation of PCR products using REDExtract-N-Amp™ Plant PCR Kit (Sigma-Aldrich Co.). Primers used for this experiment are listed on supporting Table S3; PCR products containing the region of predicted base changes were submitted to conventional Sanger sequencing.

dCARE

Primers for dCARE are listed on supporting material session (Table S4). They were designed to amplify 150-bp amplicons that contained the candidate mutations in distances of +24 to +85 bases from the 3' end of the primer containing A-type extension required for Ion Torrent PGM sequencing. The sheared genomic DNA from pooled F2 recombinants previously used for Illumina sequencing was the template for amplification. The amplicon library was generated by a fusion PCR method following manufacturer's instructions (Ion Amplicon Library Preparation – Fusion Method, Life Technologies). Amplicons were purified using Agencourt AMPure beads (Beckmann Coulter) and quantified using a nanodrop photometer. Equimolar concentrations of each amplicon were pooled to ensure even coverage of the mutant bases, and the pooled library was sequenced in an Ion Torrent PGM (Life Technologies), yielding maximum 3,000 reads per amplicon. Reference and mutant allele frequencies were estimated from raw reads as previously described (Hartwig et al., 2012).

Molecular cloning

Unless otherwise stated, the generation of *STR1* (At1g79230) constructs were performed using standard molecular cloning techniques. The *STR1* promoter sequence (1.8 Kb) was amplified from genomic DNA isolated from *atsfh1-1* leaves using a forward primer that allows directional cloning in pENTR-D-TOPO (Life Technologies), and a reverse primer that introduces Acc65I and SalI restriction sites at the end of the promoter sequence. The fragment was cloned using pENTR-D-TOPO Cloning Kit (Life Technologies), following the manufacturer's protocol. The *STR1* coding sequence was isolated from a cDNA library prepared from whole Arabidopsis seedlings (Col-0) and amplified in pJET blunt cloning vector using CloneJET PCR Cloning Kit (Thermo Scientific). *STR1* ORF was then ligated downstream the promoter sequence using Acc65I/SalI restriction sites, generating pENTR-D-TOPO-*STR1prom-ORF*. This entry clone was finally recombined into pGWB601 destination vector (Nakamura et al., 2010) using Gateway LR Clonase II enzyme mix (Life Technologies). Oligonucleotides used for this experiment are listed on supporting Table S5.

References

Austin, R.S., Vidaurre, D., Stamatiou, G., Breit, R., Provart, N.J., Bonetta, D., Zhang, J., Fung, P., Gong, Y., Wang, P.W., *et al.* (2011). Next-generation mapping of Arabidopsis genes. Plant J *67*, 715-725.

Bankaitis, V.A., Malehorn, D.E., Emr, S.D., and Greene, R. (1989). The *Saccharomyces cerevisiae* SEC14 gene encodes a cytosolic factor that is required for transport of secretory proteins from the yeast Golgi complex. J Cell Biol *108*, 1271-1281.

Bauer, M., Dietrich, C., Nowak, K., Sierralta, W.D., and Papenbrock, J. (2004). Intracellular localization of Arabidopsis sulfurtransferases. Plant Physiol *135*, 916-926.

Bohme, K., Li, Y., Charlot, F., Grierson, C., Marrocco, K., Okada, K., Laloue, M., and Nogue, F. (2004). The Arabidopsis COW1 gene encodes a phosphatidylinositol transfer protein essential for root hair tip growth. Plant J *40*, 686-698.

Burow, M., Kessler, D., and Papenbrock, J. (2002). Enzymatic activity of the Arabidopsis sulfurtransferase resides in the C-terminal domain but is boosted by the N-terminal domain and the linker peptide in the full-length enzyme. Biol Chem *383*, 1363-1372.

Carol, R.J., and Dolan, L. (2002). Building a hair: tip growth in *Arabidopsis thaliana* root hairs. Philos Trans R Soc Lond B Biol Sci *357*, 815-821.

Cleves, A.E., McGee, T.P., Whitters, E.A., Champion, K.M., Aitken, J.R., Dowhan, W., Goebl, M., and Bankaitis, V.A. (1991). Mutations in the CDP-choline pathway for phospholipid biosynthesis bypass the requirement for an essential phospholipid transfer protein. Cell *64*, 789-800.

Cleves, A.E., Novick, P.J., and Bankaitis, V.A. (1989). Mutations in the SAC1 gene suppress defects in yeast Golgi and yeast actin function. The Journal of cell biology *109*, 2939-2950.

Clough, S.J., and Bent, A.F. (1998). Floral dip: a simplified method for Agrobacterium-mediated transformation of *Arabidopsis thaliana*. Plant J *16*, 735-743.

Cuperus, J.T., Montgomery, T.A., Fahlgren, N., Burke, R.T., Townsend, T., Sullivan, C.M., and Carrington, J.C. (2010). Identification of MIR390a precursor processing-defective mutants in Arabidopsis by direct genome sequencing. Proc Natl Acad Sci U S A *107*, 466-471.

Fang, M., Kearns, B.G., Gedvilaite, A., Kagiwada, S., Kearns, M., Fung, M.K., and Bankaitis, V.A. (1996). Kes1p shares homology with human oxysterol binding protein and participates in a novel regulatory pathway for yeast Golgi-derived transport vesicle biogenesis. Embo J *15*, 6447-6459.

Garcia, I., Castellano, J.M., Vioque, B., Solano, R., Gotor, C., and Romero, L.C. (2010). Mitochondrial beta-cyanoalanine synthase is essential for root hair formation in *Arabidopsis thaliana*. Plant Cell *22*, 3268-3279.

Garcia, I., Gotor, C., and Romero, L.C. (2014). Beyond toxicity: A regulatory role for mitochondrial cyanide. Plant Signal Behav *9*.

Grierson, C., and Schiefelbein, J. (2002). Root hairs. The Arabidopsis book / American Society of Plant Biologists *1*, e0060.

Hartwig, B., James, G.V., Konrad, K., Schneeberger, K., and Turck, F. (2012). Fast isogenic mapping-by-sequencing of ethyl methanesulfonate-induced mutant bulks. Plant Physiol *160*, 591-600.

Kwasniewski, M., Nowakowska, U., Szumera, J., Chwialkowska, K., and Szarejko, I. (2013). iRootHair: a comprehensive root hair genomics database. Plant Physiol *161*, 28-35.

Lister, R., Gregory, B.D., and Ecker, J.R. (2009). Next is now: new technologies for sequencing of genomes, transcriptomes, and beyond. Curr Opin Plant Biol *12*, 107-118.

Nakamura, S., Mano, S., Tanaka, Y., Ohnishi, M., Nakamori, C., Araki, M., Niwa, T., Nishimura, M., Kaminaka, H., Nakagawa, T., *et al.* (2010). Gateway binary vectors with the bialaphos resistance gene, bar, as a selection marker for plant transformation. Bioscience, biotechnology, and biochemistry *74*, 1315-1319.

Nakamura, T., Yamaguchi, Y., and Sano, H. (2000). Plant mercaptopyruvate sulfurtransferases: molecular cloning, subcellular localization and enzymatic activities. Eur J Biochem *267*, 5621-5630.

Oldroyd, G.E., and Downie, J.A. (2008). Coordinating nodule morphogenesis with rhizobial infection in legumes. Annu Rev Plant Biol *59*, 519-546.

Ossowski, S., Schneeberger, K., Clark, R.M., Lanz, C., Warthmann, N., and Weigel, D. (2008). Sequencing of natural strains of *Arabidopsis thaliana* with short reads. Genome research *18*, 2024-2033.

Papenbrock, J., Guretzki, S., and Henne, M. (2011). Latest news about the sulfurtransferase protein family of higher plants. Amino Acids *41*, 43-57.

Peiser, G.D., Wang, T.T., Hoffman, N.E., Yang, S.F., Liu, H.W., and Walsh, C.T. (1984). Formation of cyanide from carbon 1 of 1-aminocyclopropane-1-carboxylic acid during its conversion to ethylene. Proc Natl Acad Sci U S A *81*, 3059-3063.

Phillips, S.E., Vincent, P., Rizzieri, K.E., Schaaf, G., Bankaitis, V.A., and Gaucher, E.A. (2006). The diverse biological functions of phosphatidylinositol transfer proteins in eukaryotes. Crit Rev Biochem Mol Biol *41*, 21-49.

Ploegman, J.H., Drent, G., Kalk, K.H., Hol, W.G., Heinrikson, R.L., Keim, P., Weng, L., and Russell, J. (1978). The covalent and tertiary structure of bovine liver rhodanese. Nature *273*, 124-129.

Rothberg, J.M., Hinz, W., Rearick, T.M., Schultz, J., Mileski, W., Davey, M., Leamon, J.H., Johnson, K., Milgrew, M.J., Edwards, M., *et al.* (2011). An integrated semiconductor device enabling non-optical genome sequencing. Nature *475*, 348-352.

Schaaf, G., Ortlund, E.A., Tyeryar, K.R., Mousley, C.J., Ile, K.E., Garrett, T.A., Ren, J., Woolls, M.J., Raetz, C.R., Redinbo, M.R., *et al.* (2008). Functional anatomy of phospholipid binding and regulation of phosphoinositide homeostasis by proteins of the sec14 superfamily. Mol Cell *29*, 191-206.

Schneeberger, K., Ossowski, S., Lanz, C., Juul, T., Petersen, A.H., Nielsen, K.L., Jorgensen, J.E., Weigel, D., and Andersen, S.U. (2009). SHOREmap: simultaneous mapping and mutation identification by deep sequencing. Nat Methods *6*, 550-551.

Uchida, N., Sakamoto, T., Kurata, T., and Tasaka, M. (2011). Identification of EMS-induced causal mutations in a non-reference *Arabidopsis thaliana* accession by whole genome sequencing. Plant Cell Physiol *52*, 716-722.

Uchida, N., Sakamoto, T., Tasaka, M., and Kurata, T. (2014). Identification of EMS-induced causal mutations in *Arabidopsis thaliana* by next-generation sequencing. Methods Mol Biol *1062*, 259-270.

Vincent, P., Chua, M., Nogue, F., Fairbrother, A., Mekeel, H., Xu, Y., Allen, N., Bibikova, T.N., Gilroy, S., and Bankaitis, V.A. (2005). A Sec14p-nodulin domain phosphatidylinositol transfer protein polarizes membrane growth of *Arabidopsis thaliana* root hairs. The Journal of cell biology *168*, 801-812.

Watanabe, M., Kusano, M., Oikawa, A., Fukushima, A., Noji, M., and Saito, K. (2008). Physiological roles of the beta-substituted alanine synthase gene family in Arabidopsis. Plant Physiol *146*, 310-320.

Westley, J., Adler, H., Westley, L., and Nishida, C. (1983). The sulfurtransferases. Fundamental and applied toxicology : official journal of the Society of Toxicology *3*, 377-382.

Acknowledgements

We thank Elke Sauberzweig for technical support. We also thank Dr. Christa Lanz (MPI Tübingen) who provided support during the preparation of the gDNA library and Illumina sequencing, Jörg Hagmann (MPI Tübingen) for the help with the mapping analyses and Dr. Franziska Turck (MPIZ Cologne) for valuable advice and for support with the dCARE analyses.

Supporting Material

Table S1. List of T-DNA insertion lines of SHOREmap candidates. Zygosity status identified by genotyping at least 10 individuals from first offspring of acquired seeds.

Name	NASC ID	Gene ID	Location of T-DNA	Personal ID	Zygosity Status
SAIL_272_C04	N812605	At1g80070	Exon	IL_Chr1-1_A	heterozygous
SALK_015593.51.50.x	N515593	At1g79230	Intron	IL_Chr1-2_A	heterozygous
SALK_015689.50.70.x	N515689		Intron	IL_Chr1-2_B	heterozygous
SAIL_210_C05	N860551		Exon	IL_Chr1-2_C	homozygous
GABI_850D04	N754149	At1g78580	Intron	IL_Chr1-3_B	heterozygous
SALK_142995.39.50	N657845		Intron	IL_Chr1-3_C	heterozygous
SAIL_365_E05	N862564	At1g76320	Exon	IL_Chr1-4_A	homozygous
SALK_045754.31.85.x	N662319		Exon	IL_Chr1-4_B	heterozygous
SALK_146549.45.40.x	N646549		Exon	IL_Chr1-4_C	heterozygous
SAIL_97_E04	N804663		Exon	IL_Chr1-4_D	heterozygous
SALK_151730.48.05.x	N664348	At1g74690	Promoter	IL_Chr1-7_A	homozygous
SALK_013815.54.75.x	N653041		Exon	IL_Chr1-7_B	homozygous
SALK_046145.44.20.x	N546145		Promoter	IL_Chr1-7_C	heterozygous
SALK_046146.42.60.x	N546146		Promoter	IL_Chr1-7_D	heterozygous
GABI_085G10	N312679		Exon	IL_Chr1-7_E	heterozygous
SALK_022627.41.60.x	N665530	At1g75160	Promoter	IL_Chr1-8_A	homozygous
SAIL_761_C10	N834026		Promoter	IL_Chr1-8_B	heterozygous
SM_3_526	N56507		Exon	IL_Chr1-8_C	heterozygous

Table S2. List of oligonucleotides used for genotyping T-DNA insertion lines of SHOREmap candidates

Name	Sequence (5'-3')	Target
IL_Chr1-1_A_F	GGTGCTGGAAAGCTAATATCC	At1g80070
IL_Chr1-1_A_R	GTCATGTTTGTATGACAATGGA	
IL_Chr1-2_A_F	GTCAGTCCGATAACCTTTCAGA	At1g79230
IL_Chr1-2_A_R	CTGAACAAGTTATTGTAACACAAG	
IL_Chr1-2_C_F	GATGAGCGAAACCACACTTAGT	At1g79230
IL_Chr1-2_C_R	GCACCCAAACTTTTTCATGTCC	
IL_Chr1-3_A_F	CTAAATGCCTTAAGGAGTACAAC	At1g78580
IL_Chr1-3_A_R	ACCTCTATATATGTACCATGGA	
IL_Chr1-3_B_F	GTTTTCGGAAAGTAACATGACAC	At1g78580
IL_Chr1-3_B_R	CCTTTCTGCCAGCAAATCTTTC	
IL_Chr1-3_C_F	CAGTTGATGTTGTCCAAGGAAG	At1g78580
IL_Chr1-3_C_R	CCTCGAGACTAAAGAATTAGATG	
IL_Chr1-4_A_F	GTGAAATCCAACGATTCTCGTC	At1g76320
IL_Chr1-4_A_R	GCATAACTTTAGGTTTTTGACCAC	
IL_Chr1-4_B_F	CTTTTAAGCAATGTGCTGTTACG	At1g76320
IL_Chr1-4_B_R	CACCAACAGTTTCAGATTGAGC	
IL_Chr1-4_C_F	GATTGATCTTTCTTCACTTGTGC	At1g76320
IL_Chr1-4_C_R	CTTATCCTAACAACAAGTGGAAC	
IL_Chr1-4_D_F	GTCCAGGAAGAAAATCAATATGG	At1g76320
IL_Chr1-4_D_R	GATAAATTAGTTGAGTAGGAGATC	
IL_Chr1-7_A_F	gcttattattagagttgattagaac	At1g74690
IL_Chr1-7_A_R	cctaaaaccatcactgttttctc	
IL_Chr1-7_B_F	ctgtatgtggagaatttggatca	At1g74690
IL_Chr1-7_B_R	CTGCAATCTCTCGTTGGATTCT	
IL_Chr1-7_C_F	gtggattttgagtcatttagggt	At1g74690
IL_Chr1-7_C_R	GTCTTTGGAACCACTAGATTTAG	
IL_Chr1-7_D_F	ccagatctggtaatttcacttca	At1g74690
IL_Chr1-7_D_R	CCAAGCAATACATTCTTCAACCA	
IL_Chr1-7_E_F	gtatatcctaacatgagctctttg	At1g74690
IL_Chr1-7_E_R	GCTGTTAGTTTCTTGATTCCAAG	
IL_Chr1-8_A_F	gaggatccatctaatctatctca	At1g75160
IL_Chr1-8_A_R	gaggatccatctaatctatctca	
IL_Chr1-8_B_F	tgcaatatgataggggataattg	At1g75160
IL_Chr1-8_B_R	gatgtgacataatcatggatttac	
IL_Chr1-8_C_F	GAATATGCACGCTCTCATGAAG	At1g75160
IL_Chr1-8_C_R	gctaataatcgctacacattcca	
IL_Chr1-8_D_F	tgagatagattagatggatcctc	At1g75160
IL_Chr1-8_D_R	caagtgaaagacttgaattctaac	
LBb1	gcgtggaccgcttgctgcaact	SALK T-DNA left border
LB1_SAIL	GCCTTTTCAGAAATGGATAAATAGCCTTGCTTCC	SAIL T-DNA left border
LB2_SAIL	GCTTCCTATTATATCTTCCCAAATTACCAATACA	SAIL T-DNA left border
LB3_SAIL	TAGCATCTGAATTTCATAACCAATCTCGATACAC	SAIL T-DNA left border
LBo8409_GABI	ATATTGACCATCATACTCATTGC	GABI T-DNA left border
LBoriL_GABI	ATATTGACCATCATACTCATTGC	GABI T-DNA left border

Table S3. List of oligonucleotides used validating SHOREmap candidates

Name	Sequence (5'-3')	Target
F_AT1G80070	GTCTTTTCTCTTTGCTTGACAGAG	At1g80070
R_AT1G80070	GTAATTGTTCAAGTTCCACAAC	
F_AT1G79230	GAGAAAATTTATCAAGGACAAACC	At1g79230
R_AT1G79230	CTTAAGCAGAGAATGATAGTTAAC	
F_AT1G78580	GTGTATTCCCGTGTTCCTTG	At1g78580
R_AT1G78580	GTATGGAGAAACCATCCAAC	
F_IIAT1G78580	CGTGAAACAATACAAAACATCTGC	At1g78580
R_IIAT1G78580	CAGAAATAATGGTCTGCTAAGAC	
F_AT1G76320	CTAATGCTAGAAGATAGGTATG	At1g76320
R_AT1G76320	GCAAGAGCAGTAAATATCTGAC	
F_AT1G72110	GATTGCTCAAAGTAACAATGGAG	At1g72110
R_AT1G72110	CAAAGGTACTTGCAGCAATGTAAG	
F_AT1G74580	GTCAATTTGGGGTACAAGTTTC	At1g74580
R_AT1G74580	GTTCGTAAGCATAATACGTGATAC	
F_AT1G74690	CATGCTTCTGGAAACCAGTTC	At1g74690
R_AT1G74690	CTCTCAACTACAGGATTATGTAC	
F_AT1G74690_b	CTTCATCACCAAAAGTGCTACC	At1g74690
R_AT1G74690_b	GATGATTCCCTTGTCTTCTCAAC	
F_AT1G75160	GATGCACAGCGAGTTTGTTCT	At1g75160
R_AT1G75160	CAACGAATATGTAATCGTCGATG	
F_AT1G69770	CAGATCTTTCAATTGTGCAGAAAC	At1g69770
R_AT1G69770	GTGACGAGGTTCAAACCAGAC	
F_AT1G61310	ATGGGGAGTTGTTTTTCTTTTC	At1g61310
R_AT1G61310	CCATACCTGGACAGCTTCAAG	

Table S4. List of oligonucleotides used for the generation of Ion Torrent amplicon library

Name	Sequence (5'-3')	Target
1A-Targ_F	CCATCTCATCCCTGCGTGTCTCCGACTCAGgacagGATTCTTGGGATAGGG	At1g80070
1A-Targ_R	CCATCTCATCCCTGCGTGTCTCCGACTCAGCCCATCATGTCTCTGGTGTG	
1trP1-Targ_F	CCTCTCTATGGGCAGTCGGTGATgacagGATTCTTGGGATAGGG	
1trP1-Targ_R	CCTCTCTATGGGCAGTCGGTGATCCCATCATGTCTCTGGTGTG	
2A-Targ_F	CCATCTCATCCCTGCGTGTCTCCGACTCAGgattcatgatgagttttgagcag	At1g79230
2A-Targ_R	CCATCTCATCCCTGCGTGTCTCCGACTCAGattcaggaaatgccaacCTG	
2trP1-Targ_F	CCTCTCTATGGGCAGTCGGTGATgattcatgatgagttttgagcag	
2trP1-Targ_R	CCTCTCTATGGGCAGTCGGTGATattcaggaaatgccaacCTG	
3A-Targ_F	CCATCTCATCCCTGCGTGTCTCCGACTCAGgcagAGGTGTATTCCCGTGT	At1g78580
3A-Targ_R	CCATCTCATCCCTGCGTGTCTCCGACTCAGTTGGGACTGAAAGCTTCTGG	
3trP1-Targ_F	CCTCTCTATGGGCAGTCGGTGATgcagAGGTGTATTCCCGTGT	
3trP1-Targ_R	CCTCTCTATGGGCAGTCGGTGATTTGGGACTGAAAGCTTCTGG	
4A-Targ_F	CCATCTCATCCCTGCGTGTCTCCGACTCAGGCATGAAGCACCTGAGTTGA	At1g76320
4A-Targ_R	CCATCTCATCCCTGCGTGTCTCCGACTCAGTCCTTCCTCACTCTCCTTCG	
4trP1-Targ_F	CCTCTCTATGGGCAGTCGGTGATGCATGAAGCACCTGAGTTGA	
4trP1-Targ_R	CCTCTCTATGGGCAGTCGGTGATTCCTTCCTCACTCTCCTTCG	
7A-Targ_F	CCATCTCATCCCTGCGTGTCTCCGACTCAGTCGAGGCTGAGTCTGCTAAA	At1g74690
7A-Targ_R	CCATCTCATCCCTGCGTGTCTCCGACTCAGGGCTCTATCGACTGGCTTGA	
7trP1-Targ_F	CCTCTCTATGGGCAGTCGGTGATTCGAGGCTGAGTCTGCTAAA	
7trP1-Targ_R	CCTCTCTATGGGCAGTCGGTGATGGCTCTATCGACTGGCTTGA	
8A-Targ_F	CCATCTCATCCCTGCGTGTCTCCGACTCAGTTCTTAGACGCCGTTTGCAT	At1g75160
8A-Targ_R	CCATCTCATCCCTGCGTGTCTCCGACTCAGGCTGAAGTAACCCCATACCG	
8trP1-Targ_F	CCTCTCTATGGGCAGTCGGTGATTTCTTAGACGCCGTTTGCAT	
8trP1-Targ_R	CCTCTCTATGGGCAGTCGGTGATGCTGAAGTAACCCCATACCG	

Table S5. List of oligonucleotides used for cloning STR1 promoter and coding sequences

Name	Sequence (5'-3')	Target
Chr1-2_Prom_F	CACCcttcttctctgacaaactctcc	At1g79230 promoter
Chr1-2prom_Acc65I_SalI_R	aaaGTCGACaaaGGTACCatccacctcaaatattctctcg	
Acc65I_Chr1-2_ORF_F	tttGGTACCATGGCCTCGACCCTTTTCTC	At1g79230 ORF
Chr1-2_ORF_SalI_R	ataGTCGACTCATGAAGAAGATTCAACACTCTC	

CHAPTER 4

RESURRECTION OF A FUNCTIONAL PHOSPHATIDYLINOSITOL TRANSFER PROTEIN FROM A PSEUDO-SEC14 SCAFFOLD BY DIRECTED EVOLUTION

Gabriel Schaaf[*†#], Marek Dynowski[†‡], Carl J. Mousley[*], Sweety D. Shah[*], Peihua Yuan[*], Eva M. Winklbauer[†], Marília Kaphan Freitas de Campos[†], Kyle Trettin[*], Mary-Chely Quinones[§], Tatyana I. Smirnova[§], Lora L. Yanagisawa[‖], Eric A. Ortlund[¶], and Vytas A. Bankaitis[*#]

[*] Department of Cell & Developmental Biology, Lineberger Comprehensive Cancer Center, University of North Carolina School of Medicine, Chapel Hill, North Carolina 27599-7090, USA; [†] ZMBP, Plant Physiology, Universität Tübingen, 72076 Tübingen, Germany; [‡]Rechenzentrum, Universität Freiburg, 79104 Freiburg, Germany; [§]Department of Chemistry, North Carolina State University, Raleigh, NC 27695, USA; [‖]Department of Cell Biology, University of Alabama-Birmingham School of Medicine, Birmingham, AL 35294, USA [¶]Department of Biochemistry, Emory University School of Medicine, Atlanta, GA 30322, USA

[#] **Co-Corresponding Authors**

This chapter has been published:

Schaaf et al. (2011). Resurrection of a functional phosphatidylinositol transfer protein from a pseudo-Sec14 scaffold by directed evolution. **Mol Biol Cell**, 22(6), 892-905.
(Republished according to ASCB license and publishing agreement)

Abstract

Sec14-superfamily proteins integrate the lipid metabolome with phosphoinositide synthesis and signaling via primed presentation of phosphatidylinositol (PtdIns) to PtdIns kinases. Sec14 action as a PtdIns-presentation scaffold requires heterotypic exchange of phosphatidylcholine (PtdCho) for PtdIns, or vice versa, in a poorly understood progression of regulated conformational transitions. We identify mutations that confer Sec14-like activities to a functionally inert pseudo-Sec14 (Sfh1), which seemingly conserves all of the structural requirements for Sec14 function. Unexpectedly, the "activation" phenotype results from alteration of residues conserved between Sfh1 and Sec14. Using biochemical and biophysical, structural, and computational approaches, we find the activation mechanism reconfigures atomic interactions between amino acid side chains and internal water in an unusual hydrophilic microenvironment within the hydrophobic Sfh1 ligand-binding cavity. These altered dynamics reconstitute a functional "gating module" that propagates conformational energy from within the hydrophobic pocket to the helical unit that gates pocket access. The net effect is enhanced rates of phospholipid-cycling into and out of the Sfh1* hydrophobic pocket. Taken together, the directed evolution approach reveals an unexpectedly flexible functional engineering of a Sec14-like PtdIns

transfer protein—an engineering invisible to standard bioinformatic, crystallographic, and rational mutagenesis approaches.

Introduction

Phosphorylated derivatives of PtdIns, or PIPs, are elementary components of membrane-associated signaling systems in eukaryotes (Majerus, 1997; Fruman et al., 1998; McLaughlin and Murray, 2005; Ile et al., 2006; Strahl and Thorner, 2007). The remarkable diversity of PIP signaling is established by two major factors. First, enzymes that produce PIPs are differentially localized within cells -- thereby facilitating compartment-specific enrichment of individual PIP species. Second, PIP chemical heterogeneities are interpreted by proteins harboring headgroup-binding domains with appropriate positional specificities. The diversity in PIP signaling promoted by chemical heterogeneity is subject to further amplification by combinatorial mechanisms that couple biological recognition of a PIP-dependent event to a second molecular interaction (Balla, 2005; Lemmon, 2008). Such coincidence detection is termed a 'back-loaded' strategy on the principle that diversification occurs once the PIP has been generated (Bankaitis et al., 2010).

Recent studies demonstrate that production of an individual PIP species by a specific PtdIns kinase evokes diverse biological outcomes in a single cell (Routt et al., 2005). Those findings are difficult to explain by back-loaded mechanisms alone. Rather, front-loaded strategies also contribute to diversification of PIP signaling outcomes (Schaaf et al., 2008; Bankaitis et al., 2010). The principle that underlies front-loaded mechanisms highlights an intrinsic biological inadequacy of PtdIns kinases (particularly PtdIns 4-OH kinases), which are insufficient interfacial enzymes when confronted with the dual issues of: (i) substrate PtdIns presented in liposomal contexts, and (ii) competing activities that degrade PIPs. Productive action of these enzymes is subject to what we term 'instructive' activation (Bankaitis et al., 2010). Sec14-like PITPs are the instructive components in 'front-loaded' regulation of PtdIns 4-OH kinase activities in yeast by virtue of their roles as primeable 'PtdIns-presentation' modules. For Sec14, effective presentation requires heterotypic PtdIns/PtdCho-exchange (Schaaf et al., 2008). The Sec14-protein superfamily is diverse, and a PtdIns-binding "bar-code" is recognized in nearly all members of the superfamily. PtdCho-binding signatures are not broadly conserved, however – forecasting that lipids other than PtdCho are 'sensed' by Sec14-like proteins, and that metabolism of these lipids might also be coupled to PIP synthesis by Sec14-like proteins. Thus, the Sec14-superfamily might link diverse territories of the lipid metabolome with 'instructed' PIP signaling (Schaaf et al., 2008; Bankaitis et al., 2010). This interface is of interest given the causal links between Sec14-like protein deficiencies and human disease (Ouachi et al., 1995; Benomar et al., 2002; Bomar et al., 2003; Meier et al., 2003; D'Angelo et al., 2006).

Understanding the mechanics of how Sec14-like PITPs execute PL-exchange is of central importance given heterotypic PL-exchange reactions lie at the heart of the mechanisms by which these proteins integrate lipid metabolism with PIP signaling (Bankaitis et al., 2010). To interrogate the

functional engineering of Sec14-like proteins, we employed a directed evolution approach to resurrect Sec14-like activities in a protein (Sfh1) that substantially lacks them. We find single residue substitutions, involving conserved residues, are sufficient to endow the Sfh1 'pseudo-Sec14' with Sec14-like activities in yeast (Sfh1*). These properties are associated with enhanced abilities of Sfh1* to cycle PL in/out of the protein interior in vitro and stimulate PtdIns kinase activities in vivo. The resurrected Sec14-like activities result from altered atomic interactions involving an unusual hydrophilic microenvironment within the hydrophobic Sfh1 ligand-binding cavity. These altered dynamics facilitate conformational transitions in core structural elements that control PL exchange from the Sfh1 hydrophobic pocket. Taken together, these studies provide new mechanistic insights into the functional design of a Sec14-like PITP.

Results

Isolation of SFH1* alleles that endow Sfh1 with Sec14-like activities.

Enhanced expression of Sfh1, the protein most closely related to the essential yeast Sec14, fails to rescue phenotypes associated with Sec14 defects. Moreover, Sfh1 does not catalyze robust PtdIns- or PtdCho-transfer activity in vitro (Li et al., 2000). Yet, Sfh1 shares 64% primary sequence identity with Sec14 and conserves all of the obvious Sec14 structural motifs critical for PtdIns- and PtdCho-binding (Schaaf et al., 2008). These findings suggest that Sfh1 is a 'pseudo-Sec14' that is either unable to effectively undergo the conformational dynamics that accompany PL transfer reactions in Sec14, or that these transitions fundamentally differ from those of Sec14. Our description of Sfh1 as a 'pseudo-Sec14' holds no implied evolutionary connotation. This convenient descriptor simply reflects that Sfh1, while highly homologous to Sec14, is not functionally an active Sec14.

To better understand the mechanics for how Sec14-like PITPs function at the single molecule level, we sought to 'resurrect' Sec14-like activities in Sfh1. To that end, missense mutations were incorporated into the *SFH1* gene by error-prone PCR and in vivo gap repair, and reconstituted plasmids driving expression of mutagenized *SFH1* genes were introduced into a *sec14-1^{ts} ura3-52* yeast strain. Transformants were co-selected for growth at 37°C and uracil prototrophy. From an estimated 1 x 10^6 potential Ura^+ transformants, 486 Ura^+Ts^+ transformants were recovered (ca. 0.05% of potential Ura^+ transformants). Of these, 100 were saved for detailed analysis. In all cases, the Ts^+ growth phenotype was plasmid-linked on the basis of two criteria. First, plasmid loss induced by *URA3* counter-selection with 5-fluoro-orotic acid was accompanied by loss of the Ts^+ phenotype. Reciprocally, *SFH1* plasmids were recovered from each of the parental Ura^+Ts^+ transformants and re-introduced into naïve *sec14-1^{ts}* mutants by selection for Ura^+. In each case, the Ts^+ phenotype was co-inherited with plasmid. We refer to these *SFH1* activation alleles as *SFH1**.

Single substitutions activate Sec14-like functions in Sfh1.

Of the 100 *SFH1** isolates, complete nucleotide sequences were determined for 40 clones. These analyses demonstrated the *SFH1** isolates contained an average of 4.4 nucleotide and 3.1 amino acid substitutions per gene and gene product, respectively (Figure 1A, Supplemental Figure S1). Two hot spots for *SFH1** activation alleles were identified. One hot spot includes Sfh1 residues Y_{109} and Y_{113}, while the other highlights the sequence between residues I_{131} and T_{141} (Figure 1A; Supplemental Figure S1). The Y_{109}/Y_{113} hotspot involves an enigmatic hydrophilic patch on the floor of the Sfh1 hydrophobic cavity (Smirnova et al., 2006; Schaaf et al., 2008). This patch is configured in close proximity to the *sn*-2 acyl chain of bound PtdCho (Figure 1B) and PtdIns (Figure 1C). The hydrophilic patch surface is organized by residues Y_{109}, Q_{111}, Y_{124}, and E_{126} and involves several coordinated H_2O molecules one of

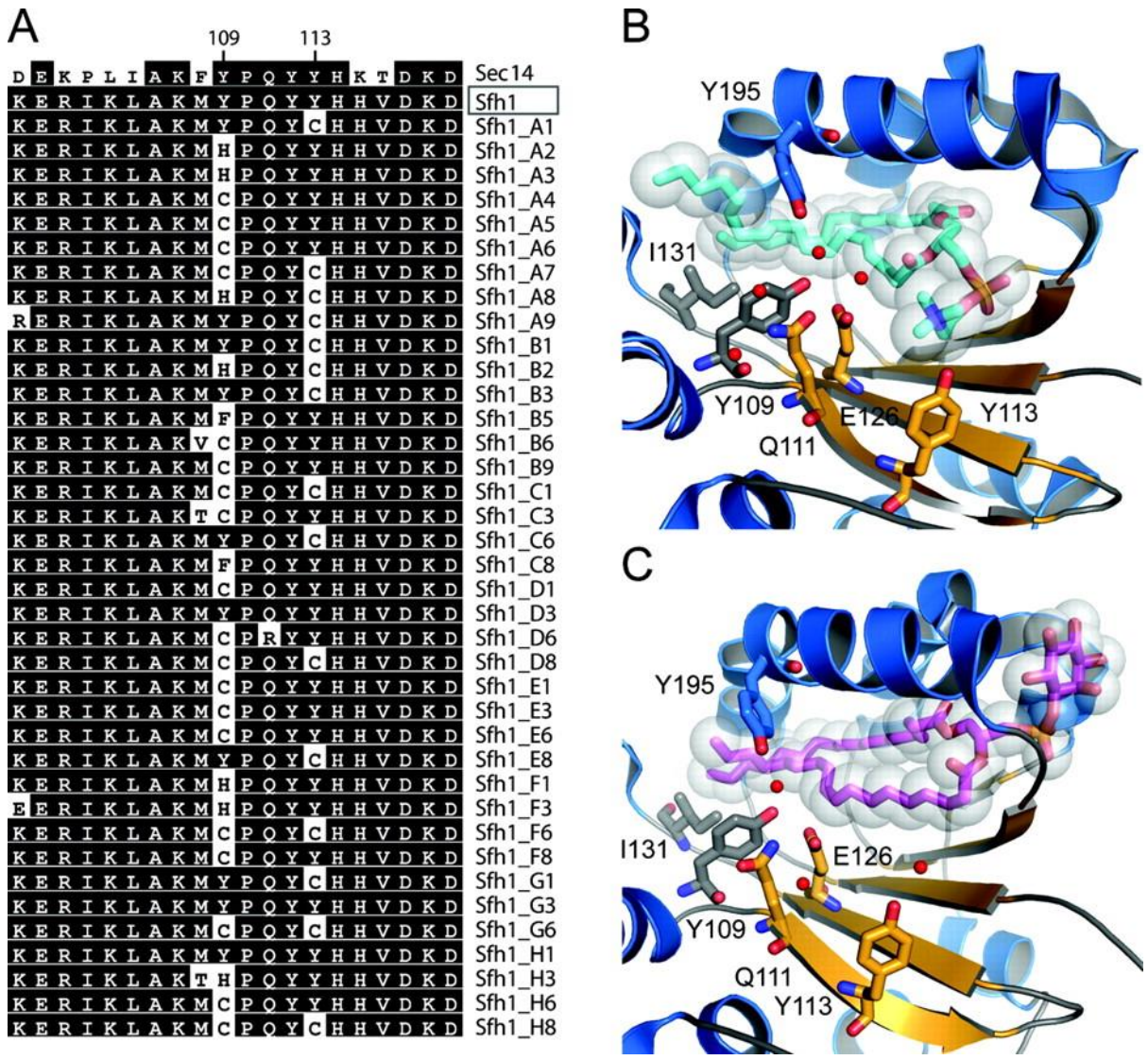

Figure 1. *SFH1** activation alleles. **(A)** Protein alignment of Sfh1* mutants obtained in the primary directed evolution screen. Depicted are amino acid residues 100-119. The sequences of Sec14 and the Sfh1 wild-type protein are presented for comparison. **(B and C)** Ribbon diagrams illustrating the hydrophilic patch at the floor of the hydrophobic PL-binding pocket. Sfh1 residues that are substituted by missense mutations in Sfh1* are shown as sticks. Water molecules are presented as red spheres. PtdCho is rendered in cyan as sticks and transparent spheres in the Sfh1-PtdCho structure (pdb 3B7Q, **B)**, while PtdIns is rendered in magenta as sticks and transparent spheres in the Sfh1-PtdIns structure (pdb 3B7N, **C**).

which resides in close proximity to Y_{113}. The $Q_{204}R$ substitution was also identified in the *SFH1** screen. As Sfh1^{Q204R} is unique among the Sfh1* in that it is far removed from the hydrophilic patch, details of its characterization will be presented elsewhere.

Incorporation of individual $Y_{109}C$, $Y_{109}H$, $Y_{109}F$ and $Y_{113}C$ substitutions into an otherwise wild-type Sfh1 protein demonstrated sufficiency of these substitutions for Sfh1* (Figure 2A). Since several substitutions at residue Y_{109} yielded Sfh1*, the analyses were extended by determining whether the $Y_{109}A$ substitution (a side-chain deletion) had the same effect. Indeed, $Y_{109}A$ conferred Sfh1* properties to an otherwise unadulterated Sfh1 (Figure 2A).

Since the $Y_{109} \rightarrow$ F, C, H, A and $Y_{113} \rightarrow$ C all represent Sfh1* substitutions, and all affect the enigmatic hydrophilic patch, we tested whether Sfh1^{E126A} and Sfh1^{Q111A} (i.e. substitutions not encountered in the original activation screen) similarly manifests Sfh1* properties when expressed from centromeric and episomal plasmids in *sec14-1^{ts}* and *sec14Δ* shuffle strains. Both Sfh1^{E126A} and Sfh1^{Q111A} scored as Sfh1*. Sfh1^{E126A} was particularly potent in this regard (Figure 2A). Sfh1^{Q111A} was less so -- primarily due to reduced stability of this protein (see below).

Characterization of Sec14-like activities in Sfh1* proteins.

Expression of any one of these *SFH1** gene products rescued robust growth of both a *sec14-1^{ts}* strain and its isogenic PLD-deficient derivative (*sec14-1^{ts} spo14Δ*) at the restrictive temperature of 37°C (Figure 2A). The ability of *SFH1** expression to effect phenotypic rescue of *sec14-1^{ts}* growth defects in the *spo14Δ* genetic background speaks to potency of the activation phenotype as PLD deficiency strongly exacerbates *sec14-1^{ts}*–associated growth phenotypes. By comparison, *SFH1* expression fails to rescue *sec14-1^{ts}* growth defects at 37°C – even after prolonged incubation (Figure 2A). The potencies of *SFH1** alleles were also apparent in plasmid shuffle assays that score their ability to restore viability to *sec14*Δ strains (Phillips et al., 1999; Experimental Procedures). Expression of *SFH1** from low-copy plasmids failed to support shuffle of YEp(*SEC14*), even when *SFH1** gene products with two independent activation substitutions were expressed (e.g. Sfh1^{Y109C,Y113C}). We tested 14 double mutant and 2 triple mutant combinations in this regard and, in no case, did we observe intragenic synergy between *SFH1** mutations (data not shown). While *SFH1* expression failed to support plasmid shuffle under any condition, shuffle of the YEp(*SEC14*) plasmid was observed when *SFH1** expression was driven under control of the powerful plasma membrane ATPase (*PMA1*) promoter from episomal vectors (Figure 2A).

*SFH1** protein expression from low copy plasmids supports protein accumulation to levels that do not exceed those of endogenous Sec14 (Supplemental Figure S2). Moreover, *SFH1* and *SFH1** gene products generally accumulated to comparable steady-state levels, demonstrating the *SFH1** phenotype is not a trivial result of increased protein expression or stability. Exceptions included Sfh1^{Y109A} and Sfh1^{Q111A} – both of which exhibited reduced protein stability at 37°C relative to Sfh1 (Supplemental Figure S2). This property is reflected in the modest Sfh1* phenotypes associated with Sfh1^{Q111A}. However, expression of Sfh1^{Q111A} rescues growth of *sec14-1^{ts}* yeast at 35°C (data not shown), and

rescues *sec14Δ* lethality when expressed from episomal expression plasmids (Figure 2A). The observation that $Y_{109}A$ effects a strong Sfh1* phenotype, despite reduced expression levels, testifies to its potency.

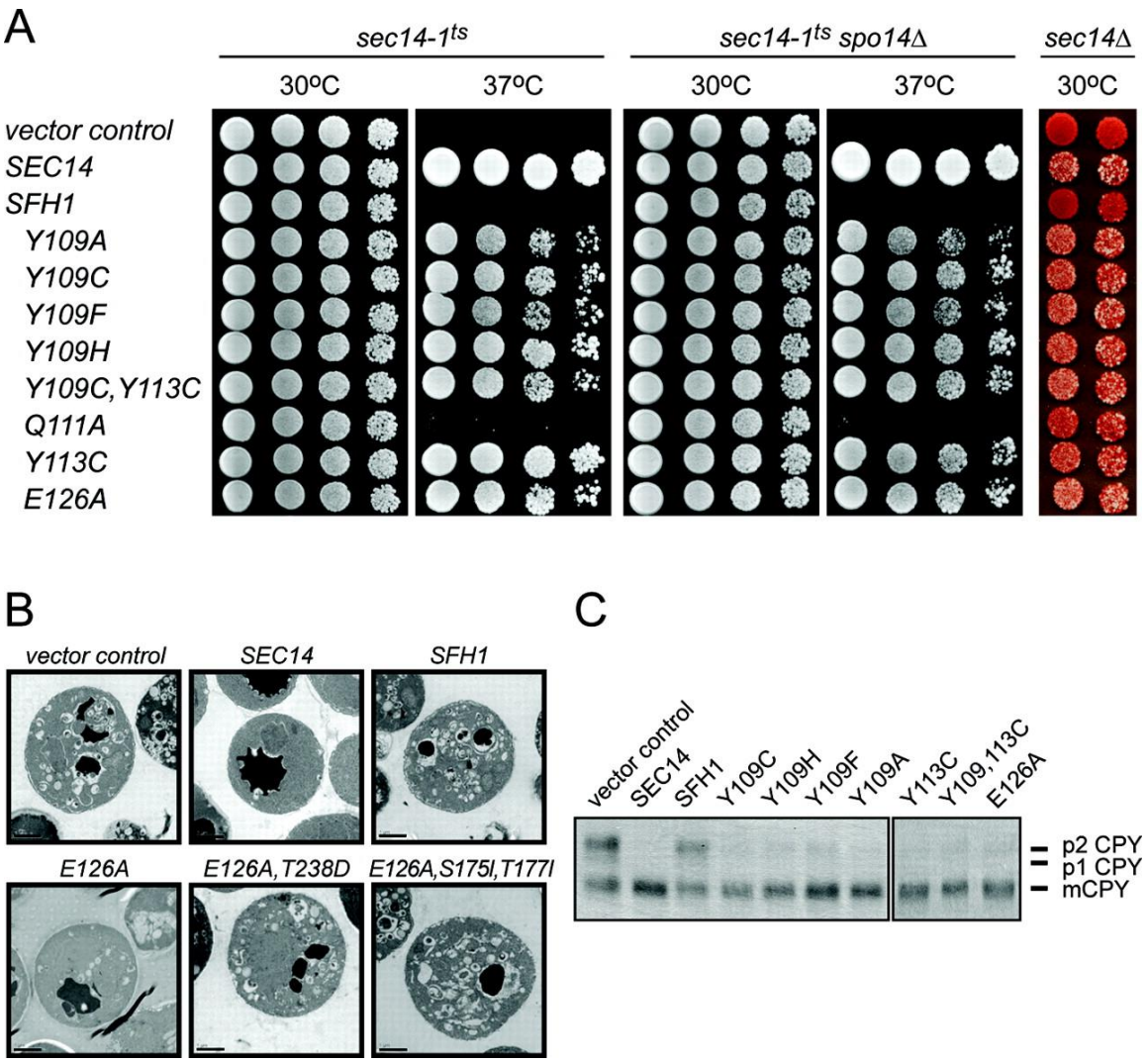

Figure 2. Functional characterization of Sfh1* proteins. **(A)** Left and middle panel, isogenic *sec14-1^{ts}* and *sec14-1^{ts} spo14Δ* yeast strains (as indicated on top) transformed with YCp(*URA3*) plasmids carrying either *SFH1* or the designated *SFH1** alleles were spotted in 8-fold serial dilutions onto YPD agar plates. Rescue at the restrictive temperature (37°C) report Sec14-like activity. YCp(*URA3*) and YCp(*SEC14, URA3*) plasmids served as negative and positive controls, respectively. Right panel, an *ade2 ade3 sec14Δ* yeast strain carrying a parental YEp(*SEC14, LEU2, ADE3*) plasmid (strain CTY558; see Experimental Procedures) was transformed with high-copy YEp(*URA3*) plasmids harboring *SFH1* or the designated *SFH1** alleles and dilution spotted onto YPD agar plates. Segregation with appearance of white colonies that acquire leucine and histidine auxotrophies, report loss of parental YEp(*SEC14, LEU2, ADE3*) and hence functionality of the mutant *SFH1** product. YEp(*URA3*) alone and YEp(*SEC14, URA3*) plasmids served as negative and positive controls, respectively. **(B)** Thin-section electron microscopy. A *sec14-1^{ts}* yeast strain (CTY1-1A) expressing the indicated gene (or allele) from a YCp vector was cultured in YPD medium at 30°C and subsequently shifted to the 37°C for 2 hrs. Cells were fixed, embedded in Spurr's resin, stained with uranyl acetate and imaged by transmission electron microscopy. Representative images are shown (bar = 1µm). **(C)** A *sec14-1^{ts}* yeast strain (CTY1-1A) carrying the indicated YCp expression plasmids was shifted to 37°C for 2 hr, and radiolabeled with [^{35}S] amino acids for 35 min followed by a 25 min chase. Immunoprecipitated CPY forms were separated by SDS-PAGE and visualized by autoradiography. Core glycosylated p1 CPY (diagnosing ER and early Golgi pools), TGN p2 CPY and vacuolar mCPY are identified at right.

Sfh1* expression and TGN/endosomal membrane trafficking.

Phenotypic rescue of Sec14 insufficiencies translates to enhanced ability of Sfh1* to execute Sec14-like functions in protein trafficking through the TGN/endosomal system. The accumulation of cytoplasmic toroid structures that represent defective cargo-laden TGN/endosomal compartments was readily apparent in thin-section electron micrographs of *sec14-1^{ts}* mutants incubated at restrictive temperatures, and Sfh1 expression failed to rescue this aberrant morphology (Figure 2B). By contrast, this morphological phenotype was alleviated in *sec14-1^{ts}* mutants by Sfh1^{Y109A}, Sfh1^{Y113C} or Sfh1^{E126A} expression. Moreover, introduction of the T_{238}D or S_{175}I,T_{177}I missense substitutions (which specifically compromise PtdIns- and PtdCho-binding, respectively; see below) functionally ablated the Sec14-like functions of these Sfh1* proteins.

Pulse-radiolabeling experiments demonstrate transit of CPY through the yeast secretory pathway to the vacuole is restored in Sec14-deficient cells by Sfh1* (Figure 2C). In a *sec14-1^{ts}* strain ectopically expressing Sfh1, pulse-radiolabeled CPY was recovered in approximately equimolar fractions as TGN/endosomal p2-CPY and mature vacuolar mCPY forms after a 25 min chase at 37°C. The persistence of p2-CPY post-chase reports a trafficking defect from TGN/endosomes to the vacuole. Cells reconstituted with physiological levels of Sec14 expression presented a single radiolabeled CPY species, the mCPY, under the same experimental conditions. Even modest Sfh1* expression was sufficient to yield CPY profiles that largely recapitulated those recorded for the Sec14-proficient condition. While a persistent p2-CPY fraction remained detectable in the face of Sfh1* expression, this fraction was reduced ca. 5-fold relative to that recorded in the face of ectopic Sfh1 expression (Figure 2C). The persistence of p2-CPY under conditions of low-copy plasmid-driven *SFH1** expression indicates the cognate gene products remain suboptimal Sec14 surrogates.

FM4-64 tracer experiments similarly demonstrated that Sfh1* are superior to Sfh1 in potentiating membrane flow through a Sec14-deficient endosomal system. Whereas Sec14-deficient cells internalize the lipophilic dye efficiently, these accumulate FM4-64 in punctate endosomal compartments and fail to chase the tracer into the vacuole (Figure 3). Reconstitution of Sec14-deficient cells with Sec14 rescued these defects. Significant delivery of FM4-64 to vacuolar compartments was already apparent by 7.5 min of chase, and the endosomal FM4-64 pool quantitatively trafficked to vacuoles during the 30 min chase (Figure 3). Sfh1 expression did not rescue FM4-64 delivery from endosomal compartments to the vacuole, but Sfh1^{Y109C}, Sfh1^{Y113C}, Sfh1^{Y109C,Y113C} or Sfh1^{E126A} expression supported an obvious (yet partial) improvement in dye trafficking from Sec14-deficient endosomes to the vacuole (Figure 3).

Sfh1* mutations increase Sfh1-mediated stimulation of PIP synthesis

Sfh1* competence in stimulating PIP production in vivo was quantified by reconstituting *SFH1** expression from low-copy vectors in a *sec14Δ cki1* 'bypass Sec14' yeast strain (see Experimental Procedures). This strain exhibits low basal PIP levels as a consequence of *sec14* nullizygosity (Phillips et al., 1999; Routt et al., 2005; Schaaf et al., 2008). Reconstitution of Sec14 expression elevates

PtdIns(3)P, PtdIns(4)P and PtdIns(4,5)P_2 levels by ca. 2-fold relative to the parental negative control (Figure 4A). While Sfh1 expression was ineffectual in this regard, even modest expression of Sfh1^{Y109A}, Sfh1^{Y113C} or Sfh1^{E126A} elevated PIP levels significantly (Figure 4A).

Similar conclusions were drawn from experiments where the influences of Sfh1* proteins and Sfh1 were compared in the isolated context of Stt4 PtdIns 4-OH kinase activity. To measure Sfh1*-mediated potentiation of specific yeast PtdIns 4-OH kinase activity in a native intracellular environment,

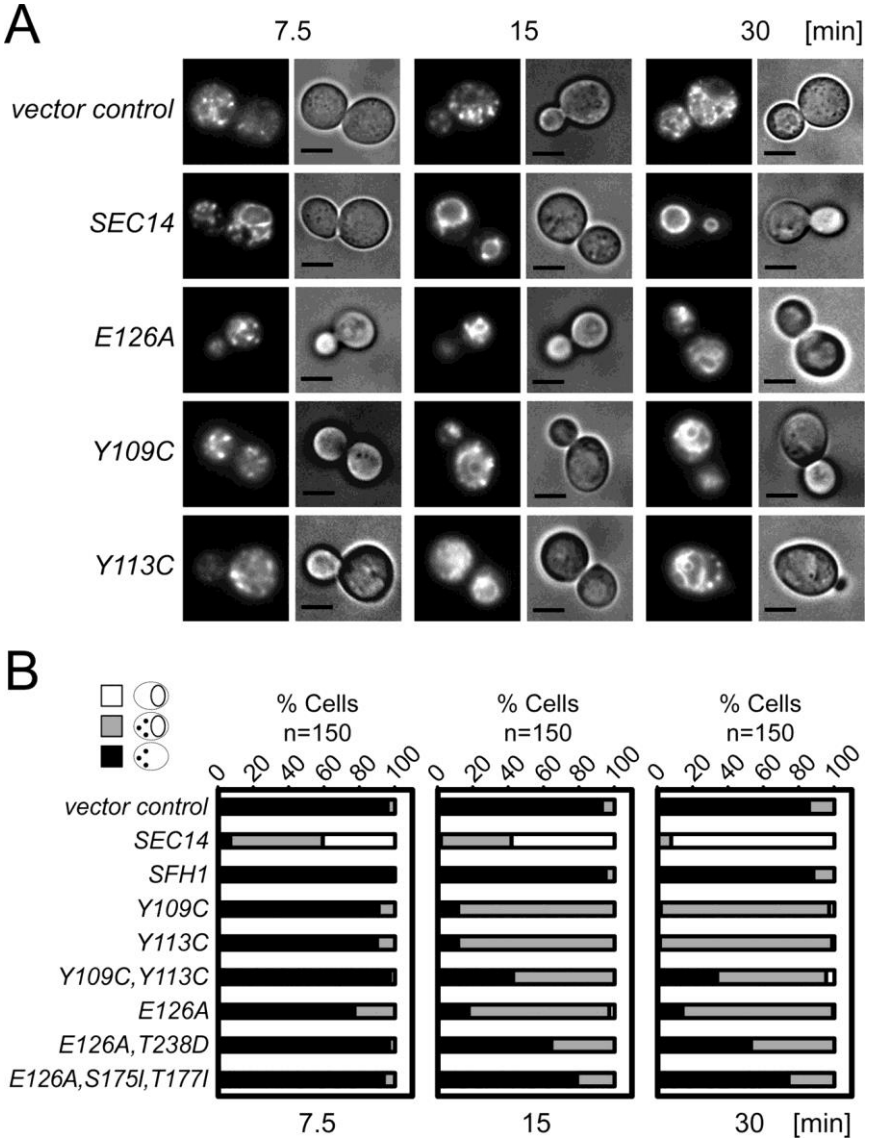

Figure 3. Sfh1* and endocytic membrane trafficking from the plasma membrane to the vacuole. A *sec14-1^{ts}* yeast strain (CTY1-1A) carrying the indicated YCp expression plasmids (at top) were cultured at 25°C to early-logarithmic growth phase in uracil-free minimal medium and shifted to 37°C for 2 h. Cells were then pulsed with FM4-64 (10 μM for 10 min), rapidly sedimented and reconstituted in fresh medium without FM4-64 to initiate chase. Aliquots were removed at the indicated times of chase, poisoned with an NaN_3/NaF cocktail (final concentration of 10 mM each), and kept on ice in the dark prior to visualization. FM4-64 profiles were imaged using a Nikon E600 fluorescence microscope. The YCp(*URA3*) and YCp(*SEC14*) conditions represent negative and positive controls, respectively. **(A)** Representative images are shown. Bar = 5 μm. **(B)** Distributions of imaging profiles (key shown at left) are quantified as % of total cells analyzed (150 for each condition). Quantitative chase of FM4-64 from the plasma membrane into the terminal vacuolar compartment is depicted in white, partial delivery in gray, and strictly endosomal localization of tracer in black.

[^{3}H]-Ins radiolabeling experiments were performed in *sec14-1^{ts} sac1* yeast strains expressing the Sfh1 proteins of interest. The *sec14-1^{ts} sac1* double mutants are defective in Sac1 PIP phosphatase activity, and exhibit a dramatic and selective expansion of the PtdIns(4)P pool generated by the Stt4 PtdIns 4-OH kinase (Guo et al., 1999; Rivas et al., 1999; Nemoto et al., 2000; Foti et al., 2001). Reconstitution of Sfh1^{Y109A}, Sfh1^{Y113C} or Sfh1^{E126A} expression in *sec14-1^{ts} sac1* mutants effected significant enhancements in PtdIns(4)P levels at 37°C (Figure 4B). PtdIns(4)P levels were indifferent to Sfh1 expression.

PtdIns- and PtdCho-binding are required for manifestation of SFH1* phenotypes

Individual PtdIns- and PtdCho-binding activities are essential for productive Sec14 biological activity, and these cooperate in stimulating PtdIns 4-OH kinase activity in vivo via a mechanism proposed to involve Sec14-mediated PtdIns-presentation to lipid kinase (Schaaf et al., 2008; Bankaitis et al., 2010). To determine whether PL-binding in general is required for elaboration of Sec14-like activities by Sfh1*, 'pinch-close' mutants that abrogate binding of all PLs were incorporated into the context of several SFH1* alleles. Residues L_{179}, I_{196} and V_{199} organize a region of the Sfh1 hydrophobic cavity which defines PtdCho and PtdIns acyl-chain-binding space. Thus, introduction of bulkier amino acids (e.g. W) at these positions results in steric incompatibility with PL-binding by Sfh1 or Sec14 (Schaaf et al. 2008). As expected, recombinant Sfh1^{Y113C,L179W,I196W} was defective in PL-transfer activity (Supplemental Figure S3A and B), and the triple mutant proteins were stable in vitro and in vivo (Supplemental Figure S3C and D). Neither expression of Sfh1^{Y113C,L179W,I196W}, nor of Sfh1^{Y113C,L179W,V199W}, rescued growth defects associated with the sec14-1^{ts} allele (Figure 4C). The Sfh1^{E126A} 'pinch-close' derivative was also generated, but this triple mutant protein was unstable in vivo (data not shown).

Incorporation of T_{238}D into the Sfh1* context, i.e. a substitution which specifically interferes with coordination of the PtdIns headgroup phosphate (Schaaf et al., 2008), evoked the expected ablation of PtdIns-transfer activity (Supplemental Figure S3A). Sfh1^{Y113C,T238D} and Sfh1^{E126A,T238D} were both stable polypeptides in vivo and in vitro (Supplemental Figure S3C and D), and expression of these proteins failed to rescue growth defects of *sec14-1^{ts}* yeast at restrictive temperatures (Figure 4C). Sfh1 residues S_{175} and T_{177} play important roles in coordinating the PtdCho headgroup phosphate within the Sfh1 binding pocket, and combinatorial substitution of these residues with bulky aliphatic amino acids (e.g. I) is nonpermissive for PtdCho-binding (Schaaf et al., 2008). The PtdCho-binding-deficient derivatives of both Sfh1^{Y113C} (Sfh1^{Y113C,S177I,T177I}) and Sfh1^{E126A} (Sfh1 ^{E126A,S175I,T177I}) were stable polypeptides (Supplemental Figure S3C and D), and in vitro PL-transfer assays confirmed the expected biochemical defects for these two proteins. Sfh1^{Y113C,S175I,T177I} exhibited a > 25-fold reduction in PtdCho-transfer activity relative to Sfh1^{Y113C} and retained PtdIns transfer activity (Supplemental Figure S3A and B). Expression of Sfh1^{Y113C,S175I,T177I} or Sfh1^{E126A,S175I,T177I} from low-copy vectors failed to rescue growth of *sec14-1^{ts}* strains at restrictive temperatures (Figure 4C).

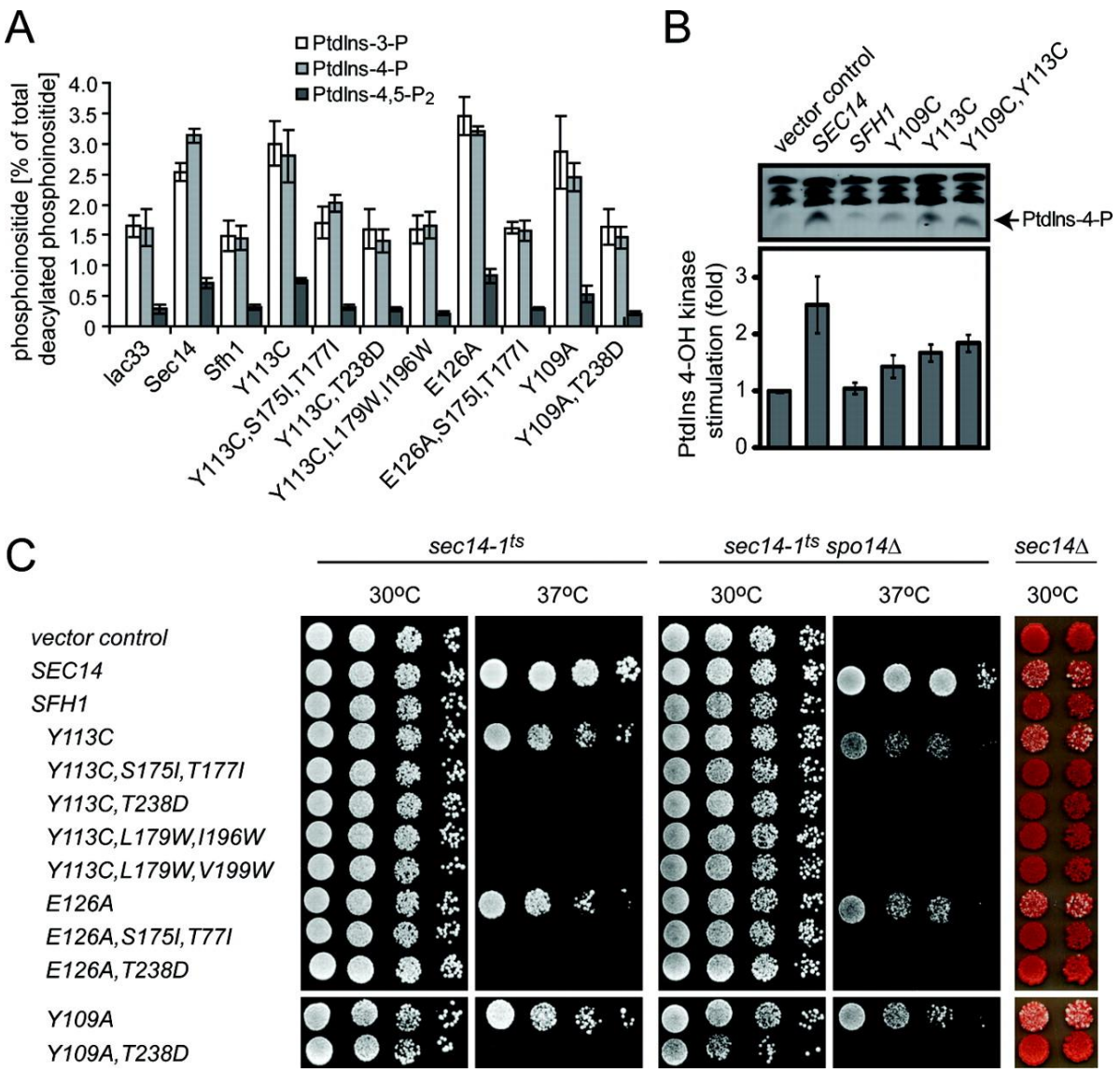

Figure 4. Potentiation of PtdIns 4-OH kinase activities. **(A)** The *sec14Δ cki1* 'bypass Sec14' yeast strain CTY303 was transformed with YCp(*URA3*) plasmids carrying *SEC14, SFH1* or the designated *SFH1** alleles. YCp(*URA3*) derivatives served as a negative control. Transformants were radiolabeled at 30°C for 12 hr with 20µCi/ml [^{3}H]-*myo*-inositol. Deacylated PIPs were separated by HPLC and quantified (see Experimental Procedures). PtdIns-3-P, PtdIns-4-P, and PtdIns(4,5)P_2 are indicated. Average values are and standard deviations are presented (n = 4). **(B)** Strain CTY100 (*sec14-1^{ts} sac1Δ*; Cleves et al., 1989) carrying YCp plasmids for expression of the indicated genes were radiolabeled to steady-state with [^{3}H]-inositol (Schaaf et al., 2008; Ile et al., 2010). After a 3 hour shift to 37ºC, phospholipids were extracted and resolved by thin layer chromatography (top panel). PtdIns-4-phosphate species is identified at left. The PtdIns-4-phosphate band intensities were measured by densitometry and expressed as a PtdIns-4-phosphate/PtdIns ratio for purposes of normalization. The normalized ratio was then compared to the URA3 control condition (set to 1.0 on the relative scale). The data represent the averages and standard deviations obtained from at least three independent experiments. **(C)** Left and middle panel, derivatives of isogenic *sec14-1^{ts}* and *sec14-1^{ts} spo14Δ* yeast strains (as indicated on top) carrying designated YCp(*URA3*) plasmids were spotted in 8-fold serial dilutions onto YPD agar plates. Complementation of growth defects at 37°C report Sec14-like in vivo function. Right panel, an *ade2 ade3 sec14Δ* yeast strain carrying a YEp(*SEC14, LEU2, ADE3*) plasmid (strain CTY558; see Experimental Procedures) was transformed with high-copy YEp(*URA3*) plasmids carrying *SFH1* or the designated *sfh1** alleles and dilution spotted onto YPD agar plates. Appearance of white segregant colonies that acquire leucine and histidine auxotrophies, report loss of parental YEp(*SEC14, LEU2, ADE3*) and hence indicate functionality of the mutant *SFH1** gene product.

Moreover, enhanced expression of Sfh1^{Y113C,S175I,T177I} or Sfh1^{E126A,S175I,T177I} driven by high-copy vectors failed to rescue lethality associated with the *sec14Δ* allele (Figure 4C).

The failures of the various PL-binding-defective variants of *SFH1** to rescue *sec14-1^{ts}*-associated growth defects translated to defects in regulation of PIP homeostasis. Stable variants of Sfh1* impaired for PL binding (Sfh1^{Y113C,L179W,I196W}), specifically defective in either PtdCho-binding (Sfh1^{Y113C,S177I,T177I} and Sfh1^{E126A,S177I,T177I}), or specifically defective in PtdIns-binding (Sfh1^{Y113C,T238D} and Sfh1^{E126A,T238D}), were all incompetent for augmentation of PtdIns(3)P, PtdIns(4)P or PtdIns(4,5)P_2 production in the *sec14Δ cki1Δ* yeast strain (Figure 4A). As expected, in every case, PtdIns- and PtdCho-binding were each individually required for Sfh1*-dependent rescue of CPY transit through the TGN/endosomal system (data not shown).

SFH1* alleles and polar interactions in the hydrophilic microenvironment

The data suggest a relationship between Sfh1* mechanisms and the functional status of the enigmatic hydrophilic patch. The Y_{109} → F, C, H, A, the Q_{111}→ A, the Y_{113}→ C, and the E_{126}→ A Sfh1* substitutions are all predicted to weaken polar contacts within this polar motif. In this regard, the Y_{109}F substitution maintains the shape and size of the side chain but abolishes the ability to establish side chain hydrogen bonds by lack of the phenolic hydroxyl group. We therefore tested whether Sfh1* substitutions exhibited allele-specificities consistent with weakened polar interactions within this motif. Indeed, in contrast to the cognate Sfh1^{E126A} example, Sfh1^{E126D} (i.e. protein in which polar contacts within the hydrophilic patch are presumably conserved) presented severely attenuated Sfh1* phenotypes -- despite its in vivo stability (Supplemental Figure S4A and B). The residual Sfh1* character associated with the E_{126}D substitution suggests that the length of the side chain (and thus spacing within the hydrophilic patch) contributes to these polar interactions.

Sfh1 and Sec14 share substantial primary sequence conservation within the hydrophilic patch. Indeed, most residues within a 4Å radius of Sfh1 residue Y_{109} are conserved between the two proteins. These conservations include Sfh1 (Sec14) residues: A_{106} (A_{104}), K_{107} (K_{105}), Y_{109} (Y_{107}), P_{110} (P_{108}), Q_{111} (Q_{109}), E_{126} (E_{124}), E_{127} (E_{125}), L_{128} (L_{126}), M_{145} (M_{143}), and Y_{195} (Y_{193}). Sfh1^{Y195A} was of interest because the corresponding substitution interferes with cooperative interactions between residues Y_{195} and Y_{109} – i.e. interactions that organize polar contacts with ordered water in the hydrophilic patch. When tested in both high- and low-copy expression contexts, Sfh1^{Y195A} exhibited Sfh1* properties (data not shown). These results are congruent with the idea that strong polar interactions within the hydrophilic patch are incompatible with Sfh1*.

Primary sequence divergences between Sfh1 and Sec14 in the hydrophilic region include: L_{105} (I_{103}), M_{108} (F_{106}) and I_{131} (V_{129}). M_{108} was excluded from analysis because structural models indicate the side chain protrudes away from the hydrophilic surface and is not involved in the polar interactions of interest. By contrast, I_{131} (a residue identified as an Sfh1* hotspot; see above) lies close to the C_{11} and C_{18} positions of the PtdCho and PtdIns *sn*-2 acyl chains, respectively. I_{131} extends the hydrophilic patch boundary towards the headgroup-distal ends of bound PtdCho or PtdIns *sn*-1 and *sn*-2 acyl chains

(Supplemental Figure S4C). Sfh1^{I131V} expression rescued growth defects associated with *sec14-1^{ts}* and the isogenic *sec14-1^{ts} spo14Δ* double mutant (Supplemental Figure S4A).

Sfh1^{E126A} crystal structure

The crystal structure of Sfh1^{E126A} in complex with a bound 16:0/18:0 PtdEtn was determined to 1.8Å resolution (Supplemental Table S1). A structure was also solved for an Sfh1^{E126A}::PtdCho complex, but the resolution was inferior (2.8Å). For this reason, and because both amino-PLs occupy the same site within the Sfh1 hydrophobic pocket (Schaaf et al., 2008), the PtdEtn-bound complex was analyzed. Sfh1^{E126A}::PtdEtn displays the canonical closed conformation which superimposes onto the Sfh1::PtdEn structure with an r.m.s.d. of 0.15Å for all protein atoms. In the Sfh1::PtdEn complex, the E_{126} side-chain

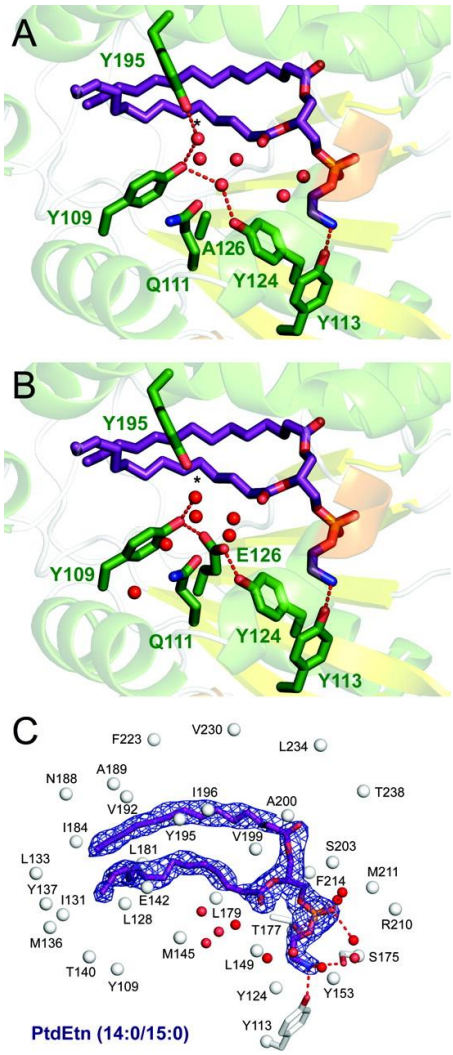

Figure 5. Crystal structure of Sfh1^{E126A} bound to PtdEtn. The hydrophilic patch in: **(A)** Sfh1^{E126A}::PtdEtn, and **(B)** Sfh1::PtdEtn (pdb 3B74). The patch is formed by residues Y_{109}, Q_{111}, Y_{113}, Y_{124} and E_{126}. The protein atoms are rendered as green sticks, bound PtdEtn is depicted as purple sticks, ordered waters are depicted as red spheres and H-bonds are shown as dashed lines. The *sn*-2 acyl chain C5 position is highlighted by *. **(C)** $2F_O - F_C$ composite omit electron density (contoured at 1σ) for the bound PtdEtn. Residues within 4.2 Å of the bound PL are shown as white spheres and waters are shown as red spheres. Residues that coordinate the headgroup moieties are shown as sticks with H-bonds represented as dashed lines.

makes direct contacts with Y_{109} and Y_{124}, and Y_{124} participates in an H-bond interaction with Q_{111} (Figure

5B). Atomic displacement parameters for these residues are 16.8, 17.2 and 16.9Å^2 in the Sfh1::PtdEn complex, and 17.7, 17.9 and 16.9Å^2 in the Sfh1^{E126A}::PtdEn complex, respectively. As in the Sfh1::PtdEn complex (Schaaf et al., 2008) PtdEtn is stabilized by 14 van der Waals interactions and coordinated via hydrogen bonds by residues Y_{113} and S_{175} and by one H_2O molecule (Figure 5C).

Inspection of the ligand-binding pocket reveals that the primary difference between Sfh1 and Sfh1^{E126A} is the configuration of ordered H_2O that fills the hydrophilic patch directly underneath the bound PL. In Sfh1, the E_{126} side-chain carboxylate moiety engages in strong H-bond interactions with residues Y_{109} and Y_{124} and is part of a larger H-bond network that extends to residue Y_{195} and involves another conserved H_2O. The E_{126} side-chain carboxylate interaction is replaced by an H_2O in the Sfh1^{E126A}::PtdEn complex (Figure 5A and B), a configuration that preserves the H-bonding network and hydrophilic character of this region of the hydrophobic pocket. The H_2O molecule coordinated by residues Y_{109} and Y_{195} displays atomic displacement parameters of 9.8 and 23.2 Å^2 in the Sfh1^{E126A}::PtdEn and Sfh1::PtdEtn complexes, respectively. These data report that E_{126}A causes a remarkably subtle destabilization of the hydrophilic patch and suggest altered water behavior in this region is a primary contributor to Sfh1* phenotypes (see below).

Sfh1* and PtdCho-binding/exchange.

While the structural data suggest E_{126}A relieves theY_{109} side-chain from its normally strong interaction with E_{126} in favor of an interaction with this newly positioned H_2O molecule, the nearly complete structural identity between Sfh1 and Sfh1^{E126A} otherwise offers little insight into why the E_{126}A resuscitates Sec14-like activities in Sfh1. One plausible mechanism is that Sfh1* are endowed with superior capacities to cycle PL into and out of the hydrophobic pocket. To monitor protein::PL interactions directly, continuous wave (CW) EPR spectroscopy was used to compare the parameters of PtdCho binding by Sfh1 and Sfh1*. Spin-labeled *n-doxyl*-PtdCho molecules were used to survey protein::PtdCho interactions across the lipid molecule. In these experiments, the EPR signal from liposomal *n-doxyl*-PtdCho species appears as a broad single line of ca. 25-27 G peak-to-peak width. Such a spectrum is readily modeled by a Lorentzian function and reflects the strong dipole-dipole and exchange interactions that occur when nitroxide moieties are packed in close proximity. Upon sequestration of *n-doxyl*-PtdCho within the Sfh1 or Sfh1* lipid-binding cavity, spin-spin interactions between *n-doxyl*-PtdCho molecules are eliminated with the result that a sharper EPR spectrum is produced.

Figure 6A displays the CW X-band spectra recorded when individual *n-doxyl*-PtdCho species were incubated with Sfh1, Sfh1^{Y113C} or Sfh1^{E126A}. For all spin probe positions analyzed, the contribution of liposomal *n-doxyl*-PtdCho registered as a broad line most readily observed at the wings. Contributions from the liposomal *n-doxyl*-PtdCho were subtracted from the experimental spectra, yielding the component corresponding to protein-bound *n-doxyl*-PtdCho. Relative contributions from protein-bound and liposomal forms were quantified by a double integration of the corresponding spectral components. These analyses demonstrate Sfh1 fails to incorporate *5*- and *7-doxyl*-PtdCho, while only poor binding

was measured for the *10*- and *12-doxyl*-PtdCho -- only ca. 1-2% of the Sfh1 molecules incorporated those spin-labeled species (Figure 6A, left panel; Figure 6B). *16-doxyl*-PtdCho was also inefficiently incorporated by Sfh1. Some 20% of total Sfh1 loaded with this spin-labeled PtdCho. These X-band CW EPR data demonstrate Sfh1 exhibits poor loading capacities for all *n-doxyl*-PtdCho-binding substrates.

By contrast, both Sfh1* proteins showed enhanced capacities for *n-doxyl*-PtdCho incorporation. For Sfh1^{Y113C}, weak incorporation was observed for *5*- and *7-doxyl*-PtdCho (10-15% of total protein loaded), moderate incorporation was measured for *10*- and *12-doxyl*-PtdCho (30-40% of total protein loaded), and Sfh1^{Y113C} was quantitatively loaded with *16-doxyl*-PtdCho (Figure 6A, right panel; Figure

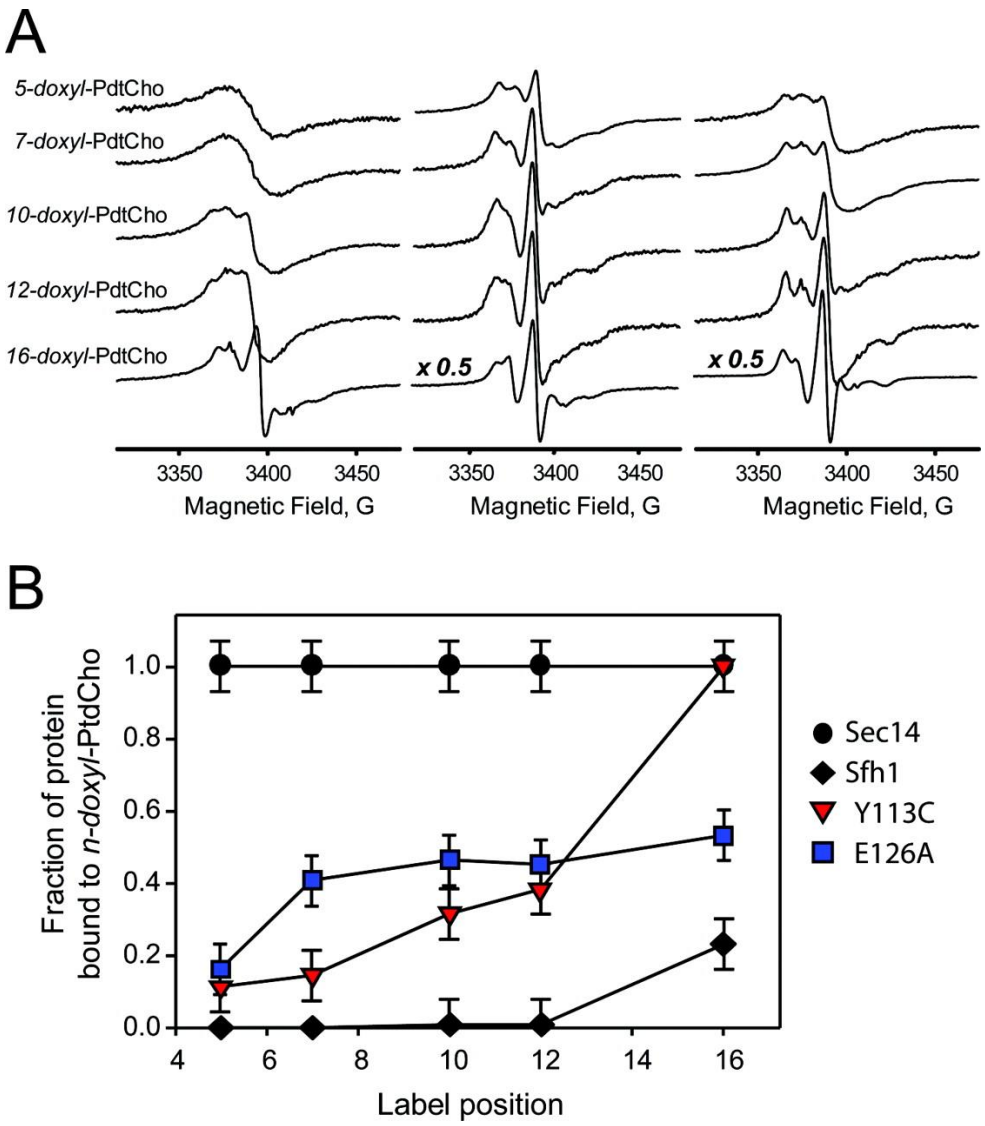

Figure 6. Spin-labeled PtdCho-binding parameters for Sfh1* proteins. **(A)** Room temperature (T=23°C) X-band CW EPR spectra from *n-doxyl*-PtdCho prepared as multilamellar lipid dispersion after mixing with Sfh1 protein and its mutants in approximately 2:1 lipid-to-protein molar ratio (left panel, Sfh1; central panel, Sfh1 ^{E126A}; right panel, Sfh1 ^{Y113C}). Modulation amplitude is 0.5 G, and spectra are intensity normalized using double integration. **(B)** Binding of of *n-doxyl*-PtdCho to protein as function of the label position along the *sn-2* acyl chain after mixing *n-doxyl*-PtdCho prepared as multilamellar lipid dispersion with proteins in approximately 2:1 lipid-to-protein molar ratio. Fraction of protein containing *n-doxyl*-PtdCho bound: circles, *n-doxyl*-PtdCho bound to Sec14; diamonds, *n-doxyl*-PtdCho bound to Sfh1; triangles, *n-doxyl*-PtdCho bound to Sfh1^{Y113C}; squares, *n-doxyl*-PtdCho bound to Sfh1^{E126A}.

6B). Sfh1^{E126A} was more impressive with regard to its capacity for *n-doxyl*-PtdCho incorporation. This protein was quantitatively occupied with *5-doxyl*-PtdCho, and demonstrated significant incorporation of *7-*, *10-*, *12-* and *16-doxyl*-PtdCho as well (40 to 50 % of total protein loaded across the range of probe positions; Figure 6A, central panel; Figure 6B). By comparison, Sec14 is quantitatively loaded with each of the *n-doxyl*-PtdCho species under these experimental conditions (Figure 6B; Smirnova et al, 2006; Smirnova et al, 2007). The acquired capability of Sfh1* to load with *n-doxyl*-PtdCho into the hydrophobic pocket is not likely due to relief of steric problems associated with accommodating the spin label within the hydrophobic pocket. The effects were scored even when spin-label position was physically distant from the operant Sfh1* substitution.

The EPR data project that Sfh1* substitutions are associated with enhanced cycling of PL into and out of the protein interior. We therefore expected that Sfh1* proteins would exhibit increased specific activities of PtdIns- and/or PtdCho-transfer relative to Sfh1. This prediction was tested by comparing the PtdIns- and PtdCho-transfer activities of Sfh1* to those of purified Sec14 and Sfh1. All proteins were stable during the course of the PL-transfer experiments (Supplemental Figure S3C) -- thereby permitting quantitative comparisons. His$_8$-Sec14 exhibited robust PtdIns- and PtdCho-transfer activities, whereas His$_8$-Sfh1 showed > 5-fold reductions in specific activities for PtdIns- and PtdCho-transfer relative to His$_8$-Sec14 (Supplemental Figure S3A and B). All three Sfh1* tested (His$_8$-Sfh1^{Y109A}, His$_8$-Sfh1^{Y113C} and His$_8$-Sfh1^{E126A}) presented increased PtdIns transfer activity relative to His$_8$-Sfh1. Similar outcomes were recorded for PtdCho-transfer activities of His$_8$-Sfh1^{Y109A} and His$_8$-Sfh1^{Y113C}. Both Sfh1* proteins exhibited a >5-fold increase in PtdCho-transfer relative to His$_8$-Sfh1. His$_8$-Sfh1^{E126A} presented a 2-fold increase in PtdCho-transfer activity relative to His$_8$-Sfh1 (Supplemental Figure S3A and B). Taken together, these data demonstrate Sfh1* exhibit significantly enhanced (i.e. Sec14-like) abilities to cycle PL from the lipid-binding pocket relative to Sfh1.

Molecular dynamics simulations.

Because the transition pathway between 'closed' and 'open' forms of the Sec14/Sfh1-fold that accompanies PL-exchange cannot be directly monitored experimentally, MD simulations were employed to model how Sfh1* conformational dynamics may differ from those of Sfh1 and more closely resemble those of Sec14. Unrestrained MD simulations were carried out with PL-bound Sfh1 and models of PL-bound Sec14, Sfh1^{Y109A}, Sfh1^{Y113C} and Sfh1^{E126A}. For the Sfh1^{E126A} ::PL structures PtdIns and PtdCho were modeled into the crystal structure of Sfh1^{E126A}::PtdEtn (see Supplemental Materials). Surveys of the rmsd values of backbone atoms in snapshots written every 2 ps, during the course of 3 independent simulations, indicated that all systems consistently reached equilibrium within the 14 ns production run (Supplemental Figure S5). All independent simulations exhibited fluctuations (Δ rmsd) < 0.8Å within the last 2 ns (12 ns-14 ns). Unless otherwise noted, this interval was analyzed.

The primary difference between Sfh1::PL structures and a previously crystallized apo-Sec14 is the repositioning of the Sfh1 A_9/T_3 structural element which controls access of PL to the hydrophobic pocket (A_{10}/T_4 in Sec14; Sha et al., 1998; Ryan et al., 2007; Schaaf et al., 2008). The large motions of

this helical gate, which occur in the transitions between 'open' and 'closed' Sec14 conformers, are essential for PL exchange and in vivo activity (Ryan et al., 2007). We were therefore interested in simulating the conformational transitions that occur when PL-bound Sec14, Sfh1 or Sfh1* are used as starting structures. To this end, root mean square fluctuations (rmsf) of Cα atoms of all protein residues were extracted from the MD simulations and analyzed. In the case where dynamics of the 'open' PL-free Sec14 starting structure were simulated, rmsf values exceeded 5 Å for helical gate residues $_{229}$KPFLD$_{233}$ (Ryan et al., 2007). The corresponding rmsf values for all PL-bound starting structures remained < 2.5 Å, however (Figure 7). Thus, the large conformational transitions required for PL exchange do not occur in PL-bound Sec14, Sfh1 or Sfh1* within the time frame of our MD simulations. This is not surprising given that the simulations were performed in a virtual aqueous environment with no membrane system to promote completion of the 'closed' to 'open' transition and to encourage egress of PL from the hydrophobic pocket.

Overall, Sec14-PL bound structures exhibited fluctuation profiles similar to those of their Sfh1 counterparts with rigid body motions of Sfh1 helices A_6, A_8 and A_9 (corresponding Sec14 helices are A_7, A_9 and A_{10}) (Figure 7). Fluctuations of the A_{10} element of the Sec14 helical gate were obviously larger in both the PtdIns and the PtdCho structures relative to fluctuations in the corresponding A_9 element of the Sfh1 and Sfh1* helical gate (Figure 7). Likewise, the Sec14 A_9 helix exhibited increased fluctuations in both PL-bound structures as compared to the corresponding helix A_8 in Sfh1 and Sfh1* -- with the exception that the Sfh1^{Y109A}::PtdCho complex also exhibited similarly enhanced fluctuations in the A_8 helix (Figure 7). Because Sfh1 helices A_8 and A_9 (Sec14 A_9 and A_{10}) are in intimate contact in the PL-bound conformation, we speculate increased fluctuations in Sfh1^{Y109A} helix A_8 reflect enhancements in the initial motions of the conformational transition that results in opening of the helical gate – thereby accounting for the strong Sfh1* phenotype associated with the Y_{109}A substitution (Figure 7).

The MD simulations also consistently identified common Sfh1*-specific and Sec14-like behaviors in key structural motifs. Sec14 residues $_{271}$DES$_{273}$ exhibit rmsf values of > 1.6Å in Sec14::PtdCho simulations. Interestingly, all Sfh1*::PtdCho simulations exhibited significantly enhanced fluctuations of the corresponding $_{273}$HNP$_{275}$ motif relative to the Sfh1::PtdCho control. The rmsf values for Sfh1^{Y109A} (1.9Å), Sfh1^{Y113C} (2.24Å) and Sfh1^{E126A} (1.6Å) are measured against rmsf values of < 1.4Å for this motif when Sfh1::PtdCho was used as starting structure. These findings are of particular interest because: (i) conformational transitions involving this specific motif closely correlate with dynamics of the helical gate in the 'open' PL free Sec14 structure (Ryan et al., 2007), and (ii) this element lies in immediate proximity to the Sec14 G_{266}D (i.e. *sec14-1^{ts}*) missense substitution (G_{268} in

Sfh1) which ablates both in vitro PL-exchange activity and in vivo Sec14 function at restrictive temperatures (Ryan et al., 2007).

Altered interactions between the B_1LB_2 and the $A_{11}LT_4$ substructures in Sfh1*

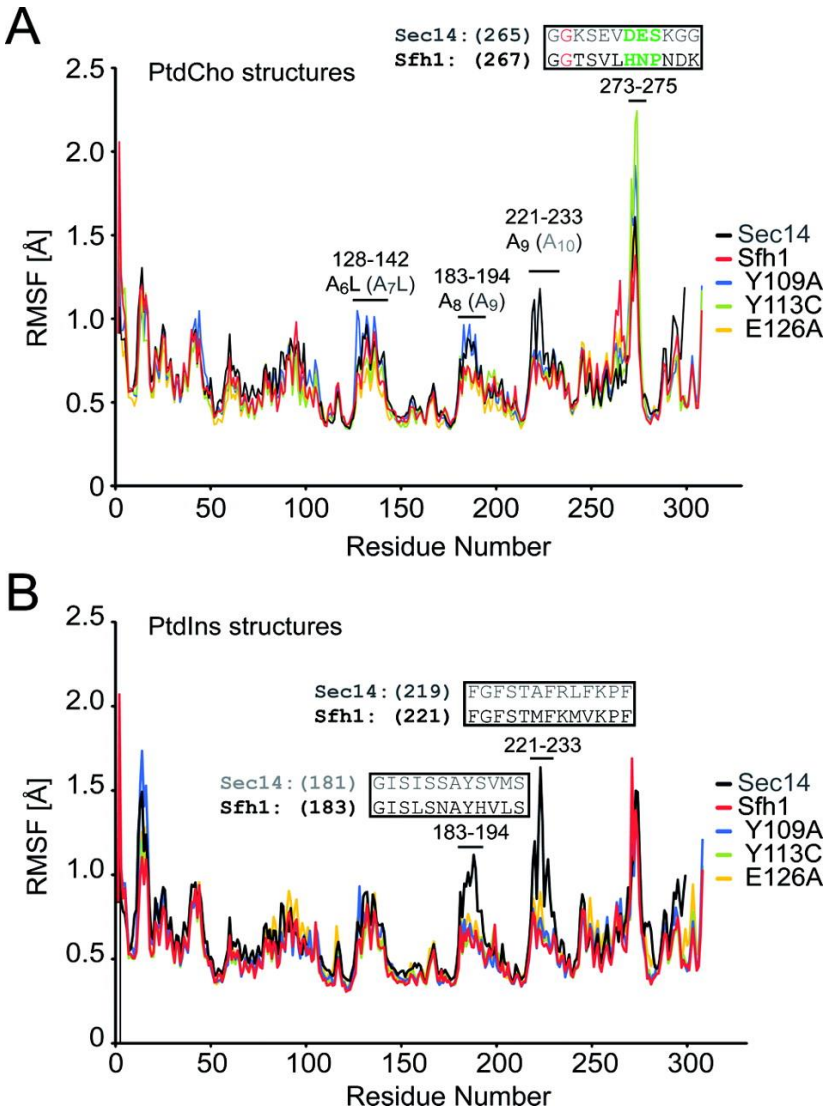

Figure 7. Conformational transitions of PL-bound structures. (**A and B**) Root mean square fluctuation (rmsf) values of Cα atoms of all protein residues were extracted from MD simulations of PtdCho (**A**) and PtdIns structures (**B**). Average Cα atomic position fluctuations from three simulations are plotted as a function of residue number (N to C terminus) for Sec14-PL, Sfh1-PL and Sfh1*-PL (colors as indicated). Selected regions of high mobility are highlighted in black letters (Sfh1 and Sfh1*) or grey letters (Sec14). Sec14 residue G_{266} and corresponding Sfh1 residue G_{268} are depicted in red, the Sec14 $_{271}DES_{273}$ motif and corresponding Sfh1 $_{273}HNP_{275}$ motif are depicted in green (**A**).

The Sec14 B_1LB_2 and $A_{12}LT_5$ substructures comprise a 'gating module' which transduces conformational information to the $A_{10}T_4A_{11}$ helical gate via an extensive H-bond network. The $_{114}TDKDGR_{119}$ component of the B_1LB_2 element plays a particularly important role in that conformational coupling (Ryan et al., 2007). The corresponding gating module elements in Sfh1 are B_1LB_2 (including the $_{116}VDKDGR_{121}$ component) and $A_{11}LT_4$. Strikingly, the core Sfh1* residues lie immediately C-terminal (Y_{109}) to or within (Q_{111}, Y_{113} and E_{126}) the B_1LB_2 element, and these residues

flank the $_{116}$VDKDGR$_{121}$ component. To investigate whether the H-bonding network of residues comprising the hydrophilic patch is functionally involved in the Sfh1* phenotype, we searched for altered H-bond interactions in this network in the context of Sfh1*. Alterations of interest were defined by consistent absolute values of change of >10% occupancy (i.e. the percent of time an individual hydrogen bond is present) in all Sfh1* mutants relative to Sfh1. In the Sfh1::PtdCho complex, 48 residues are in H-bond contact with the core Sfh1* residues (Supplemental Figure S6). Additional H-bond interactions are observed with residues of the A_7LA_8 helical motif and residues of the C-terminal string motif (Supplemental Figure S6).

Increased H-bonding occupancy was consistently recorded in all Sfh1*::PtdCho simulations for 5 H-bond pairs. The most dramatic increase of H-bonding was observed for the interaction of the E_{126} backbone with the phenolic –OH group of Y_{266}. While the occupancy in Sfh1::PtdCho simulations was < 9.5%, it increased to 48% and 49% in the Sfh1^{Y109C} and Sfh1^{Y113C} contexts, respectively. The backbone H-bonding interaction between residue A_{126} and Y_{266} in Sfh1^{E126A} likewise exhibited a significant increase to 21% occupancy (Supplemental Table S2). The neighboring E_{127}-K_{265} side chain interaction also increased robustly in all Sfh1* simulations. While the side chain interaction showed an occupancy of 75% in the Sfh1::PtdCho context, this value increased to 95%, 88% and 97% in the corresponding Sfh1^{Y109C}, Sfh1^{Y113C} and Sfh1^{E126A} simulations, respectively (Supplemental Table S2). These data signify increased interactions between the C-terminal region of B_2 and the T_4 in the Sfh1*::PtdCho structures (Figure 8A; Supplemental Figure S6). Two potential consequences of those increased interactions include: (i) the loop region between the B_1 and the B_2 strands undergoes conformational changes (as evidenced by increased H-bonding between loop residues D_{117} and R_{121} of the $_{116}$VDKDGR$_{121}$ component of the gating module -- Figure 8B; Supplemental Figure S6), and (ii) the unstructured regions that flank the T_4 are brought into closer proximity to each other as indicated by increased side chain interactions between E_{260} and S_{270} (Figure 8B and C; Supplemental Figure S6; Supplemental Table S2).

To address the functional relevance of the increased E_{126}-Y_{266} interaction the Y_{266}F and Y_{266}D substitutions were introduced into the context of Sfh1^{Y113C}. These substitutions were anticipated to ablate H-bonding by lack of the side chain H-donor (Y_{266}F) for interaction with the E_{126} backbone, or to cause an electrostatic clash (Y_{266}D) with the terminal carboxylate of the E_{127} side chain. Neither double mutant protein rescued *sec14-1^{ts}* associated growth defects -- even though the in vivo stability of each mutant polypeptide was preserved (Figure 8E). Thus, increased interaction between the N-terminal part of β-strand B_2 with the T_4 turn of substructure $A_{11}LT_4$ is a consistent, and functionally important, feature of the mechanisms underlying Sfh1*.

Consistent alterations in the H-bond network between the B_1LB_2 and $A_{11}LT_4$ structural elements

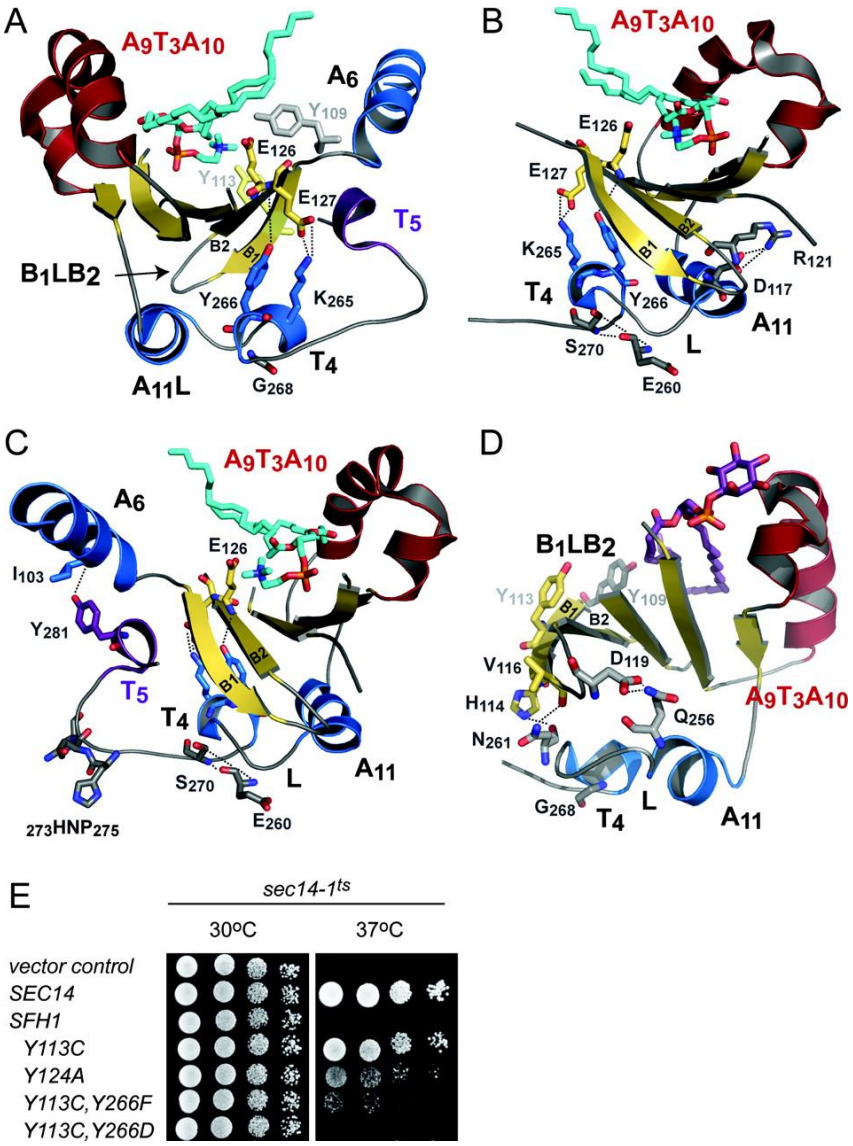

Figure 8. Model of Sfh1*-dependent alterations in H-bonding. (**A-D**) Ribbon diagrams illustrate H-bonds that are altered consistently in Sfh1* mutants relative to Sfh1 (see material and methods). The $A_9T_3A_{10}$ gating module is depicted in red; T_5 is depicted in magenta, all other α-helices are presented in blue. Unstructured regions are in grey and β-strands are presented in yellow. PtdCho is shown as cyan stick (**A-B**) while PtdIns is rendered in magenta (**D**). Relevant H-bonds are presented as dashed lines. The B_1LB_2 substructure consists of β1- and β2 β-strands and the intervening loop region. The second substructure $A_{11}LT_4$ includes helix A_{11} and extends till helix T_4. Sfh1* mutants show increased interaction between the C-terminal part of the β2-strand and the T_4 turn (mediated by H-bonding pairs E_{126} -Y_{266} and E_{127} - K_{265}, **A**). Increased H-bonding between D_{117} and R_{121}, and between E_{260} and S_{270} are possible consequences of this interaction (**B**). Decreased H-bonding between I_{103} and Y_{281} provide a rational for increased fluctuations of the immediately N-terminally positioned $_{273}HNP_{275}$ motif in the MD simulations (**C**). Decreased H-bonding of $A_{11}LT_4$ loop residue N_{261} with H_{114} and V_{116} reduces interactions between the loop regions of the B_1LB_2 and $A_{11}LT_4$ substructures in Sfh1* mutants (**D**). (**E**) Serial dilution spotting of the *sec14-1*^{ts} yeast strain transformed with YCp(*URA3*) plasmids carrying either *SFH1* or the designated *sfh1** alleles on YPD agar plates. Rescue at 37°C reports Sec14-like activity. YCp(*URA3*) and YCp(*SEC14*, *URA3*) plasmids served as negative and positive controls, respectively.

were also recorded in Sfh1*::PtdIns simulations. Those alterations were characterized by reduced H-bonding occupancy between the loop regions of the B_1LB_2 and $A_{11}LT_4$ (Figure 8D; Supplemental Figure

S7). Both elements strongly interact with each other in Sfh1 via 4 H-bonds: (i) the imidazole NH of H_{114} interacting with the N_{261} carbonyl, (ii) a Q_{256}-D_{119} side-chain interaction, (iii) a Q_{256}-D_{117} side-chain interaction, and (iv) interaction of the N_{261} side-chain with the V_{116} carbonyl. Three of these four interactions (H_{114}-N_{261}; Q_{256}-D_{119}; V_{116}-N_{261}) are significantly reduced in Sfh1* (Supplemental Tables S2, S3). The latter two involve the $_{116}$VDKDGR$_{121}$ component of the gating module – again, emphasizing enhanced B_1LB_2 dynamics as a mechanistic feature of the Sfh1* phenotype.

A consistent Sfh1*-dependent decrease in H-bond occupancy was also recorded for the interaction of the side chain carboxylate of activation residue E_{126} with the phenolic hydroxyl group of Y_{124} (Supplemental Table S2). That the reduced H-bonding between these two residues contributes to the enhanced Sec14-like activities of Sfh1* is demonstrated by rescue of *sec14-1^{ts}*-associated growth defects by Sfh1^{Y124A} expression (Figure 8E) – even though Sfh1^{Y124A} shows decreased stability in vivo (data not shown).

Sfh1* enhance conformational fluctuations of the helical gate.

To assess the effects of Sfh1*-dependent alterations in the H-bond network (which connects the B_1LB_2 and the $A_{11}LT_4$ substructures) on the dynamics of the helical gate, the inter-atomic distances between the Cα atoms of Y_{190} (A_8) and T_{225} (A_9) were monitored in Sec14::PtdIns, Sfh1::PtdIns and Sfh1*::PtdIns structures – as were inter-atomic distances between Cα atoms of K_{197} (A_8) and F_{233} (A_9; Figure 9A). Variations in this latter inter-atomic distance are useful for distance-monitoring analyses that report opening and closing of the helical gate in the apo-Sec14 molecule (residues K_{195} and F_{231} in that context; Ryan et al., 2007). In agreement with the rmsf plots (Figure 7), Y_{190}-T_{225} Cα distance fluctuations were larger than those recorded for K_{197}-F_{233} (Figure 9B and C) -- suggesting that initial helical gate movements in the PtdIns-occupied polypeptides are mostly restricted to the C-terminal regions of helices A_9 and A_8. Interestingly, while rmsf values of A_9 and A_8 residues were indistinguishable between Sfh1 and Sfh1* (except for Sfh1^{Y109A}, Figure 7), average fluctuations in the inter-atomic Y_{190}-T_{225} Cα distance were enhanced in all Sfh1*::PtdIns structures relative to the Sfh1::PtdIns structure (Figure 9B and C). These findings project that fluctuations in an Sfh1* context uniquely and productively translate into increased rigid body motions of helix A_9 . These behaviors correlate Sfh1* with increased conformational fibrillations of the helical gate -- suggesting a primary mechanism for Sfh1* is a lowering of the energy barrier for initiating the ‘closed’-to-‘open’ transition necessary to facilitate PL exchange.

Discussion

An understanding of the mechanisms by which Sec14-like PITPs integrate lipid metabolism with PIP signaling requires a detailed description of the mechanics by which these proteins execute

heterotypic PL-exchange. This information is of central importance given PL-exchange lies at the heart

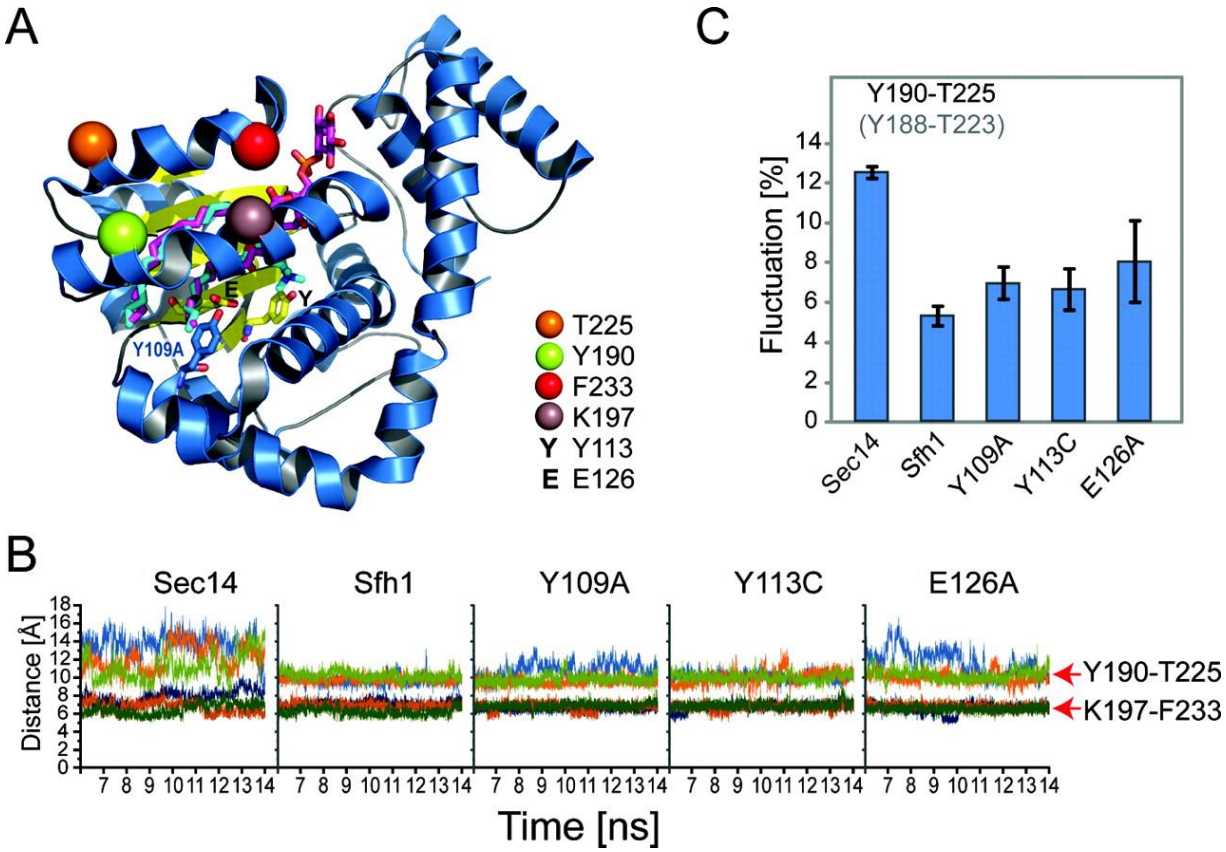

Figure 9. Helical gate motions and Sfh1*. **(A)** Ribbon diagram highlighting the positions of residues T_{225} (orange), Y_{190} (green), F_{233} (red) and K_{197} (purple) in the composite structure derived from crystals containing both Sfh1::PtdIns and Sfh1::PtdCho unit cells (pdb 3B7Z). **(B)** Plots monitoring the distances between the Cα atoms of residue pairs Y_{190}-T_{225} and K_{197}-F_{233} (as indicated in line charts). The last 8 ns of three independent simulations are shown in blue, orange and green, respectively. Data obtained from PtdIns-bound starting structures of Sec14, Sfh1, Sfh1^{Y109A}, Sfh1^{Y113C} and Sfh1^{E126A} are presented. Distances are given as a function of time (nanoseconds). **(C)** Distance fluctuations were calculated as relative standard deviation of Cα atomic distances for residue pairs Y_{190}-T_{225} (left panel) and K_{197}-F_{233} (right panel). Averages and standard errors of fluctuations of 3 independent simulations are presented. Calculations from simulations using the PtdIns-bound starting structures of Sec14, Sfh1, Sfh1^{Y109A}, Sfh1^{Y113C} and Sfh1^{E126A} are shown.

of the mechanisms by which these proteins stimulate the activities of PtdIns kinases in vivo (Schaaf et al., 2008; Bankaitis et al., 2010). Such questions assume larger significance given the broad conservation, across the Sec14-superfamily, of the structural elements that control ligand-cycling into/from the protein interior – including cases of Sec14-like proteins whose dysfunction results in human disease (Ryan et al., 2007; Schaaf et al., 2008; Bankaitis et al., 2010). The available data suggest that the dynamics which govern the intra-molecular motions (and biological activities) of Sec14-like proteins share general mechanistic principles. These dynamics are complex, and involve coordination of chemical interactions on the protein surface (e.g. membrane binding), with those in the protein interior (e.g. with bound PL), and with the conformational transitions that gate access to the ligand-binding pocket. At present, we have no clear appreciation of the rules which govern the functional dynamics of Sec14-superfamily proteins. Herein, we describe how Sec14-like functions are activated in the natural

pseudo-Sec14 (Sfh1). The directed evolution approach employed in this study yielded gain-of-function Sfh1 derivatives. These Sfh1* provide a novel prism through which the functional engineering of a Sec14-like protein can be observed. The concepts culled from these analyses are invisible to standard bioinformatic, crystallographic and rational mutagenesis approaches.

We reach five major conclusions in this study: **(1)** Single residue substitutions are sufficient to endow Sfh1 with significantly enhanced abilities for promoting Sec14-dependent membrane trafficking events, and for stimulation of PtdIns 4-OH kinase activities in vivo. These substitutions show an informative allele-specificity. **(2)** Missense substitutions that produce Sfh1* involve residues conserved between Sec14 and Sfh1. Most of these residues cluster in an enigmatic hydrophilic microenvironment buried deep within the Sfh1 (and Sec14) hydrophobic pocket. **(3)** Both PtdIns- and PtdCho-binding are required for Sfh1*-mediated potentiation of PtdIns 4-OH kinase activity in vivo -- indicating Sfh1* must execute heterotypic PtdIns/PtdCho-exchange reactions for productive biological function. **(4)** Sfh1* are associated with increased cycling of PL into and out of the protein interior. **(5)** MD simulations project Sfh1* facilitate a network of conformational transitions that enhance the dynamics of the helical substructure which gates the hydrophobic pocket. The collective results indicate Sfh1 is a pseudo-Sec14 because it cannot efficiently propagate the intramolecular conformational transitions which support the robust heterotypic PL-exchange required for potentiation of PtdIns 4-OH kinase activity in vivo. These data also reveal mechanisms for how such transitions can be restored.

Kinetic basis for mechanism of Sfh1*

Because no intragenic synergies in potency of *SFH1** phenotypes were observed (i.e. in combinatorial arrangements of the mutations studied in this report), we suggest a common activation mechanism is involved in the Sfh1* examples highlighted here. Furthermore, the data point to a kinetic basis for the Sfh1* activation mechanism rather than a thermodynamic one. Our previous experiments demonstrated that Sfh1 is able to quantitatively load with PtdIns or PtdCho under thermodynamically controlled (i.e. equilibrium) conditions (Schaaf et al., 2008). Yet, we demonstrate enhanced PL-cycling is a feature of the Sfh1* mechanism, and MD simulations indicate increased frequencies of helical gate opening (Figure 9). These independent analyses are both consistent with models where PL-exchange is kinetically favored in Sfh1* contexts. Finally, we calculated free binding enthalpies for Sec14, Sfh1, Sfh1^{Y109A}, Sfh1^{Y113C} and Sfh1^{E126A} considering internal energies (bonds, angle and torsion), van der Waals and electrostatic energies, nonpolar and electrostatic contributions to the solvation free energy, and contributions from the gas phase (see Supplemental Material and Methods). The relative protein-PL binding enthalpies calculated from MD simulations indicated the binding affinities of Sfh1, Sfh1* and Sec14 for PtdIns were significantly stronger than for PtdCho (Supplemental Figure S8A). However, no significant Sfh1*-specific differences were discerned between binding enthalpies for the PtdIns- or PtdCho structures.

Functional connectivity between the hydrophilic microenvironment and the helical gate.

The hydrophilic patch residues whose alteration generates Sfh1* (i.e. Y_{109}, Q_{111}, Y_{113}, E_{126}) reside in, or lie immediately adjacent to the B_1LB_2 -- i.e. one of the two substructures that define a critical conformational element termed the gating module (G-module; Ryan et al., 2007). As such, these directly influence the very elements which conduct propagation of conformational energy between the hydrophobic pocket floor and the helical substructure that gates access to the Sfh1 hydrophobic pocket. High resolution structural data demonstrate the Sfh1* substitutions effect a remarkably subtle rearrangement of the hydrophilic microenvironment. However, both structural analyses and MD simulations indicate Sfh1* reconfigure interactions between side-chains and ordered H_2O molecules in this region. Analyses of the 'gain-of-function' Sfh1* substitutions demonstrate that the interaction between the C-terminal region of strand B_2 (residues E_{126}, E_{127}) with the T_4 turn in the string motif (residues K_{265}, Y_{266}) is critical for the Sfh* phenotype. By contrast, strong interactions between the loop regions of the B_1LB_2 (H_{114}, V_{116}, D_{119}) and $A_{11}LT_4$ (Q_{256}, N_{261}) substructures are incompatible with Sfh1*.

A role of buried water?

The fact that Sfh1* substitutions involve Sfh1 residues which are conserved with Sec14 highlights the limitations of primary sequence alignments, with or without high resolution structural information, in annotating protein function or in determining dynamic aspects of protein function. The Sfh1* demonstrate that strong polar inter-side chain interactions (i.e. E_{126}-Y_{124}; E_{126}-Y_{109}) are incompatible with the conformational dynamics required for Sec14-like functions in the Sfh1 context. The collective data suggest that interactions of these key side-chains with water differ between Sfh1 and Sec14, and that internal waters play an important functional role in the regulation of H-bond interactions within the hydrophobic pocket.

While the hydrophobic PL-binding cavity would seem an unlikely environment for active water flux, fatty acid-binding proteins exhibit significant internal water rearrangements coincident with ligand binding and release (Lücke et al., 2002; Modig et al., 2003). The available evidence indicates this is also the case for Sec14/Sfh1. The internal water content of the hydrophobic pocket differs in the holo Sfh1::PtdIns and Sfh1::PtdCho complexes as a direct result of the differential PtdIns- and PtdCho-binding strategies, and water flux is suggested to contribute to the energetics which drive heterotypic PL-exchange (Schaaf et al., 2008). The hydrophilic microenvironment plays a central role in this flux as it organizes a network of coordinated waters with the Y_{109}, Q_{111}, Y_{124} and E_{126} side-chains playing primary roles (Schaaf et al., 2008, Figure 5B). Indeed, we find a surprisingly robust turnover of H_2O in this region (as defined in Supplemental Material and Methods, Supplemental Figure S8B) -- even after equilibrium conditions are reached (Supplemental Figure S8C). For instance, the average residence of H_2O molecules in the proximity of core Sfh1* residues within a 2 ns time window is < 51% and < 60% for Sfh1::PtdCho and Sfh1::PtdIns, respectively (Supplemental Figure S8C). These residence values are reduced to 25 % for the complete course of the 14 ns MD simulation (data not shown). Of note, the

variability of simulated H_2O turnover is both significantly and consistently increased in Sfh1* (Supplemental Figure S8C and D). While a functional role for internal water is an attractive idea, it remains to be determined whether increased fluctuations in water turnover are essential features of Sfh1* activation mechanisms. This remains an open question for future address.

Sec14 and Sfh1* -- like, yet unlike

Interestingly, Sfh1* do not precisely follow the Sec14 engineering blueprint for regulating their acquired Sec14-like conformational dynamics and activities. For example, decreased interactions of the T_4 turn with β-strand B_2 (i.e. $Y_{266}F$, $Y_{266}D$) are incompatible with Sfh1*. Yet, the corresponding Sec14 residue is F_{264} -- not Y_{264}. The F_{264} residue seemingly disqualifies Sec14 from coupling the conformational transitions of these two conserved substructures through the specific H-bonding mechanism utilized by Sfh1*. Employ of an alternative conformational coupling mechanism for biologically-sufficient rates of PL-exchange reports a significant plasticity for how functional re-activation can be achieved in operationally inactive Sec14-like proteins. Another line of evidence to that effect is provided by the $Q_{204}R$ Sfh1* substitution. Although not characterized in this report, $Sfh1^{Q204R}$ involves a residue spatially removed from the physically clustered Sfh1* residues upon which we focus here. The mechanism by which Sec14-like functions is resurrected in $Sfh1^{Q204R}$ is almost certainly distinct from the mechanism(s) which applies to Sfh1* substitutions which cluster in the hydrophilic microenvironment.

Finally, the results described in this report hold out the prospect that plasticity in conformational coupling can be employed for the purpose of bypassing the normal requirements for specific structural elements in Sec14 (or a model Sec14-like protein). This capability might have interesting applications. A number of inherited human disease mutations in proteins of the Sec14-superfamily compromise the G-module; i.e. the structural unit which transmits conformational information to the helical gate (Ryan et al., 2007). It might be feasible to 'reactivate' such mutant proteins with small molecules that reprogram the conformational transitions upon which the biological activity of the Sec14-like protein depends.

Materials and Methods

Yeast strains

Strains CTY182 (MATα *ura3-52 lys2-801 Δhis3-200*), CTY1-1A (MATα *ura3-52 lys2-801 Δhis3-200 sec14-1^{ts}*), CTY 100 (MATα *ura3-52 lys2-801 Δhis3-200 sec14-1^{ts} sac1-26*), CTY159 (MATα *ura3-52 lys2-801 Δhis3-200 sec14-1^{ts} kes1*) CTY1079 (MATα *ura3-52 lys2-801 Δhis3-200 sec14-1^{ts} spo14Δ::HIS3*), CTY1098 (MATα *ura3-52 lys2-801 Δhis3-200 sec14-1^{ts} kes1*), CTY303 (MATα *ura3-52 lys2-801 Δhis3-200 Δsec14, cki1::HIS3*) and CTY558 (MATα *ade2 ade3 leu2 Δhis3 ura3-52 sec14Δ1::HIS3 YEp*[*SEC14, LEU2, ADE3*]), BY4741 (MAT*α his3Δ1 leu2Δ0 met15Δ0 ura3Δ0*)

have been described previously (Cleves et al., 1991b; Fang et al., 1996; Xie et al., 1998; Phillips et al., 1999; Li et al., 2000; Euroscarf: http://web.uni-frankfurt.de/fb15/ mikro/euroscarf/index.html).

Reagents

Standard reagents were purchased from Sigma (St. Louis, MO) or Fisher (Pittsburgh, PA). All PLs – including nitroxide-labeled PtdCho species [1-acyl-2-(*n*-(4,4-dimethyloxazolidine-*N*-oxyl)stearoyl)-*sn*-glycero-3-phosphocholines; *n-doxyl*-PtdCho], with the doxyl label incorporated at *n* = 5, 7, 10, 12, or 16 of the *sn-2* acyl chain, were purchased from Avanti (Alabaster, AL). Monoclonal Anti-V5 antibodies were obtained from Invitrogen, Carlsbad, CA; secondary antibodies from Bio-Rad Laboratories, (Hercules, CA).

Media, genetic techniques and PL-transfer assays

Genetic methods, media, CPY pulse chase experiments, and PL-transfer assays have been described (Kearns et al., 1998; Phillips et al., 1999; Li et al., 2000; Yanagisawa et al., 2002; Schaaf et al., 2008). PIPs were extracted from yeast radiolabeled to steady-state with [^{3}H]-myo-inositol, deacylated, and glycero-inositol phosphate derivatives were resolved and quantified by anion-exchange chromatography (Guo et al., 1999; Rivas et al., 1999). Measurements of PtdIns(4)P produced specifically by the Stt4 PtdIns 4-OH kinase were performed using *sec14-1^{ts} sac1Δ* strains radiolabeled to steady-state with [^{3}H]-myo-inositol as previously described (Phillips et al., 1999; Schaaf et al., 2008; Ile et al., 2010).

Protein expression, purification and loading with PL

His_8-Sfh1^{E126A} was purified from *E. coli* as described previously (Schaaf et al., 2006; 2008). To obtain Sfh1^{E126A}::PtdCho complexes, 16:0/18:1 PtdCho dissolved in $CHCl_3$ was dried under N_2 in glass tubes. Lipid films were resuspended in 150 mM NaCl, 20 mM Tris pH 7.5 and sonicated until clear. Liposomes were incubated with 40:1 molar ratio of PtdCho::Sfh1^{E126A} for 1 hr at 37°C. Complexes were re-purified by binding and extensive washing on Talon cobalt-affinity resin (BD Biosciences, Clontech) followed by dialysis and gel filtration chromatography.

Crystallization and structure determination.

His_8-Sfh1^{E126A}::PtdEtn crystals were grown by sitting drop vapor diffusion at 22 °C from solutions containing 1.5 μL of protein at ~2.5 mg/mL (1.8 mg/mL) and 1.5 μL of crystallant: 25.5 % (w/v) PEG 4000, 11.9 % (v/v) glycerol and 170 mM sodium acetate, 85 mM Tris, pH7.5. Crystals were grown in cryoprotectant and flash-cooled in liquid N_2. Data to 1.8 Å resolution were collected at 100 K at the South East Regional Collaborative Access Team (SER-CAT) beamline at Argonne National Laboratory, and processed and scaled with HKL2000 (Otwinowski, 1993). Initial phases were determined using the Sfh1::PtdEtn structure (3B74) as a molecular replacement search model (Schaaf et al., 2008). Model building and refinement were performed using standard methods in Coot (Emsley

and Cowtan, 2004) and CCP4 (CCP4, 1994), respectively. The final model contains 1 His_8-$Sfh1^{E126A}$ monomer (residues 4 – 309) and 1 bound PtdEtn in the asymmetric unit.

Preparation of aqueous dispersion of n-doxyl-PtdCho and protein binding

Multilamellar aqueous dispersions of *n-doxyl*-PtdCho's were prepared in a phosphate pH 6.8 buffer as previously described (Smirnova et al., 2007). Loading of Sfh1 proteins with *n-doxyl*-PtdCho was achieved by mixing a 130 μM protein solution with two-fold molar excess of 100% spin-labeled multilamellar liposomes and incubating at room temperature till no changes in EPR spectra were observed. In case of Sfh1, the EPR signals were also recorded 2 days after the mixing to verify the absence of any slow binding events. Effective order parameter, S^{eff}, was calculated as described in (Schorn and Marsh, 1997):

$$S^{eff} = \frac{(A_{II} - A_{\perp})A_0}{\frac{1}{3}(A_{II} + 2A_{\perp})\Delta A} \qquad [1]$$

where $A_{II} = A_{out}$, *i.e.*, the outer hyperfine splitting, and $A_{\perp}$ is calculated from A_{in}, a half of the inner hyperfine splitting expressed in Gauss:

$$\begin{aligned} A_{\perp} &= (A_{in} + 0.85) \quad for\ S^{app} < 0.45 \\ A_{\perp} &= A_{in} + 1.32 + 1.86\log(1 - S^{app}) \quad for\ S^{app} > 0.45 \\ S^{app} &= (A_{out} - A_{in}) / \Delta A \end{aligned} \qquad [2]$$

where A_0 is the isotropic nitrogen hyperfine coupling constant and ΔA is the maximum extent of the axial nitrogen hyperfine anisotropy. Although previously we have shown that the values of ΔA and A_0 can vary with position of the label along the *sn*-2 acyl chain for Sec14p-bound *n-doxyl*-PtdCho, we used the same values A_0 and ΔA for all *n-doxyl*-PtdCho-protein complexes. A_0 and ΔA were set to those measured for *5-doxyl*-PtdCho in isopropanol (Smirnova et al., 2007).

EPR spectroscopy and spectral analysis.

Continuous wave X-band (9.0-9.5 GHz) EPR spectra were acquired with a Century Series Varian E-109 (Varian Associates, Palo Alto, CA) EPR spectrometer and digitized to 2048 data points per spectrum. Spectrometer settings were: microwave power 2 mW, magnetic field modulation frequency was 100 kHz with <1 G amplitude to avoid over-modulation, magnetic field scan was 160 G. Sample temperature was 23.0 ± 0.1°C controlled by a home-built variable temperature system (Alaouie and Smirnov, 2006).

Supplemental information

Supplemental information includes eight figures and three tables and is available at http://www.ncbi.nlm.nih.gov/pmc/articles/PMC3057712/bin/E10-11-0903_index.html.

Acknowledgements

This work was supported by grant GM44530 from the National Institutes of Health to V.A.B., and it supported the efforts of G.S., C.J.M., S.D.S, P.Y. K.T., and L.L.Y. G.S., M.D., E.M.W., and M.K.F.C. are supported by grants SCHA 1274/1-1 and Emmy Noether grant 1274/2-1 from the Deutsche Forschungsgemeinschaft, T.S. and M.C.Q. are supported by NSF-0843632, and E.O. is supported by Emory University Start-up Funds. We acknowledge the UNC Lineberger Comprehensive Cancer Center Genome Analysis and Nucleic Acids Core facilities. We also thank *bwGrid*, member of the German D-Grid initiative, founded by the Ministry for Education and Research and the Ministry for Science, Research and Arts Baden-Württemberg, for providing computational resources (http://www.bw-grid.de). Contact information for: MD simulation data (marek-dynowski@web.de); EPR data (tismirno@ncsu.edu), and structural determination (eric.ortlund@emory.edu).

Conflict of Interest

The authors declare no conflicts of interest.

Abbreviations used

CPY, carboxypeptidase Y; EPR, electron paramagnetic resonance; MD, molecular dynamics; PtdCho, phosphatidylcholine; PtdEtn, phosphatidylethanolamine; PtdIns, phosphatidylinositol; PIPs, phosphoinositides; PITP; PtdIns-transfer protein; PLD, phospholipase D; PL, phospholipid; rmsd, root mean square deviation; rmsf, root mean square fluctuation; TGN, trans-Golgi network.

References

Alaouie, A.M., Smirnov, A.I. (2006) Ultra-stable temperature control in EPR experiments: Thermodynamics of gel-to-liquid phase transition in spin-labeled PL bilayers and bilayer perturbations by spin labels. J. Mag. Res. *182*, 229-238.

Balla, T. (2005) Inositol-lipid binding motifs: signal integrators through protein–lipid and protein–protein interactions. J. Cell Sci. *118*, 2093–2104.

Bankaitis, V. A., Aitken, J. R., Cleves, A. E., and Dowhan, W. (1990). An essential role for a phospholipid transfer protein in yeast Golgi function. Nature *347*, 561-562.

Bankaitis, V.A., Mousley, C.J., and Schaaf, G. (2010) The Sec14-superfamily and mechanisms for crosstalk between lipid metabolism and lipid signaling. Trends in Biochem. Sci *35*, 150-160.

Benomar, M., Yahyaoui, F., Meggouh, A., Bouhouche, M., Boutchich, N., Bouslam, N., Zaim, A., Schmitt, M., Belaidi, H., Ouazzani, R., Chkili, T., and Koenig, M. (2002). Clinical comparison between AVED patients with 744 del A mutation and Friedreich ataxia with GAA expansion in 15 Moroccan families. J. Neurol. Sci. *198*, pp. 25–29.

Bomar, J.M., Benke, P.J., Slattery, E.L., Puttagunta, R., Taylor, L.P., Seong, E., Nystuen, A., Chen, W., Albin, R.L., Patel, P.D., *et al* (2003) Mutations in a novel gene encoding a CRAL-TRIO domain cause human Cayman ataxia and ataxia/dystonia in the jittery mouse. Nature Genetics *35*, 264-269.

Cleves, A.E., McGee, T. P., Whitters, E. A., Champion, K. M., Aitken, J. R., Dowhan, W., Goebl, M., Bankaitis, V.A. (1991b). Mutations in the CDP-choline pathway for phospholipid biosynthesis bypass the requirement for an essential phospholipid transfer protein. Cell *64*, 789–800.

Cleves, A.E., Novick P. J., Bankaitis, V.A. (1989). Mutations in the SAC1 gene suppress defects in yeast Golgi and yeast actin function. J. Cell Biol. *109*, 2939 - 2950.

D'Angelo, I., Welti, S., Bonneau, F., and Scheffzek, K 2006. A novel bipartite phospholipid-binding module in the neurofibromatosis type 1 protein. EMBO Rep. 7, 174-179.

Emsley, P. and Cowtan, K. (2004) Coot, model-building tools for molecular graphics. Acta Crystallographica D*60*, 2126-2132.

Fang, M., Kearns, B.G., Gedvilaite, A., Kagiwada, S., Kearns, M., Fung, M.K.Y., and Bankaitis, V.A. (1996) Kes1 shares homology with human oxysterol binding protein and participates in a novel regulatory pathway for yeast Golgi-derived transport vesicle biogensis. EMBO J. *15*, 6447–6459.

Foti, M., Audhya, A., Emr, S.D. (2001) Sac1 lipid phosphatase and Stt4 PtdIns-4-kinase regulate a pool of PtdIns(4)P pool that functions in control of the actin cytoskeleton and vacuole morphology. Mol. Biol. Cell 12, 2396-2411.

Fruman, D.A., Meyers, R.E., Cantley, L.C. (1998) Phoisphoinositide kinases. Annu. Rev. Biochem. *67*, 481-507.

Guo, S., Stolz, L.E., Lemrow, S.M., and York, J.D. (1999) SAC1-like domains of yeast SAC1, INP52, and INP53 and of human synaptojanin encode polyphosphoinositide phosphatases. J. Biol. Chem. *274*, 12990-12995.

Ile, K.E., Kassen, S., Cao, C., Vihtehlic, T., Shah, S.D., Huijbregts, R.P.H., Alb, J.G., Jr, Stearns, G.W., Brockerhoff, S.E., Hyde, D.R., and Bankaitis, V.A. (2010) The zebrafish class 1 phosphatidylinositol transfer protein family, PITPβ isoforms and double cone cell outer segment integrity in retina. Traffic *11*, 1151 - 1167.

Ile, K.E., Schaaf, G., and Bankaitis, V.A. (2006). Phosphatidylinositol transfer proteins and cellular nanoreactors for lipid signaling. Nature Chem. Biol. *2*, 576-583.

Kearns, M.A., Monks, D.E., Fang, M., Rivas, M.P., Courtney, P.D., Chen, J., Prestwich, G.D., Theibert, A.B., Dewey, R.E,., and Bankaitis, V.A. (1998) Novel developmentally regulated phosphoinositide binding proteins from soybean whose expression bypasses the requirement for an essential phosphatidylinositol transfer protein in yeast. EMBO J. *17*, 4004–4017.

Lemmon, M.A. (2008) Membrane recognition by phospholipid-binding domains. Nat Rev Mol Cell Biol *9*, 99-111.

Li, X., Routt, S., Xie, Z., Cui, X., Fang, M., Kearns, M.A., Bard, M., Kirsch, D., and Bankaitis, V.A. (2000) Identification of a novel family of nonclassical yeast PITPs whose function modulates activation of phospholipase D and Sec14p-independent cell growth. Mol Biol. Cell *11*, 1989-2005.

Lücke, C., Huang, S., Rademacher, M., and Rüterjans, H. (2002) New insights into intracellular lipid binding proteins, the role of buried water. Protein Sci. *11*, 2382-2392.

Majerus, P.W. (1997) Inositol phosphatases and kinases in cell signaling. FASEB J. 11, A1297.

McLaughlin, S., and Murray, D. (2005) Plasma membrane phosphoinositide organization by protein electrostatics. Nature *438*, 605-611.

Meier, R., Tomizaki, T., Schulze-Briese, C., Baumann, U., and Stocker, A. (2003). The molecular basis of vitamin E retention: structure of human tocopherol transfer protein. J. Mol. Biol. *331*, 725-734.

Modig, K., Rademacher, M., Lücke, C., and Halle, B. (2003) Water dynamics in the large cavity of three lipid-binding proteins monitored by 17O magnetic relaxation dispersion. J. Mol. Biol. *332*, 965–977.

Nemoto, Y., Kearns, B.G., Wenk, M.R., Chen, H., Mori, K., Alb, J.G., Jr., De Camilli, P., and Bankaitis VA (2000) Functional characterization of a mammalian Sac1 and mutants exhibiting substrate specific defects in PIP phosphatase activity. J. Biol. Chem. *275*, 14446-14456.

Ouachi, K., Arita, M., Kayden, H., Faycal, H., Hamida, M.B., Sokol, R., Arai, H., Inoue, K., Mandel, J.-L., and Koenig, M. 1995. Ataxia with vitamin E deficiency is caused by mutations in the α-tocopherol transfer protein. Nature Genetics *9*, 141-145.

Phillips, S. E., Sha, B., Topalof, L., Xie, Z., Alb, J. G., Klenchin, V. A., Swigart, P., Cockcroft, S., Martin, T. F. J., Luo, M., Bankaitis, V. A. (1999). Yeast Sec14p deficient in phosphatidylinositol transfer activity is functional in vivo. Mol. Cell. *4*, 187-197.

Rivas, M.P., Kearns, B.G., Xie, Z., Guo, S., Sekar, M.C., Hosaka, K., Kagiwada, S., York, J.D. and Bankaitis, V.A. (1999) Relationship between altered phospholipid metabolism, diacylglycerol, 'bypass Sec14', and the inositol auxotrophy of yeast sac1 mutants. Mol. Biol. Cell *10*, 2235-2250.

Routt, S.M., Ryan, M.M., Tyeryar, K., Rizzieri, K., Roumanie, O, Brennwald, P.J., and Bankaitis, V.A. (2005) Nonclassical PITPs activate phospholipase D via an Stt4p-dependent pathway and modulate function of late stages of the secretory pathway in vegetative yeast cells. Traffic *6*, 1157-1172.

Ryan, M.M., Temple, B.R.S., Phillips, S.E., and Bankaitis, V.A. (2007) Conformational dynamics of the major yeast phosphatidylinositol transfer protein Sec14: Insights into the mechanisms of PL exchange and diseases of Sec14-like protein deficiencies. Mol. Biol. Cell *18*, 1928-1942.

Schaaf, G., Betts, L., Garrett, T.A., Raetz, C.R.H., and Bankaitis, V.A. (2006). Crystallization and preliminary X-ray diffraction analysis of phospholipid-bound Sfh1p: A member of the *Saccharomyces cerevisiae* Sec14p-like phosphatidylinositol transfer protein family. Acta Crystallographica F *62*, 1156-1160.

Schaaf, G., Ortlund, E., Tyeryar, K., Mousley, C., Ile, K., Woolls, M., Garrett, T., Raetz, C.R.H., Redinbo, M., and Bankaitis, V.A. (2008) The functional anatomy of phospholipid binding and regulation of phosphoinositide homeostasis by proteins of the Sec14-superfamily. Molecular Cell *29*, 191-206.

Schorn, K. and Marsh, D. (1997) Extracting order parameters from powder EPR lineshapes for spin-labelled lipids in membranes. Spectrochimica Acta A. *53*, 2235-2240.

Sha, B., Phillips, S. E., Bankaitis, V. A., and Luo, M. (1998). Crystal structure of the *Saccharomyces cerevisiae* phosphatidylinositol transfer protein Sec14p. Nature *391*, 506-510.

Smirnova, T., Chadwick, T.G., MacArthur, R., Poluekov, O., Song, L., Ryan, M., Schaaf, G., and Bankaitis, V.A. (2006) The chemistry of PL binding by the *Saccharomyces cerevisiae* phosphatidylinositol transfer protein Sec14 as determined by electron paramagnetic resonance spectroscopy. J. Biol. Chem. *281*, 34897-34908.

Smirnova, T., Chadwick, T.G., van Tol, J., Ozarowski, A., Poluektov, O., Schaaf, G., Ryan, M.M., and Bankaitis, V.A. (2007) Local polarity and hydrogen bonding inside the Sec14 PL-binding cavity: High-field multifrequency studies. Biophys. J. *92*, 3686-3695.

Strahl, T., and Thorner, J. (2007) Synthesis and function of membrane phosphoinositides in budding yeast, *Saccharomyces cerevisiae*. Biochim. Biophys. Acta *1771*, 353-404.

Xie, Z., Fang, M., Rivas, M.P., Faulkner, A., Sternweis, P.C., Engebrecht, J., and Bankaitis, V.A. (1998) Phospholipase D activity is required for suppression of yeast phosphatidylinositol transfer protein defects. Proc. Natl. Acad. Sci. U.S.A. *95*, 12346-12351.

Yanagisawa, L., Marchena, J., Xie, Z., Li, X., Poon, P.P., Singer, R., Johnston, G., Randazzo, P.A., and Bankaitis, V.A. (2002). Activity of specific lipid-regulated ARFGAPs is required for Sec14p-dependent Golgi secretory function in yeast. Mol. Biol. Cell *13*, 2193-2206.

Supplementary Figure Legends

Supplementary Figure S1. *SFH1** activation alleles. Protein alignment of Sfh1* mutants obtained in the primary directed evolution screen. The sequence of the Sfh1 wild-type protein is presented on top for comparison. Two hot spots for *SFH1** activation alleles are apparent. One hot spot highlights Sfh1 residues Y_{109} and Y_{113}, while the other includes residues between Sfh1 residues I_{131} and T_{141}.

Supplementary Figure S2. Immunoblots of lysates prepared from *sec14Δ cki1* 'bypass Sec14' yeast transformants grown at 30°C (upper panel) and grown at 30°C followed by a 12 hr challenge at 37°C

(lower panel). Yeast transformants carried the designated YCp(*URA3*) plasmids allowing expression of C-terminally V5-tagged Sec14, Sfh1 and Sfh1*. Equal amounts of total protein were loaded, and V5-tagged proteins and Kes1 (normalization control) were visualized with monoclonal antibodies specific for each. Transformants carrying the YCp(*URA3*) plasmid alone served as a negative control.

Supplementary Figure S3. Biochemical properties of Sfh1* with defects in PL-binding.

(A and **B)** Purified recombinant Sec14, Sfh1, and mutant Sfh1 proteins were assayed in a step series of 5-fold mass increases (0.2, 1, and 5 µg) for PtdIns- **(A)** and PtdCho- **(B)** transfer activity. Average values and standard deviations are given (n=3). **(C)** Designated recombinant protein samples were incubated with membranes under conditions employed for the PtdIns transfer assay (see Supplemental Material and Methods) and then centrifuged at 20,800 x g for 10 min. Aliquots of supernatant were collected, resolved by SDS-PAGE and stained with Coomassie blue. Recombinant proteins employed for PL-transfer assays are stable and soluble as indicated by similar amounts of 'input' (recombinant protein prior to the PL-transfer reaction) and 'output' stain. **(D)** Immunoblots of lysates prepared from *sec14Δ cki1* 'bypass Sec14' yeast transformants grown at 30°C (upper panel) and grown at 30°C followed by a 12 hr challenge at 37°C (lower panel). Yeast transformants carried the designated YCp(*URA3*) plasmids allowing expression of C-terminally V5-tagged Sec14, Sfh1 and Sfh1*. Equal amounts of total protein were loaded, and V5-tagged proteins and Kes1 (normalization control) were visualized with monoclonal antibodies specific for each. Transformants carrying the YCp(*URA3*) plasmid alone served as a negative control.

Supplementary Figure S4. *SFH1** and allele-specificity. **(A)** Derivatives of isogenic *sec14-1^{ts}* and *sec14-1^{ts} spo14Δ* yeast strains transformed with designated YCp(*URA3*) plasmids were spotted in 8-fold serial dilutions onto YPD agar plates. Complementation of growth defects at 37°C report Sec14-like in vivo function (left and middle panel). Right panel, an *ade2 ade3 sec14Δ* yeast strain carrying a YEp(*SEC14, LEU2, ADE3*) plasmid (strain CTY558; see Experimental Procedures) was transformed with high-copy YEp(*URA3*) plasmids carrying *SFH1* or the designated *SFH1** alleles and spotted in 5-fold serial dilutions onto YPD agar plates. Appearance of white segregant colonies that acquire leucine and histidine auxotrophies, report loss of parental YEp(*SEC14, LEU2, ADE3*) and indicate functionality of the mutant *sfh1** gene product. **(B)** Immunoblots of lysates prepared from *sec14Δ cki1* 'bypass Sec14' yeast transformants grown at 30°C (upper panel) and after challenging at 37°C for 12 hr (lower panel). Transformants carried the designated YCp(*URA3*) plasmids allowing expression of C-terminally V5-tagged Sec14, Sfh1 and Sfh1*. Equal amounts of total protein were loaded, and V5-tagged proteins and Kes1 (normalization control) were visualized with specific monoclonal antibodies. Transformants carrying the YCp(*URA3*) plasmid alone (vector control) were employed as a negative control.

Supplementary Figure S5. MD simulations and equilibrium conditions. The root mean square deviation (rmsd) values of backbone atoms of a series of structural snapshots were written every 2 ps

during the course of 3 independent simulations. Fluctuations (Δrmsd) were below 0.8 Å for all systems within the last 2 ns of the 14 ns production run indicating that all PL-bound structures reached equilibrium conditions during the MD simulation.

Supplementary Figures S6. H-bonding network in PtdCho-structures. H-bonds that were represented in at least one simulation of at least one structure with an occupancy >10 % were included in the H-bonding analyses. Depicted here are residues that are connected via H-bonds to the core activation hydrophilic patch residues Y_{109}, Q_{111}, Y_{113} and E_{126}. The resulting H-bond network includes residues of the B_1LB_2, the A_7LA_8, the $A_{11}LT_4$ substructures and string motif residues C-terminal of the $A_{11}LT_4$ substructure. Interactions that are characterized by a consistent total increase of >10 % occupancy in all Sfh1* mutants relative to Sfh1 are labeled 'increase'. Those interactions that are characterized by a consistent total decrease of >10 % occupancy in all Sfh1* mutants are labeled 'decrease'. Substructure identity of residues is visualized by different colors as indicated.

Supplementary Figure S7. H-bonding network in PtdIns-structures. H-bonds that were represented in at least one simulation of at least one structure with an occupancy >10 % were included in the H-bonding analyses. Depicted here are residues that are connected via H-bonds to the core activation hydrophilic patch residues Y_{109}, Q_{111}, Y_{113} and E_{126}. The resulting H-bond network includes residues of the B_1LB_2, the A_7LA_8, the $A_{11}LT_4$ substructures and string motif residues C-terminal of the $A_{11}LT_4$ substructure. Interactions that are characterized by a consistent total increase of >10 % occupancy in all Sfh1* mutants relative to Sfh1 are labeled 'increase'. Those interactions that are characterized by a consistent total decrease of >10 % occupancy in all Sfh1* mutants are labeled 'decrease'. Substructure identity of residues is visualized by different colors as indicated.

Supplementary Figure S8. PL-Binding enthalpies, **w**ater occupancy and water turnover in the hydrophilic cavity of the hydrophobic pocket. **(A)** PL-binding enthalpies. Free energies were calculated using the single molecular dynamics trajectory method and the MM-GBSA approach (Kollman et al., 2000). The free energy terms include internal energies (bond, angle and torsion), the van der Waals and electrostatic energies, nonpolar and electrostatic contributions to the solvation free energy and contributions from the gas phase (see material and methods). PtdIns binding enthalpies are lower (more negative) than PtdCho binding enthalpies in all PL-bound structures. Consistent differences that distinguish Sfh1* proteins from Sfh1 were not observed. **(B)** Illustration of the cavity formed between the hydrophilic patch and the *sn-2* acyl chain. The cavity was calculated as a sphere around the center of mass of Sfh1 (Sec14) and PL *sn-2* acyl chain residues (specified in Supplemental Experimental Procedures) that are depicted as yellow spheres. Activation residues Y_{109}, Y_{113}, Y_{124}, and E_{126} are presented as sticks. **(C)** Average residence times of water molecules were calculated for the last 2 ns of MD simulation. Standard deviations of 3 independent simulations are given. Note the high variability in residence times for the Sfh1* mutants compared to Sfh1 as indicated by the standard deviation. **(D)**

Variability of water residence time was calculated as the relative standard deviation of 3 independent water residence times calculated in (B).

Supplementary Table Legends

Supplementary Table S1. Refinement statistics.

[a] $R_{sym} = \Sigma|I- \langle I\rangle|/ \Sigma|I|$, where I is the observed intensity and <I> is the average intensity of several symmetry-related observations.

[b] $R_{working} = \Sigma||F_o|-|F_c||/ \Sigma|F_o$, where Fo and Fc are the observed and calculated structure factors, respectively.

[c] $R_{free} = \Sigma||F_o|-|F_c||/ \Sigma|F_o$ for 7% of the data not used at any stage of the structural refinement.

Supplementary Table S2. H-Bond interactions in Sfh1, Sfh1* and Sec14. Overall H-bond occupancies (sums of individual donor and acceptor H-bonds) of H-bonding pairs are presented for PtdCho **(A)** and PtdIns **(B)** bound structures of Sfh1, Sfh1^{Y109A}, Sfh1^{Y113C}, Sfh1^{E126A} and Sec14. H-Bond donors are presented in the first column; H-bond acceptors are presented in the second column. If H-bond acceptors also act as H-bond donors (and vice versa) this is indicated in the last column. Individual H-bonds interactions that are defined by a consistent and absolute change of >10 % occupancy in all Sfh1* mutants relative to Sfh1 are highlighted in blue (reduced H-bonding in Sfh1*) or in red (increased H-bonding in Sfh1*).

Supplementary Table S3. Interaction between the loop regions of the B_1LB_2 and the $A_{11}LT_4$ substructures. Overall H-bonding occupancies (sums of individual donor and acceptor H-bonds) of H-bonding pairs that connect the loop regions of the B_1LB_2 and the $A_{11}LT_4$ substructures (H_{114}-N_{261}, V_{116}-N_{261}, D_{117}-Q_{256}, and D_{119}-Q_{256}) are presented. The sum of all occupancies of these interactions (given in the last row) suggests a reduced interaction between the loop regions of the B_1LB_2 and the $A_{11}LT_4$ substructures in all Sfh1* mutants. Occupancies of the corresponding Sec14 interactions are provided for comparison.

Supplementary Figures and Tables

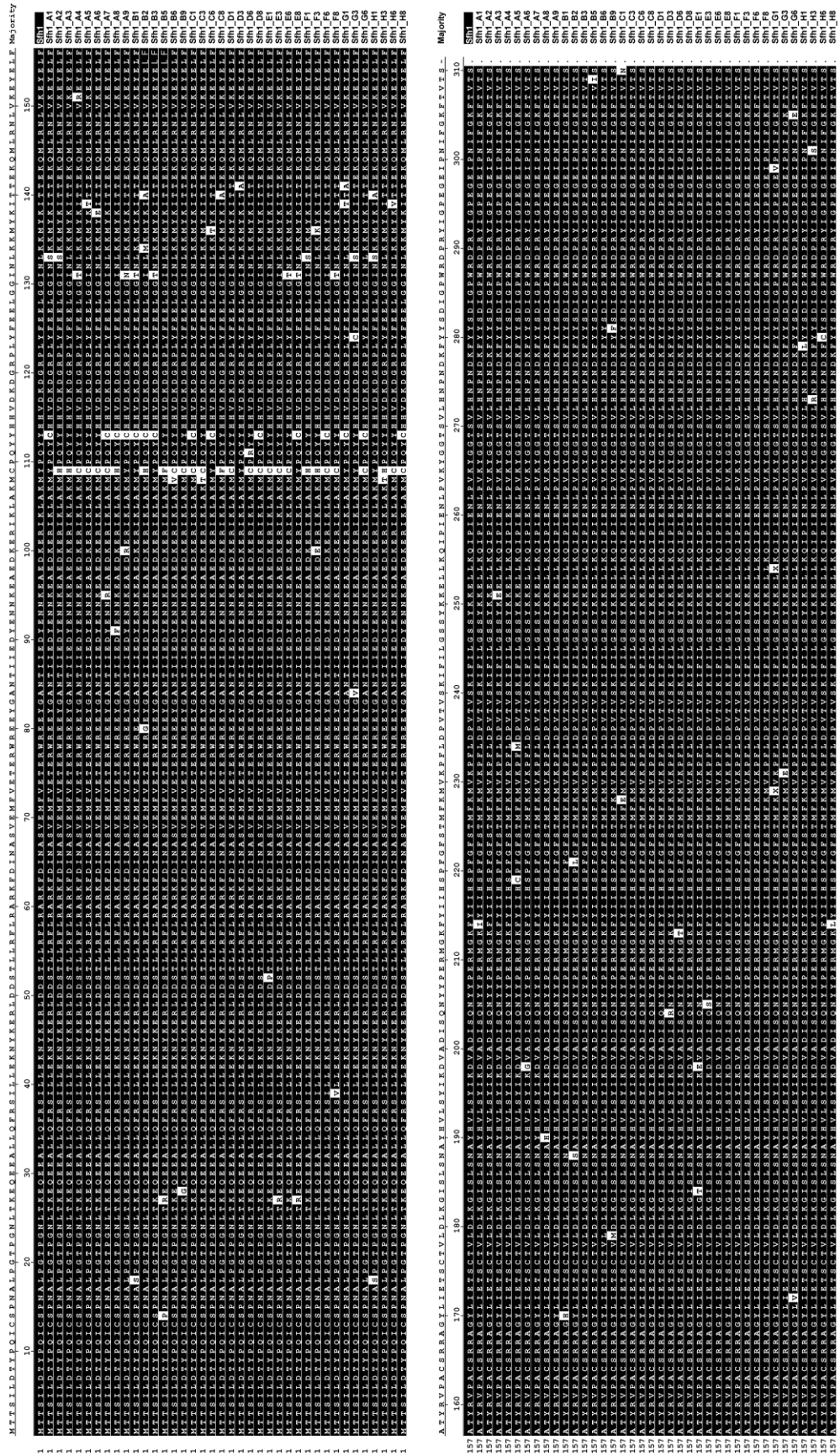

Supplementary Figure S1

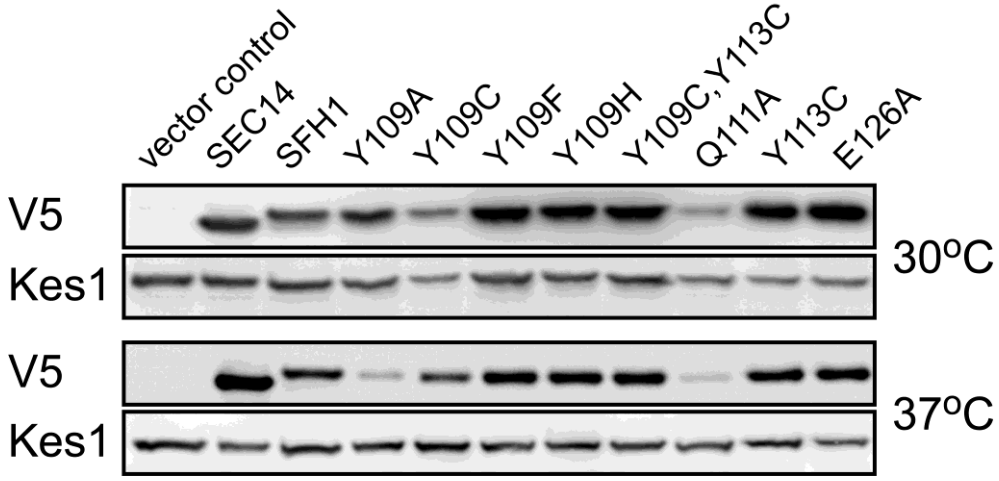

Supplementary Figure S2

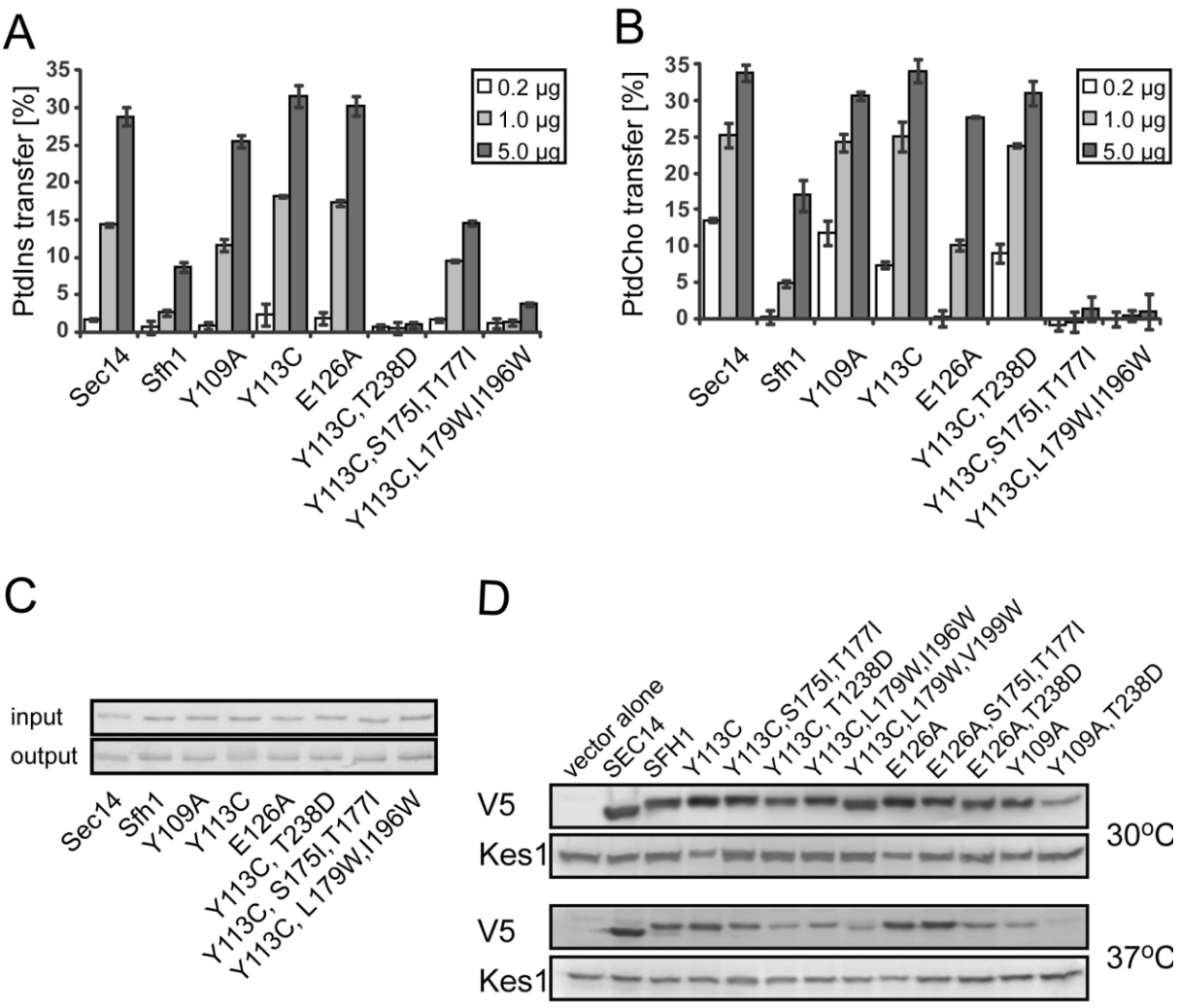

Supplementary Figure S3

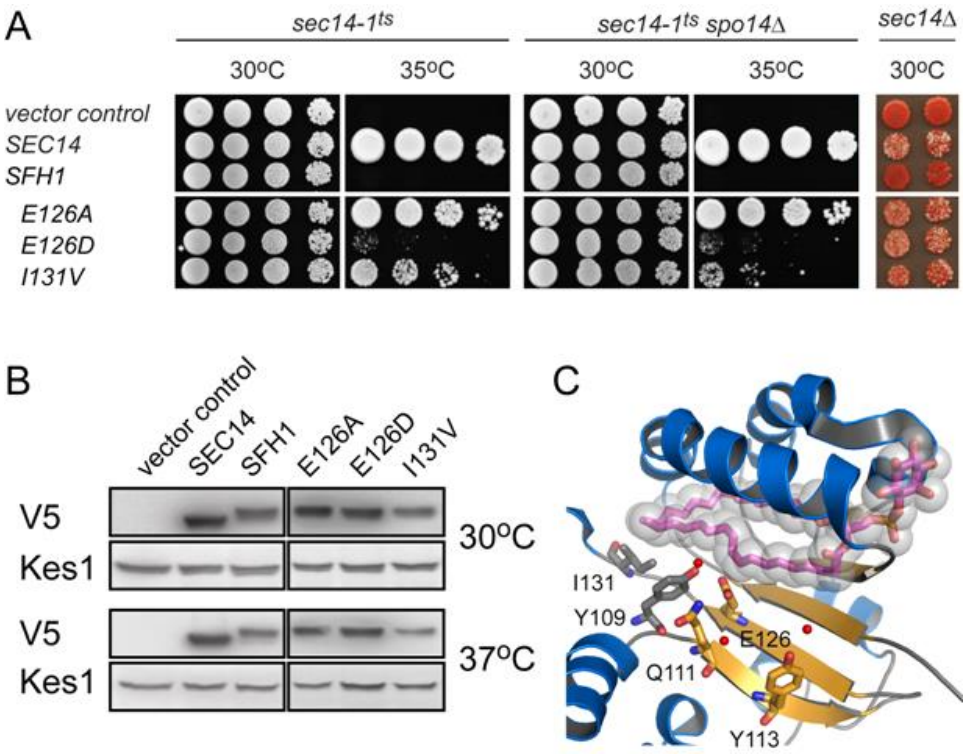

Supplementary Figure S4

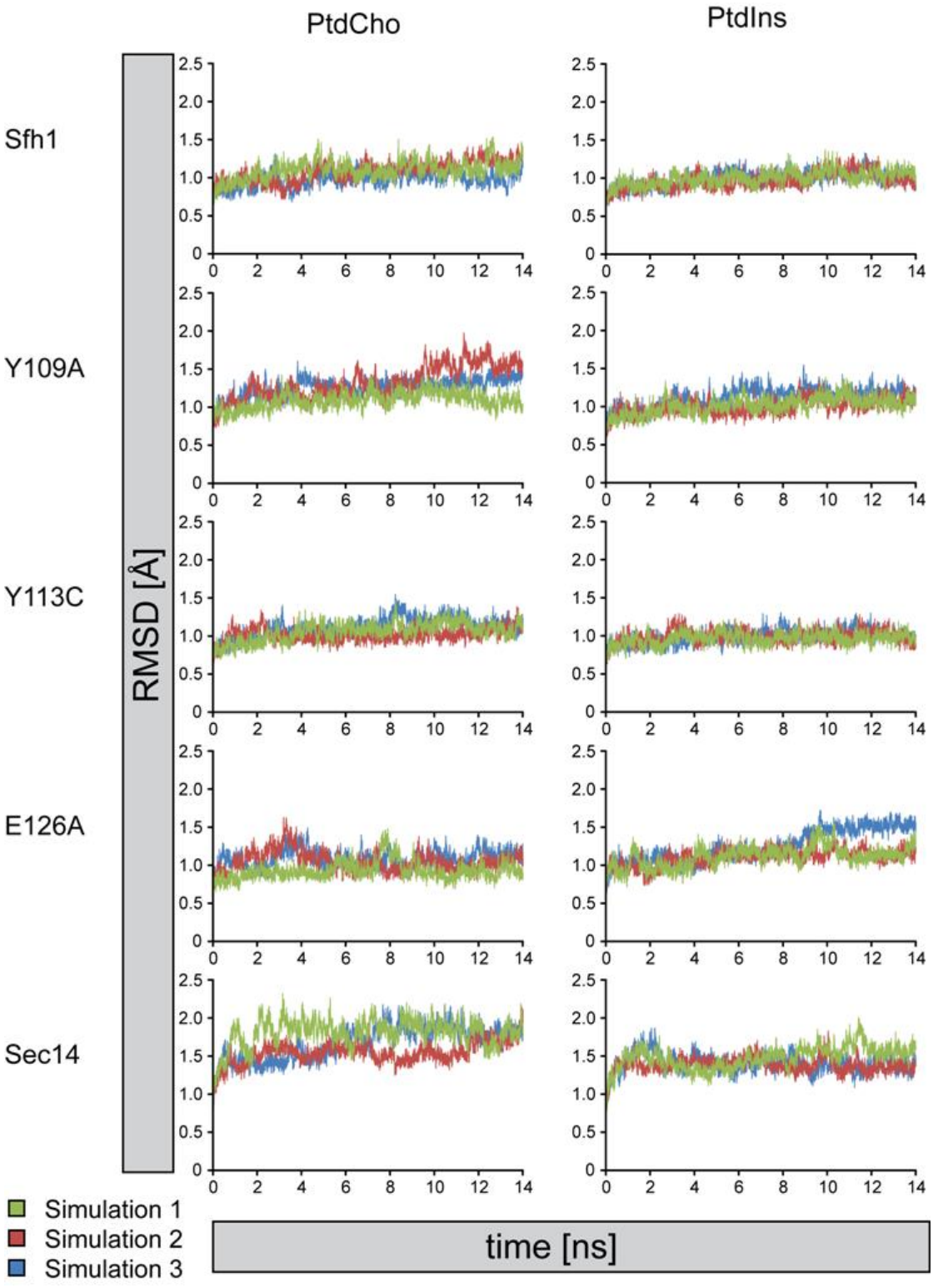

Supplementary Figure S5

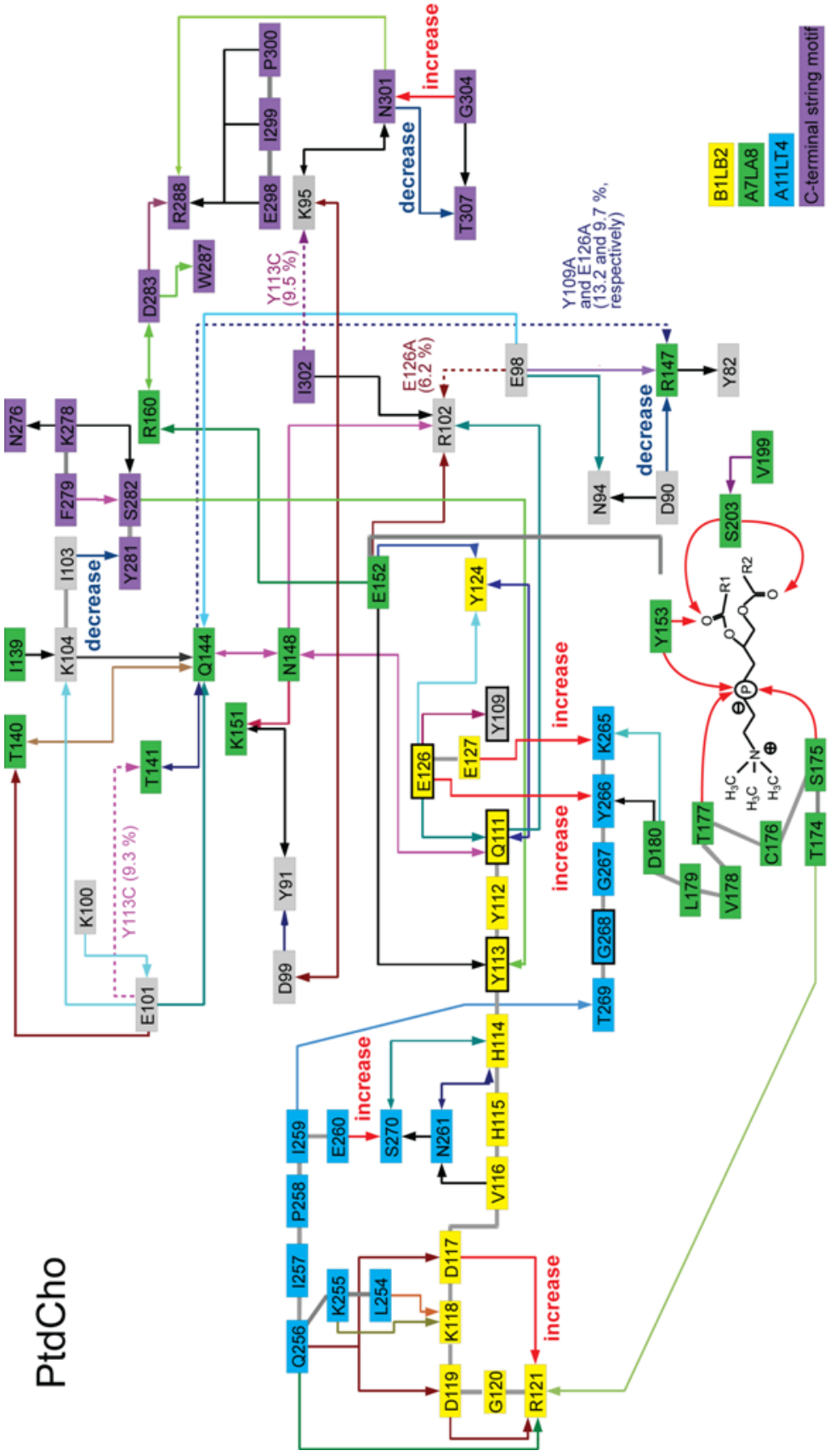

Supplementary Figure S6

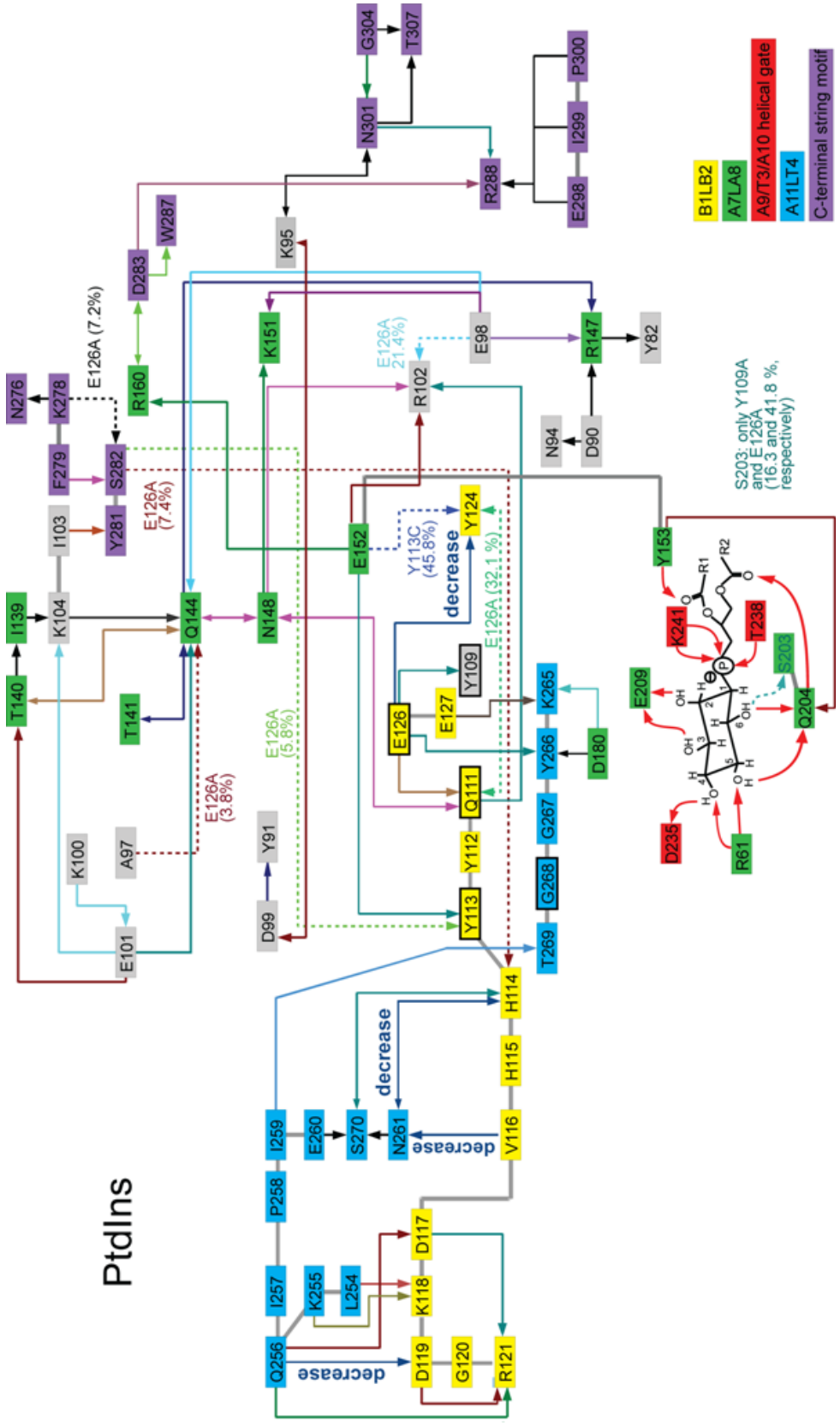

Supplementary Figure S7

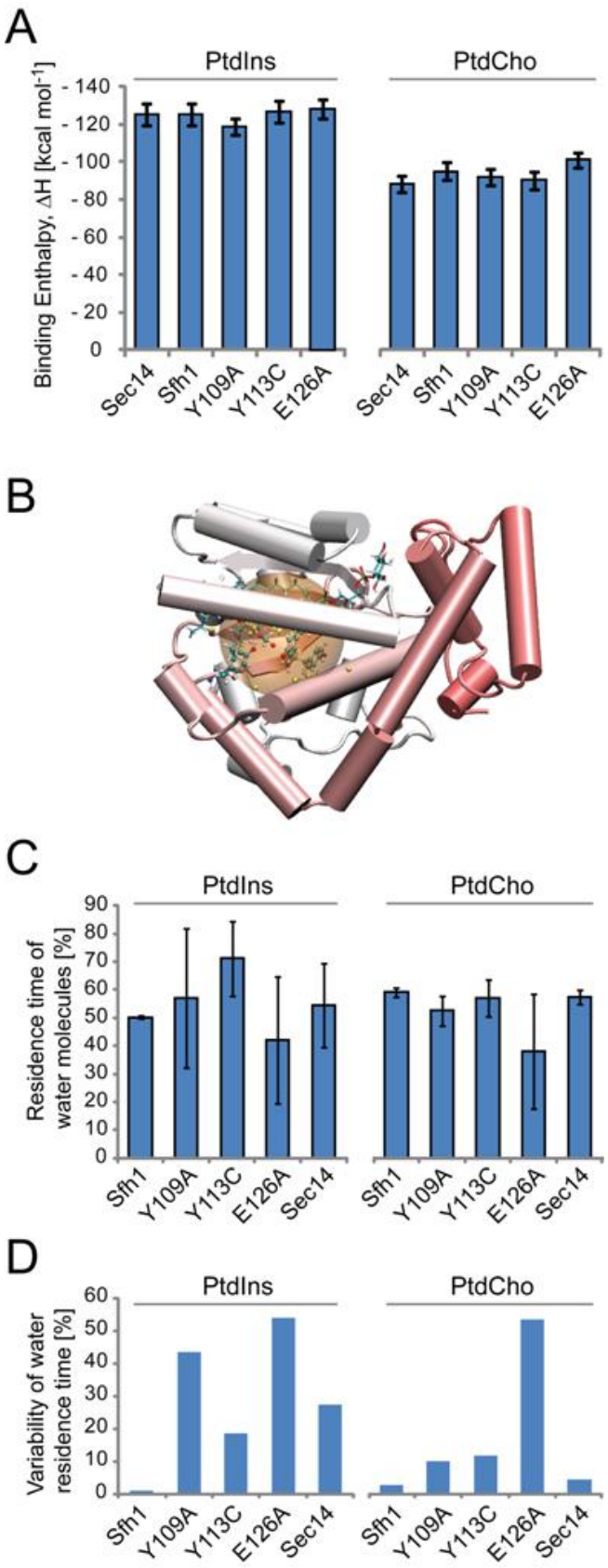

Supplementary Figure S8

Supplementary TableS1

Data Collection and Refinement Statistics	
Resolution (highest shell), Å	1.8 Å (1.86 – 1.80)
Space Group	$P2_12_12_1$
Unit Cell Dimensions	a=49.5, b=71.3, c=99.7 α=γ=β= 90.0
No. of Reflections	31603
R_{sym} (highest shell)	9.3% (30.6%)
Completeness (highest shell)	93.9% (78.3%)
Ave. Redundancy (highest shell)	3.9 (3.3)
I/σ	13.0 (3.6)
Monomers per asymmetric unit (AU)	1
No. of protein atoms/AU	2518
No. of ligand atoms/AU	45
No. of waters/AU	222
$R_{working}$ (R_{free})	17.6% 21.9%)
Ave. B-factors, Å^2	
Protein	23.5
Ligand	31.5
Water	30.7
Ion	-
R.m.s. deviations	
Bond lengths, Å	0.006
Bond angles, °	1.2
PDB ID	

Supplementary Table S2

Available at http://www.ncbi.nlm.nih.gov/pmc/articles/PMC3057712/bin/E10-11-0903_index.html

Supplementary TableS3

	Sec14	**Sfh1**	**Y109A**	**Y113C**	**E126A**
H114-N261	4.9	15.1	0.5	2.0	2.7
V116-N261	83.5	67.9	40.1	21.6	46.6
D117-Q256	73.40	55.5	53.2	49.0	53.4
D119-Q256	5.5	52.2	37.8	39.0	15.7
Sum of occupancies	167.4 (87.8%)	**190.6 (100 %)**	131.6 (69%)	111.6 (58.5 %)	118.3 (62.1 %)

Supplementary Materials and Methods

Constructs and random mutagenesis.

DNA manipulations were carried out using standard procedures (Sambrook and Russel, 2001). The *SFH1* ORF was excised from pGEM-*SFH1* (Schaaf et al., 2006) and inserted into multicopy yeast episomal expression vector pDR195 (Rentsch et al., 1995) at the NotI restriction sites, resulting in plasmid pDR195-*SFH1*. To generate a centromeric construct where *SFH1* expression is controlled by the yeast *SEC14* promoter, the *SFH1* ORF was amplified from pGEM-*SFH1* with oligonucleotides 5´-GCCTGTAGCATCAAACCAAACCTTCATCGCCCTAAAACACA ctcgagATGACAACCAGCATACTCGATAC- 3´ and 5´- TCTTTTCTCTCTCGAAAAAAA AATGTCTTTAAAAATAATAccgcggTTAGCTGGTAACAGTAAATTTACC- 3´. The haploid yeast strain BY4741 (Euroscarf, Y00000) was co-transformed with the resulting PCR product and vector YCplac33-*SEC14* (Phillips et al., 1999) that had been linearized with *BamH*I to allow GAP repair by *in vivo* recombination. Recombination sites are underlined in the sequences given above, and *Xho*I and SacII restriction sites (lower case) were introduced into the forward and reverse primer, respectively, to allow further subcloning reactions. Plasmids were rescued from yeast transformants, amplified in *E. coli* and analyzed by DNA sequencing to confirm that the Sec14 gene was correctly replaced by the *SFH1* ORF in the resulting plasmid YCplac33-*SFH1*.

To incorporate the V5-epitope tag into Sfh1 and its derivatives, the *SFH1-ORF* was amplified using forward primer 5´- ctcgagATGACAACCAGCATACTCGATAC- 3´ and two reverse primers 5´-ATCGAGACCGAGGAGAGGGTTAGGGATAGGCTTACCTCCTCCAGA TCCGCTGGTAACAGTAAATTTACCAAA- 3´ and 5´-ccgcggTTACGTAGAATCGAGACC GAGGAGAGGG- 3´. The forward and second reverse primer were clamped with *Xho*I and *Sac*II restriction sites (small case), respectively, to facilitate subcloning into pDR195. A short sequence encoding a GSGG linker (highlighted in gray in the sequence given above) was followed by a sequence encoding the V5-tag (underlined). The PCR product was inserted into vectors pDR195-*SFH1* and YCPlac33-*SFH1* by virtue of the *Xho*I/*Sac*II restriction sites and thereby replaced the untagged *SFH1-ORF* in these constructs.

To generate an episomal plasmid suitable for *in vivo* cloning of mutagenized PCR-products by gap repair, complementary oligonucleotides 5´-TCGAAAATAATTAAAATT TATAATTTTAAAAGAATTCGGATCCGGCCCGGGCGGCCTGCAGTCGACTCGAGC- 3´ and 5´-GATCGCTCGAGTCGACTGCAGGCCGCCCGGGCCGGATCCGAATTCTTTTAAA ATTATAAATTTTAATTATTT- 3´ were hybridized and ligated into the *Xho*I and *BamH*I sites of pDR195 (Rentsch et al., 1995), generating pDR199. Both restriction sites were destroyed upon ligation and an *EcoR*I and an adjacent *BamH*I restriction site were introduced (underlined). These sites were used to linearize pDR199 prior to gap repair. Random mutagenesis was carried out by amplifying the *SFH1* ORF from pGEM-*SFH1* with oligonucleotides 5´- CCCAGCCTCG

AAAATAATTAAAATTTATAATTTTAAAAGACTGCAGATGACAACCAGCATACTCGA TACT - 3´and 5´- AAGCTGGATCGCTCGAGTCGACTGCAGGCCGCCCGGGCCGTTAGC TGGTAACAGTAAATTTACC - 3´ (recombination sites for pDR199 gap repair are underlined).

Mutagenesis and selection for SFH1 gain-of-function mutants

To induce mutations, polymerase chain reactions were carried out with Taq DNA polymerase in the presence of 120 μM $MnCl_2$, a decreased concentration of dATP (0.3 x) and 35 PCR cycles. PCR-products were precipitated with EtOH, washed and resuspended in 100 mM LiAc/ TE (pH7.5) buffer. To allow *in vivo* recombination and to screen for *SFH1** activation mutants *sec14-1^{ts}* yeast cells (CTY1-1A) were co-transformed with linearized pDR199 and the purified mutagenized *SFH1* PCR products. Transformants were plated on defined uracil-free medium and incubated at 37°C for 5 days. A defined fraction of transformants was also incubated at 30°C to estimate transformation efficiency. Plasmids conferring growth at 37°C were subjected to DNA sequencing analysis. Individual mutations were introduced in YCplac33-*SFH1* by site-directed mutagenesis (QuickChangeTM, Stratagene), and mutant *SFH1** ORFs were subcloned into pDR195 for high copy expression using *Xho*I and *Sac*II restrictions sites.

Molecular Dynamics Simulations

For the simulations of Sfh1 with PtdIns (PDB ID: 3B7N) or PtdCho (3B7Q) the initial coordinates were obtained from the Protein Databank. Structural models of the activation mutants Sfh1^{E126A}, Sfh1^{Y109A}, and Sfh1^{Y113C} were constructed by substituting the corresponding amino acids in the 3B7N and 3B7Q with PyMOL using backbone dependent rotamers. Models of PL-bound Sfh1^{E126A} were obtained by superimposing the Sfh1^{E126A}-PtdEtn structure (PDB ID: xyz, this work) with either 3B7N (PtdIns) or 3B7Q (PtdCho) using ProFit (http://www.bioinf.org.uk/software/profit/). The PtdEtn molecule was then substituted by either PtdIns (from 3B7N) or PtdCho (from 3B7Q) to obtain the Sfh1^{E126A}-PtdIns and the Sfh1^{E126A}-PtdCho structures, respectively.

Modeller9v7 (Šali and Blundell, 1993) was used to create a structural homology model of closed Sec14 for molecular dynamics simulations. Modified structures of Sfh1 (PDB ID: 3B7Z) and Sec14 (PDB ID: 1AUA) were used as templates. The primary structure of Sec14 is 63% identical to that of Sfh1. Non-protein atoms were removed from the template structures as well as amino acids forming the closed A10/T4/A11 helical gate ($_{211}$KFYIINAPFGFSTAFRLFKPFL DPVTVSKIFILGSSYQKEL$_{251}$) of the template 1AUA structure. Five models were produced and the one with the best value of the "Modeller Objective Function" was chosen for subsequent simulations. Afterwards the model structure was minimized for 400 steps keeping backbone atoms fixed during the first 300 steps. PtdIns and PtdCho were embedded by structural fitting with ProFit into the models of closed Sec14-PtdIns and Sec14PtdCho, respectively. The crystal structures of Sfh1 (3B7N and 3B7Q) with bound lipids were superimposed onto the model of Sec14. Thereafter the atomic coordinates were copied into the Sec14 coordinate file. The resulting protein-lipid complexes were minimized for 1000 steps with the steepest

descent algorithm followed by 1000 steps using the conjugate gradient algorithm, while the atomic coordinates of the lipids were fixed.

The molecular dynamics simulations were performed with the SANDER and PMEMD module of AMBER 10 (Case et al., 2008). The force field parameters from the standard amber ff03 force field (Duan et al., 2003) were used for the protein. The antechamber module was used to obtain the force field parameter for PtdIns and PtdCho based on the general AMBER force field (GAFF, Wang et al., 2004) and partial atomic charges were calculated with AM1-BCC. Water molecules solved in the crystal structure were maintained and a rectangular water box with a buffering distance of 12 Å around the system was constructed using LEaP (AmberTools 1.4). The TIP3P (Jorgensen et al., 1983) water model was used. The systems were neutralized by the addition of counter ions. Long-range electrostatic interactions were estimated using the particle mesh Ewald method (Toukmaji et al., 2000). Bonds involving protons were constrained with the SHAKE algorithm using the default tolerance (1.0 x 10-5Å) and time steps of 2fs. Lennard-Jones interactions were truncated at 12Å and the non-bonded list was updated every 25 steps. Each system was minimized for 1000 steps using the steepest descent algorithm followed by 1000 steps using the conjugate gradient algorithm where all atoms of the complex were restrained to their initial positions with a weak force constant of 2 kcal mol^{-1} $Å^{-2}$. The minimization was followed by 50-ps constant volume dynamics with gradually heating from 0.1 K to 300 K. Pressure and temperature were then held constant for 50 ps until the system reached a density of 1 g cm^{-3}. Afterwards, 14 ns of unconstraint molecular dynamics simulations were performed using periodic boundary conditions. Temperature (300 K) and pressure (1 atm) were kept constant using the weak coupling algorithm. Coordinates for analysis were saved every 2 ps.

Molecular Dynamics Data Analyses

The ptraj module of AmberTools 1.4 was used for trajectory processing and analyses of root mean square deviation (rmsd) values, interatomic distances, hydrogen bonding and atomic positional fluctuations. The φ and ψ dihedral angles measuring residue backbone conformations were also reported using ptraj. Unless otherwise stated, data analyses are reported for the 12 to 14 ns time frames of the simulations so that analyses could be focused on a time window where the backbone rmsd of the structures indicated only minor structural changes.

Estimation of PL-protein binding enthalpies

The free energies were calculated using the single molecular dynamics trajectory method and the MM-GBSA approach (Kollman et al., 2000). Multiple snapshots of the ligand, receptor and the ligand-receptor complex were extracted every 10 ps from the same trajectories at the interval 12-14 ns. All water and counter ions were stripped. Formula [1] was used to calculate the binding free energies of 200 snapshots that were then averaged.

$$\Delta G_{bind} = \langle G_{complex} \rangle - \langle G_{protein} \rangle - \langle G_{ligand} \rangle \qquad [1]$$

The free energy terms include the contributions from gas phase, solvation and entropic effects:

$$G = E_{gas} + G_{solvation} - TS$$

$$E_{gas} = E_{int} + E_{vdW} + E_{ele} \quad [2]$$

$$G_{sol} = G_{GB} + G_{sa}$$

where E_{gas} is the sum of the internal energies (bond, angle and torsion) and the van der Waals and electrostatic energies. The modified Generalized Born solvation model GB^{OBC} (Onufriev et al., 2004) was used for calculating the electrostatic contribution to the solvation free energy (G_{sol}). The nonpolar contribution to the solvation free energy is calculated by:

$$G_{SA} = \gamma * SASA + b \quad [3]$$

where the parameters γ and b were set to 0.0072 kcal mol^{-1} $Å^{-2}$ and 0 kcal mol^{-1}, respectively. The solvent accessible surface area (SASA) was determined by LCPO (Weiser et al. 1999). The interior dielectric constant was set to 1 (default) and the exterior dielectric constant to 80. Entropic contributions were omitted, since only binding affinities between identical lipids and proteins with single amino acid substitutions were compared.

Estimation of water turnover in the hydrophobic cavity

The cavity formed between the hydrophilic patch and the *sn*-2 acyl chain of PtdIns- or PtdCho was approximated for each frame of the trajectory by calculating the geometric center of the Cα atoms from Sfh1(Sec14) residues E_{142} (E_{140}), L_{146} (L_{144}), L_{149} (L_{147}), Y_{153} (Y_{151}), L_{123} (L_{121}), Y_{124} (Y_{122}), F_{125} (F_{123}), E_{126} (E_{124}), E_{127} (E_{125}), L_{128} (L_{126}) and PL *sn*-2 carbon atoms (C_3-C_{14}). Water molecules within a sphere with a radius of 7Å around the geometric center were recorded every 2 ps for the entire simulation. Occupancies of individual water molecules were calculated as percentages of occupied frames relative to total frames.

Supplementary Literature Cited

Case D. A. *et al*. (2008) AMBER *10*, San Francisco, CA: University of California

Duan, Y., Wu, C., Chowdhury, S., Lee, M.C., Xiong, G., Zhang, W., Yang, R., Cieplak, P., Luo, R., and Lee, T. (2003) A point-charge force field for molecular mechanics simulations of proteins based on condensed-phase quantum mechanical calculations. J. Comput. Chem. *24*, 1999–2012.

Kollman, P.A., Massova, I., Reyes, C., Kuhn, B., Huo, S., Chong, L., Lee, M., Lee, T, Duan, Y., Wang W., and Donini, O. (2000) Calculating structures and free energies of complex molecules: combining molecular mechanics and continuum models. Acc. Chem. Res. *33*, 889–897.

Massova, I., and Kollman, P.A. (1999) Computational Alanine Scanning To Probe Protein-Protein Interactions: A Novel Approach To Evaluate Binding Free Energies. J. Am. Chem. Soc. *121*, 8133–8143.

Onufriev, A., Bashford, D., and Case, D.A. (2004) Exploring protein native states and large-scale conformational changes with a modified generalized born model. Proteins: Struct., Funct., Genet. *55*, 383–394.

Rentsch, D., Laloi, M., Rouhara, I., Schmelzer, E., Delrot, S., and Frommer W.B. (1995) NTR1 encodes a high affinity oligopeptide transporter in Arabidopsis. FEBS Lett. *370*, 264-268.

Šali, A., and Blundell, T.L. (1993) Comparative protein modelling by satisfaction of spatial restraints. J. Mol. Biol. *234*, 779-815.

Toukmaji, A., Sagui, C., Board, J., and Darden, T. (2000) Efficient particle mesh Ewald based approach to fixed and induced dipolar interactions. J. Chem. Phys. *113*, 10913–10927.

Wang, J., Wolf, R.M., Caldwell, J.W., Kollamn, P.A., Case, D.A. (2004) Development and testing of a general Amber force field. J. Comput. Chem. *25*, 1157–1174.

Weiser, J., Shenkin, P.S., Still, W.C. (1999) Approximate atomic surfaces from linear combinations of pairwise overlaps (LCPO). J. Comput. Chem. *20*, 217–230.

CHAPTER 5

A BLUEPRINT FOR FUNCTIONAL ENGINEERING: SINGLE POINT MUTATIONS RECONSTITUTE PHOSPHATIDYLINOSITOL PRESENTATION IN A PSEUDO-SEC14 PROTEIN

Eva M. Winklbauer[1,†], Marília K. F. de Campos[1,†], Marek Dynowski[1,2†], Gabriel Schaaf[1*]

[1] ZMBP, Plant Physiology, Universität Tübingen 72076 Tübingen, Germany
[2] Rechenzentrum, Universität Freiburg, 79104 Freiburg, Germany

[†] **These authors contributed equally to this work** *** Corresponding author**

Addendum to:

Schaaf et al. (2011). Resurrection of a functional phosphatidylinositol transfer protein from a pseudo-Sec14 scaffold by directed evolution. **Mol Biol Cell**, 22(6), 892-905.

This chapter has been published:

Winklbauer et al. (2011). A blueprint for functional engineering: Single point mutations reconstitute phosphatidylinositol presentation in a pseudo-Sec14 protein. **Commun Integr Biol**, 4, 674-678.

Abstract

Phosphoinositides, phosphorylated species of phosphatidylinositol (PtdIns), are critical regulatory lipids in all eukaryotic cells. The molecular mechanisms that lead to the phosphorylation of an individual PtdIns- or phosphoinositide molecule remain largely unkown even though lipid kinases and phosphatases involved in these processes have been studied in detail. The observation by us and others that liposomal PtdIns (and phosphoinositide) molecules are poor *in vitro* substrates for kinases and phosphatases raises the question of how these enzymes execute their function in living cells. Recent work indicates that Sec14, the founding member of a large superfamily of eukaryotic proteins, is crucial for the process of PtdIns phosphorylation. The collective data suggest that Sec14 mediates a heterotypic phospholipid exchange reaction of PtdIns with phosphatidylcholine (PtdCho) during which PtdIns becomes vulnerable for kinase attack and thereby promotes the generation of phosphoinositides (Bankaitis et al., 2010; Schaaf et al., 2008). In a recent paper we address the molecular mechanism of this phospholipid (PL) exchange reaction in a pseudo-Sec14 protein (Sfh1) that we rendered functional by a directed evolution approach. We find that enhanced PL-cycling into and out of the hydrophobic pocket of these activated Sfh1 mutants depends on the reconfiguration of interactions between a C-terminal string motif and the floor of the hydrophobic pocket that results in increased oscillations in a helical gate that controls pocket access. Here we further discuss our findings and propose molecular

dynamics simulations as a tool to approach energetically unfavorable transition states and to identify novel protein-ligand interactions invisible to X-ray crystallography.

Text

Sec14 is an essential protein required for the efficient biosynthesis of distinct pools of phosphatidylinositol-4-phosphate (PtdIns(4)P) in yeast (Phillips et al., 2006). Inactivation of Sec14 causes severe trafficking defects (Bankaitis et al., 1990; Bankaitis et al., 1989) in agreement with an essential role of PtdIns(4)P to recruit and activate regulatory proteins involved in the formation of secretory vesicles at the yeast *trans*-Golgi network (TGN) (Mizuno-Yamasaki et al., 2010; Strahl and Thorner, 2007).

Structural appreciation of phospholipid binding by Sec14 proteins suggests a role in PtdIns presentation

In a previous study addressing the mechanism of Sec14-stimulated PtdIns(4)P production, we crystallized and functionally characterized Sec14 homolog Sfh1, in complex with PtdEtn and Sec14's physiological lipid ligands phosphatidylinositol (PtdIns) and phosphatidylcholine (PtdCho) (Schaaf et al., 2006; Schaaf et al., 2011). Our structural and functional analyses suggest that **i)** the hydrophobic cavity of Sfh1 (and Sec14) is large enough to entirely accommodate a single phospholipid (PL) molecule; **ii)** PtdIns and PtdCho bind at distinct yet overlapping sites; **iii)** binding of both PtdIns and PtdCho are essential activities of Sec14; and **iv)** both individual PtdIns and PtdCho binding activities have to reside in *cis* to reconstitute a functional Sec14 protein that allows stimulation of PtdIns(4)P production *in vivo*. Our collective data suggest that Sec14 mediates a PL exchange reaction that results in presentation of PtdIns to PtdIns 4-OH kinases. The requirement for heterotypic PL exchange (PtdCho for PtdIns, or vice versa) to efficiently stimulate PtdIns 4-OH kinase activity suggests a high complexity of PtdIns(4)P biosynthesis. Surprisingly, Sfh1, which shares 64% primary sequence identity with Sec14 and conserves all of the structural motifs critical for PtdIns and PtdCho binding, does not substitute for Sec14 *in vivo* even under conditions of high protein expression (Li et al., 2000; Schaaf et al., 2011).

A directed evolution approach to activate the nonfunctional Sec14 homolog Sfh1

In an attempt to elucidate the topology of productive Sec14-like heterotypic PL exchange and to understand the inefficiency of Sfh1 in stimulating PtdIns(4)P production, we randomly mutagenized Sfh1 and screened for Sfh1 mutants (named Sfh1*) that were now able to rescue growth defects associated with Sec14 deficiency in yeast. To our surprise, single missense substitutions identified in this screen that endow Sfh1* with Sec14-like activities affect residues *conserved* between Sec14 and Sfh1 (Figure 1A, B). These Sfh1* mutations reside in an enigmatic hydrophilic patch at the floor of the

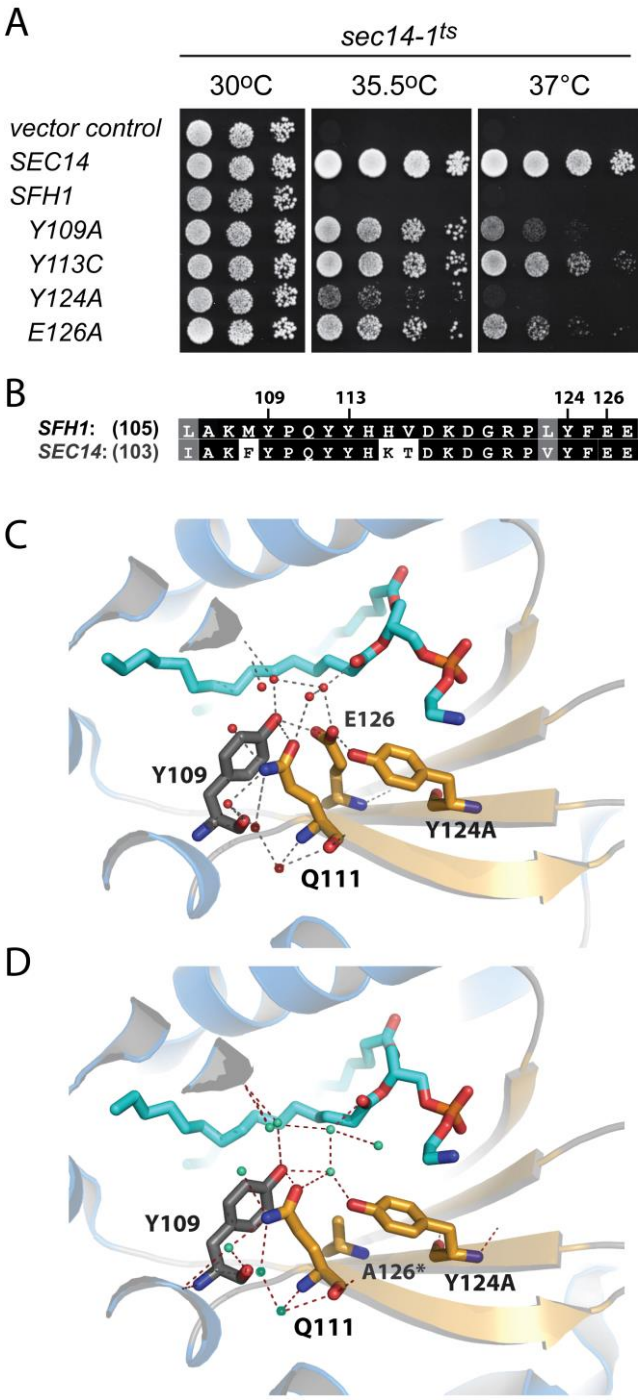

Figure 1. Functional characterization of Sfh1* activation mutants. (A) The *sec14-1*^{ts} yeast strain was transformed with YCp(*URA3*) plasmids carrying either *SFH1* or the designated *SFH1** alleles and transformants were spotted in serial dilutions onto YPD agar plates. Rescue at restrictive temperatures (35.5°C and 37°C, middle and right panel, respectively) reports Sec14-like activity. Centromeric plasmids YCp(*URA3*) and YCp(*SEC14*, *URA3*) were employed as negative and positive controls, respectively. (B) Sequence alignment of Sec14 and Sfh1. Shown is a selected region that includes the hydrophilic patch and residues substituted by missense mutations in Sfh1* (as indicated). Conserved amino acids are depicted in black, similar amino acids depicted in grey. (C, D) Ribbon diagrams illustrating the hydrophilic patch at the floor of the hydrophobic PL-binding pocket. Sfh1 residues that are substituted by missense mutations in Sfh1* (except Y113) are shown as sticks. PtdEtn is rendered in cyan, H-bonds are shown as dashed lines. Structures of the Sfh1::PtdEtn complex (C, pdb ID 3B74) and the Sfh1^{E126A}::PtdEtn complex (D, pdb ID 3Q8G) are shown. Note that an intricate H-bonding network remains intact in the Sfh1^{E126A}::PtdEtn complex by virtue of an immobilized H_2O molecule that occupies the space of the missing E126 carboxy group (D).

hydrophobic PL binding pocket (Figure 1C). To investigate the structural consequences of these missense substitutions, we crystallized Sfh1^{E126A}, an activation Sfh1* with robust Sec14-like activities, in complex with the aminophospholipid PtdEtn and its structure was solved at high resolution (pdb ID 3Q8G;) (Schaaf et al., 2011). To our surprise, the Sfh1^{E126A} ::PL complex superimposes onto the Sfh1::PL complex with a root mean square deviation (rmsd) below 0.2Å suggesting that the E126A substitution does not cause any major conformational changes. This finding was further corroborated by investigating the immediate environment of the missense substitution. The carboxy group of E126 connects the phenolic hydroxyl of Y124 with the side chains of Y109/Q111 via strong hydrogen bonding that also involves several immobilized H_2O molecules and therefore seems to play a key role in maintaining the integrity of the hydrophilic patch. Surprsingly, patch residues Y109, Q111, and Y124 appear unaltered in the Sfh1^{E126A} structure with respect to position and side chain orientation. Furthermore, the strong interactions observed within the hydrophilic patch of the wild type structure appear to be intact in Sfh1^{E126A}::PtdEtn (Figure 1C, D). Interestingly, the hydrogen bonding network of the hydrophilic patch stays intact by immobilization of an additional H_2O molecule that occupies the space filled by the E126 carboxy group in the wild type structure (Figure 1C, D). From these structural analyses, the strong activation phenotype of Sfh1^{E126A} remains largely elusive and suggests that activation of Sfh1 does not require conformational alterations in the thermodynamically most stable PL bound state that we crystallized here. Rather, it suggests that the E126A mutation alters energy levels and/or the topology of PL exchange intermediates.

Reconfiguration of atomic interactions in Sfh1* correlate with increased phospholipid cycling

Since energetically unfavorable transitional states generally escape conventional crystallographic methods, we decided to approach exchange intermediates by molecular dynamics (MD) simulations. Computational simulations of protein dynamics provide high-resolution information when complemented by laboratory experiments (Ludewig and Dynowski, 2009). MD simulations were successfully applied to investigate solute transport through membrane-spanning channels (de Groot and Grubmuller, 2001; Dynowski et al., 2008; Tajkhorshid et al., 2002), and helped to identify transient conformational states of signaling proteins (Gardino et al., 2009). We carried out MD-simulations for PtdIns- and PtdCho-bound complexes of Sfh1, various Sfh1* (including Sfh1^{E126A}) and Sec14. Two major conclusions could be drawn from these analyses: **i)** Sfh1* activation mutants consistently reconfigure an H-bonding network between the B_1LB_2 substructure at the floor of the hydrophobic pocket and residues at the C-terminal string motif (Figure 2A), **ii)** these reconfigured atomic interactions result in conformational coupling that transduces conformational energy from the C-terminus and hydrophobic pocket to the $A_9T_3A_{10}$ helical motif that gates hydrophobic pocket access (Figure 2A, see also Schaaf et al., 2011). In particular, we find consistently *increased* hydrogen bonding in all Sfh1*::PtdCho complexes between the C-terminal half of the B_2 strand with the C-terminal T_4 turn and consistently *decreased* hydrogen bonding in all Sfh1*::PtdIns complexes between the loop regions of the B_1LB_2 and the C-terminal $A_{11}LT_4$ substructures (Figure 2A). These consistent alterations correlated

with increased fluctuations of the helical gate, suggesting that they increase cycling of PL into and out of the hydrophobic PL binding pocket. To test whether this is indeed the case, we performed experimental assays that monitor protein-mediated PL transfer between two distinct liposomal populations and provide a sensitive readout of the protein's ability to extract and release a PL molecule from/into a liposomal membrane (Schaaf et al., 2008). In these experiments, Sfh1* activation mutants consistently showed increased transfer (and thus cycling) for both PtdCho and PtdIns (Figure 2B, see also Schaaf et al., 2011), supporting the predictions from our MD simulations.

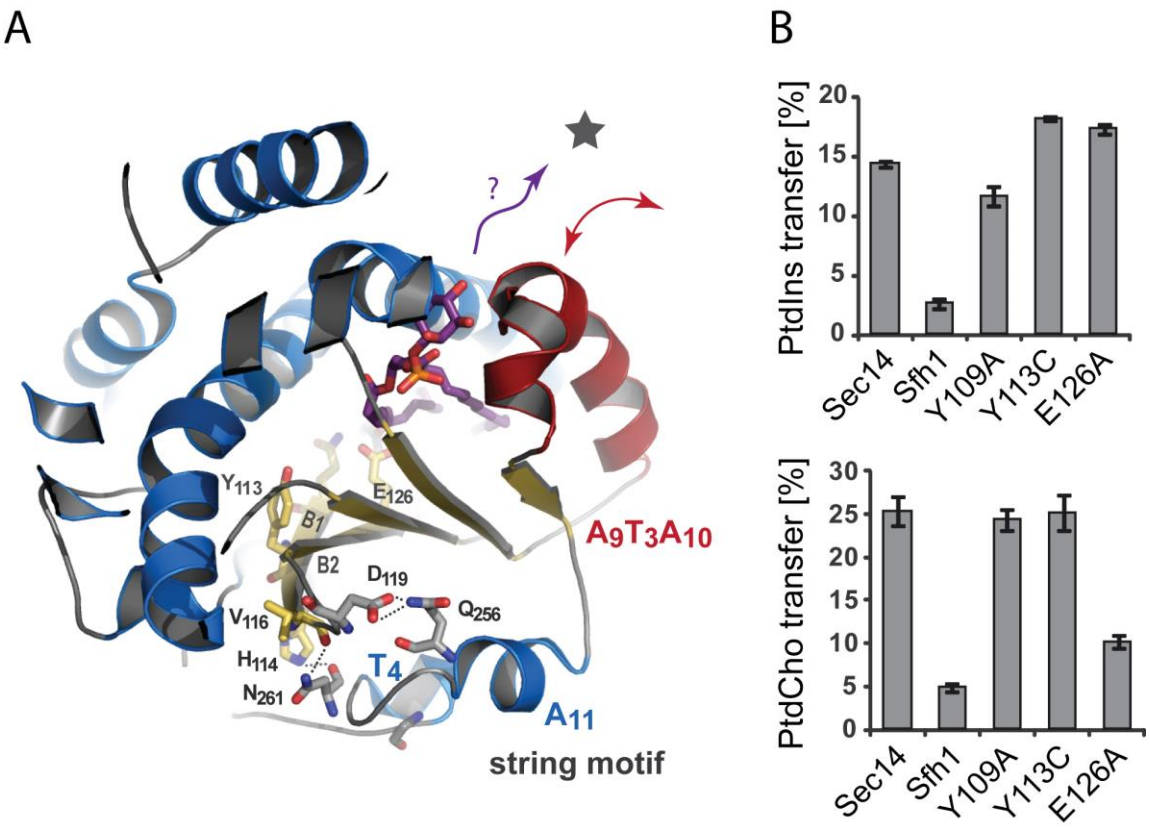

Figure 2. Biochemical properties of Sfh1* and model of Sfh1*-dependent alterations in H-bonding and helical gate oscillations. (A) Ribbon diagram illustrates H-bonds that are altered consistently in PtdIns bound Sfh1* mutants as deduced from MD simulations. The $A_9T_3A_{10}$ gating module is depicted in red; all other α-helices are presented in blue. Unstructured regions are in grey and β-strands are presented in yellow. PtdIns is rendered in magenta. Relevant H-bonds are presented as dashed lines. The B_1LB_2 substructure consists of β1- and β2 β-strands and the intervening loop region. Sfh1* mutants show decreased H-bonding of $A_{11}LT_4$ loop residue N261 with both H114 and V116 and decreased H-bonding of A11 residue Q256 with B1LB2 loop residue D119. Altered H-bonding occupancies coincide with increased helical gate oscillations (depicted by red arrow). The topology of PtdIns exit (purple arrow) and the coordinates of kinase attack (asterisk) remain elusive. (B) Biochemical properties of Sfh1* with defects in PL-binding. Purified recombinant Sec14, Sfh1, and mutant Sfh1 proteins were assayed for PtdIns- (upper panel) and PtdCho- (lower panel) transfer activity. Proteins were assayed at 1 µg / 500 µL reaction volume as described in Schaaf et al. (2011). Average values and standard deviations are given (n=3).

Atomic interactions between critical Sfh1/Sec14 substructures – mechanistic insights in Sec14 dysfunction causing human disease?

Interestingly, the structural motifs identified in our work are also present in human Sec14 proteins including α-tocopherol transfer protein (αTTP), SNPF, cellular retinaldehyde binding protein (CRALBP) and the neurofibromin 1 (NF1) ras GTPase activating protein, for which no physiological ligand of the Sec14-domain has been identified yet. Strikingly, dysfunctions in these proteins cause human disease and many of the disease causing mutations lie within the B_1LB_2 substructure and the helical gate of these proteins, suggesting a general significance of these motifs for Sec14 function (Gardino et al., 2009; Schaaf et al., 2011).

Molecular dynamics simulations as a tool to predict transient Sec14::PL exchange intermediates

MD-simulations employed in our directed evolution approach (Schaaf et al., 2011) provided a rational for the Sfh1* activation mechanism. To further deepen the structural appreciation of exchange intermediates that escape conventional structural and biochemical analyses, we used here MD-simulations to identify transient H-bonds that are absent in high resolution crystal structures but might be of functional importance to mediate conformational transitions independent of the Sfh1* activation mechanism. Initial coordinates for Sfh1::PtdCho were obtained from the Protein Databank (PDB ID: 3B7Q), and a structural model as described previously (Schaaf et al., 2011) provided coordinates for the Sec14::PtdCho complex. Unconstraint MD simulations were carried out for 14 ns in triplicate essentially as described (Schaaf et al., 2011) and structural snapshots that were written every 2 ps during the last 2 ns of the simulation (12 to 14 ns) employed to identify H-bonds coordinating the PtdCho ligand. Our high resolution crystal structure suggested that polar interactions of SfhI with PtdCho is mediated by strong hydrogen bonding of S175 and T177 with the phosphate oxygens of the PL headgroup (Schaaf et al., 2008). Evaluation of our MD simulations supported this observation with respect to T177 with a predicted H-bonding occupancy of 64% (Figure 3). However, only a minor contribution (23% H-bonding occupancy) of S175-mediated PtdCho coordination was observed in these MD simulations (Figure 3). To our surprise, MD simulations suggested a novel robust H-bonding interaction of the S203 side chain hydroxyl group with the headgroup acyl oxygens that is completely invisible in the high resolution Sfh1::PtdCho structure. While simulations predict 74% and 8% occupancy of S203-mediated H-bonding of the PtdCho *sn*-2 and *sn*-1 acyl oxygen, respectively (i.e. 82 % occupancy of S203 mediated PtdCho-coordination), distances of the S203 hydroxyl group to both acyl oxygens exceed 5Å in the high resolution crystal structure and hence in theory should cause negligible polar interactions. A similar situation is observed in the context of the Sec14::PtdCho complex, where all three hydroxyl amino acids (here S173, T175, and S201) are conserved and where MD simulation likewise predicted a very robust interaction of S201 with the *sn*-2 acyl oxygen pf PtdCho (74% H-bonding occupancy), while predicting no interaction of S173 with the phosphate group at all (Figure 3).

In agreement with a less important role of S173 in PtdCho headgroup coordination as predicted by MD simulations, Ile, Val, and Trp substitutions at Sec14 position 173 did not cause any reduction in complementation efficiency of *sec14-1*^{ts}-associated growth defects or *sec14Δ*-associated lethality (Schaaf et al., 2008). It remains to be shown by mutational analyses and biochemical characterization whether Sfh1 residue S203 (and likewise Sec14 residue S201) is indeed involved in PtdCho-headgroup coordination and whether this interaction is physiologically important. Our preliminary data at this point support the idea that MD-simulations are powerful to describe Sec14-ligand interactions that are invisible to X-ray crystallography.

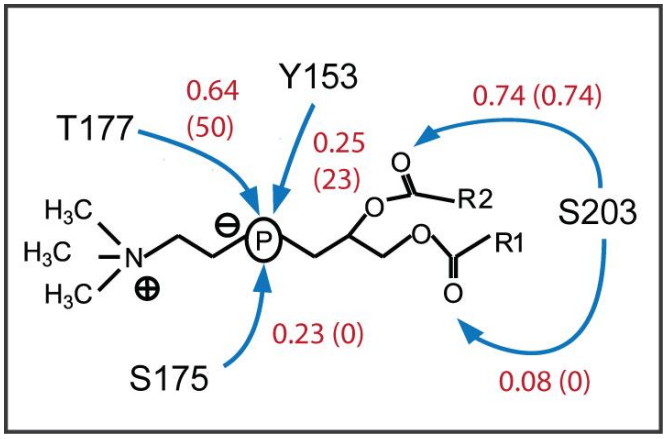

Figure 3. MD simulation analysis predicts a novel Protein/PtdCho interaction in Sfh1 and Sec14. H-bonding occupancies of PtdCho by Sfh1 and Sec14 residues (values for Sec14 are given in parenthesis) as predicted by MD-simulations. Note that the strong interaction of S203 to the acyl oxygen of *sn*-2 is absent in the high resolution structure obtained by X-ray crystallography.

Acknowledgements

We would like to thank Kristina E. Ile for critically reading this manuscript. We acknowledge *bwGrid*, member of the German D-Grid initiative, founded by the Ministry for Education and Research and the Ministry for Science, Research and Arts Baden-Württemberg, for providing computational resources (http://www.bw-grid.de). Contact information for MD simulation data, Marek.Dynowski@rz.uni-freiburg.de. This work was supported by Emmy Noether grant 1274/2-1 from the Deutsche Forschungsgemeinschaft.

References

Bankaitis, V.A., Aitken, J.R., Cleves, A.E., and Dowhan, W. (1990). An essential role for a phospholipid transfer protein in yeast Golgi function. Nature *347*, 561-562.

Bankaitis, V.A., Malehorn, D.E., Emr, S.D., and Greene, R. (1989). The *Saccharomyces cerevisiae* SEC14 gene encodes a cytosolic factor that is required for transport of secretory proteins from the yeast Golgi complex. The Journal of cell biology *108*, 1271-1281.

Bankaitis, V.A., Mousley, C.J., and Schaaf, G. (2010). The Sec14 superfamily and mechanisms for crosstalk between lipid metabolism and lipid signaling. Trends in biochemical sciences *35*, 150-160.

de Groot, B.L., and Grubmuller, H. (2001). Water permeation across biological membranes: mechanism and dynamics of aquaporin-1 and GlpF. Science *294*, 2353-2357.

Dynowski, M., Schaaf, G., Loque, D., Moran, O., and Ludewig, U. (2008). Plant plasma membrane water channels conduct the signalling molecule H2O2. Biochem J *414*, 53-61.

Gardino, A.K., Villali, J., Kivenson, A., Lei, M., Liu, C.F., Steindel, P., Eisenmesser, E.Z., Labeikovsky, W., Wolf-Watz, M., Clarkson, M.W., *et al.* (2009). Transient non-native hydrogen bonds promote activation of a signaling protein. Cell *139*, 1109-1118.

Li, X., Routt, S.M., Xie, Z., Cui, X., Fang, M., Kearns, M.A., Bard, M., Kirsch, D.R., and Bankaitis, V.A. (2000). Identification of a novel family of nonclassic yeast phosphatidylinositol transfer proteins whose function modulates phospholipase D activity and Sec14p-independent cell growth. Mol Biol Cell *11*, 1989-2005.

Ludewig, U., and Dynowski, M. (2009). Plant aquaporin selectivity: where transport assays, computer simulations and physiology meet. Cell Mol Life Sci *66*, 3161-3175.

Mizuno-Yamasaki, E., Medkova, M., Coleman, J., and Novick, P. (2010). Phosphatidylinositol 4-phosphate controls both membrane recruitment and a regulatory switch of the Rab GEF Sec2p. Dev Cell *18*, 828-840.

Phillips, S.E., Vincent, P., Rizzieri, K.E., Schaaf, G., Bankaitis, V.A., and Gaucher, E.A. (2006). The diverse biological functions of phosphatidylinositol transfer proteins in eukaryotes. Crit Rev Biochem Mol Biol *41*, 21-49.

Schaaf, G., Betts, L., Garrett, T.A., Raetz, C.R., and Bankaitis, V.A. (2006). Crystallization and preliminary X-ray diffraction analysis of phospholipid-bound Sfh1p, a member of the *Saccharomyces cerevisiae* Sec14p-like phosphatidylinositol transfer protein family. Acta Crystallogr Sect F Struct Biol Cryst Commun *62*, 1156-1160.

Schaaf, G., Dynowski, M., Mousley, C.J., Shah, S.D., Yuan, P., Winklbauer, E.M., de Campos, M.K., Trettin, K., Quinones, M.C., Smirnova, T.I., *et al.* (2011). Resurrection of a functional phosphatidylinositol transfer protein from a pseudo-Sec14 scaffold by directed evolution. Mol Biol Cell *22*, 892-905.

Schaaf, G., Ortlund, E.A., Tyeryar, K.R., Mousley, C.J., Ile, K.E., Garrett, T.A., Ren, J., Woolls, M.J., Raetz, C.R., Redinbo, M.R., *et al.* (2008). Functional anatomy of phospholipid binding and regulation of phosphoinositide homeostasis by proteins of the sec14 superfamily. Mol Cell *29*, 191-206.

Strahl, T., and Thorner, J. (2007). Synthesis and function of membrane phosphoinositides in budding yeast, *Saccharomyces cerevisiae*. Biochim Biophys Acta *1771*, 353-404.

Tajkhorshid, E., Nollert, P., Jensen, M.O., Miercke, L.J., O'Connell, J., Stroud, R.M., and Schulten, K. (2002). Control of the selectivity of the aquaporin water channel family by global orientational tuning. Science *296*, 525-530.